國立中山大學材料與光電科學學系

博士論文

塊狀金屬玻璃與複材之塑性分析及剪帶變形機構

Analysis of Plasticity and Shear Band Deformation Mechanism in Bulk Metallic Glasses and Composites

研究生：陳海明 撰

指導教授：黃志青 博士

中華民國 九十八 年 十一 月

A dissertation presented in partial fulfillment of the requirements

for the degree of Doctor of Philosophy

Analysis of Plasticity and Shear Band Deformation Mechanism in Bulk Metallic Glasses and Composites

by

Hai-Ming Chen

This study was conducted under the supervision of

Prof. **Jacob Chih-Ching Huang**

Department of Materials and Optoelectronic Science

National Sun Yat-Sen Univeristy

November, 2009

國立中山大學研究生學位論文審定書

本校材料與光電科學學系博士班

研究生陳海明（學號：D953060003）所提論文

塊狀金屬玻璃與複材之塑性分析及剪帶變形機構
Analysis of Plasticity and Shear Band Deformation Mechanism in Bulk Metallic Glasses and Composites

經本委員會審查並舉行口試，符合博士學位論文標準。

學位考試委員簽章：

高伯威	鄭憲清
黃志青	朱瑾
鍾文昌	

指導教授　黃志青

系主任/所長　鍾文昌

誌謝

中山大學依山傍水蘊含著豐富自然景觀，面對浩瀚海洋徐徐的海風總是能夠不斷地帶給我研究上的靈感，西灣夕陽更是經常浮現在腦海中珍貴的回憶。

回顧這幾年在研究所的日子，首先我要感謝恩師黃志青教授在論文研究與撰寫上的指導，感謝老師不遺餘力的諄諄教誨。研究上，老師一直都給予自由的空間，令我能夠恣意地的發揮自我以及盡情地從事論文研究，特別在遭遇瓶頸時，老師的鼓勵與建議總是適時地幫助我們，使我們即使跌倒也能夠再爬起來面對的挑戰，追求高深的目標，於此誠摯地獻上一聲：「老師，謝謝你！」學生我對於恩師為人處事的風範亦感到敬佩景仰，與老師相處更令我學習到教科書上所沒有教導的知識，與老師相伴從事研究救有如沐浴在春風中真的是一件很快樂的事。承蒙義守大學材料系鄭憲清教授及其實驗室學生們的鼎力相助，對於本人的論文研究有莫大的助益，於此特表感謝。

由衷地感謝恩師與中山大學材料系高伯威教授、謝克昌教授、台灣科技大學高分子系朱瑾教授以及義守大學材料系鄭憲清教授不辭辛勞地擔任論文口試委員，寶貴的意見與指正令本論文之內容更加完善更添色彩，令我獲益良多。此外，特別感謝赴美國從事學術研究交流的三個月期間，田納西大學材料系聶台岡教授於研究上分享其卓越的見解令我的研究繽紛多元，聶教授於生活起居無為不至的照顧令我雖遠在他鄉亦倍感窩心，同時感謝聶教授的學生們宋雙喜、王長利與王璐於研究上的討論互動，經常帶給我許多的靈感。感謝 Andrew Chuang、E-Wen Huang、Vincent Wang 以及 Meng Meng 在田納西在日常生活上的照顧，三個月的美國田納西行孕育出豐富的收穫與回憶。

研究所期間深受許多人的幫助，有你們的幫忙令我可更專心地從事研究。感謝中山大學貴重儀器中心各技術員陳貴香、李秀月以及王良珠小姐提供儀器與協助樣品測試。感謝中山大學奈米科技研發中心顏采蓉與鹿文卿小姐協助研究相關事務。感謝黃谷正教官在校園生活的照顧。感謝所辦朱惠敏、顏秀芳和陳秀玉小姐在行政公務處理的幫忙。感謝系上華應騏大哥在做人做事上態度的教導，令小弟我獲益匪淺。感謝熱心的孫得凱

學長在儀器測試操作上細心的教學。

精采的研究歲月中，先感謝實驗室金屬玻璃的第一把交椅洪子翔學長，子翔學長將其研究經驗毫無保留地傳授，懇切耐心的指導令我有好的研究基礎，此刻的成果學長功不可沒。感謝實驗室博士後研究員杜興蒿博士的跨海相助，杜博士的建議對本研究有相當大的助益。感謝實驗室另一位博士後研究員李敬仁博士，每每與他討論常令我茅塞頓開增廣見聞，李博士的研究精神以及對實驗熱忱的態度更是值得效法的對象。感謝遠在美國佛羅里達大學的鄭宇庭學長，不時的關懷與鼓勵令我可以一次又一次地突破研究上的瓶頸。感謝張志溢學長，於茶餘飯後的閒聊總是令我抒解心中的壓力。羅有杰博士獨特的個性與豐富的知識，往往於關鍵時刻一句話就能夠扭轉情勢，令我敬佩景仰。摯友賴炎暉博士溫和的個性，善良的一顆心溫暖了整個實驗室，有他在的環境可謂是充滿著祥和的分圍，其為人令我讚嘆不已。感謝實驗室這些可愛的學弟妹，永遠踩足馬力在研究努力不懈的拼命三郎周鴻昇學弟，待人貼心憑著一個微笑就能征服人心的斯威特劉名哲學弟，充滿幹勁淺力無窮多次完成不可能任務的裴帥裴浩然學弟，才華洋溢的阿湯湯振緯學弟，溫和耿直的肌溝郭哲男學弟，陽光燦爛的宋大豪學弟，本土早根性的孫碩陽學弟，還有實驗室學弟們林逸志、陳柏佑、官聖堯、王顗任以及可愛的學妹胡婷婷，有你們的相伴令我的研究生活更多彩多姿，不會孤單寂寞處處充滿著快樂的回憶。

接著感謝我的同儕好友小麻蔡育霖、樂咖林俊宏、阿強陳景強、冰紅茶高弘杰、時尚男陳靖允、賴肥賴俊誠以及材料所的美女李宜珊，你們的鼓勵與陪伴讓我更珍惜這份回憶，這段期間大家一起奮鬥，互相支持，扯出的荒唐事以及成就的豐功偉業，這些酸甜苦辣是我這輩子無價的財富。

最後我要特別地感謝我的父母和弟弟以及愛護我的親戚們，在學業上或生活上一直都默默的支持我，不遲辛勞的付出，讓我能夠無後顧之憂的向前邁進面對挑戰，你們關懷愛護的恩情無以回報，我愛你們。這份榮耀歸給上帝，感謝主！

陳海明 謹誌

於中山西灣

Content

List of Tables

List of Figures

中文摘要

近幾年來,如何改善塊狀金屬玻璃(bulk metallic glass)的脆性是一個很重要的議題。本研究中，藉由熱力學的計算，我們成功地製備出具有液態相分離結構的鋯鎳銅鋁($Zr_{63.8}Ni_{16.2}Cu_{15}Al_5$)塊狀金屬玻璃。基於在均質的非晶結構中分佈著液態相分離，相分離鋯基塊狀金屬玻璃的壓縮塑性可以被改善至高達 15%。透過研究不同壓縮應變量的相分離鋯基塊狀金屬玻璃，其結果顯示塊狀金屬玻璃變形方式為，先約 2%的彈性變形，接著混亂眾多的剪切帶(shear band)會在變形初期形成，然後逐漸地發展成一個主要的剪切帶，並且此剪切帶幾乎支配整個塑性變形直到破壞之前。同時，沿著剪切平面上之主要剪切帶的局部應變會隨著越遠離剪切帶起始形成位置越遠而降低。為了更進一步地去分析此主要的剪切帶，影像紀錄器被應用來紀錄完整的試片變形的過程，根據影像結果發現，應力應變圖塑性區間中的鋸齒狀現象(Serration phenomenon)與影像中每次的剪切滑移有著一對一相符合的結果,說明這些鋸齒狀現象是由在變形的過程中試片間歇性的滑移所引起。

隨後，高取樣速度的應變量測計被使用來研究鈀基塊狀金屬玻璃($Pd_{40}Ni_{40}P_{20}$)之應力應變圖中的鋸齒狀現象與剪切帶傳播(shear band propagation)。由於兩片應變量測計是直接地黏貼在測試試片的兩側，故一旦剪切帶形成開始傳播時，兩側的應變量測計會立即補抓到一突然性的位移變化量。基於位移時間曲線，剪切帶傳播速度可以被量測並且發現此速度對外加應變速率並不敏感。在高應變速率下，鋸齒狀現象消失的原因並非是缺乏剪切帶的形成也並非是剪切帶速度改變，而只是因為突然性的位移變化量之訊號被運行中的外加應變速率所淹蓋過去。同時，利用此剪切帶傳播的速度可以計算出剪切帶傳播期間的剪切帶黏度，而此黏度值與一般在高溫過冷液體區間均勻變形下所得到的黏度值相似。比較五種不同的塊狀金屬玻璃，如脆性的鎂基、金基、銅基、延性的鈀基以及具有相分離的鋯基塊狀金屬玻璃，我們發現金屬玻璃的塑性與剪切帶傳播間的動態有

著密切的關係，在本質上延展性越好的金屬玻璃其剪切帶傳播的速度會比較慢。

藉由添加二十五體積百分比的具孔隙性鉭顆粒來強化鎂基塊狀金屬玻璃，此鎂基塊狀金屬玻璃複材的塑性可以被改善至高達約 10%，與一般文獻上沒有塑性能力的鎂基塊狀金屬玻璃有著很大的區別。然而，在應力應變圖的塑性區間中卻缺乏鋸齒狀的現象。使用應變量測計來研究此鎂基塊狀金屬玻璃複材的剪切帶傳播，結果亦顯示沒有補抓到任何突然性的位移變化量。基於此塊狀金屬玻璃複材微結構的形貌，鋸齒狀現象的消失與缺乏長程的剪切帶傳播有關。透過將一均質玻璃基地區分成許多的分隔區塊，在目前的鎂基塊狀金屬玻璃複材中，只有短程的剪切帶傳播在運行著。考慮強化相顆粒之間的間距以及強化相顆粒的尺寸大小，我們提出一個模型可以成功地解釋塊狀金屬玻璃複材裡剪切帶傳播的發展，同時，此模型對於在設計具延展性的金屬玻璃複材來說將會是個有助益的指標。

Abstract

On the toughening of bulk metallic glasses (BMGs), successful results in the phase-separated $Zr_{63.8}Ni_{16.2}Cu_{15}Al_5$ BMG have achieved compressive ductility over 15% through the computational-thermodynamic approach. In this study, the phase-separated $Zr_{63.8}Ni_{16.2}Cu_{15}Al_5$ BMG was compressed to nominal strains of 3%, 7%, and 10% at low strain rates (~10^{-4} s^{-1}) and the results demonstrated that the BMG exhibited apparent uniform deformation initially, followed by visible local shear bands development. Afterwards, a single shear along the principal shear plane was soon developed and mainly dominated the whole deformation process. The principal shear contributed more than 2/3 of the overall plastic strain until failure. It was also found that the local shear strain varied along the principal shear plane and decreased monotonically from the shear band initiation site. Subsequently, in-situ compression experiments were conducted to monitor the change of sample shape during deformation in order to properly correlate with the stress-strain curve. The observed images showed that there was a one-to-one correspondence between the intermittent sample sliding and flow serration in the plastic region of stress-strain curve.

Further investigations on flow serration were conducted on the $Pd_{40}Ni_{40}P_{20}$ BMG through the compression experiments equipped with high-sensitivity strain gauges directly attached to two opposite sides of the test sample. There was an accompanied displacement burst when a shear band starts to propagate during deformation and this displacement burst would be accurately captured by the high-sensitivity strain gauges. Based on the displacement-time profile for one serration, shear-band propagating speed can be estimated and found to be insensitive to the applied strain rates (or the applied crosshead speeds). The disappearance of flow serration at high strain rates should be a result that the signal of

displacement burst was overwhelmed by the applied strain rate. Using the shear strain rate data, the measured viscosity within a propagating shear band was found to be relatively low, which is in similar to the viscosity values reported in the supercooled liquid region during homogeneous deformation. In comparison with shear band propagation in the brittle $Mg_{58}Cu_{31}Y_6Nd_5$ and $Au_{49}Ag_{5.5}Pd_{2.3}Cu_{26.9}Si_{16.3}$, moderately ductile $Cu_{50}Zr_{43}Al_7$ and $Pd_{40}Ni_{40}P_{20}$, and highly ductile phased-separated $Zr_{63.8}Ni_{16.2}Cu_{15}Al_5$ systems, the ductility of BMGs appears to be closely related to the dynamics during shear band propagation. The more ductile in nature the metallic glass is, the slower the shear band propagating speed would become.

We also made attempts to investigate the shear band propagation in the porous Mo particles reinforced $Mg_{58}Cu_{28.5}Gd_{11}Ag_{2.5}$ bulk metallic glass composites (BMGCs) with up to 10% compressive failure strain. It was found that flow serration was absent in the stress-strain curve. Using high-sensitivity strain gauges, no distinct displacement burst was detected in the displacement-time profile. The diappearance of flow serration for the current porous Mo particles reinforced $Mg_{58}Cu_{28.5}Gd_{11}Ag_{2.5}$ BMGC is apparently associated with the lack of long-range shear band propagagtion. By employing the approach of separating the homogeneous amorphous matrix into many individual compartments, only short-range shear band propgagation is possible in the current Mg-based BMGC. An effective free spacing considering the spacing between two porous Mo particles and porous Mo particle size was applied to interpret the development of shear band propagation and is a useful indicator for the design of BMGC with high ductility.

Chapter 1 Introduction

1.1 Amorphous alloys

Amorphous alloys are disordered materials that lack crystalline periodicity. The structure of amorphous alloys could be defined by the absence of long-range-order (LRO) structure in contrast to crystalline materials showing the periodically atomic arrangement configuration with repeating unit cell. However, the atomic arrangement of amorphous alloys is not completely random, but maintains a greater degree of short range order (SRO) than that in a liquid, as shown in Figure 1. Due to their structure, amorphous alloys have also been called as liquid metals, non-crystalline metals, glassy metals, or metallic glasses.

Generally, high cooling rates are required to produce amorphous alloys in the form of ribbons, flakes, powders or rods. If a melt metallic liquid is quenched rapidly, the heterogeneous atoms do not have sufficient time and energy to rearrange for crystal nucleation. Then the liquid reaching the glass transition temperature is solidified as an amorphous alloy. Great efforts have been made to enhance this category of materials into bulk size. More and more global researchers discover many methods to fabricate amorphous alloys by employing much lower cooling rates or various combinations of alloy compositions. The increased demand for hard, strong and anticorrosive materials which can resist severe environmental conditions has stimulated extensive investigation on bulk metallic glasses (BMGs). BMGs can expand the applications in engineering area further by eliminating the limit of sample size.

Amorphization of metallic materials might result in sometimes excellent properties in

mechanical strength and toughness compared with those of the corresponding crystalline alloys. Over the past decades, BMGs have attracted extensive interests due to their unique mechanical and physical properties attributed to the atomic structure of amorphous phase [1-7], such as high strength, large limit of elastic deformation, good shaping and forming in the viscous state, reasonable corrosion resistance, as well as good fatigue properties, which are different from the corresponding crystalline alloys. The fundamental properties and application fields of amorphous alloys are listed in Table 1.1 [5].

1.2 Early developments of metallic glasses

The formation of metallic glasses was first fabricated by Duwez et al. [8] in 1960 by using a splat quenching approach in the binary Au-Si alloy, it was recognized that this is the first method to rapidly quench from melt metallic liquid to metallic glass ribbons. Subsequently, the techniques of melt quenching have been extensively innovated to produce various metallic glasses. Researches on metallic glasses had attracted increasing attentions in 1970s and 1980s when casting processes was developed producing ribbons, wires, and sheets for the commercial manufacture [9]. However, a high cooling rate was required to prepare metallic glasses and thus limited their geometry to thin sheets and wires.

A few years later, Chen et al. [10] produced amorphous spheres of ternary alloy system in Pd-Si-N (N = Ag, Cu or Au). The $Pd_{77.5}Cu_6Si_{16.5}$ metallic glass could be fabricated with the order of millimeter scale in diameter (0.5 mm) and show the existence of glass transition. In some Pd-Cu-Si and Pd-Ag-Si alloys, the temperature interval in supercooled liquid region was extended to 40 K, which enables worldwide researchers to perform the detailed studies in metallic glasses. In 1974, Chen [11] made systematic investigations on ternary Pd-T-P alloys (T = Ni, Co or Fe) and these alloys could be prepared with a casting thickness of 1 mm.

1.3 Birth of bulk metallic glasses

The Pd-Ni-P system was considered as the production of first bulk metallic glass (BMG) developed by Chen [12] in 1974 if one defines the millimeter scale as bulk. In the beginning of 1980s, Drehamn et al. [13] returned to investigate the Pd-Ni-P alloy system. By subjecting the samples to surface etching, followed by a succession of heating and cooling cycles, they decreased heterogeneous nucleation of crystals and then successfully produce glassy ingots in $Pd_{40}Ni_{40}P_{20}$ with a diameter of 5 mm. In 1984, Kui et al. [14] extended a critical casting thickness of the $Pd_{40}Ni_{40}P_{20}$ alloy up to 10 mm by using a boron oxide fluxing method. In the late 1980s, Inoue's group of Tohoku University in Japan investigated the rare-earth materials with Al and Fe metals. While Inoue and his coworkers studied rapid solidification for these systems, they found a wide supercooled liquid region in the Al-La-Ni and Al-La-Cu alloy systems [15, 16]. Cylindrical BMG samples with diameters up to 5 mm or sheets with similar thicknesses were made fully glassy in the $La_{55}Al_{25}Ni_{20}$ alloy by casting into the copper mold with water cooling, and, later, the $La_{55}Al_{25}Ni_{10}Cu_{10}$ alloy was fabricated with a diameter up to 9 mm using the same method [17, 18].

In 1991, Inoue's group developed the ternary Mg–Cu–Y and Mg–Ni–Y alloys with the largest glass forming ability (GFA) obtained in $Mg_{65}Cu_{25}Y_{10}$ [19]. Meanwhile, Inoue's group also developed a family of Zr–Al–Ni–Cu alloys exhibiting a high GFA and good thermal properties. The critical casting thickness of the $Zr_{65}Al_{7.5}Ni_{10}Cu_{17.5}$ alloy was raised up to 15 mm and the supercooled liquid region was extended to 127 K [20]. In 1997, Inoue's group revisited the $Pd_{40}Ni_{40}P_{20}$ alloy and replaced 30% Ni (in at. %) by Cu. As a result, they produced an alloy with a diameter of 72 mm [21]. The Pd–Cu–Ni–P family has been considered as a alloy system with the highest GFA to date. The critical casting thicknesses of metallic glasses over the years are illustrated in Figure 1.2 [22]. Subsequently,

Inoue [23] succeeded in finding new multicomponent alloy systems mainly consisting of common metallic elements and proposed the empirical rules to form BMGs with a high GFA and lower critical cooling rate. The evolution of these alloys demonstrated that composition plays an important role in the critical size of BMG.

Due to the cost and heavy weight of Pd metal, the light weight metallic glasses such as Mg, Al, Ti and Zr-based alloys with the aim of improving the specific strength were developed. So far, researches in the area of BMG are significantly growing. Many researchers have been searching for new alloy compositions and investigating the microstucture, thermal properties, mechanical behaviors and deformation mechanism of these alloys. The amorphous matrix of Zr-Al-Cu-based BMG containing nanocrystalline phases could exhibit high strength and good ductility. the mechanical properties are better than those seen in some monolithic BMGs [24, 25]. After that, more and more investigators in the world would pay attentions on the metallic glasses and metallic glass composites with nanocrystals.

1.4 Status of bulk metallic glasses

As well known, ductile crystalline alloys possess large plastic deformation due to their easy-slip deformation feature and good strain-hardening ability. Nevertheless, the plastic deformation in BMGs subjected to highly localized shear band formation is inhomogeneous at room temperature [1, 26]. Shear bands propagate fast because of the lack of strain hardening so that BMGs are very easy to fracture catastrophically before or upon yielding occurrence and are unable to accommodate remarkable plastic strain until failure [27, 28]. The lack of plasticity resulting from work-softening and shear localization makes BMG difficult to be extensively applied in engineering fields. To overcome the dilemma, intensive efforts have been made and promising strategies have been developed in the past decades

[29-36]. Generally, it could be divided into two ways: one is intrinsic toughening by increasing the Poisson's ratio [29, 30], and the other is extrinsic toughening by developing a composite microstructure within the glassy matrix [31-36].

Except for the above approaches, some other methods still have been tried for the improvement in toughness of BMG [37-43]. As proposed by Zhang et al. [37], the mechanical performance of BMGs was improved in bending and compression by controlling surface residual stresses induced by shot peening. Yu et al. [38] found that high-pressure pretreatment at room temperature also can significantly improve the mechanical performance of BMG. Especially for compressive plasticity, it increases with increasing pressure. Besides, the sample geometry also plays an important role in the formation of shear bands and the capability of plastic deformation [39-43]. As the aspect ratio (height to diameter) of cylindrical test sample is lowered down to less than 1, shear band propagation was constrained and multiplication of shear bands is prone to form so that BMGs present a large deformation with apparent plastic strain more than 10%. This is true not only for ductile Zr-based BMGs with a higher Poisson ratio (0.35-0.4) [39-42], but also for brittle Mg-based BMGs with a lower Poisson ratio (0.3-0.35) [43]. The geometric effects would impose the improvement of mechanical performance of BMGs.

Although the deformation mechanisms of BMG are yet to be investigated in details, it is known that, after an initial elastic deformation, BMGs deform by highly shear localization. Unlike crystalline metals, the interactions of dislocations will produce strain-hardening and homogeneous deformation. Conversely, once plasticity is initiated in BMG, it remains localized in narrow zones, which is called as shear band, and does not spread throughout the material. As a result of inhomogeneous deformation, BMG samples always shear off at ~45^{o} with respect to the loading axis along a major shear plane with plastic strains < 2% in

compression and essentially zero ductility in tension [28, 44]. Even in ductile Pd- or Zr-based systems, these BMGs still lack sufficient plasticity. Recently, many efforts in the ductility of BMG shed light that BMGs seem to have potential to exhibit remarkable plasticity if they are inhered in some unique structures. This prospect may be a turning point for BMG and will make BMG infinite potentials for applications in many fields.

1.5 Motivation

One of the current critical issues for BMG appears to toughen their brittle nature. In conventional engineering materials such as intermetallic compounds and ceramics, we can improve mechanical properties by the formation of duplex or multiphase microstructure which can provide effective obstacles for the propagating micro-cracks. The premature fracture of BMG is induced from the excessive propagation of shear bands, as micro-cracks of crystalline materials. Following these ideas, the development of a phase-separated microstructure is expected to be of potential interest in terms of the ductility improvement of BMGs. The early efforts to obtain BMGs with phase separation usually involve the addition of alloying elements with a positive enthalpy of mixing into the master alloy systems and, thus, surely make the resultant BMGs to bear with a lower GFA [45, 46].

From a viewpoint of ductile BMG with a high GFA, we note that the Zr–Cu–Ni–Al alloy system is a good candidate, since it includes an atomic pair with a slight positive enthalpy of mixing between Ni and Cu elements [47]. The relationship of heats of mixing heat (ΔH_{mix}) among the component elements in the Zr-Ni-Cu-Al alloy system is listed in Table 1.2. However, the positive ΔH_{mix} between Cu and Ni is very slight (+4 kJ/mol), how to point out the alloy composition exhibiting phase separation appears to be a scientific challenge. A computational thermodynamic approach is applied to pinpoint the optimum

composition in the Zr–Cu–Ni–Al alloy system, explicitly described in Chapter 3 of this thesis. Based on this approach, the two-liquid miscibility phase equilibrium in the liquid-temperature region can be identified in the Zr-Cu-Ni-Al system. By employing the concept of phase separation within the homogeneous glassy matrix, it can be expected that the brittle nature of BMG would be toughened to overcome the awkward situation of limiting ductility.

Another crucially important issue for BMG is to analyze the flow serration and shear band deformation mechanism during the plastic deformation of BMG, especially for the dynamics during shear band propagation. To clarify this issue, a monolithic BMG with homogeneous glassy microstructure is necessary for easily discussing shear band propagation and a ductile BMG is essential for sufficient plasticity analyzing for flow serrations as well. We notice that the Pd-Ni-P alloy system, widely investigated in early 1980s, satisfies these conditions. Furthermore, the monolithic Mg-based BMG, a typical representative of brittle BMGs, always fragments into several pieces by catastrophic fracture once the limited elastic is attained. This inspires us to compare the difference of shear band dynamics in ductile Pd-based BMG and brittle Mg-based BMG. In contrast with monolithic Mg-based BMG, the porous Mo particles reinforced Mg-based BMG composite, exhibiting a significant improvement in ductility, is also worthy of studying the interaction between the reinforcement and shear bands.

In this study, the toughened Zr-based BMG with phase separation compressed to various plastic strain stages was analyzed in terms of their mechanical behaviors, especially for plastic strain and deformation mode. To shed light on the shear-band dynamics, the investigation on flow serration and shear-band propagation was subsequently carried out. We compare three various types of BMGs, ductile Pd-based BMG, brittle Mg-based BMG and Mg-based BMG composite reinforced with porous Mo particles, and discuss the relationship

between shear-band dynamics and ductility of BMGs.

Chapter 2 Background

2.1 Evolution of fabrication methods

The fabrication methods of amorphous alloys could generally be divided into the following three types [48]: (1) from gas state to solid state: sputtering and vacuum evaporation; (2) from liquid state to solid state: splat quenching method, single or two-roller quenching process, chill block melt spinning process (CMBS), planar flow casting process (PFC), spray forming process, casting method by a conventional metallic mold and high pressure die casting method, and (3) from solid state to solid state: ion implantation, ion beam mixing, mechanical alloying (MA) and accumulative roll bonding (ARB).

The liquid quenching method operated at the cooling rate of 10^3 ~ 10^8 K/s is the major method widely applied to fabricate different types of amorphous alloys such as powders, wires, ribbons and bulks. The process of liquid quenching method can generally be described in the way that alloys are first heated to the melted liquid condition, after melting homogeneously, the alloys are sucked, poured or injected into the casting metallic mold with a high cooling rate to result in amorphous alloys.

The fabrication of amorphous alloy started from the splat quenching method by Klement et al. [8] on the $Au_{75}Si_{25}$ alloy systems in 1960. This was recognized to be the first report of formation of amorphous alloys by quenching liquid. A schematic diagram of the splat quenching method is as illustrated in Figure 2.1. However, this method could not produce the uniform shape and size of amorphous alloys. In 1970s, these limitations of amorphous alloys have been removed by the two roller technique proposed by Chen and Miller [49], as

illustrated in Figure 2.2. This method is the one in which uniform long samples are produced due to flattening out quenching of dropped alloys between two rotating wheels. It is a continuous process to be applied for preparing thin solidified films or foils.

In 1976, the chill block melt spinning method (CMBS) was developed by Liebermann and Graham [50], as shown in Figure 2.3. The CBMS method involves the formation of a melt jet by the elimination of a melt alloy through an orifice and the impingement of this jet against a rapidly moving substrate surface. The puddle which results from continuing impingement of melt jet serves as a local reserver from which ribbon is continuously formed and chilled. Among various rapid solidification processes, the single roller chill block melt spinning is the most popular method due to its simplicity in fabrication and effectiveness of rapidly solidified ribbons.

In 1980, Narasimhan and his coworkers [48] developed the planar flow casting (PFC) process for the fabrication of rapidly quenched tapes in which nozzle is held very close to moving substrate surface. The schematic diagram is illustrated in Figure 2.4. The major difference between CBMS and PFC is that the nozzle of the PFC process is brought closer to the quenching wheel, so that the melt is more stable to suppress oscillation of puddle. The PFC process not only enhances process stability but also allows a better control of ribbon dimension. The PFC process improves the quality of amorphous ribbons and makes wider amorphous ribbons easily.

Until 1991, Inoue et al. [19] succeeded in the fabrication of BMG in Mg-Cu-Y alloy system with a diameter of 4 mm by pouring the melt into water-cooled copper mold, like a conventional casting method. Next year, the same group [51] succeeded in producing the $Mg_{65}Cu_{25}Y_{10}$ bulk metallic glasses with a increased diameter up to 7 mm by using

high-pressure die casting method. As the worldwide efforts, BMGs could expand the application area further by eliminating limitation of amorphous alloy in size.

2.2 Systems of bulk metallic glasses

So far, a large number of BMGs have been reported. The alloy system of BMGs could conveniently be divided into two main types, as shown in Table 2.1 [5]. Table 2.1 summarizes the types of BMG systems reported to date and the calendar years when details of each alloy system were published. Generally, BMGs can be simply separated into nonferrous and ferrous alloy systems. The nonferrous alloy systems include Mg-Ln-M (Ln = lanthanide metal, M = Ni, Cu or Zn), Ln-Al-TM (TM = VI~VIII group transition metal), Ln-Ga-TM, Zr-Al-TM, Zr-Ti-Al-TM, Ti-Zr-TM, Zr-Ti-TM-Be, Zr-(Nb, Pd)-Al-TM, Pd-Cu-Ni-P, Pd-Ni-Fe-P, Pd-Cu-B-Si, and Ti-Ni-Cu-Sn systems. On the other hand, the ferrous alloy systems involve Fe-(Al, Ga)-metalloid (P, C, B, Si, Ge), (Fe, Co, Ni)-(Zr, Hf, Nb)-B, Fe-Co-Ln-B, and Ni-Nb-(Cr, Mo)-(P, B) alloys. The ferrous alloy systems have been developed during last four years after the synthesis of nonferrous alloy systems.

The components of BMG are classified into five categories, as summarized in Table 2.2 [5]. First group consists of ETM (or Ln), Al and LTM as exemplified for the Zr-Al-Ni and Ln-Al-Ni systems, where ETM is IVB~VIB Group Transition Metal and LTM is VIIB~VIIIB Group Transition Metal. Second group is composed of LTM, ETM and metalloid as indicated by Fe-Zr-B and Co-Nb-B systems. Third group is LTM (Fe)-(Al, Ga)-metalloid systems, and Fourth group is indicated by Mg-Ln-LTM and ETM (Zr, Ti)-Be-LTM systems. However, Fifth systems as Pd-Cu-Ni-P and Pd-Ni-P systems are composed only of two kinds of group element (LTM and metalloid), which are different from the combination of three types of group elements for the alloys belonging to the four previous groups.

It is noticed that BMGs could be produced in many important engineering alloy systems, such as Fe-, Co-, Ni-, Ti-, Mg-, Pd-, Cu- and Zr-based alloy systems. Furthermore, the maximum diameter of BMGs done by the investigators worldwide generally tends to increase in the order of Pd > Zr > Mg or Ln > Fe > Ni > Co or Ti systems.

2.3 Indexes of glass forming ability

Metallic glasses could be produced by rapid quenching from the melt liquid to solid when quenching rate exceeds its critical cooling rate. GFA is related to the ease of glass forming. It is very crucial indicator to understand the origins of glass formation and also important for designing and developing new metallic glasses. Generally speaking, the high GFA of as-cast metallic glasses means a larger size of a metallic glass is obtained easily under a lower cooling rate. So far, many literatures reported that the GFA is associated with thermal properties [52-54], atomic sizes [55-59], compositions [60-65] and electronic configurations [66-73] of metallic glasses, respectively.

The GFA of alloy is evaluated in terms of the critical cooling rate (R_c) for forming metallic glasses, which is the minimum cooling rate keeping the melt amorphous alloy without any precipitation of crystals during solidification process. The smaller R_c, generally, the higher GFA of alloy system should be. However, R_c is a parameter which is difficult to evaluate precisely. So far, extensive efforts have been devoted to searching for a simple and creditable criterion for quantifying GFA of metallic glasses. As a result, many criteria have been proposed to describe the relative GFA of metallic glasses on the basis of characteristic temperatures measured by differential thermal calorimetry (DSC) or differential thermal analysis (DTA).

The most extensively used criterion is the reduced glass transition temperature, T_{rg} [74, 75] (= T_g/T_l, where T_g is the glass transition temperature and T_l is the liquidus temperature) and the supercooled liquid region, ΔT_x (= T_x-T_g, where T_x is the onset crystallization temperature and T_g is the glass transition temperature). As proposed by Lu et al. [74, 75], T_{rg} shows a better correlation with GFA than that given by T_g/T_m [76] for BMGs, where T_m is the solidus temperature. Usually the ΔT_x and T_{rg} are popularly used as indicators of GFA for metallic glasses. The tendency for R_c is prone to decrease with increasing T_{rg}, as shown in Figure 2.5. From the viewpoint of T_{rg} (= T_g/T_l), T_l is dependent on composition, selecting a proper composition close to deep eutectic point is useful for the probability of cooling fast through the supercooled liquid region without any occurrence of crystallization, i.e., the GFA of alloy would be increased. As to another parameter ΔT_x (= T_x-T_g), the thermal stability of alloy could be increased by increasing T_x, i.e., a good thermal stability for metallic glass with a wide ΔT_x indicates that metallic glass has superior resistance against crystallization from the supercooled liquid upon heating. Figure 2.6 shows that R_c decreases with increasing ΔT_x so that the size of metallic glasses would be increased.

Although both ΔT_x and the ratio of T_g/T_l are used as indicators of GFA for metallic glasses, both indicators still did show contrasting trends versus GFA in many alloy systems. Waniuk et al. [77] confirmed that the T_g/T_l value is well correlated with GFA in Zr–Ti–Cu–Ni–Be alloys, whereas the supercooled liquid region, ΔT_x, has no relationship with GFA in the least. Those glassy compositions with the largest ΔT_x are actually the poorest glass formers in this alloy system. Inoue et al. [78, 79] also proved that the GFA for metallic glasses is more closely associated with T_g/T_l values in Cu-Zr-Ti ternary systems rather than ΔT_x. On the other hand, the ratio of T_g/T_l is not reliable enough to infer relative GFA in $Pd_{40}Ni_{40-X}Fe_XP_{20}$ (X = 0 to 20) alloy systems [80]. On the contrary, ΔT_x is claimed to be a reliable and useful criterion for the optimization of BMG formation in this systems.

Later, a new criterion for critical cooling rate and critical thickness to reflect the GFA of BMGs was proposed by Lu and Liu [81, 82]. The new parameter γ was defined for inferring the relative GFA among all BMGs, which can be expressed as follows:

$$\gamma = \frac{T_x}{T_g + T_l}. \tag{2-1}$$

As illustrated in Figure 2.7, to obtain an amorphous alloy with a good GFA, two purposes must be considered. One is the stabilization of liquid phase, and the other is resistance of crystallization. If an amorphous alloy has a lower T_l, it means that melting liquid phase can be maintained at low temperatures under a cooling step. If an amorphous alloy shows a lower T_g, it means that metastable glass phase is more stable at low temperatures. These both cases indicate that liquid phase is stability. On the contrary, while amorphous alloy has higher T_x, it suggests that glassy phase must crystallize at quite high temperature upon heating. The summary of ΔT_x, T_{rg}, γ, critical cooling rate R_c and critical section thickness Z_c obtained by DSC and DTA for various alloy systems is listed in Table 2.3. Regardless of alloy system, the relationship between γ and critical cooling rate R_c (K/s) as well as critical section thickness Z_c (mm) has been formulated as follows:

$$R_c = 5.1\times10^{21}\exp(-117.19\gamma), \tag{2-2}$$

$$Z_c = 2.8\times10^{-7}\exp(41.7\gamma). \tag{2-3}$$

Note that these two equations can be utilized to roughly estimate R_c and Z_c when γ is measured readily from DSC or DTA measurements. Furthermore, the new parameter γ reveals a stronger correlation with GFA than T_{rg} and has been successfully applied to glass formation in the BMG systems.

Subsequently, several parameters or criteria have continuously been proposed to evaluate the GFA for metallic glasses by different methods, such as $\Delta T_{rg} = (T_x - T_g)/(T_l - T_g)$ [56], $\phi = T_{rg}(\Delta T_x/T_g)$ [83], $\delta = T_x/(T_l - T_g)$ [84]. However, there are still not reliable criteria to predict the GFA of metallic glasses in various alloy systems. Following the previous arguments by Lu and Liu [81, 82], recently a modified γ parameter, γ_m, was proposed by Du et al. [85]. The γ_m value couples two terms, liquid phase stabilization ($\Delta T_x/T_l$) and crystallization resistance (T_x/T_l), and can be expressed as below:

$$\gamma_m = \frac{T_x - T_g}{T_l} + \frac{T_x}{T_l} = \frac{2T_x - T_g}{T_l}. \qquad (2\text{-}4)$$

The γ_m parameter reflects the effects of T_g, T_x and T_l based on the measurement of devitrification for glassy samples, similar to the previous γ parameter. Because all related factors are correctly and carefully considered for the liquid phase stability and crystallization resistance during glass formation, this γ_m parameter appears to show the best correlation with the GFA for BMGs among all parameters reported so far. The statistical correction factor, R^2, can show effectiveness and consistency of various GFA parameters. It is believed that the higher R^2 value, the more reliable correlation between the proposed GFA parameter. The γ_m parameter exhibits the highest R^2 value among different GFA parameters based on the corresponding experimental data. Similar to the γ value, the relationship between the γ_m value and critical cooling rate R_c (K/s) of amorphous alloys can be formulated as follows:

$$\log R_c = 14.99 - 19.441\gamma_m. \qquad (2\text{-}5)$$

This γ_m value could be calculated easily according to the data on T_g, T_x and T_l measured by DSC and DTA and will be a simple and user-friendly indicator for GFA of BMGs.

2.4 Empirical rules for the formation of amorphous alloys

Since the discovery of amorphous alloys, a number of attempts have been made to understand the mechanism of amorphization for the prediction of alloy composition with better GFA. There are several various methods to produce BMGs, but investigators worldwide gradually intend to understand that the correct designed alloy composition system would lead to metallic glasses with a critical cooling rate as low as 1-100 K/s. In the past decade, the Inoue's group had developed a series of amorphous alloy systems with high GFA, and, then, they summarized and proposed three simple empirical rules [5, 23] for the design of alloy composition to fabricate BMGs. These are (1) multicomponent systems consisting of more than three elements; (2) significant difference in atomic size ratios above 12% among the main constituent elements; (3) negative heats of mixing among the main constituent elements. If there are more than three different elements mixed together and the difference in atomic size is large above 12%, the moving atoms will be retarded when quenching the melt into a solid state and the atoms cannot rearrange easily in the solidified process and, consequently, the atomic configuration of alloy system tends to form a high dense random packing, as shown in Figure 2.8. According to the thermodynamic theory, the heat of mixing is regarded as the ability of atomic bonding in an alloy system. Larger negative heat of mixing means that the ability of atomic bonding for distinct atoms is stronger than that for the same atoms, namely, distinct atoms tend to get together and arrange in a random way when the melt is quenched in a solidified process. The larger negative heats of mixing for constituent elements could contribute to stabilization of the liquid phase by changing the local atomic structure.

As illustrated in Figure 2.9, an alloy system satisfied with above three empirical rules, which has a higher dense degree of randomly packed atomic configurations in a supercooled

liquid, will have high solid/liquid interfacial energy which is favorable for the suppression of nucleation and growth of a crystalline phase. The liquid can have the difficulty of atomic rearrangement, leading to a decrease of atomic diffusivity and an increase of viscosity in a liquid. Therefore, the liquid will show a high glass transition temperature, T_g. In any event, the multicomponent alloys satisfied with three empirical rules always have very deep eutectic point with low liquidus temperatures, T_l, leading to high T_{rg} value [5].

Although these empirical rules are certainly useful for selecting multicomponent alloy system to form BMGs, the development of new BMGs is still a very time-consuming process. In order to identify promising glass forming compositions, it is required to experimentally map out the GFA of every single composition in a given alloy system. In multicomponent alloy systems, hundreds of alloy compositions have been prepared and evaluated for glass formation. Therefore, finding a more specific criterion for easy glass forming alloy systems would be very beneficial.

There are many other empirical criteria for forming metallic glasses with a good GFA. Egami [64] suggests a correlation between atomic size and its concentration in certain metallic glasses. Shek et al. [69] have proposed that the composition of metallic glasses and their crystalline counterparts should possess a constant value of e/a (the average valence electron number per atom). Fang et al. [71] also have proposed that an empirical criterion between bonding parametric functions which consists of electronegativity difference (ΔX) and atomic size parameters (δ) to the relationship and the width of supercooled liquid region of Mg-based bulk metallic glasses, as summarized in Figure 2.10. Chen et al. [72] introduced atomic size and e/a ratio as two criteria to find the best BMG forming composition. The electronegativity has also been used to explain the GFA of the Al- and Mg-based alloys, showing a nearly linear relationship with GFA.

Besides the above three empirical rules [5, 23], the specific composition around the eutectic point also plays an important role in the formation of amorphous phases. Comparing the quenching process of compositions 1 and 2 in Figure 2.11, from the viewpoint of metallurgy, for composition 1 the melt would pass through a larger temperature interval, leading to the probabilities of crystallization before reaching T_g. On the other hand, since composition 2 is around the deep eutectic point, i.e., it has the smallest temperature interval between the T_l and T_g, the melt could maintain liquidus state to lower temperature and immediately transform from liquid to solid to form amorphous alloy. The composition of alloy system located at the temperature around the deep eutectic point by quenching would cause a lower T_l to enhance the GFA of BMG.

The composition of amorphous alloy appears to be a critically important factor for the GFA of BMG. Great efforts were made in the improvement of GFA by the addition of alloy elements on BMGs. As proposed by Xi et al. [86], a series of novel $Mg_{65}Cu_{25}RE_{10}$ BMGs (RE = rare earth elements, such as Gd, Nd, Sm, Dy) with different critical diameters and near eutectic compositions were obtained. The GFA of the Mg-Cu-RE alloy systems strongly depends on atomic size and electronegativity of the alloy RE elements. Some studies [87, 88], regarding the effects of minor alloying additions on GFA, reported that minor alloying addition has shown dramatic effects on the glass formation and thermal stability of many BMGs. Lu and Liu [88] suggested to add a small amount of alloying additions (usually, less than 2 at%) into the existing BMGs for the purpose of improving their GFA. Experimental evidence indicates that alloy additions of small atoms with atomic radius smaller than 0.12 nm (such as B and Si) or large atoms with atomic radius larger than 0.16 nm (such as Y and Gd) are most effective in enhancing GFA of metallic glasses. Further improvement of GFA has been reported in the Mg-Cu-Y alloy systems where Cu is partially substituted with other alloy elements, such as Ag, Pd, or Zn. For example, $Mg_{65}Cu_{15}Ag_{10}Y_{10}$ [89],

$Mg_{65}Cu_{15}Ag_5Pd_5Y_{10}$ [90, 91], $Mg_{65}Cu_{20}Zn_5Y_{10}$ [92] and $Mg_{54}Cu_{28}Ag_7Y_{11}$ [93] alloys all exhibit a high GFA, enabling the fabrication of BMGs in rods with diameters of 6, 7, 6 and 16 mm, respectively, by a conventional Cu mold injection casting method. Even in the Mg-Cu-Ag-Gd alloy system, the $Mg_{54}Cu_{26.5}Ag_{8.5}Gd_{11}$ BMG [93] can succeeded in the fabrication in a rod with a diameter of 25 mm. On the other hand, B containing Ma-based metallic glasses with alloying additions of small atoms replacing Cu also shows remarkable effectiveness on the improvement of thermal stability and GFA [94, 95].

The forming ability of BMGs gradually becomes more matured under the great efforts of global researchers. As aforementioned, we can generalize a conclusion for the criteria of BMG formation. The bulk glass forming alloys should satisfy: (1) the multicomponent alloy systems consist of more than three elements, (2) there is a significant difference, > 12%, in the atomic size ratios of the major constituent elements, (3) negative heats of mixing occur among the major elements, and finally (4) alloy compositions need to be close to the deep eutectic point. Generally speaking, the alloys satisfied with above these empirical rules would easily form BMG with a good GFA.

2.5 Characterization of amorphous alloys

Amorphous alloys have unique physical and chemical properties which are different from the traditional crystalline alloys due to their disordered structure. Table 1.1 summarizes the fundamental properties and shows the application fields of bulk amorphous and nanocrystalline alloys. The various properties of amorphous alloy are described below.

2.5.1 Mechanical properties

The unique mechanical properties of BMGs appear to be the most promising characteristics for applications, which are notably different from those of corresponding crystalline alloys. Due to the randomly atomic arrangement configuration and dense packing structure, amorphous alloys only allow limited atomic displacements to resist deformation when an external stress is applied. As a result of the absence of dislocation mechanisms in crystalline alloys, the basic mechanical properties of amorphous alloys displays the following characteristics [5-7]: (1) high fracture strength (σ_f) and higher hardness compared with the corresponding crystalline alloys, (2) low Young's modulus (E) but much higher elastic limitation of about 2% which exceeds the 0.2% yield limit of corresponding crystalline alloys, (3) much higher elastic energy up to the yield point compared with the corresponding crystalline alloys, and (4) absence of distinct plastic deformation at room temperature due to inhomogeneous deformation mode. The above-mentioned properties can be illustrated in Figure 2.12 [23]. Moreover, the relationship between tensile fracture strength, Vickers hardness and Young's modulus for various BMGs is shown in Figure 2.13, together with the data on conventional crystalline alloys. There is a distinct difference in these fundamental mechanical properties between two states of alloys.

Generally, BMGs have high tensile or compressive σ_f of 840-2100 MPa combined with E of 47-102 GPa, depending on alloy compositions [5]. The three-point bending flexural stress and deflection curves of the Zr-Al-Ni-Cu and Zr-Ti-Al-Ni-Cu BMGs have been measured [96, 97]. These BMGs have high bending flexural strength values of 3000-3900 MPa which are 2.0-2.5 times higher than those for Zr- and Ti-based crystalline alloys. Figure 2.14 shows the bending and rotating beam fatigue strength as a function of fatigue cycle until failure for the $Zr_{65}Al_{10}Ni_{10}Cu_{15}$ [23] and $Pd_{40}Cu_{30}Ni_{10}P_{20}$ [98] BMGs, respectively, together with the data under tensile stress conditions for various melt-spun amorphous ribbons. As the present Zr- and Pd-Cu-based BMGs have a good combination of various mechanical

properties, which could not be obtained from conventional crystalline alloys, some engineering applications based on the difference are in progress.

2.5.2 Magnetic properties

Permeability and coercive force are two fundamental properties of magnetic materials. In terms of permeability, magnetic materials can be classified as either soft or hard magnetic properties. For soft magnetic materials, they are used in devices subjected to alternating magnetic fields and in which energy losses must be low such as the transformer cores. Soft magnetic amorphous alloys have also been prepared in muticomponent systems, like Fe-(Al,Ga)-(P,C,B,Si), Co-Cr-(Al,Ga)-(P,B,C), Fe-(Co,Ni)-(Zr,Nb,Ta)-B, and Co-Fe-Nb-B [99-103]. On the other hand, hard magnetic materials have the high remanence, coercivity and saturation flux density, as well as low initial permeability and high hysteresis energy losses. The muticomponent Gd-(Fe,Co), Tb-(Fe,Co), Nd-Fe(-Al) and Pr-Fe(-Al) [104-107] amorphous systems have been reported as hard magnetic materials that used for magneto-optical recording materials.

Applications of magnetic glasses are mainly based on their superior soft magnetic properties. Sensors for electronic article inspection have become a major application of amorphous materials. In addition, thin sheets of glassy materials are first produced by melt spinning and subsequently annealed, resulting in the formation of nanocrystals in a glassy matrix. These nanocomposites still sustain their soft magnetic properties and have a higher saturation magnetization as well as a lower magnetostriction than the purely glassy materials. These magnetic nanocomposites are currently used in transformer cores, in magnetic sensors, and for magnetic shielding [5, 23].

2.5.3 Chemical properties

BMGs shows good mechanical properties which is probably used as structural materials. Meanwhile, BMGs display good corrosion resistance in various kinds of corrosive solutions. Due to homogeneous single phase structure which is lack of grain boundaries, dislocations and other defects in crystals, amorphous alloys have outstanding corrosion resistance which is superior to the corresponding crystalline alloys. In addition, corrosion resistance could be improved by adding alloy elements in an amorphous alloy [108-112].

As proposed by Inoue et al. [5], the corrosion resistance is remarkably improved by the dissolution of Nb or Ta. In this study, the corrosion resistance of melt-spun amorphous alloys was examined in Zr-TM-Al-Ni-Cu (TM=Ti, Cr, Nb, Ta) systems in HCl and NaCl solutions. It was found that the Nb- and Ta-containing amorphous alloys exhibit good corrosion resistance in their solutions at room temperature. The corrosion resistance is the best for the Nb-containing alloy, followed by the Ti-containing alloy and then the Zr-Al-Ni-Cu alloy, indicating the remarkable effectiveness of Nb addition even in the NaCl solution. As well known, magnesium and its alloys lack good corrosion resistance, extremely influencing their applications. Hence it is very important to develop the new Mg-based alloys with excellent chemical properties against environment effects. Yao et al. [113] reported that the corrosion resistance of melt-spun ternary $Mg_{65}Ni_{20}Nd_{15}$ and $Mg_{65}Cu_{25}Y_{10}$ amorphous alloys is higher than those of binary $Mg_{82}Ni_{18}$ and $Mg_{79}Cu_{21}$ alloys. Due to the homogeneous microstructure, amorphous alloys with good corrosion resistance suggest the viability in the industry application, such as surgical and biomedical uses.

2.5.4 Other properties

It is reasonable to say that amorphous alloys are good anti-radiation materials since amorphous alloys have the denser random packing structure than the corresponding crystalline alloys. Li et al. [114, 115] reported that reasonable superconducting properties was observed in BMGs, which are based on the electrical resistivity and critical field measurements. Finally, the ability of hydrogen storage is also shown in many amorphous alloys and their decomposing efficiency for hydrogen is up to 100% [116]. For example, the Zr–Al–Ni–Cu BMGs with a wide supercooled liquid region were found to exhibit a distinct plateau stage in the hydrogen pressure–concentration-isotherm relation, though the desorption ratio of hydrogen gas is very low (15%) [117]. Subsequently, the desorption ratio remarkably increases by choosing Mg-based BMGs and the desorption ratio reaches approximately 100% [118]. Therefore, BMGs are good candidate for hydrogen storage materials.

2.6 Mechanical behaviors of metallic glasses

2.6.1 Stress-strain curves and fracture morphologies

Figure 2.15 shows the typical compressive and tensile stress–strain curves of $Zr_{59}Cu_{20}Al_{10}Ni_8Ti_3$ BMGs at different applied strain rates from 4.5 x 10^{-5} to 3 x 10^{-2} s^{-1} at room temperature [44]. In tension test, BMGs show only an initial elastic deformation behavior and catastrophic fracture without yielding. In contrast to tensile test, BMGs under compressive test show an initial elastic deformation behavior with an elastic strain of about 2% and then begin to yield, followed by some plastic deformation until fracture, which is obviously different from the tensile test. Usually, the average tensile fracture stress of BMGs is slightly lower than the average compressive fracture stress. In addition, the fracture stress of BMGs under tensile and compressive loading is insensitive to the applied stain rate of testing machine, as shown in Figure 2.15.

The fracture morphology under tensile loading is distinctly different from that of compressive test even though tensile and compressive samples similarly fractured in a shear mode. Figure 2.16 shows that typical tensile and compressive fracture angle of the $Zr_{59}Cu_{20}Al_{10}Ni_8Ti_3$ BMGs. Generally, the tensile and compressive fracture angles of most BMGs deviate from 45^o [28, 44, 119]. The fracture angle of BMG under tensile test is always smaller than 45^o. On the contrary, the compressive fracture angle is always larger than 45^o.

Typical fracture morphologies of the $Zr_{59}Cu_{20}Al_{10}Ni_8Ti_3$ BMGs with tensile and compressive fracture surfaces are shown in Figure 2.17 [28, 44, 119]. In tensile test, the fracture surface reveals not only the so-called vein-like structures, but also the circular core structures, as shown in Figure 2.17(a). The arrows indicate the origin of circular cores on the fracture surface. The veins radiate from the circular cores and propagate far away from the cores. As well known, uniaxial tensile stress can be decomposed into the resolved shear stress along the failure plane and the resolved normal stress perpendicular to the failure plane. The resolved normal stress is outward the fracture plane, leading to the formation of circular cores. Subsequently, the resolved shear stress along the failure plane causes the propagation of veins. In compressive test, the fracture surface is relatively flat and displays a typical shear fracture feature. The typical feature of fracture surface under compressive loading is mainly the vein-like structures which spread over the whole fracture surface. The vein-like structure always extends along the shear direction that parallel to fracture plane, as marked by the arrow in Figure 2.17(b). Similarly, uniaxial compressive stress can also be decomposed into the resolved shear and normal stresses. The normal stress is unable to produce a circular core in fracture plane since it is inward the fracture plan, whereas the shear stress still yields the formation and propagation of veins. The difference in fracture behaviors of the two different testing modes could be attributed to the effect of loading modes, which will be further described in the following sections.

2.6.2 Temperature effect

Over the past two decades, the most reported mechanical tests of BMGs are generally limited to room temperature or high temperature within the supercooled liquid region. The mechanical behaviors of BMGs can be classified in to two types of inhomogeneous deformation at room temperature and homogeneous deformation at a high temperature within the supercooled liquid region [120, 121]. A schematic deformation mechanism map, steady-state strain rate as a function of stress and temperature, of a metallic glass is illustrated in Figure 2.18. The mechanical behaviors of BMGs at room-temperature uniaxial mechanical tests during inhomogeneous deformation have been described above. The mechanical behaviors of BMGs during homogeneous deformation usually occur at high temperatures and an apparent plasticity phenomenon is observed at low stresses. For convenience, the homogeneous deformation can be divided into three parts based on the viscosity of the material [121]. Firstly, for $T > T_l$, the material has a viscosity of ~10^{-3} Pa·s, and this material can be characterized as "fluid" or "liquid" matter. The viscosity changes only slowly with temperature in this regime and the strain rate contours are almost horizontal. Secondly, for $T \approx T_g$, the material has a viscosity between 10^{15} and 10^{-10} Pa·s, and this material could be called as "viscous" matter. The viscosity drops very fast with increasing temperature, and the strain rate contours are almost vertical around T_g. Finally, for $T < T_g$, the material has a viscosity above 10^{15} Pa·s and this material can be called as "solid " matter. In this regime, viscosity does not change very fast with increasing temperature and the strain rate contours become more horizontal.

At low temperatures, the deformation of BMG is inhomogeneous and dominated by localized shear bands. At high temperatures, usually above a critical temperature of T_g, the homogeneous deformation of BMG will be as an ideal Newtonian viscous flow and the strain

rate sensitivity m value will be equal to 1 in the following constitutive equation:

$$\sigma = k\dot{\varepsilon}^m , \tag{2-6}$$

where σ is the yield stress, k is a constant, and $\dot{\varepsilon}$ is the strain rate. In this regime, BMG will exhibit the superplastic-like behavior. The easy formability of BMG at the temperature within the supercooled liquid region enables these materials to be potentially produced for micro-electro-mechanical systems (MEMS) in the micrometer and nanometer scale, as shown in Figure 2.19 [122, 123].

On the other hand, the mechanical behaviors of BMGs at cryogenic temperatures have been recently presented for comparison with those at room temperature. As proposed by Li et al. [124, 125] and Fan et al. [126-128], uniaxial compression tests were performed on the Zr-based BMGs at the ambient (300 K) and cryogenic (77 K) temperatures. Compared to room-temperature compression, the strength of Zr-based BMG increases at the cryogenic temperature but is accompanied by the decrease in plastic strain, as shown in Figure 2.20 [124]. Figure 2.21 displays the dependence of strength variation as a function of testing temperatures in compression and microhardness [124]. In the work [125], Both fracture morphologies of deformed samples at 300 and 77 K demonstrate a combination of two types of vein patterns, one is the void-like and the other is river-like, indicating that fracture surface is independent of the testing temperature, as presented in Figure 2.22. On the basis of a collection of data, Li et al. [125] proposed a linear relationship between the normalized strength (σ/E) and normalized temperature (T/T_g), which can be expressed as the following:

$$\frac{\sigma}{E} = 0.0253 - 0.0106\frac{T}{T_g}, \tag{2-7}$$

where E is elastic modulus, T_g is the glass transition temperature and T is the testing

temperature, as illustrated in Figure 2.23. Because the E and T_g are often constants for that specific material, the strength of BMGs increases with decreasing temperature.

2.6.3 Strain rate effect

So far, several studies related to the effect of strain rate on the deformation behaviors of BMGs have been reported [129-132]. As reported by Mukai et al. [133], the fracture stress as well as strain of the $Pd_{40}Ni_{20}P_{20}$ BMG was found to slightly decrease with increasing applied strain rate, ranging from 3.3 x 10^{-5} to 1.7 x 10^{3} s^{-1}. The flow serration of stress-strain curves disappeared when the applied strain rate is over a critical value. The authors attributed the weakening and fragility of BMG at high strain rates to the absence of multiple shear band formation. Xiao et al. [131] studied the strain rate effects on fracture morphologies of Zr-based BMGs under tension test. Figure 2.24 shows that the fracture surface of the $Zr_{52.5}Al_{10}Ni_{10}Cu_{15}Be_{12.5}$ BMG in tension at low strain rates. The typical vein-like, circular core and ridge-line structures appear on the fracture surface of glassy sheets. The origin of fracture seems to be the center of shear band as shown in the right micrograph of Figure 2.24. Once the localized shear bands form, they would rapidly propagate around while being exerted by an applied force. The encounter of the neighboring shear bands results in the formation of ridge lines and, then, these ridge lines of shear bands ultimately turn off and cause the catastrophic failure, as described in the previous section. By contrast, the fracture morphologies at high strain rates under tensile deformation almost consisted of microvoid-coalescence dimples, as shown in Figure 2.25, which could be explained by a localized melting mechanism during deformation process.

Fan et al. [127] reported the strain rate effect on mechanical strength for Zr-based BMGs at various temperatures from the cryogenic temperature (77 K), ambient (300 K) to high

temperature (593 K). In this work, the strength of BMGs tested at 300 K is not sensitive to strain rate. Nevertheless, at high and cryogenic temperatures, BMGs show the strain rate sensitivity, suggesting that shear band deformation is related to thermally activated process. Currently, Jiang et al. [134] reported that, using an infrared camera, the in-situ dynamics shear-banding operation was observed in the geometrically constrained BMGs (height to diameter ratio = 0.5) at various strain rates. Figure 2.26 shows the dependence of stress as a function of the Zr-based BMGs for the flow serrations of stress-strain curves at various strain rates. As compared with these curves, the serrated flow phenomenon is prone to temporarily decrease with increasing strain rate. In this work [134], it was found that the higher strain rate, the fewer observed shear band and coarser shear band spacing on the sample outer appearance, which can be seen in Figure 2.27. It can generally give a conclusion that shear band tends to decrease with increasing applied strain rate.

2.6.4 Sample size effect

Many conventional compression tests have been performed on the samples with a diameter of 3 or 4 mm, or above. Currently, some investigators reported the dramatic effect on the mechanical behaviors of BMGs when the sample size is reduced down to a critical size. In such studies [135-144], the BMG with a smaller sample size generally presents the enhanced strength and plasticity, compared with the larger one with the same chemical composition under compression test.

Zheng et al. [135] presented that all reported Mg-based BMGs are of the brittle nature, indicating that their plastic strain before failure is either nonexistent at all or very small under compression test. They have developed a new $Mg_{61}Cu_{28}Gd_{11}$ BMG with a highest GFA among all known ternary Mg-based BMGs. Then, the conventional compression tests were

conducted on the samples with a diameter as large as 4 mm and as small as 1 mm for comparison. The samples with 1 mm in diameter exhibit a higher strength and plasticity than those with 4 mm in diameter. Table 2.4 summarizes the previously reported mechanical properties of Mg-based BMGs under compression tests. It seems to have no reliable measurement for the Mg-based BMGs, especially for strength, as shown in Table 2.4. In terms of strength, for a small volume, the probability of finding a defect is very low, such as pores, un-melted particles, oxides and inclusions, so that it is beneficial to measure the intrinsic strength and plasticity for the sample with a smaller critical size. Huang et al. [144] reported on the dramatic effect of sample size on the plasticity of Ti-based BMG. The plasticity of BMG tends to increase with decreasing sample size from 6 mm to 1 mm in diameter. The better outstanding mechanical performance of BMG with a smaller sample size is concerned with a higher amount of free volume formed by a relatively faster quenching during solidification. The same effect have also been seen in the Zr-based BMGs [136, 138], namely the smaller one is more ductile.

In the last few years, the researches on the sample size effect were extended to the BMG micropillars with a critical sample size in the micrometer scale [139-143]. In smaller size-scaled BMG micropillars, microcompression test was applied to measure the mechanical properties of samples. Huang's group [142, 143] reported that the sample size effect on the yield strength of the ductile Zr-based BMG micropillars with diameters of 1 and 3.8 μm was found to be highly sensitive to sample size [143], which is also observed on the brittle Mg-based BMG micropillars [142]. The yield strength of the BMG micropillars is 30%–100% increment over the bulk samples. As discussed first by Schuster et al. [141] and later by Lee et al. [142] and Lai et al. [143], the increase in strength with decreasing sample size can be rationalized by the Weibull statistics. It appears to be able to determine the intrinsic strength and plasticity of BMG at the situation of small sample sizes.

2.6.5 Geometric constraint effect

The sample geometry significantly plays an important role in mechanical behaviors of BMG under room-temperature compression test [39-43, 145-151]. The compressive plastic strain of cylindrical BMG sample commonly increases with decreasing aspect ratio (height to diameter, h/d) and the strength maintains almost invariable due to geometric constraint effect [39-43]. The dependence of yield strength and plastic strain as a function of aspect ratio of the Zr-based BMGs is shown in Figure 2.28 [39]. In general, for unconstrained samples with a higher aspect ratio which is larger than 1, shear bands can operate freely throughout the whole diameter of sample, resulting in the smaller plastic strain before failure. In contrast, for constrained samples, as the aspect ratio is lowered down to less than 1, shear bands is not able to operate freely throughout the whole diameter of the sample, so that these samples are characterized by larger plastic strain. This suggests that shear band propagation induced during the early stage of compression are constrained by the upper and bottom platens and then the multiplication of shear bands is prone to form, resulting in the apparent ductility.

Not only for the ductile Zr-based BMGs [39-42], but the geometric effect could also be observed in the brittle Mg-based BMGs [43]. As proposed by Chen et al. [43], the room-temperature compression tests were conducted on the Mg-based samples with various h/d ratios from 2, 1, 0.5 to 0.25. Especially for the sample with h/d = 0.25, the plastic strain is significantly enlarged up to 20%. The fracture surface for the sample with h/d = 2 shows cleavage features, as the typical characteristic nature of the Mg-based BMGs. However, for the sample with h/d = 0.25, it shows highly dense vein-like structures spreading over the whole fracture surface, as shown in Figure 2.29.

With the fact that the aspect ratio of sample would influence the shear band propagation

as well as the mechanical responses of BMGs, the sample alignment and geometric shape, leading to lateral motion resistance and longitudinal constraint, certainly influence the mechanical behaviors of BMG as well [145-147, 150]. Wu et al. [146] proposed the concept of ‘‘stress gradient enhanced plasticity’’ for the moderation of catastrophic failure of BMG samples by designing various geometries (orthogonal, monoclinic and transitional, which can be seen in Figure 2.30) in which a large stress gradient exists. For the ideal orthogonal sample, the stress gradient is constant, indicating that there appears be high stress concentration throughout the whole sample during deformation. However, for the monoclinic and transitional samples, the stress concentration would be localized in two opposite corners of sample. The lateral motion resistance and longitudinal constraint may restrict further sample sliding along the shear plane, resulting in the enhanced plastic strain, which is, in fact, an artifact. It suggests that special care should be taken in sample preparation and alignment during machine testing in order to avoid any artifact plasticity of BMGs.

2.6.6 Reinforcement effect on BMG composites

To improve the plasticity of BMG, how to prevent shear bands from free propagation is a very crucially important issue. For this purpose, BMG composites (BMGCs) have been developed by inducing a second phase to the monolithic amorphous matrix structure [24, 25, 28, 31, 152-157]. The second phase can act as a block to arrest or retard the catastrophic failure through the interaction between reinforcements and initially formed shear bands. In this case, the second phase can be the precipitated crystalline phases [24, 25, 152-154], in-situ precipitation of dendrite phase [31], metal fibers [28], or finely dispersed porosities [155]. The excellent mechanical performances, such as remarkable strength and macroscopic plasticity, could be improved in these BMGCs.

Fan and Inoue [25] measured the mechanical properties of the $Zr_{60}Cu_{20}Pd_{10}Al_{10}$ BMG and BMGCs with various volume fraction of precipitated crystalline phases, Zr_2(Cu,Pd), via annealing under compression test. They found that the plastic strain of the $Zr_{60}Cu_{20}Pd_{10}Al_{10}$ BMGC can be improved in comparison with that of the as-cast $Zr_{60}Cu_{20}Pd_{10}Al_{10}$ BMG while no distinct plastic strain is recognized in the $Zr_{55}Ni_5Cu_{30}Al_{10}$ BMG, as shown in Figure 2.31. The summarized mechanical properties of the $Zr_{60}Cu_{20}Pd_{10}Al_{10}$ BMGCs are also plotted in Figure 2.32. There appears to be an increase in the compressive yield strength, maximum fracture strength, Young's modulus and plastic strain with increasing volume fraction of crystals. However, it is worthy to note that the plastic strain of the $Zr_{60}Cu_{20}Pd_{10}Al_{10}$ BMGCs significantly deteriorates down to 0% when volume fraction of crystals exceeds a critical value (27%), indicating that the appropriate volume fraction of reinforcement is a key point for the ductility improvement of BMGC.

As to Mg-based BMG, which is one classical representative of brittle BMG, it always breaks into several pieces by catastrophic fracture once elastic limit is attained. From the viewpoint of reinforcement, Pan et al. [158] pointed out that the Mg-based BMGCs reinforced with ductile Nb particles of 20-50 μm shows a high strength of 900 MPa and large plasticity of 12%, as shown in Figure 2.33. The ductile Nb particles can effectively retard the shear band propagation to prevent from catastrophic fracture. The deformed Nb particles uniformly distribute loading to surrounding BMG matrix to promote the initiation and branch of numerous secondary shear bands, which can be seen in Figure 2.34. The ductile Nb reinforced BMGCs exhibits a great resistance to crack growth as well. In the above-mentioned studies, the results imply that, by appropriate alloy design, BMGC has great potential in serving as an engineering material.

2.7 Deformation mechanisms of metallic glasses

Since 1970s, the mechanical properties of metallic glasses have been extensively investigated [1, 159], but the underlying deformation mechanisms still remain less confirmed till now. The purpose in this section is to present an overview of deformation mechanisms for metallic glasses.

As well known, crystalline alloys are subjected to elastic deformation, followed by yielding, plastic deformation and then finally fracture during deformation process. Crystalline alloys start plastic deformation when the resolved shear stress is over the critical resolved shear stress (CRSS) along a specific slip plane. A dislocation is formed and starts to move along the slip direction of a slip plane. Unlike crystalline alloys, metallic glasses do not show a long-range order periodically, namely, there is no slip system in metallic glasses and, thus, plastic deformation of metallic glasses does not proceed along the slip systems. A two-dimensional schematic diagram of atomic deformation mechanisms for metallic glasses is illustrated in Figure 2.35 [27]. As shown in Figure 2.35, there are numerous small spaces between atoms, which are called free volumes. Metallic glasses only allow small displacement change in atomic neighborhood under applied loading. The local rearrangement of atoms in metallic glass is a relatively high energy and high stress process. To make a metallic glass to further deform, a larger applied stress would often be required so that the clusters of atoms tend to move together by a dominant shearing like a band.

Generally, the feature of metallic glasses presented in their stress-strain curves shows the absence of sufficient plastic deformation. The plastic deformation of metallic glasses could be classified into two types: one is slight plastic deformation with the nominal work softening and the other is distinct plastic deformation accompanied with flow serrations. The

flow serration phenomenon which occurs before final failure indicates the operation of localized shear band deformation. On the whole, BMGs deform through a process of highly localized shearing in a narrow band, once shear localization has begun, the trend for shear-softening would urge deformation in order to accommodate some shear strains and finally fail along one major and dominant shear plane under either uniaxial compressive or tensile tests [27]. Due to highly localized shear band formation [1, 26], the plastic deformation of metallic glasses is inhomogeneous at room temperature.

A correlated viewpoint on the mechanism of plastic flow in metallic glasses was proposed by Turnbull and his coworkers [160, 161] by using a classical free volume model. Subsequently, in 1977, Spaepen [121] applied this free volume mechanism to the case of glassy and interpreted the local rearrangement of atoms in metallic glasses during deformation. From the viewpoint of free volume model [121], Argon [162] further proposed a concept to demonstrate that the deformation mechanism for metallic glasses is atomic-scaled shear distortion. As proposed by Argon [162], this theory is based on the thermally activated shear transformations initiated around free volume regions under an applied shear stress, defined as a “shear transformation zone” (STZ). The STZ is essentially a local cluster of atoms that undergoes an inelastic shear distortion from one relatively low energy configuration to a second configuration, passing an activated configuration of higher energy and volume [27]. Furthermore, the STZ which includes a free volume site and its adjacent atoms is considered as a basic shear unit for metallic glasses during deformation. These atomic-scaled STZs deform together under an applied shear stress to produce shear deformation, as illustrated in Figure 2.36.

STZs which approximately consist of a few hundreds of atoms in volume are usually observed in simulation works, which stretch over the variety of simulated compositions and

empirical inter-atomic potentials [163-166]. Although the structure, size and energy scales of STZ may change from one to the next within a glass, STZ is a usual event for the deformation of metallic glasses. An STZ is not a structural defect in metallic glasses, dissimilar to the way that a lattice dislocation is a defect of atomic arrangement for crystalline alloys. Actually, STZ is called as flow defect now. Therefore, an STZ is an event defined in local volume by its transience and not a feature of glass structure. However, this is not to say that the STZ event is independent of glass structure. From the viewpoint of the activation of kinetic energy, when a metallic glass is subjected to a shear stress which is over a critical value, a single STZ first nucleates in the vicinity of a free volume site without significant atomic rearrangements in its surrounding glassy matrix. Secondary STZs may subsequently occur in the vicinity of the first STZ by the assistance of a local strain field and free volume formed by the first STZ. The later formation of STZ will follow a similar manner. Once the shear strain with a critical number of STZs reaches a maximum in the initial zone, the shear band that consists of these local STZs starts to propagate, resulting in the macroscopic yielding of metallic glass [167]. It is reasonable to imagine that the sites of higher free volume would more readily accommodate shear band, suggesting that the amount and distribution of free volume may dominate the plastic deformation of metallic glasses. Thus, the mechanism during shear band propagation which evolves from STZs could be considered as a process of the competition between the creation and annihilation of free volume.

The plastic deformation of metallic glasses is essentially an accumulation of local shear strains by the operation of STZs and the redistribution of free volume. Both of STZ and free volume models light up the tide for the deformation mechanisms of metallic glasses [120, 167-173], but the mechanical responses of metallic glasses do not keep fully consistent in various alloy systems so far. It is still worthy of studying this crucial issue further.

2.8 Fracture mechanisms of metallic glasses

From the previous description, the fracture processes of BMG under tensile and compressive loading are significantly different. The difference could be attributed to the effect of loading modes. Hence, it is important to understand the stress state and yielding criterion of materials.

As well known, the Mohr circle is a powerful tool to analyze the stress state of materials. It was proposed by Otto Mohr in 1882 and the Mohr circle can illustrate the principle stresses and stress transformations via a simple graphical format. If stresses act on a 2-D matter as illustrated in Figure 2.37, the stress state in the x'-y' coordinate system can be shown as

$$\left(\sigma_{x'} - \frac{\sigma_x + \sigma_y}{2}\right)^2 + \tau_{x'y'}{}^2 = \left(\frac{\sigma_x - \sigma_y}{2}\right)^2 + \tau_{xy}{}^2 \ , \qquad (2\text{-}8)$$

where the σ_x and σ_y are normal stresses, respectively, and τ_{xy} is shear stress in the x-y coordinate system. The $\sigma_{x'}$ and $\tau_{x'y'}$ are normal stress and shear stress in the x'-y' coordinate system. Equation 2-8 follows the equation of a circle of the form $(x - a)^2 + y^2 = R^2$. Thus, the Mohr circle is a circle in $\sigma_{x'}$-$\tau_{x'y'}$ coordinates with a radius equal to τ_{max} and the center shifted $(\sigma_x + \sigma_y)/2$ to the right of the origin.

In terms of yielding behavior of materials, the criteria which have been found most appropriate to describe yielding in polycrystalline metals are the Tresca (critical shear stress criterion) and von Mises (critical distortion energy criterion) criteria. Both criteria principally depend on the maximum shear stress (τ_{max}) and neglect any effect of the hydrostatic force or the stress normal to the plane of shear yielding. The Tresca criterion is based on the hypothesis that a material fractures when its τ_{max} is larger than a critical shear stress (τ_0). The

τ_{max} can be written as

$$\tau_{max} = \frac{\sigma_{max} - \sigma_{min}}{2} \geq \tau_o , \quad (2\text{-}9)$$

where the σ_{max} and σ_{min} are the maximum and minimum principal stresses, respectively. Furthermore, the von Mises criterion which was proposed in 1913 can be expressed as

$$\frac{1}{\sqrt{6}}[(\sigma_1 - \sigma_2)^2 + (\sigma_2 - \sigma_3)^2 + (\sigma_3 - \sigma_1)^2]^{\frac{1}{2}} \geq \tau_o = \frac{\sigma_0}{\sqrt{3}}, \quad (2\text{-}10)$$

where σ_0 is the critical yielding normal stress and σ_1, σ_2 and σ_3 are the principal stresses. Both Tresca and von Mises criteria are fundamentally similar. However, the yield locus of Tresca criterion is linear but the von Mises criterion is curvature. Furthermore, in terms of Tresca criterion, the fracture of materials always occurs along the maximum shear stress plane at a critical shear stress. All samples should preferentially fracture along the maximum shear stress plane with one angle of 45^o no matter whether in tension or compression. In contrast, the yield of materials must be along the maximum shear plane at 60^o deviation with respect to the loading axis for the von Mises criterion. Figure 2.38 shows that the Tresca and von Mises criteria can be demonstrated based on the Mohr circle for the tensile sample.

As proposed by Donovan [174] and Zhang et al. [28, 44, 119, 175], BMGs always fracture along a plane deviating from the maximum shear stress plane, namely, the fracture angles of sample in compression and tension (θ_c and θ_T) would deviate from 45^o, which is neither in agreeable with the Tresca criterion nor the von Mises criterion. In fact, the BMG samples always fracture with $\theta_c < 45^o$ with respect to the loading axis, in contrast to $\theta_T > 45^o$ in tension, as previously shown in Figure 2.16. Table 2.6 lists the tensile (θ_T) and compressive (θ_C) fracture angles of various BMGs. It is found that the fracture angle is ~55^o

divergence under tension test and ~42^{o} divergence under compressive tests. Due to the asymmetry of tensile and compressive fracture angles, many researchers have attempted considering the effect of loading modes and, then, great efforts have been made. For BMGs, the hydrostatic force and stress normal to the plane of shear yielding play a crucially important role in the fracture process and yielding. Recently, some literatures [28, 44, 78, 119, 133, 174-186] found that the yielding behavior of BMGs follows the Mohr-Coulomb criterion rather than the Tresca and von Mises criteria. Based on the Mohr-Coulomb criterion, the cases in tension and compression should be considered individually, and the critical yielding stress is no longer a constant but depends on the normal stress across the plane much like the sliding friction. Since the stress state in tension or compression on any shear plane will distribute on the Mohr's circle, the critical fracture stresses of BMG can be illustrated using the Mohr's circle, as shown in Figure 2.39 [119]. When the Mohr's circles touch the critical fracture line, the tangency points will correspond to the critical tensile and compressive fracture stresses.

As proposed by Zhang et al. [44, 119, 175], when the BMG is subjected to a normal compressive or tensile stress (σ_C or σ_T) on a plane, the critical compressive or tensile shear stress (τ_C or τ_T) of materials on this plane can be expressed as

$$\tau_C = \tau_o + \mu_C \sigma_C , \tag{2-11a}$$

$$\tau_T = \tau_0 - \mu_T \sigma_T , \tag{2-11b}$$

where μ_C and μ_T are two constant for compression and tension, respectively. According to the yielding criterion, the resolved shear stress (τ_θ) must larger than the critical yielding shear stress and, thus, the critical shear fracture conditions for a BMG sample can be easily obtained, as expressed by Equation 2-12:

$$\tau_\theta^C \geq \tau_0 + \mu_C \sigma_\theta^C , \tag{2-12a}$$

$$\tau_\theta^T \geq \tau_0 - \mu_C \sigma_\theta^T , \tag{2-12b}$$

where $\sigma_\theta^C/\sigma_\theta^T$ and $\tau_\theta^C/\tau_\theta^T$ are the normal and shear stresses on the shear plane at compressive and tensile fracture, respectively. As illustrated in Figure 2.40(a), the σ_θ^C and τ_θ^C can be calculated from the following equations:

$$\sigma_\theta^C = \sigma_F^C sin^2(\theta) , \tag{2-13a}$$

$$\tau_\theta^C = \sigma_F^C sin(\theta)cos(\theta) . \tag{2-14a}$$

And as illustrated in Figure 2.40(b), the σ_θ^T and τ_θ^T can also be expressed as

$$\sigma_\theta^T = \sigma_F^T sin^2(\theta) , \tag{2-13b}$$

$$\tau_\theta^T = \sigma_F^T sin(\theta)cos(\theta) . \tag{2-14b}$$

By substituting the above σ_θ^C, σ_θ^T, τ_θ^C and τ_θ^T into Equation 2-12, respectively, one gets

$$\sigma_F^C sin(\theta)cos(\theta) \geq \tau_0 + \mu_C \sigma_F^C sin^2(\theta) , \tag{2-15a}$$

$$\sigma_F^T sin(\theta)cos(\theta) \geq \tau_0 - \mu_C \sigma_F^T sin^2(\theta) . \tag{2-15b}$$

Equation 2-15 can also be simplified and, then the critical compressive and tensile fracture stress (σ_F^C and σ_F^T) can be expressed as

$$\sigma_F^C \geq \frac{\tau_0}{sin(\theta)[cos(\theta) - \mu_C sin(\theta)]} , \tag{2-16a}$$

$$\sigma_F^T \geq \frac{\tau_0}{\sin(\theta)[\cos(\theta) + \mu_T \sin(\theta)]} . \quad (2\text{-}16b)$$

According to Equation 2-16, the compressive and tensile fracture stresses strongly depend on the shear angle (θ). When θ = θ_C or θ_T, the fracture would occur at the minimum stress, namely, there is a minimum value of the two fracture stresses at different shear angle. In principle, BMGs should preferentially fracture along a favorable shear plane at the minimum applied stresses. Therefore, the minimum applied fracture stresses (σ_F^C and σ_F^T) should be in accordance with the measured fracture angle (θ_C and θ_T). For compressive and tensile fracture, the relationship of minimum σ_F^C at θ_C or σ_F^T at θ_T can be expressed as

$$\frac{\partial(1/\sigma_F^C)}{\partial\theta} = \frac{1}{2\tau_0}[\cos(2\theta_C) - \mu_C \sin(2\theta_C)] = 0 , \quad (2\text{-}17a)$$

$$\frac{\partial(1/\sigma_F^T)}{\partial\theta} = \frac{1}{2\tau_0}[\cos(2\theta_T) + \mu_T \sin(2\theta_T)] = 0 . \quad (2\text{-}17b)$$

In the equation 2-17, the minimum σ_F^C and σ_F^T would occur with $\theta_C = 43^o$ and $\theta_T = 54^o$, thus, two constants μ_C and μ_T for compression and tension can be expressed as

$$\mu_C = \left(\frac{\cos(2\theta_C)}{\sin(2\theta_C)}\right) = 0.07 , \quad (2\text{-}18a)$$

$$\mu_T = -\left(\frac{\cos(2\theta_C)}{\sin(2\theta_C)}\right) = 0.324 . \quad (2\text{-}18b)$$

According to Equation 2-18, the μ_T (0.324) is notably larger than μ_C (0.07), indicating that the normal tensile stress should play a more important role in the fracture process of BMG than the normal compressive stress. Figure 2.41 [44] shows the dependence of the normal, shear and two fracture stresses on fracture plane as a function of fracture angle under tensile and compressive loading. This is the evidence that fracture plane is not exact along the shear

angle of 45^{o} with respect to the loading axis. Accordingly, the fracture behavior of BMG follows the Mohr-Coulomb criterion rather than the Tresca and von Mises criteria.

Chapter 3 Experimental procedures

By employing a computational-thermodynamic approach to predict the optimum composition within the two-liquid-phase region, the cylindrical ingots of phase-separated Zr-based BMGs with a diameter of 2 mm were prepared. The analyses of amorphous nature, thermal properties and mechanical behaviors of the as-cast samples were subsequently carried out. The plastic strain and deformation mode of the ductile Zr-based BMGs compressed to different predetermined strains at room temperature and low strain rate were investigated. To shed light on the shear-band dynamics, the flow serration and shear band propagation during inhomogeneous deformation of various BMGs, including the ductile Pd-based BMG, brittle Mg-based BMG and Mg-based BMG composite reinforced with porous Mo particles, were studied using high-sensitivity strain gauges directly attached to the sides of test sample. The flow chart of experimental procedures is displayed in Figure 3.1.

3.1 Raw materials

The compositions of $Zr_{63.8}Ni_{16.2}Cu_{15}Al_5$ (in at%), $Pd_{40}Ni_{40}P_{20}$ and $Mg_{58}Cu_{31}Y_6Nd_5$ were selected for preparing the BMGs; meanwhile, the composition of $Mg_{58}Cu_{28.5}Gd_{11}Ag_{2.5}$ was selected as the raw alloy for preparing the BMGC. The purities of pure elements were as follows, zirconium, copper, aluminum are all as pure as 99.99% and nickel is as pure as 99.9% in the Zr-Ni-Cu-Al system. In the Pd-Ni-P system, palladium and ingot of nickel phosphide compound (Ni_2P) are as pure as 99.9%. In the Mg-based alloy systems, magnesium and other component elements are 99.99%. Moreover, the pure molybdenum (99.9% in purity) particles are taken as the reinforcements in the amorphous samples. Table 3.1 summarizes the fundamental data related to the component elements.

3.2 Computational thermodynamic approach

How to pinpoint the composition of alloy exhibiting phase separation is a very crucial issue. In this section, we would like to introduce a computational thermodynamic approach to identify the two-liquid miscibility phase equilibrium in the liquid-temperature region for the Zr-Ni-Cu-Al alloy systems, as inspired by Hsieh and Chang et al. [87, 187, 188].

Yan et al. [189] has used a thermodynamic approach to predict the tendency of multicomponent metallic alloys for glass formation. They applied this approach to the quaternary Zr-Ti-Ni-Cu alloys and found that the thermodynamically calculated compositions of liquid alloys shows the five-phase invariant equilibriums, which is in agreement with those determined experimentally by Lin and Johnson [190]. This approach also gives new alloy compositions within the two liquid-phase region and with good GFA in the quaternary Zr-Ni-Cu-Al system. An outstanding feature of this approach is that the thermodynamic models of phases simply involve the multiple chemical and topological interactions among component elements through the consideration of enthalpy and entropy terms. Before using this method on the current quaternary Zr-Ni-Cu-Al system, we need to employ a concept with thermodynamic description according to the description of a multicomponent system obtained by the Calphad approach [191-193].

The concept in terms of thermodynamic description means that the parameters of thermodynamic models for all phases in a system are available. The thermodynamic description of higher order systems, i.e. more than three components, can be obtained by extrapolation from those of lower order systems, normally binaries and ternaries. Experience has shown that this trend is indeed the case while the formation of new quaternary phases is not available and the homogeneities of lower-order intermetallic phases do not extend to the

higher order compositional space [192]. For the quaternary Zr-Ni-Cu-Al system, there are six constituent binaries and four constituent ternaries. So far, no quaternary intermetallic phase could be found in the attainable literatures. However, using the quaternary thermodynamic description and the commercial software PANDAT [194, 195], the isotherms and isopleths could be calculated in the quaternary Zr-Ni-Cu-Al system.

For the quaternary Zr-Ni-Cu-Al system, the complete isotherm is a tetragonal volume under a constant pressure and, then, a two-dimensional section can be determined from cutting with constant Al content. This provides the useful information for the selection of alloy compositions. In this study, the selected *X* alloy for $Zr_{63.8}Ni_{16.2}Cu_{15}Al_5$ within the two immiscibly liquid-phase regions can be found in the 1050℃ isothermal section at the Zr-rich corner under 5 at% Al constant content, as illustrated in Figure 3.2. From which the isopleth C-C in Figure 3.2 is calculated between $Al_5Ni_{40}Zr_{55}$ and $Al_5Cu_{25}Zr_{70}$ composition regions, as illustrated in Figure 3.3. According to this diagram, the *X* alloy with the optimum composition of $Zr_{63.8}Ni_{16.2}Cu_{15}Al_5$ is located in the two-liquid-phase region, and the compositions of calculated two-liquid phases are characterized as the Ni-rich $Zr_{68.4}Ni_{23.9}Cu_{6.6}Al_{1.1}$ and the Cu-rich $Zr_{61.7}Ni_{12.8}Cu_{18.8}Al_{6.7}$, respectively. Based on this computational thermodynamic approach, the $Zr_{63.8}Ni_{16.2}Cu_{15}Al_5$ BMG rods were prepared by arc melting and suction casting.

3.3 Sample preparations

The master cylindrical rods of the Zr-, Pd-, Mg-based BMGs and BMGCs were fabricated using a conventional copper mold casting method after homogeneous melting in a purified argon atmosphere. This method is generally recognized as the most convenient way to prepare the BMGs and BMGCs. In this study, the BMG and BMGC samples were

prepared by the group of Prof. Jang in the I-Shou University. The detailed experiments are described below.

3.3.1 Arc melting

For the purpose of melting the component elements uniformly before next casting process, arc melting is first performed to prepare the preliminary Zr-Ni-Cu-Al and Pd-Ni-P ingots in an arc furnace under a purified argon atmosphere. Raw materials were taken appropriate amount and placed on a copper mold. Note that the elements with a lower melting point should be placed on the bottom of copper mold. In contrast, the elements with a highest melting point were put on the top of copper mold, which is close to the neighborhood of negative electrode of tungsten. This procedure was conducted in order to avoid elements with a higher melting point melting heterogeneously during arc melting, so as to make the homogenous mixing composition of the ingot. On the other hand, since the boiling point of Mg (1363 K) is close to or lower than the melting points of Cu, Ag, Y, Gd and Nd, it is not suitable to arc melt pure Mg with other elements. Instead, the Cu-(Ag,Gd,Y,Nd) ingots were first prepared by arc melting so that the ingot can be melt with pure Mg in the subsequent injection casting. A schematic diagram for the arc melting furnace is illustrated in Figure 3.4.

Before the arc melting process, in order to avoid the ingot oxidizing, the high-purity argon gas needs to be continuously purged into the arc-melting furnace to flush oxygen away and, then, to turn on the vacuum pump to achieve a high vacuum atmosphere environment without impurities inside the arc-melting furnace. This process was repeated at least three times to ensure high vacuum inside the arc-melting furnace. After preparing the aforementioned procedures, the inner environment of arc-melting furnace was refilled with

high purity argon gas of 200 torr to keep a positive pressure. Subsequently, a high voltage was added between two electrodes and the arc was formed with extensive heat and bright light. To increase the heat exchange rate to enable the melt to be rapidly quenched, cold water was required to flow in the cooling system throughout the bottom of copper mold. The elements could be mixed together and formed the preliminary ingots under a Ti-gettered argon atmosphere. Besides, the melting process was repeated at least three times to confirm the homogeneous mixing, which is favorable for the following suction and injection castings.

3.3.2 Suction and injection casting

When the ingots were melted homogeneously by arc melting, the melt was immediately sucked into a water-cooled copper mold that has internal cylindrical-shaped cavities to fabricate the Zr- and Pd- based alloy rods under a purified argon atmosphere. The various copper molds with the cylindrical-shaped cavities inside could be replaced to prepare the cylindrical alloy rods with various sample sizes in diameter.

Before injection casting, the induction melting was performed to form the Mg-based alloy. Firstly, the ingots prepared by arc melting and pure Mg need to be put into a pure Fe crucible placed in an induction furnace. Note that the Fe crucible needs to be sprayed a thin layer of BN to prevent the alloy from interacting with the crucible at high temperatures. After induction melting the ingots with pure Mg, the melt was poured into a copper mold to form the rectangular Mg-based alloy ingots. The dimension of the ingots is 10 mm x 30 mm x 90 mm, but they are not amorphous state yet. For injection casting, the Mg-based alloy ingots were broken to pieces and, after taking appropriate amount, put into a quartz tube covered with a thin layer of BN in the inner surface. The quartz tube was placed in the induction furnace controlled by high frequency system. To suppress the generation of Mg vapor and

confirm the constituent accuracy, the purified argon atmosphere is maintained at a positive pressure of 200 torr. The gas pouring and flushing step was performed several times to ensure the high vacuum without impurities before injection casting. Due to the lower melting points of the Mg-based alloy ingots, the ingots were melted much easier. Subsequently, the alloys placed in the quartz tube were melted completely by induction melting in an induction furnace under the purified argon atmosphere, and the melt was injected into a water-cooled copper mold with a high cooling rate system by 4 atm (60 psi) argon. The illustration of the suction and injection casting process are illustrated in Figure 3.5 and Figure 3.6, respectively.

3.4 Identifications of amorphous nature

3.4.1 X-ray diffraction analyses

The amorphous nature of all as-cast cylindrical rods fabricated by the conventional copper mold casting methods was first examined by X-ray diffraction (XRD) in this study. The SIEMENS D5000 X-ray Diffractometer with Cu K_α radiation (λ = 1.5406 Å) at 40 kV and 30 mA, equipped with 0.02 mm graphite monochrometer, was utilized. The range of diffraction angle (2θ) is within 20^o to 80^o at a scanning rate of 0.1^o per four seconds. To verify the amorphous structure of as-cast rod, the as-cast rod was cut to expose the center cross-sectional surface. The cross-sectional surface of samples were ground by silicon carbide abrasive papers with water and completely polished before XRD examination.

3.4.2 Qualitative and quantitative analyses

To confirm the homogeneous composition, the secondary electron image (SEI) and backscattered electron image (BEI) were first utilized to observe the microstructure of

samples using the JEOL JSM-6400 scanning electron microscopy (SEM). To identify the component elements and composition percentage, the samples were characterized by the SEM with energy dispersive X-ray spectrometer (EDS). The cross-sectional surface of samples was cut from the as-cast rods. After complete grinding and polishing, SEM/EDS was employed to examine the quality and quantity of designed compositions.

3.4.3 Thermal analyses

The thermal properties of samples were analyzed using the applied instruments, TA Instruments DSC 2920 differential scanning calorimeter (DSC), Perkin-Elmer Pyris Diamond DSC and Perkin-Elmer Differential Thermal Analysis (DTA), DTA7. The working condition is at a constant heating rate of 0.67 K/s (or 40 K/min). For a non-isothermal heating course, GFA parameters associated with the glass transition temperature (T_g), crystallization temperature (T_x), supercooled liquid region ($\Delta T_x = T_x - T_g$), melting temperature or solidus temperature (T_m) and liquidus temperature (T_l) can be estimated by DSC and DTA based on the resultant thermograms.

The samples were taken the appropriate amount and placed into copper crucibles for DSC and aluminum oxide crucibles for DTA, followed by being tightly sealed. To prevent from oxidation and impurities liberated upon heating and polluting the operating chamber, the pre-presence air in the chamber was flushed by pure nitrogen gas and the operating chamber was kept a positive nitrogen atmosphere upon heating.

3.5 Mechanical tests

3.5.1 Micro-indentation tests

The micro-indentation tests of samples were conducted using a Shimadzu HMV-2000 Vicker's Microhardness tester. The samples were cut from the as-cast cylindrical glassy rods to expose the center cross-sectional surface. The cross-sectional surface were required to be ground by silicon carbide abrasive papers with water and polished completely. A load of 200 g and a duration time of 15 seconds were applied. The hardness values of each sample were averaged from above 10 datum points chosen randomly.

3.5.2 Compression tests

Room-temperature compression tests were performed on the cylindrical glassy rods with 2 mm in diameter at an initial strain rate of 1×10^{-4} s^{-1} by the Instron 5582 universal testing machine. According to the stress-strain curve, the compressive strength, observed elastic modulus and plastic strain can be determined. Before starting compression test, the test sample was cut from the cylindrical glassy rod with the height-to-diameter ratio (h/d) of ~2, providing a nominal aspect ratio of 2:1, as recommended by ASTM E9-89a (2000) for testing high strength materials. To accurately measure the change of sample displacement during deformation, the Instron 5582 universal testing machine was equipped with the Instrton 2601 Linear Variable Differential Transformer (LVDT) displacement transducer. Figure 3.7 shows the Instron 5582 universal testing machine with the LVDT displacement transducer.

In the preparation of test samples, the samples were first sliced from the as-cast cylindrical rods using a Buehler diamond cutter. The two ends and cylindrical surfaces of cut samples were ground by silicon carbide abrasive papers with water and polished completely. A custom sample jig was used to carefully grind and polish the top and bottom cross-sectional surfaces not only to ensure parallelism between two ends of cut sample, but also to confirm that the two ends are exactly perpendicular to the longitudinal axis of sample.

The perfect geometry of sample should be ideally perpendicular alignment between the compression surface and cylindrical axis. If the test sample is ground and polished by hand, it is likely to produce a slight misalignment between the compression surfaces and the cylindrical axis, for example, some samples produced by this way showed tilts of ~1° or slightly more, which is a geometrical defect. Wu et al. [147] has reported the information related to this subject. Hence, the careful sample preparation is seriously required for the subsequent compression test. Figure 3.8 shows the ideal geometry of sample for the Pd-based alloy, of which the sample surface has been completely ground and polished.

Furthermore, the samples were sandwiched between two WC bearing blocks under the crossheads of the Instron testing machine. The black MOLY (molybdenum disulfide, zinc oxide in special high quality grease) was used as lubricant to decrease the friction between test samples and WC platens. Each sample was carefully centered on the loading axis to ensure the uniaxial loading. The applied strain can be calculated according to the crosshead displacement after correction for machine compliance. Multiple compression tests were performed for confirming the reliability of mechanical properties.

3.5.3 Compression tests using high-sensitivity strain gauges

Rectangular BMG samples with a nominal aspect ratio of ~2 (height to width) were sliced from the 3 mm diameter as-cast rods and polished for the current study. The 3 mm diameter rods were first prepared by arc melting pure elements under a purified argon atmosphere and, then, in situ suction casting into a water-cooled copper mold. A typical test sample has dimensions of 4.34 mm x 2.30 mm x 1.09 mm (height x width x thickness) in size. Two FLA type strain gauges (Figure 3.9(a)) produced from Tokyo Sokki Kenkyujo Company were directly attached to two opposite sides of each test sample using epoxy adhesive, as

illustrated in Figure 3.9(b). The strain gages are capable of capturing small strain of ~10^{-5}. This arrangement allowed for a direct measurement of sample strain, eliminating the need to account for machine or load cell stiffness. The axially symmetric arrangement of two strain gauges can also compensate any bending of the sample during deformation. Room-temperature uniaxial compression test was conducted with two nominal strain rates of 2 x 10^{-4} and 1 x 10^{-2} s^{-1}. Load was recorded by the load cell of the Instron 5566 universal testing machine. Strain and time obtained from two strain gages were measured with a National Instrument (NI) data acquisition system without low-pass filter. The data acquisition of this system rate is as high as 2,000 measurements per second (2000 Hz). This work was carried out with the Prof. Nieh's lab in the University of Tennessee. Figure 3.10 shows the Instron 5566 universal testing machine.

3.6 Microstructure observations

To examine the microstructure of phase separation in the as-cast Zr-based alloy, the transmission electron microscopy (TEM) was carried out for this purpose. The applied instrument is the JEOL 3010 analytical scanning transmission electron microscope (AEM) with Link EXL-II EDS. The TEM/EDS analyses were performed to identify the composition of the separated liquid phases. The TEM samples were prepared by a standard ion-beam thinning technique in a Gatan 691 ion miller machine. In addition, the operating voltage in JEOL 3010 AEM is at 200~300 kV.

Furthermore, the morphologies of fracture surfaces and side view for deformed samples were observed by JEOL JSM-6400 SEM. Some of the Mg-based samples need to be etched by the solution with 100 ml of ethanol (C_2H_5OH), 5 g of picric acid ($C_6H_2(NO_2)_3OH$), 5 ml of acetic acid (CH_3COOH) and 10 ml of water. The different morphologies for the deformed

samples are characterized to properly correlate with the compressive results, so as to clarify the possible deformation mechanisms for BMGs.

Chapter 4 Results

4.1 Sample observations

The Zr-, Pd- and Mg-based alloys plus the Mg-based alloy composites can be successfully prepared by the conventional copper mold casting method. The size of the as-cast cylindrical rods is 2-3 mm in diameter and ~40 mm in length. All as-cast cylindrical rods show lustrous appearances and smooth surfaces, indicating that complete filling into the mold cavities was achieved during suction or injection casting. In particular, the surface appearance of injection-cast Mg-based alloys displays the metal-like shine more than that of the suction-cast Zr- and Pd-based alloys. Figure 4.1 shows the surface appearance of Mg-based alloy rods with various dimensions. For the cross-sectional view cut from the as-cast cylindrical rods, the cut samples reveal no observable macro-defect over the entire sample.

4.2 Amorphous nature

4.2.1 SEM/EDS observations

Quantity analyses of the polished cross-sectional surfaces of all Zr-, Pd- and Mg-based alloys were identified by SEM/EDS under a low magnification. According to the EDS results shown in Figure 4.2, all compositions of the as-cast samples are close to the predesigned composition. To confirm the absence of any crystalline phase over the entire sample, the polished cross-sectional surface was examined by SEM/BEI composition image. It can be seen that no contrast of any crystalline precipitate, non-uniformly melting or other cast

defects are observed all over the sample, indicating that the structure of all as-cast samples is the homogeneous microstructure. Figure 4.3 shows the SEM/BEI and mapping image of the as-cast $Zr_{63.8}Ni_{16.2}Cu_{15}Al_5$ cylindrical rods. The elements of Ni, Cu and Al for the $Zr_{63.8}Ni_{16.2}Cu_{15}Al_5$ alloys are uniformly dispersed in the Zr matrix.

On the other hand, cylindrical Mg-based BMGC rods were prepared by arc melting under a purified argon atmosphere and injection casting into a water-cooled copper mould. Detail information about the preparation procedure has been presented elsewhere [36]. Figure 4.4 shows the SEM observation of porous Mo particles homogeneously dispersed in the Mg-based BMG matrix. The enlarged view of a single porous Mo particle with a spherical shape and an average size of ~50 μm is shown in Figure 4.5.

4.2.2 XRD analyses

Figure 4.6 shows the XRD pattern of the $Zr_{63.8}Ni_{16.2}Cu_{15}Al_5$ alloy obtained from the sample exposing the cross-sectional surface cut from the 2 mm diameter as-cast rods. The XRD pattern consists of a broad diffraction peak characteristic of amorphous structure without any crystalline phases in the amorphous matrix. The broad diffuse hump located at the diffraction angle of about 30^o to 40^o without distinct crystalline peaks suggests that the as-cast $Zr_{63.8}Ni_{16.2}Cu_{15}Al_5$ alloys are roughly single amorphous phase. The XRD results of both $Pd_{40}Ni_{40}P_{20}$ and $Mg_{58}Cu_{31}Y_6Nd_5$ alloys also demonstrate no apparent crystalline peak and a broad diffuse hump, indicating these two alloys have amorphous structure, as indicated in Figure 4.6. For the Mg-based BMGC, the XRD pattern demonstrates the diffuse hump from the Mg-based amorphous matrix with crystalline peaks from the Mo particles, as shown in Figure 4.7. To sum up the above results, these three BMGs for $Zr_{63.8}Ni_{16.2}Cu_{15}Al_5$, $Pd_{40}Ni_{40}P_{20}$ and $Mg_{58}Cu_{31}Y_6Nd_5$ as well as the porous Mo particles reinforced Mg-based

BMGC with a diameter of 2 mm can be successfully fabricated by a conventional copper mold method.

4.2.3 Thermal analyses

The thermal properties of the as-cast $Zr_{63.8}Ni_{16.2}Cu_{15}Al_5$ BMGs were examined by DSC at a constant heating rate of 0.67 K/s (40 K/min), as shown in Figures 4.8. The glass transition temperature (T_g), the onset crystallization temperature (T_x), the melting (or solidus) temperature (T_m) and the liquidus temperature (T_l) are all marked in the DSC thermogram in Figures 4.8. The DSC thermogram exhibits the distinct T_g and T_x upon heating, followed by a wide supercooled liquid region and then exothermic reactions due to crystallization and, finally, endothermic reactions due to melting.

The crystallization exothermic reactions for this Zr-based sample in the DSC thermogram appear as one single peak, indicating one major phase is induced upon heating. The T_g, T_x, T_m and T_l of the current $Zr_{63.8}Ni_{16.2}Cu_{15}Al_5$ BMGs are 647, 745, 1114 and 1178 K, respectively. As a result, the ΔT_x (= $T_x - T_g$) and ΔT_l (= $T_l - T_m$) for the current sample can be estimated to be 98 and 64 K, respectively. Wide temperature range in the supercooled liquid region (ΔT_x = 98 K) demonstrates that the current $Zr_{63.8}Ni_{16.2}Cu_{15}Al_5$ BMGs exhibits good thermal stability. The result of the melting behavior (ΔT_l = 64 K) indicates that the composition of the current $Zr_{63.8}Ni_{16.2}Cu_{15}Al_5$ BMG is close to the eutectic point. The GFA parameters for BMG, such as T_{rg} (= T_g/T_l) [74, 75], γ (= $T_x/(T_g + T_l)$) [81, 82], γ_m [= $(2T_x - T_g)/T_l$] [85], are often used as the criteria for forming bulk-scale size. For the current $Zr_{63.8}Ni_{16.2}Cu_{15}Al_5$ BMGs, the T_{rg}, γ and γ_m value are 0.549, 0.408 and 0.716, respectively. All GFA parameters demonstrate that the $Zr_{63.8}Ni_{16.2}Cu_{15}Al_5$ BMG exhibits a good GFA.

The GFA parameters for the as-cast $Pd_{40}Ni_{40}P_{20}$ BMGs are 91 K for ΔT_x, 0.589 for T_{rg}, 0.429 for γ, and 0.772 for γ_m, respectively. The current Pd-based BMGs also show a good resistance against crystallization upon heating. As most reported literatures, the Pd-based BMG can be easily cast to form a cylindrical rod with a large diameter since it contains few cast defects within the BMG, which will be beneficial for the subsequent mechanical tests. On the other hand, the GFA parameters of ΔT_x, T_{rg}, γ and γ_m value for the $Mg_{58}Cu_{31}Y_6Nd_5$ BMGs are 73 K, 0.549, 0.415, and 0.736, respectively [196]. Both $Pd_{40}Ni_{40}P_{20}$ and $Mg_{58}Cu_{31}Y_6Nd_5$ BMGs exhibit the good thermal stability and GFA parameters. The detailed data of thermal properties for the $Zr_{63.8}Ni_{16.2}Cu_{15}Al_5$, $Pd_{40}Ni_{40}P_{20}$ BMGs plus $Mg_{58}Cu_{31}Y_6Nd_5$ BMG are tabulated in Table 4.1.

4.2.4 TEM microstructure observations

The SEM observation displays the absence of porosities and crystalline phases in the as-cast $Zr_{63.8}Ni_{16.2}Cu_{15}Al_5$ rod. In addition, the XRD analysis reveals no apparent crystalline peak. These results effectively demonstrate the 2 mm diameter as-cast $Zr_{63.8}Ni_{16.2}Cu_{15}Al_5$ rod has single glassy structure. To explore the phase separation in this Zr-based alloy system, TEM was employed to clarify the microstructure of phase separation. Figure 4.9(a) shows that the TEM bright-field (BF) image of the as-cast $Zr_{63.8}Ni_{16.2}Cu_{15}Al_5$ BMG exhibits the apparent phase separation. One is a darker contrast and the other is a brighter contrast. The inserted selected area diffraction (SAD) pattern in Figure 4.9(a) was taken from a larger region covering both the dark and bright domains. Due to very slight difference in the atomic size for Ni and Cu (atomic radius: 1.24 Å for Ni and 1.28 Å for Cu), it is difficult to distinguish whether the diffuse halos originate from the Ni or Cu domains. Based on the TEM observations, the phase separation for the current Zr-based BMG occurs only in partial regions. Some glassy matrix regions with no phase separation are still observed, exhibiting a

simple gray contrast and single halo diffraction pattern, as shown in Figure 4.9(b). Namely, the phase separation regions locally embedded in the glassy matrix.

From the TEM/EDS composition analyses of two glassy phases in the phase separation region, the compositions of bright-contrast and dark-contrast phases are Cu-rich composition of $Zr_{62.4}Ni_{14.6}Cu_{16.7}Al_{6.3}$ and Ni-rich composition of $Zr_{68.5}Ni_{21.3}Cu_{8.1}Al_{2.1}$, respectively. The characteristic scale in size for the dark-contrast glassy phases is about 0.5-1 μm, which can be seen in Figure 4.9(a). The composition of the glassy matrix without phase separation is close to the alloy composition. Therefore, there are actually three kinds of glassy phases within the current Zr-based BMG. The overall microstructure of the current Zr-based BMG consisting of phase separation region (Ni-rich and Cu-rich glassy phases) and glassy matrix region is illustrated in Figure 4.10. Based on the foregoing results, the composition of the current Zr-based alloy is consistent with that predicted by the computational thermodynamic approach. The computational thermodynamic approach provides very useful information on the selection of alloy compositions in Zr-Ni-Cu-Al alloy system for the current study.

4.3 Mechanical tests in phase-separated Zr-based BMGs

4.3.1 Mechanical properties

The uniaxial compression tests of the phase-separated $Zr_{63.8}Ni_{16.2}Cu_{15}Al_5$ BMG were conducted on the samples with an aspect ratio of ~2 (2 mm in diameter) using the Instron 5582 testing machine at room temperature. Figure 4.11 shows the representative engineering stress-strain curve obtained from the phase-separated Zr-based BMG at a nominal strain rate of 1×10^{-4} s^{-1}, as well as the corresponding true stress-strain curve. The engineering yield stress is ~1.7 GPa and elastic strain limits is ~2%, as generally seen in most reported BMGs.

The modulus calculated from the slope of elastic section in the engineering stress-strain curve is ~90 GPa. On further deformation, the phenomenon of flow serrations is observed after yielding. The inset in Figure 4.11(a) displays the enlarged view of the engineering stress-strain curve in the plastic region, suggesting that the plastic deformation mainly proceeds through numerous flow serrations.

The engineering plastic strain as high as ~14% is achieved for the current phase-separated Zr-based BMG. This result shows the evidence of remarkable plasticity before failure, which is different from other typical Zr-based BMGs with little plasticity smaller than 2%. The current phase-separated Zr-based BMG exhibits remarkable plasticity with the global fracture strain up to 16%. Multiple compression tests demonstrate that the compressive failure strain of this alloy usually ranges from 15% to 20%, indicating the excellent ductile nature. The summarized mechanical properties of the phase-separated $Zr_{63.8}Ni_{16.2}Cu_{15}Al_5$ BMG in room-temperature compression are listed in Table 4.2. Therefore, from the industrial needs of developing high strength materials with excellent ductility, the $Zr_{63.8}Ni_{16.2}Cu_{15}Al_5$ BMG with the unique structure of phase separation may have potential.

4.3.2 Fracture characteristics

The side and fracture surface morphologies of the $Zr_{63.8}Ni_{16.2}Cu_{15}Al_5$ BMGs were characterized after compression tests by SEM. Figure 4.12 shows that the side view of sample with an aspect ratio of 2 at a strain rate of 1×10^{-4} s^{-1} fractured along a plane inclined approximately 42^o with respect to the loading axis. The compressive fracture angle of ~42^o for the current $Zr_{63.8}Ni_{16.2}Cu_{15}Al_5$ BMG is smaller than 45^o, which is in consistent with the fracture mechanism proposed by Zhang et al. [28, 44, 119, 175]. Several shear bands are observed on the side view of sample surface, as shown in Figure 4.13. In addition to the

direction of major shear band, many secondary shear bands are observed on the sample side surface, suggesting that the operation of shear bands for the current Zr-based BMG with the unique structure is very intense and complicated. From the overview on the fracture surface of deformed sample (Figure 4.14), the fracture surface is relatively flat and displays a typical shear fracture feature. It reveals the feature characteristic of ductile fracture. The vein-like patterns, highly rough regions and some intermittent fine regions are observed all over the fracture surface. All of these features are the typical products of metallic glass after compressive deformation.

In an enlarged view, the vein-like patterns can be clearly observed spreading over the fracture surface, as shown in Figure 4.15. The vein-like patterns is the typical feature of fracture surface for BMG under compressive loading. As proposed by Spaepen [197], the vein-like patterns can always imply the evidence for the direction of shear band propagation along one shear plane, as marked by the arrow in Figure 4.15. It can be seen in Figure 4.16 that there are two distinct fracture morphologies of vein-like structures on the top and highly rough region in the center. Figure 4.16, which is taken from a part within the rough region as marked by a square in Figure 4.11, presents another shear-banding morphology in the phase-separated Zr-based BMG. According to the state of shear bands, the fracture surface can be roughly divided into two parts of the region I and region II, as marked in Figure 4.17. At a higher magnification, the shear bands in region I are wavy and branched, and the periodicity of wave-like structures appears to be about 0.5-2 μm, as shown in Figure 4.18. It is worthy of pointing out that less wing-like shear bands is observed in region II, which can be seen in Figure 4.19. The intermittent fine regions among the vein-like structures are also observed on the fracture surface, suggesting the intermittent sliding of sample along one shear plane during deformation.

4.3.3 Compressed samples with various strains

4.3.3.1 The 3% sample

The cylindrical samples for the ductile phase-separated Zr-based BMG with an aspect of ~2 (2 mm in diameter) were compressed to various nominal strains at an initial strain rate of 5×10^{-4} s^{-1} by the Instron 5582 machine at room temperature. Once the sample reaches the predetermined strain, the compression test was stopped at that moment. The samples were designed to compress at various strain stages with the nominal strains from ~3%, ~7% to ~10% (including elastic and plastic strain, i.e., total compressive strain). To monitor the change of sample appearance, these compression tests were halted before failure so that the deformed samples could be observed using SEM. The SEM images of deformed samples can be examined along with their corresponding load-displacement curves.

Figure 4.20 shows the representative load-displacement curve of the sample compressed to a nominal total strain of ~3% (including ~2% elastic strain). The locations of yielding as well as the plastic displacement (Δd_{LD}) are inserted in Figure 4.20. The load-displacement curve displays no obvious sign of work hardening or softening. The SEM observations on the overall appearance of the sample with nominal strain of ~3% are shown in Figure 4.21. From the view of the overall appearance of the 3% sample, it looks quite similar to the undeformed one as the as-cast cylindrical rod. Moreover, Figure 4.21 shows that several slip lines occur at an inclination angle of ~41^{o} with respect to the loading axis, and some secondary slip lines are also indistinctly observed on the lower right of the deformed sample. These visible shear bands with different orientations indicate that several shear band systems are operating in the initial stage, responsible for the observed plasticity. Since these shear bands are small, it is difficult to estimate the contribution from each individual shear band to the overall plastic

strain at this stage. Macroscopically, the shape of the compressed sample appears to be still uniformly. However, microscopically, the plastic deformation proceeds by generating a few small local shear bands.

4.3.3.2 The 7% sample

With the further deformation at nominal strain of ~7%, Figure 4.22 is the load-displacement curve for the sample compressed to ~7% total strain. There is also no apparent work hardening or softening, which is similar to the previously reported literatures [29, 198] that metallic glasses can deform in an elastic-perfectly plastic manner. For most metallic glasses, specimens would generally be broken into two pieces after failure. At this stage, one major shear sliding is observed on the side view of deformed sample. In order to trace the shear band easily, the cylindrical surface of test samples are not fully polished. As shown in Figure 4.23, only limited number of large shear bands is operating. These shear bands have an inclination angle of ~43^{o} with respect to the loading axis, which is similar to that observed in the 3% sample. Evidently, the principal shear initiates from the upper right corner of the sample. By viewing the principal shear band from a proper angle, the offset displacement on the shear plane can be measured. Under the enlarged view in Figure 4.24, there is an offset displacement of 0.229 mm along the fracture surface and a relatively vertical displacement of 0.168 mm parallel to the loading axis. In addition, there appears a split of the sliding plane at the end of this shear sliding and a second major shear begins to appear, which can be seen in Figures 4.24 and 4.25.

4.3.3.3 The 10% sample

Figure 4.26 is the load-displacement curve for sample compressed to a total strain of

~10%. The load is virtually constant but begins to exhibit a slight decrease in the late stage. At the final stage with the nominal strain of ~10%, in Figure 4.27, the enlarged view clearly indicates that there are several major shears on the sample surface together with shear planes, which are all parallel to each other with respect to the loading axis. These shear events occur as a group of several slip steps close together. In this strain stage with a nominal strain of ~10%, the principal shear produces an offset displacement of 0.365 mm and a relatively vertical displacement of 0.271 mm parallel to the loading axis. Also noted in Figure 4.27, the presence of several secondary shear bands each produces a small offset, as marked by the circle. The offset displacements caused by these secondary shear bands are notably smaller than that caused by the principal one. Besides, the number of shear bands on sample surface in this 10% sample is also noted to be significantly higher than that in the 7% sample, suggesting shear band operation is more intense at a higher plastic strain. Figure 4.28 is a SEM image taken from the opposite side of the deformed sample, also showing a significant offset displacement associated with the shear band initiation.

The summarized data related to offset displacement at various strain stages with nominal strain from 3% to 10% are tabulated in Table 4.3. Table 4.3 could be divided into two parts: (1) load-displacement (L-D) curves, which are the data extracted from the plastic displacement in the load-displacement curves, as shown in Figures 4.20, 4.22 and 4.26. The Δd_{LD} is the displacement includes the perfectly-elastic plasticity and load drop without involving elastic deformation, namely, the total plastic displacement. (2) SEM observations, which are the offset displacement along the shear plane ($d_{p,SEM}$) and the calculated vertical displacement with respect to the loading axis determined by the principal shear ($d_{v,SEM}$). Note that in Table 4.3 only the plastic strain is listed. The total stain is simply plastic strain plus 2% of the elastic strain. Given the experimental data, the displacements obtained from the L-D curves and SEM observations are similar.

4.3.4 Continuously strained sample

In the current study, the phase-separated Zr-BMG sample normally fails after about 15-20% engineering compressive strain, as demonstrated in Figure 4.11. However, there are also some cases that a compressed sample exhibits peculiar stress-strain behavior. As shown in Figure 4.29, the room-temperature compressive stress-strain curve shows temporary load drop, followed by continuous load increase until the engineering strain is over 60%. On the basis of true stress-strain curve in Figure 4.29, the softening occurs after ~15% strain and the nominal work hardening occurs once the strain exceeds 25% and, then, it can achieve the compressive strain higher than 100%. This result is similar to the "superplastic"-like behavior [30, 34, 199]. Meanwhile, the converted "engineering stress" reaches a remarkable value of 9 GPa, and the converted "true stress" also reaches nearly 3 GPa. The stress-strain curve appears to exhibit a strong work hardening. In Figure 4.29, the outer appearance of deformed sample looks like a single pancake. The outer appearance of deformed sample exhibits the fusion of the upper and lower halves of the sample without a catastrophic fracture into pieces. Figure 4.30 shows that the numerous and intense shear-banding operation can be observed on the sample surface, which is higher than the previous one in Figure 4.13. In fact, the extraordinary mechanical behavior is an artifact. This artifact will be discussed in section 5.1.

4.4 Mechanical tests in Pd-based BMGs

4.4.1 In-situ compression tests

The conventional compression tests were conducted on the monolithic $Pd_{40}Ni_{40}P_{20}$ BMGs at room temperature. A representative compressive stress-strain curve, with the elastic section corrected, is shown in Figure 4.32. The macroscopically yielding stress and elastic

modulus are ~1.8 GPa and ~100 GPa, respectively. The sample underwent the initial ~2% elastic strain, followed by ~2% plastic strain in a manner of perfectly-elastic plasticity until failure. The plastic deformation is accomplished with several flow serrations. Note that, in the corresponding load-displacement curve of this alloy, flow serration actually occurred before yielding, as indicated in Figure 4.33. The values for plateau load and first occurrence on load drop are 1.81 GPa and 1.46 GPa, respectively. The first load drop occurs at a stress level which is ~0.8 of the plateau yielding stress. The inset in Figure 4.33 shows an enlarged view of the first serration and the corresponding time.

To clarify the deformation mode of BMG, we selected a monolithic Pd-based BMG with single glassy structure and used a video camera to monitor in-situ compressive deformation of sample. Room-temperature in-situ compression tests were conducted on the cylindrical $Pd_{40}Ni_{40}P_{20}$ BMG samples using an Instron 5566 machine equipped with a Panasonic WV-BP330 CCD digital camera and a BAUSCH & LOMB microscope (20x). The captured in-situ images were recorded at a video rate of 29 frames per second (~0.033 sec/frame) by a JVC SR-MV40 type DVD recorder. The equivalent spatial resolution of the image is estimated to be 1 μm. A typical sample size is 4.11 mm in height and 2.08 mm in diameter, providing a normal aspect ratio of 2:1. The applied strain rate is at a low strain rate of 1×10^{-4} s^{-1}. The datum acquisition rate was determined to be 10 ms (100 measurements per second).

Figure 4.34 is the representative load-displacement curve plus the corresponding time for the deformed $Pd_{40}Ni_{40}P_{20}$ sample under in-situ compression test. The load-displacement curve shows five major serrations in plastic region, including the failure in serration #5. Note that the amplitude of some load drops is smaller than other major serrations, such as the load drop between serration #1 and serration #2. By judging from the in-situ image of the $Pd_{40}Ni_{40}P_{20}$ sample, the principal shear event obviously occurs along the shear plane. It was

also observed that intermittent sliding during the principal shear event occurs during deformation. Figure 4.35 shows the five stages taken from the in-situ image, including the final image at failure (Figure 4.35(a)) and four principal shear events (Figures 4.35(b)-(e)) as well as their corresponding time at which serrations occur. Figure 4.35(b) shows that the visible principal shear firstly occurs with a shear angle of 43^{o} in serration #1. Afterward, each serration is accomplished by shear displacement before and after an intermittent sliding, as shown in Figures 4.35(c)-(e). Table 4.4 summarizes the comparison of shear displacements before and after an intermittent sliding in Figures 4.35.

4.4.2 Compression tests equipped with high-sensitivity strain gauges

To further analyze the flow serration and shear band propagation, the monolithic $Pd_{40}Ni_{40}P_{20}$ BMG compressed at room temperature and a low strain rate was characterized using high-sensitivity strain gauges directly attached to two opposite sides of test sample. Test samples are the rectangular Pd-based BMG samples with aspect ratio of ~2. Figure 4.36 shows the representative engineering stress-strain curve obtained from the $Pd_{40}Ni_{40}P_{20}$ BMG compressed at the strain rate of 2 x 10^{-4} s^{-1}. The elastic modulus and plateau stress (σ_{max}) are ~90 and ~1.7 GPa, respectively, which are in agreement with the reported values [133]. σ_{max} denotes the stress level at which the stress-strain curve reaches an apparent steady-state after yielding. Macroscopically, the strain-strain curve for the Pd-based BMG is noted to exhibit numerous flow serrations, especially in the plastic region. Again, the first detectable serration occurs at ~1.4 GPa (~0.83σ_{max}) for the rectangular sample, well before the macroscopic yielding. It was noticed that the first onset of yielding in the BMG micropillar samples is over 2 GPa [142, 143]. Therefore, the early onset of yielding in the current BMG sample appears to be associated with the fact that a relatively high population of structure flaws is in the current mm-sized test sample as compared to the μm-sized sample. The stress-strain curve

can be conveniently divided into two stages, Stage 1 and Stage 2, as indicated in the insert of Figure 4.36. The separation line of these two stages is at a strain of about 2%, which is usually recognized as the separation for elastic and plastic deformation.

Since flow serration is a result of shear band propagation, there is an accompanied displacement burst when a shear band starts to propagate during deformation, and this displacement burst could be accurately captured by the high-sensitivity strain gauges. As well known, the dependence of displacement as a function of time taken from the Instron 5566 testing machine shows a linear relationship. In fact, the linear relationship is a result of the applied crosshead speed. In contrast to the system records from Instron testing machine, the dependence of displacement as a function of time obtained from the strain gauges exhibits numerous displacement bursts caused by shear band propagation, as shown in Figure 4.37. The insert in Figure 4.37 shows the enlarged view of one displacement burst. Note that the datum acquisition rate for high-sensitivity strain gauges is up to 2000 measurements per second in the current study. It suggests that an appropriate recorder equipped with a high data acquisition rate plays an important role while studying flow serration, especially for such fast shear-band propagation.

To shed lights on the shear band dynamics, the analysis of the displacement bursts in both Stages 1 and 2 that recorded from the attached strain gages were subsequently carried out. As shown in Figures 4.38(a) and 4.38(b), the size of displacement burst in Stage 2 is generally larger than that in Stage 1, namely, the amplitude of flow serration after yielding is generally larger than those before yielding. An enlarged view of displacement-time profile taken from representative displacement bursts in Stages 1 and 2 are shown in Figures 4.38(c) and 4.38(d), respectively. Obviously, both Figures 4.38(c) and 4.38(d) consist of three steps: acceleration (Step I), steady state (Step II), and deceleration (Step III). In Stage 2, the elapsed

time at Step I is ~0.5 ms, which is very short. This is the resolution limit in the current experiments. The elapsed time during the steady-state propagation (Step II) lasts only ~1-2 ms. Based on the formula, $(\Delta L/\cos\theta)/\Delta t$ (where θ is the shear angle of fracture, ΔL and Δt are size and elapsed time of displacement burst, respectively), the shear-band propagating speed on the shear plane can be estimated. Taking in account the sample shear angle of 42^{o} for the current Pd-based BMG, the average shear-band propagating speed at the steady state of Stage 2 is estimated to be ~530 μm/s. This speed is noted to be ~680 times faster than the applied crosshead speed (0.78 μm/s) of the machine, also marked in the graph. It is evident that a propagating shear band initially accelerates and, then, the propagating shear band reaches a steady sate. Finally, the propagating shear band decelerates and is arrested, suggesting that a mechanism of the blocking in a shear band after steady-state propagation is operating.

The dependences of displacement burst and shear-band propagating speed as a function of compressive strain for the $Pd_{40}Ni_{40}P_{20}$ BMG compressed at the strain rate of 2×10^{-4} s^{-1} are plotted in Figures 4.39 and 4.40, respectively. For clarity, the stress levels at the first displacement burst ($0.83\sigma_{max}$) and the transition of Stage 1 and Stage 2 ($0.93\sigma_{max}$) are also marked in Figures 4.39 and 4.40. In spite of data variation, there exists a general trend in Figures 4.39 and 4.40, namely, both the burst size and shear-band propagating speed increase with increasing compressive strain. The initial small serrations in Stage 1 may be caused by random shear bands. The large serrations in Stage 2 after yielding were demonstrated to be mainly caused by the intermittent sample sliding events which were actually a result of preferential shear band formation on an existing shear band in a BMG sample. This result is in agreement with the notion that shear along a pre-existing shear band is easier than to create a new shear band at random locations.

Taking into account plus the sample shear angle of 42^{o} and shear band thickness of

about 10 nm [200, 201], which is the a general consensus on the shear band thickness in BMGs so far, the steady-state strain rate within a propagating shear band in Figure 4.38(d) is estimated to be about 530/(10/1000) = 5.3 x 10^{-4} s^{-1}. Analysis of all displacement bursts indicates that the steady-state strain rates of propagating shear bands in Stage 2 for the current Pd-based BMG range from 5.1 x 10^{3} s^{-1} to 3.2 x 10^{5} s^{-1}, which are extremely fast.

Knowing the steady-state strain rate and stress at which shear band forms, the viscosity within a propagating shear band can be calculated and is shown in Figure 4.41 as a function of compressive strain using the following equation:

$$\eta = \frac{\tau}{\dot{\gamma}} = \frac{(P/A)\cos\theta\sin\theta}{(\Delta L/\cos\theta)/\Delta t/d}, \quad (4\text{-}1)$$

where P is the load, A is the cross-sectional area of test sample, θ is the shear angle of fracture, ΔL and Δt are size and elapsed time of displacement burst, respectively. Notably, for the current Pd-based BMG, the viscosity within the propagating shear band is between 2.9 x 10^{3} to 1.6 x 10^{5} Pa·s, which is similar to the viscosity reported for BMGs deformed at the temperatures in supercooled liquid region and at low strain rates [202-211]. Compared with the previously reported data in the Pd-based BMG [204-206, 208], even the temperature and strain rate range are quite different, it illustrates the point that the shear-band viscosity during inhomogeneous deformation in the current study is close to the value reported for homogeneous deformation at high temperatures. The relatively low viscosity within the propagating shear band is consistent with our general sense that shear resistance within a propagating shear band would become low, namely, the softening of shear band.

Compression tests of the $Pd_{40}Ni_{40}P_{20}$ BMG were also conducted at a higher applied strain rate of 1 x 10^{-2} s^{-1} to investigate the strain rate effect on shear-band propagation speed

in Stage 2. It was found that average shear-band propagating speed appeared to be insensitive to the applied strain rate (or the applied crosshead speed), at least within the strain rate range of the current study (specifically, ~530 μm/s at 2 x 10^{-4} s^{-1} and ~500 μm/s at 1 x 10^{-2} s^{-1}). However, the results also showed that the average amplitude of serration is larger (0.53 μm), but the number of serration (58) is fewer at the low stain rates as compared with those at high strain rates (0.30 μm and 114). This is consistent with the results of Jiang et al. [134], who observed that more small shear bands were formed at higher strain rates than lower strain rates in a Zr-based BMG.

Additional attempts were made to investigate the shear band dynamics in another metallic glasses, brittle Mg-based BMG system. A summary of flow serration in two different BMGs, the brittle $Mg_{58}Cu_{31}Y_6Nd_5$ and the ductile $Pd_{40}Ni_{40}P_{20}$, compressed at a low strain rate of 2 x 10^{-4} s^{-1} is listed in Table 4.5. As shown in Table 4.5, there are no significant differences among these alloy systems. The first onset of displacement burst, and steady-state strain rate and viscosity within a propagating shear band all appear to be within the same range for both alloy systems. However, the shear-band propagating speed is faster in the brittle Mg-based BMG. This result is well consistent with our general sense that the more brittle BMG would show the faster shear band propagation. In contrast, the more ductile in nature the metallic glass is, the slower the shear-band propagating speed would become.

4.5 Mechanical tests in the Mg-based BMGC

In this study, the $Mg_{58}Cu_{28.5}Gd_{11}Ag_{2.5}$ alloy was selected as amorphous matrix for preparing BMGC and the porous ductile Mo particles was used to toughen the brittle Mg-based BMG, as proposed by Jang et al. [36].

Room-temperature uniaxial compression tests were conducted on the cylindrical rods with aspect ratio of~ 2 (2 mm in diameter) at a nominal strain rate of 2 x 10^{-4} s^{-1} using an Instron 5566 universal machine. The representative compressive stress-strain curves obtained from the Mg-based BMGs with 25 vol % porous Mo particles are shown in Figure 4.42. The macroscopically yield stress is ~1.0 GPa with an elastic modulus of ~60 GPa. The sample underwent the initial ~2% elastic strain, followed by ~7% plastic strain until failure, indicating that the compressive failure strain of this alloy is up to 9%. The Mg-based BMGC with porous Mo reinforcements has succeeded in the improvement on the brittle nature of monolithic Mg-based BMG. It is of interest that Figure 4.43(a) shows an enlarged view of the plastic region right after yielding. There is no serration observed at the early stage. Afterward, there appears to show the indistinct and weak serrations right before failure in Figure 4.43(b). Nevertheless, it needs to notice that the stress amplitude of serration is as low as below 10 MPa. In our general sense, the stress amplitude of serration is usually in the range of 30-40 MPa for most reported Zr- or Pd-based BMGs.

By observing the in-situ compression image of the Mg-based BMGC, it is hard to fully distinguish the principal shear event along one shear plane, which is in contrast to the previous Pd-based BMG. For the monolithic Pd-based BMG, the relatively upper part of sample distinctly slides along the principal shear plane against the relatively lower sample during the whole deformation process. However, for the Mg-based BMGC, the intermittent sliding of the principal shear along one shear plane would become visible only at the moment before failure. The fractured sample shows two shear-off pieces, which is different from the most brittle Mg-based BMGs which show catastrophic failure. It suggests that the homogeneous distribution of porous Mo particles can effectively hinder or block the shear sliding along the principal shear plane.

To clarify the flow serration in detail, we further employed high-sensitivity strain gauges directly attached to two opposite sides of the test sample for the analysis of shear band propagation, the way performed similar to the previous Pd-based BMG. Figure 4.44 shows the displacement as a function of time taken from the strain gauges for the current Mg-based BMGC reinforced with porous Mo particles. The marked square demonstrates that there is no distinct occurrence of displacement burst, suggesting that it is consistent with the disappearance of flow serration in the stress-strain curve. This result indeed indicates that the shear-band propagating operation during deformation is blocked or arrested. In micro-indentation test, several traces of shear band propagation are observed in the left side of micro-indentation mark far away the porous Mo particles, as shown in Figure 4.45(a). In contrast, when the tip of the micro-indenter was indented toward the porous Mo particles and when the micro-indentation mark was exactly located between two porous Mo particles, as indicated in Figure 4.45(a), it is evident that there is no shear banding observed between the micro-indentation mark and porous Mo particles. Moreover, when the tip of the micro-indenter was indented right onto one single porous Mo particle, no shear band is triggered within the single porous Mo particle, as shown in Figure 4.45(b). Based on the in-situ compression test and compression test equipped with high-sensitivity strain gauges, flow serration of stress-strain curve is caused by shear band propagation. Hence, it suggests that the diappearance of flow serration for the current Mg-based BMGC is apparently associated with the lack of long-range shear band propagagtion. By employing the approach of separating the homogeneous amorphous matrix into many individual compartments, only short-range shear band propagation is possible in the current Mg-based BMGC.

Chapter 5 Discussion

5.1 Plastic strain and deformation mode of BMGs

The current phase-separated Zr-based BMG exhibits a high compressive strength (~1.8 GPa) and remarkable plastic strain of over 15% at room temperature as indicated in Figure 4.11, and sometimes even to over 100% true strain (~70% engineering strain) as shown in Figure 4.29. Assuming a uniform deformation (which is actually not), the converted true stress-true strain curve gives a true strain value of over 100%, similar to the "superplastic"-like behavior previously reported [30, 34, 199]. Meanwhile, the converted "engineering stress" reaches a remarkable value of 9 GPa, and the converted "true stress" also reaches nearly 3 GPa, as shown in Figure 4.29. In addition, the stress-strain curve appears to exhibit a strong work hardening. However, the surprising results inspire many thoughts. Does the work hardening phenomenon really exists, especial for the metallic glass with the absence of dislocation? Is there really room-temperature compressive "superplastic"-like behavior for metallic glasses? What is the reason for this phenomenon? If we just examine the initial state for the undeformed sample and final states for the deformed one, plus the recorded stress-strain curve, we might not understand the actual happening during the whole deformation process and might ignore something interesting.

A careful examination of the deformed sample shown in Figure 4.30 offers a completely different conclusion. It is evident from Figure 4.30 that the upper and lower halves of the sheared sample did not fragment into two pieces catastrophically. Instead, these two halves of sample were blocked by the upper and bottom platens, welded together by deformation induced heat, and then continued to be compressed as a whole. If the two halves are closely

welded and compressed to a large extent, the final specimen would look like a single pancake full of numerous shear bands (Figure 4.31), similar to that observed in the compression specimens with an initial height-to-diameter aspect ratio of 1:1 or less [39-43]. The extraordinary high "engineering stress of ~9 GPa" or "true stress of ~3 GPa" is, in fact, an artifact caused by the nearly doubling of the compression cross-sectional area. Taking into account of the actual cross-sectional area seen in Figure 4.30, the flow stress is calculated to be within 1.7-1.8 GPa, a value that is similar to that observed in Figure 4.11. Obviously, the apparent "work hardening" is also an artifact. This demonstrates a fact that it is dangerous to interpret the mechanical behavior directly from the stress-strain curve without the knowledge of the deformation mode of test sample, which has also been pointed out by Song et al. [212].

Additional investigations on the hardness of the deformed phase-separated Zr-based samples with nominal compressive strains from 3% to 10% were conducted using a nanoindenter. The applied strain rate is at 5×10^{-2} s^{-1}. The hardness values in nanoindentation are 6.17 GPa for the undeformed sample, 6.12 GPa for the 3% sample, 5.82 GPa for the 7% sample, and 5.57 GPa for the 10% sample. The data in nanoindentation are summarized in Table 5.1. There is a general trend that the hardness in nanoindentation decreases with increasing compressive strain, namely, strain softening. It is easy to imagine that more deformation-induced defects, such as voids, would occur within BMG at a higher compressive strain. This result is consistent with the issue previously discussed that work hardening does not exist in the continuous deformed sample.

For the principal shear band in the 7% sample shown in Figure 4.23, there is an offset displacement ($d_{p,SEM}$) of 0.229 mm along the shear plane, which yields a vertical displacement ($d_{v,SEM}$) of 0.168 mm along the loading axis; this is better illustrated in Figure 4.24. In comparison, the plastic displacement measured from the load-displacement curve

(Δd_{LD}) in Figure 4.22 is ~0.235 mm. The length changes in the deformed samples were also measured using a micrometer and the measurements are consistent with that from the load-displacement curves. A 0.168 mm vertical displacement from the principal shear accounts for ~71% of the total plastic strain recorded from the load-displacment curve, indicating that more than 2/3 of the overall plastic strain is attributed to this single principal shear band at this stage. However, as will be discussed later, local shear strain along the principal shear plane varies. In fact, shear strain at the location where shear band initiates is the largest. Therefore, the 71% contribution simply represents an average value. It is also noted in Figures 4.24 and 4.25 that a second major shear begins to appear, which also contributes to the total plastic strain, although to a lesser extent.

Note that the presence of surface defects may cause random emission of shear bands or randomly multiple shear band formation, as demonstrated in the sample compressed to 1% plastic strain. Although the test samples were not polished fully before testing, these surface defects may play a minor role in the dominant fracture mode. In fact, the principal shear always initiates from the corner of sample-platform contact, suggesting that stress concentration at the corner overwhelms the effect of surface defect. Furthermore, once the principal shear develops, subsequent sample shear along this plane dominates the rest of deformation. It is possible that more shear band formation is nucleated from the surface defects but they are irrelevant to the final fracture. The principal shear is not sensitive to the surface defects.

The principal shear in the 10% sample provides an offset displacement ($d_{p,SEM}$) of 0.365 mm, corresponding to a vertical displacement ($d_{v,SEM}$) of 0.271 mm along the loading axis, as indicated in Figure 4.27. In comparison, the plastic displacement (Δd_{LD}) measured from the load-displacement curve in Figure 4.26 is 0.312 mm. For this 10% smaple, the 0.271 mm

shear offset accounts for 87% of the plastic strain measured from the load-displacement curve. Again, 87% does not represent the maximum value of local strain contributions from the principal shear plane. The maximum occurs at the location where shear band initiates. Nonetheless, the measured (macroscopic) plastic strain is primarily carried by the principal shear. Judging from the measurements in Table 4.3, as well as the load-displacement curves in Figures 4.20, 4.22 and 4.26, it is reasonable to argue that the cylindrical BMG samples have undergone apparently uniform deformation at an initial ~1% plastic strain. After this stage, one of the shear bands would gradually develop into a major one and soon takes over the plastic deformation; the overall observed plastic strain would be largely contributed by this principal shear band. For the 7% sample, the principal shear accounts for about 71% of the total plastic strain. For the 10% sample, this value increases to about 87%.

In the present study, the ductile phase-separated Zr-based BMG samples were deformed to various compressive strains at a low strain rate of 5×10^{-4} s^{-1} and, subsequently, characterized for deformation mode. In compression, the ductile phase-separated Zr-based BMG samples underwent the initial ~2% elastic strain, followed by ~1% apparent uniform plastic strain and, then, the development of the principal shear together with several secondary shear bands until ~20% plastic strain. There was no evidence of strain hardening or softening and the principal shear contributed the majority of the measured plastic strain. At a compressive strain larger than 20%, test sample experienced either fast load drop to complete failure or gradual load rise caused by the multiple contacts between compression platforms and fragmented samples. In the later case, the converted stress-strain curve would appear to indicate a highly plastic material, which is, in fact, an artifact. In principal, using a standard compressive sample with an aspect ratio of 2:1, when the compressive strain is over 25% the further deformation would has no physical meaning since the sheared two halves will be touched by the upper and bottom platens, becoming constrained deformation, as

illustrated in Figure 5.1. It is also found that the principal shear along the major shear plane mainly dominates the whole deformation process.

5.2 Local shear strain

From the view of Figures 4.21, 4.23 and 4.27, it is evident that the principal shear always initiates from the corner of sample-compression platform contact. This is somewhat anticipated since there is an unavoidable friction between the sample and compression platform. It is also noted that the local shear strain varies along the shear plane, specifically, the initial sliding distance along the principal shear plane $\Delta l_{\text{initial}}$ (as well as the resolved vertical distance $\Delta l_{\text{v,initial}}$) appears to be the largest at the initiation site, and reduces monotonically along the shear plane. Taking the 7% sample as an example, the shear in the sample is schematically illustrated in Figure 5.2. Figure 5.2(b), which corresponds to Figure 4.23, shows $\Delta l_{\text{v,initial}}$ (= 0.196 mm) at the upper right corner where the principal shear band was initiated, $\Delta l_{\text{v,mid}}$ (= 0.168 mm) at the midpoint along the shear plane, and $\Delta l_{\text{v,end}}$ (= 0.114 mm) the surface offset. In the figure, $\Delta l_{\text{v,initial}}$ can be measured by restoring the deformed part to its original undeformed state, as shown in Figure 5.2(c). These three shear displacements are converted into the local strain values of 4.73% (initial), 4.06% (midpoint), and 2.75% (end) by dividing the original length of sample, respectively. Evidently, the local shear strain is a function of distance along the shear plane. This is plotted in Figure 5.3 in which data from both the 7% and 10% samples are included. As indicated in Figure 5.3, the local shear strain along the principal shear band varied not only for the 7% sample, but also for the 10% sample. There is a trend that the local shear strain decreases monotonically with distance from the location where the shear was initiated.

Thus, the principal shear does not take place in an integrated mode. In other words, it

differs from the sliding of two rigid bodies. Apparently, some of the shear displacements (or strain) were interrupted by the crossing shear bands (nearly 90^{o} with respect to this principal shear) or stored within the sample. In either case, the principal shear experiences certain resistance along the shear direction, in a manner analogous to have the shear band diverted or deflected by obstacles in a BMG composite. For a brittle BMG, once the principal shear band is developed under compression testing, it propagates immediately after yielding and fails catastrophically. For the current phase-separated BMG which is relatively plastic, a propagating shear band encounters resistance or friction resulting from the micro-scaled separated harder glassy phase. The delay of shear band propagation and shear band interruption cause the principal shear band to slow down and, thus, promote the initiation of secondary shear bands from other orientations allowing a 15-20% strain before failure.

The sliding displacement and plastic strain measured by SEM, as listed in Table 4.3, are actually obtained from the local mid-point on the principal shear plane, namely, $\Delta l_{v,mid}$. As shown in Table 4.3, the converted plastic strains from the local mid-point ($\varepsilon_{v,mid}$) are ~4.1% for the 7% sample and ~7.4% for the 10% sample, indicating that the principal shear contributes ~71% of total plastic strain for the 7% sample and ~87% of total plastic strain for the 10% sample. On the other hand, if we use the estimated displacement by extrapolating the principal shear band at the shear band initiation point, $\Delta l_{v,initial}$, taken from the SEM observation, the converted plastic strains from the initiation point ($\varepsilon_{v,initial}$) would be ~4.9% for the 7% sample and ~8% for the 10% sample, respectively. This result suggests that these strain values are even closer to the data in the load-displacement curve (5.7% and 8.7%). It follows that the compression strain contribution from the principal shear would be ~86% for the 7% sample and 92% for the 10% sample. Based on the measurement from $\varepsilon_{v,initial}$ and $\varepsilon_{v,mid}$, both demonstrates that the overall plastic strain is indeed overwhelmingly contributed by one single principal shear from the early stage of deformation.

5.3 Intermittent sample sliding

For the ductile Zr-based BMG compressed at low strain rates (~10^{-4} s^{-1}), the dominant macroscopic deformation mode (more than 2/3 of the overall plastic strain) at room temperature is one single shear along the principal shear plane. Besides, the stress-strain curve exhibits numerous flow serrations in the plastic region, as shown in Figure 4.11. In 1973, Chen [213] proposed that flow serrations observed in compressive stress-strain curve of several Pd-based BMGs can be characterized by repeating cycles of a sudden load drop followed by elastic reloading. The reloading slope is approximately parallel to the elastic section of stress-strain curve. As shown in Figure 4.34, each reloading slope is approximately consistent with the elastic part of load-displacement curve, indicating that loading process is elastic. The unloading part in load drop is associated with inelastic displacements caused by localized shear banding. Wright et al. [214] reported that flow serration for the Zr- and Pd-based BMGs under compression testing equipped with LVDT appears to be associated with shear band emission. The load drop is not caused by the drop in viscosity induced by local heating (or local temperature rise).

To clarify flow serrations observed in stress-strain curve, a monolithic Pd-based BMG was selected for a detailed analysis of the observed serrations. The enlarged view of the serrated region is plotted in Figure 4.34, showing the multiple cycles of reloading and unloading. There are five major load drops (or flow serrations) observed in the stress-strain curve. The amplitude of these five major flow serrations is evaluated to be ~40 MPa (~130 N) for the current $Pd_{40}Ni_{40}P_{20}$ BMG, which is compatible to most reported value in literatures. As shown in Figure 4.34, the amplitude of load drops before yielding is smaller than those after yielding. The amplitude of load drop increases with increasing the plastic strain, which is consistent with the results of Torre et al. [129], who observed an increase in stress drops

with increasing strain in monolithic Zr-based BMGs [129].

From the in-situ compression experiments for the current Pd-based BMG, there is indeed a one-to-one correspondence between the intermittent sample sliding caused by the principal shear event and five major flow serrations as demonstrated in Figures 4.34 and 4.35. This result indicates that these five major flow serrations are resulted from intermittent sample sliding along the principal shear plane. Song et al. [212] also pointed out that flow serrations in the plastic region are accomplished by the shear offset caused by the principal shear event. In Figure 4.35(a), the shear offset caused by the sample sliding along the principal shear plane is estimated to be 0.028 mm. It is very close to the plastic displacement of load-displacement curve (0.034 mm). In the case of phase-separated Zr-based BMG with sufficient plasticity, for the 7% sample, the principal shear accounts for ~71% of the total plastic strain. For the 10% sample, this value increases to ~87%. Again, for the current monolithic Pd-based BMG, one single shear along the principal shear plane mainly dominated the overall plastic displacement, ~82% of total plastic strain.

The amplitude of load drop for the current Pd-based BMG is ~40 MPa. Note that, in the previous study, the Mg-based BMGC with porous Mo particles hardly shows the load variation in the plastic region of its stress-strain curve. Only few minor load variation observed right before failure, which is as low as < 10 MPa. Comparing the in-situ compression experiments for both samples, the event of principal shear sliding is clearly visible for the Pd-based BMG but not for the Mg-based BMGC with porous Mo particles. These results demonstrate that the operation of principal shear sliding is different in these two samples.

For the phase-separated Zr-based BMG, the shear motion caused by intermittent sample

sliding was also investigated. The serrated region of stress-displacement curve was analyzed and the result is presented in Figure 5.4. As indicated in the figure, the density of serrations is estimated to be 614 mm^{-1} in the selected plastic region or 1.63 μm displacement/serration, which is consistent with our general sense that the spacing between two striations observed on the fracture surface is close to the order in the scale of a few micrometers. Furthermore, the morphology of the fracture surface was examined by SEM and the result is shown in Figure 5.5. The arrow in Figure 5.5 indicates the shear direction and the viewing direction is parallel to the loading axis. It is evident that there are numerous and regularly spaced striations perpendicular to the shear direction on the fracture surface. According to the fracture angle of 41^{o}, the density of the striations along the projection of compression direction during sliding can be estimated to be ~633 mm^{-1} ($11/0.020\tan 41^{o}$) or 1.58 μm between striations, which is very comparable to the density of serrations shown in Figure 5.5. This demonstrates that there is a one-to one correspondence between the serrations observed in the stress-strain curve and the striations caused by the intermittent sample sliding on the fracture surface. As reported by Mukai et al. [133], the fracture surface of a Pd-based BMG showed an initial progressive sliding region, followed by catastrophic shear-off. Viewing the shear zone size of SEM image, the spacing between striations can be estimated to be ~2.8 μm, which is close to our current observation of ~1.6 μm. This additional evidence also suggests that the deformation of BMG is dominated by single shear along the principal shear plane. Hence, flow serration observed in the stress-strain curve is a result of shear band propagation, not caused by shear band emission.

As indicated in our present compression experiments plus the results of Song et. al. [212], the shear band propagation in the early deformation stage represents the formation of randomly multiple shear bands. These shear bands formed on sample surface but do not propagate through the test sample. By contrast, shear band propagation in plastic deformation

are mainly from consecutive shear band formation on a plane previously sheared, or single shear along the principal shear plane. In fact, shear banding in plastic deformation is like the propagation of a mode-III crack. These consecutive shears (or intermittent slides) on the principal shear plane eventually result in the observed localized shear till failure.

In Figure 4.34, each load drop in the load-displacement underwent a very small displacement in 0.07 sec with the captured 7 acquisitions. The detected points during one load drop depend on the data acquisition rate of testing machine. Note that the constant strain rate is $1 \times 10^{-4}\ s^{-1}$ and the data acquisition rate is 100 measurements per second. As well known, shear band propagation occur in an instant. The fast shear sliding along the principal shear plane may not be followed up by the relatively-slow platen movement operated at a constant strain rate. As a result, if we want to further investigate the flow serration or shear band propagation, the records taken from the universal Instron testing machine is not sufficient for analysis. Using high-sensitivity strain gauges with a higher data acquisition rate, it would be able to get more detailed data for the analysis of flow serration caused by shear band propagation.

5.4 Local heating

So far, many literatures have investigated this issue for local heating (or temperature rise) within a shear band [171, 214-219]. As well known, the characteristic of vein-like patterns spread over the fracture surface is a typical feature of fracture morphology for metallic glasses. The extended direction of vein-like patterns can exactly demonstrate the evidence for the direction of shear band propagation during deformation. The reason for the formation of vein-like patterns is attributed to a local change of viscosity within a shear band upon failure. In addition, the re-solidified droplets along with vein-like patterns can be also observed on

the fracture surface, as indicated by the arrow in Figure 5.7. The re-solidified droplets suggest that the temperature rise reaching the melting point may have occurred during the catastrophic failure. On the other hand, in Figures 4.16 and 5.5, there are still some rough regions with shear striations (or progressive shear regions) observed on the fracture surface. As demonstrated in the previous section, the progressive shear regions are the result of the intermittent slides of single shear along the principal shear plane. This suggests that the vein-like patterns and re-solidified droplets observed on the fracture surface appears to be the products after the failure of a BMG, but the progressive shear regions are not.

During deformation, local shear bands began to develop. Afterwards, the principal shear band was soon developed and, then, the intermittent sample slides along the principals shear plane occurred, leading to the progressive shear regions. As the decrease in viscosity within the principal shear band, the metallic glass can easily flow and then separates along the principals shear plane (or fracture surface). After the sample slides are sheared off upon failure, the vein-like patterns can be observed on the separated surface, as shown in Figure 4.15. The experiments by applying a shear force on a viscous material have been performed on the glass slides to demonstrate this feature [220]. This result inspires us to think over the primary cause of the formation of vein-like patterns or re-solidified droplets.

Assuming that the decrease in viscosity would depend on the sudden temperature rise within a shear band, the temperature rise within a shear band can be estimated based on the release of high stored energy which is generated by the intense plastic deformation of BMG. Figure 5.8 shows the typical compressive load-displacement curve taken from the phase-separated Zr-based BMG sample with a large plasticity of ~15%. Since flow serration is a result of shear band propagation, the energy release during shear band propagation or at failure can be roughly estimated according to the accumulated area for one serration. The

energy release (ΔE) by a single load drop, represented by the inserted triangles in Figure 5.8, can be expressed as

$$\Delta E = \int \vec{u} \cdot \vec{F} \cong \vec{u} \cdot \vec{F}/2 , \quad (5\text{-}1)$$

where $\vec{u}$ is the axial displacement and $\vec{F}$ is the applied load. Note that $\vec{u}$ is the displacement parallel to the loading axis and, therefore, the displacement on the shear plane inclined ~43^{o} with respect to the loading axis can be converted by a fracture angle of BMG. For the current phase-separated Zr-based BMG, the energy release in the serrated region is estimated to be ~10^{-4} J, which is similar to the value reported in other literatures [28, 215]. However, the energy release at the moment of failure is estimated to be ~0.4 J, which is noted to be about three orders of magnitude larger than those in the serrated region. This result suggests that the temperature rise induced by the energy release at failure is sufficiently high to make the viscosity within a shear band dramatically decrease. Even the sudden temperature rise induced by the high fractured energy release may melt the entire fracture surface and cause the catastrophic failure of a BMG, which is consistent with the evidence of re-solidified droplets on the fracture surface. By contrast, the temperature rise within a shear band well before failure should be significantly lower and would cause far less local melting due to a lower energy release.

Yang et al. [171] proposed a criterion to predict the temperature rise within a shear band. At failure, the instantaneous temperature, theoretically predicted within a shear band, is close to T_g. The catastrophic failure of BMG results from the sudden temperature rise within a shear band. Wright et al. [214] analyzed that, for the flow serrations in the plastic region before failure, the predicted temperature rise within a shear band is only a few degrees Kelvin. Thus, it seems unlikely that local heating is the primary cause of the change in viscosity

during a propagating shear band. The change in viscosity seems to be associated with excess free volume generation within a shear band. Also, Torre et al. [215] pointed out that the energy release within a shear band is slight and the temperature rise during shear band propagation is insufficient to cause local melting. Based on the aforementioned, the sudden decrease in shear band viscosity at which shear band propagates along the principal shear plane should not be caused by the sudden temperature rise. The temperature during shear band propagation is considered to be well below the melting point.

It is generally recognized that the temperature within a shear band would approach T_g so as to easily flow for a BMG. The viscosity within a shear band should be able to make shear band flow viscously. When the viscosity within a shear band approaches to a level suitable for viscous flow, a BMG will soon lose its ability to sustain the shear load with a sudden decrease in viscosity.

5.5 Softening caused by shear banding

Following the previous section, it can be imagined that the shear band consists of a layer of material with a viscosity lower than that of the rest of the sample, which weakens the plane against fracture. Thus, the basic physical process underlying the localized shear bands will cause the softening of the material.

To investigate the softening caused by shear banding, the hardness around the major shear band was examined on the phase-separated Zr-based BMG samples. The nanoindentation test was conducted on the deformed sample which has a single shear along the principal shear plane formed on the sample surface, as shown in the Figures 4.23 and 4.27. To ensure the indentation can be accurately located in the major shear band, the

micro-indenter is not suitable. Instead, the nanoindenter is very suitable. The test sample was indented following the direction perpendicular to the major shear band. As schematically illustrated in Figure 5.9, the distance perpendicular to the shear band was indented on the polished sample surface to examine the hardness change around the major shear band. The interval between two nanoindentation points was designed to be the smaller distance of 10 μm and the applied strain rate is equal to 5 x 10^{-2} s^{-1}. Note that the relative distance is symmetric from the center of major shear band.

In principle the nanoindentation located at the neighborhood of the major shear band will exhibit a lower hardness. Figure 5.10 shows the dependence of hardness and elastic modulus in nanoindentation as a function of the relative distance from the major shear band. There appears to exhibit the difference in hardness. In comparison with the average hardness value for higher points of ~6.68 GPa, the lower average value for the lower four points is ~6.11 GPa, namely, there is a degradation of ~10% in the lower four points. In Figure 5.10, the hardness apparently decreases with the distance toward the location where the major shear band was formed.

In the past, the softening phenomenon was proposed for the case that the hardness was indented on the cross-sectional area of deformed sample with a reasonable assumption which numerous shear bands is within BMG [42]. As discussed previously in Table 5.1, for the phase-separated Zr-based BMG samples compressed to various strains from 3% to 10%, the nanoindentation hardness decreases with increasing strain. In this case, more deformation-induced defects which occur within BMG at a higher compressive strain will result in a softer structure. However, the present experiments can effectively provide a clear distinction in hardness of amorphous matrix and shear bands and, meanwhile, give a direct evidence for the softening caused by shear banding. The present work demonstrates that there

is strain softening for BMGs. In other words, the shear resistance along the principal shear plane will reduce when the major shear band forms, which is in accordance with the decrease in viscosity within a shear band.

5.6 Flow serration and shear band viscosity

In Chapter 4, using the steady-state strain rate data, the viscosity within a propagating shear band for the current Pd-based BMG can be calculated and ranges from 2.9 x 10^3 to 1.6 x 10^5 Pa·s (Figure 4.41), which is in agreement with the above demonstration on the decrease in viscosity within a shear band. These viscosity values are similar to the equilibrium viscosity reported in many BMGs deformed at the temperatures in supercooled liquid region and at low strain rates [202-211].

It was pointed out that [216, 217, 219], once applied stress is over a critical level, shear band starts to propagate and there is a sudden energy release. This elastic strain energy may cause a temperature spike in a highly confined space within metallic glasses. It suggests that this sudden temperature spike is probably responsible for the acceleration (or initiation) of the shear band during Step 1, as indicated in Figure 4.38. It was also noted that, although a sudden temperature rise may occur locally, the time duration is extremely short in these studies (about a few nanoseconds) [216, 217, 219]. We notice that, for the current Pd-based BMG, the elapsed time during the steady-state shear band propagation event is in the range of milliseconds (~1-2 ms in Figure 4.38), which is noted to be several orders of magnitude larger. Such a lifetime of temperature spike (a few ns) seems to be insufficiently long to sustain the steady-state shear band propagation event (1-2 ms). Therefore, the main driving force for the steady-state shear band propagation cannot be the temperature rise.

Following the previous study [221], we apply the free volume model to explore the fast steady-state shear band propagation and relatively low viscosity. According to the free volume model of Spaepen [121], the viscosity (η) can be determined by

$$\eta = \frac{\tau}{\dot{\gamma}} = \frac{\tau}{2\nu \sin h\left(\frac{\tau\Omega}{2kT}\right)} exp\left(\frac{\alpha v^*}{v_f}\right) exp\left(\frac{\Delta G^m}{kT}\right), \quad (5\text{-}2)$$

where ν is the thermal vibration frequency, Ω is the atomic volume and ΔG^m is the activation energy. These factors are constants. Since the temperature rise only lasts within an extremely short period of time in about few nanoseconds [216] and the amplitude of stress drop is within 1%, it is reasonable to assume that the temperature (T) and shear stress (τ) are practically constant during the steady-state shear band propagation. If α = 1, ν* = 1.2 x 10^{-29} m^3/atom, the change in viscosity can be calculated by

$$\frac{\eta_2}{\eta_1} = exp\left[\alpha v^* \left(\frac{1}{v_{f2}} - \frac{1}{v_{f1}}\right)\right]. \quad (5\text{-}3)$$

It is evident in Equation 5-3 that viscosity (η) strongly depends on the excess free volume, v_f. For example, if v_{f1} is 5 x 10^{-32} m^3/atom, which is taken from the absolute free volume in a Zr-based BMG at room temperature [222], and the free volume is increased by 1%, namely, v_{f2} will be 5.05 x 10^{-32} m^3/atom. Thus, the change in viscosity would increase by one order of magnitude. It is worthy of mentioning again that the viscosities in various BMGs in or near the supercooled liquid region were usually measured by static or quasi-static mechanical tests. In these cases, the applied strain rates are typically at 10^{-5} to 1 s^{-1} [202-211, 223]. In contrast, shear band propagation is a dynamic process. As indicated in Table 4.5, the shear-band strain rate for the current Pd-based BMG is ~10^4 s^{-1}. In previous studies [203, 223], it was reported that shear viscosity decreases with increasing applied strain rate, as a result of increasing free volume creation at high strain rates. Thus, the measured low viscosity within a propagating

shear band may be a result of free volume accumulation caused by the dynamic strain rate.

To further explain this result, a self-consistent Vogel-Fulcher-Tamann (VFT) equation [223] based on the free volume model is used to analyze the viscosity within a propagating shear band during inhomogeneous deformation at room temperature. As proposed by Grest and Cohen [224, 225], viscosity is a strong function of excess free volume (ν_f) and can be expressed, in another variant of Equation 5-3, as

$$\eta = \eta_o exp\left(\frac{\nu_{crit}}{\nu_f}\right), \tag{5-4}$$

where ν_{crit} is the critical volume for flow [225], and $\eta_o = h/\nu_a = 4 \times 10^{-5}$ Pa·s is a constant (h is the Planck's constant, $\nu_a = 1.62 \times 10^{-29}$ m^3/atom is the atomic volume for this Pd-BMG). The excess free volume is obviously a function of temperature. In fact, the equilibrium free volume is approximately proportional to $T-T_o$ at high temperatures ($>T_o$), and vanishes at T_o, where T_o is the VFT temperature [223]. In addition, According to the Spaepen's report in 2006 [120], the rate of excess free volume generation during plastic deformation was reported to be proportional to the strain rate at high stresses. Combining with above two statements, the excess free volume (ν_f) is related to two terms of temperature ($T - T_o$) and strain rate ($\dot{\gamma}$), which can be expressed by

$$\nu_f = \frac{R\dot{\gamma}\eta}{G} + \beta\nu_o(T - T_o)\,. \tag{5-5}$$

Taking Equation 5-5 into Equation 5-4, the viscosity can be replaced by a self-consistent VFT equation [223] and is expressed as

$$\eta = \eta_o exp\left[\frac{\nu_{crit}}{(R\dot{\gamma}\eta)/G + \beta\nu_o(T-T_o)}\right], \tag{5-6}$$

where R is the proportional constant, β is the difference between the thermal expansion coefficients of the liquid and the glass, ν_o is the atomic volume at T_o, and G is the shear modulus of the material. β, T_o, ν_o, and R are all constants. As indicated in Equation 5-6, the decrease in viscosity can be caused by either strain rate increase or temperature increase.

In the present study, the temperature rise cannot sustain during shear band propagation, as demonstrated in the beginning in this section. Thus, the contribution of temperature rise to the decrease in viscosity must be negligible, and the viscosity is mainly determined by the strain rate term of Equation 5-6. Then, Equation 5-6 can be modified and the viscosity can be approximated by

$$\eta = \eta_o exp\left(\frac{\nu_{crit}}{R\dot{\gamma}\eta/G}\right). \quad (5\text{-}7)$$

To make a comparison, viscosity data obtained in the current study and the data taken from the same composition of the $Pd_{40}Ni_{40}P_{20}$ BMG previously reported at the temperature in supercooled liquid region of 560-620 K [205] are plotted in a double logarithmic graph in Figure 5.11.

The viscosity curves for the previously reported $Pd_{40}Ni_{40}P_{20}$ BMG are concave at all temperatures. At each temperature, the viscosity is virtually constant in the low strain rate regime, but becomes strain rate dependent in the high strain rate regime. All curves are noted to asymptotically merge into a single line at high strain rates in Figure 5.11. This trend indicates that viscosity is independent of the ambient temperature at high strain rates. The convergent line coincides exactly with the current experimental data and fits very well with the prediction for shear band propagation at room temperature based on the self-consistent VFT equation. As indicated in Figure 5.11, the overlap of these data sets at high strain rates

suggests that strain rate, thus the excess free volume creation, plays the dominant role in the dynamic of shear band propagation. Instead, the temperature rise may only play a minor role.

5.7 Flow serration and shear band propagation

In compression tests equipped with high-sensitivity strain gauges, flow serrations observed in stress-strain curve is a result of shear band propagation, as accompanied with a displacement burst. The typical displacement-time profile for one serration consists of three steps: acceleration (Step I), steady state (Step II), and deceleration (Step III). The shear-band propagating speed can be determined and found to be insensitive to the applied strain rates. It was also found that both the displacement burst size and shear-band propagating speed increase with increasing compressive strain (Figures 4.39 and 4.40).

It is worth pointing out that, based on the formula of $\sigma = K\varepsilon^n$, where σ is the applied stress, ε is the strain and K is the strength coefficient, the high "apparent" strain hardening coefficient (n = 0.38) of the current Pd-based BMG was observed during the transition from Stages 1 to 2 in Figure 4.36. Generally, the n value is between 0 and 1 and the n value lies between 0.10 and 0.50 for most metals. From the viewpoint of physics, there is actually no hardening process for BMGs. As indicated in Figures 4.33 and 4.39, the onset of first load drop (or serration) occurs well before reaching the stress level for the global yielding, i.e., the plateau stress. The bend-over of the stress-strain curve was caused by the random formation of shear bands. It is not caused by any kind of hardening mechanism. In fact, the entire sample is still in the elastic region. This deformation continues until the stress reaches the macroscopic yield strength and, then, the stress keeps a plateau stress, indicating no hardening. It is obviously different from the traditional strain hardening phenomenon occurring in crystalline materials, where dislocations move and interact after yielding and

leads to strain hardening.

As demonstrated in section 4.4.2, more and smaller shear bands were formed at higher strain rates than lower strain rates in the $Pd_{40}Ni_{40}P_{20}$ BMG. The free volume accumulation plays an important role during the dynamic event of shear band propagation. According to the free volume model proposed by Speapen [120, 121], shear band initiation mainly depends on the generation of more excess free volume and more excess free volumes can be formed at a higher applied strain rate. Therefore, it is expected that, at high strain rates, more shear bands are initiated in order to accommodate the high applied strain rate. This explains the higher serration number but smaller serration amplitude at the high stain rates than that at low strain rates in the Pd-based BMG.

The strain rate effect on flow serration and shear band propagation shows the shear-band propagating speed is insensitive to the applied strain rate, at least within the applied strain rate range of the current study (specifically, ~530 μm/s at 2 x 10^{-4} s^{-1} and ~500 μm/s at 1 x 10^{-2} s^{-1}). This result inspires us to notice the disappearance of serration in the stress-strain curve at high strain rates. In principle, flow serration can only be detected when the crosshead speed (or the applied strain rate) is lower than the shear-band propagating speed. In the current experiment for the $Pd_{40}Ni_{40}P_{20}$ BMG, the average shear-band propagating speed (~530 μm/s) at the strain rate of 2 x 10^{-4} s^{-1} is ~680 times faster than the applied crosshead speed (0.78 μm/s). By contrast, at higher strain rate of 1 x 10^{-2} s^{-1}, the corresponding shear-band propagating speed (~500 μm/s) is only about 12 times faster than the applied crosshead speed (43 μm/s). When the crosshead speed is approaching to the shear-band propagating speed, the shear band propagation would be overwhelmed by the applied crosshead speed and flow serration would disappear. This explains the absence of flow serration at high strain rates reported in the literature [226].

For example, Mukai et al. [133] showed a decreasing serration phenomenon with increasing strain rate in the $Pd_{40}Ni_{40}P_{20}$ BMG and serration completely vanished when the strain rate was over 1 x 10^{-1} s^{-1}. Therefore, the disappearance of serration in compression at high strain rates is not caused by the absence of shear band formation or a change of shear band propagation speed. It is rather caused by the fact that the shear-band propagating speed and crosshead speed are so close that the signature of displacement burst is overshadowed by the travel of applied crosshead. In other words, when the slope of the displacement-time curve shown in Figure 4.38 prior to Step 1 is close to that for Step 2, serration will disappear. The effect of strain rate on the serrations reported in most literatures is always characterized by the observation that the higher the strain rate, the less the serrations observed in the load-displacement. The above result also excludes the conventional explanation that the disappearance of flow serration was caused by multiple shear band formation.

In comparison with the flow serration in two different types of BMGs, the ductile Pd-based BMG and brittle Mg-based BMG, as listed in Table 4.5, the first onset of displacement burst (~$0.8\sigma_{max}$), and shear-band strain rate (~10^{3}-10^{5} s^{-1}) and viscosity value (~10^{3}-10^{5} Pa·s) all appear to be within the similar range for both alloy systems. However, the shear-band propagating speed in Stage 1 is faster in the more brittle Mg-based BMG. For the current Pd-based BMG at the applied strain rate of 2 x 10^{-4} s^{-1}, the average shear-band propagating speeds in Stage 1 and Stage 2 are 424 μm/s and 532 μm/s, respectively. However, in comparison with the serration of two BMGs in Stage 1 (since there is no apparent Stage 2 for the brittle Mg-based BMG), the average shear-band propagating speed of ~492 μm/s for the $Mg_{58}Cu_{31}Y_{6}Nd_{5}$ BMG is faster than that for the $Pd_{40}Ni_{40}P_{20}$ BMG (~424 μm/s). This result is well consistent with our general sense that the more ductile in nature the metallic

glass is the slower the shear band propagating speed would become. In early deformation stage (Stage 1), the brittle Mg-based BMG seems unlikely to resist against the travel of the faster shear-band propagation, leading to the catastrophic failure. By contrast, the ductile Pd-based BMG experiences the slower shear-band propagation, and, even after yielding (Stage 2), the ductile Pd-based BMG is still capable of accommodating the faster shear band propagation (532 μm/s) till failure. It is found that the dynamics of shear band propagation plays an important role in the ductility for metallic glasses.

In Table 4.5, the shear band propagation consists of three steps: acceleration, steady state, and deceleration, indicating the continuous dissipation of kinetic energy carried by a travelling shear band. Taking into account of the integral energy under one serration in the stress-strain curve, the average kinetic energy stored during each serration for the current Pd- and Mg-based BMGs is estimated to be about 2.2×10^{-4} J and 8.1×10^{-6} J, respectively. In addition, the ductile phase-separated Zr-based BMG is estimated to be about 4.1×10^{-4} J. Notably, the kinetic energy is much higher in the Pd- and Zr-based BMGs, suggesting that the Pd- and Zr-based BMGs are able to accommodate a larger kinetic energy till failure. Even in comparison with the kinetic energy in Stage 1 for both BMGs, the average value of 9.7×10^{-5} J for the Pd-based BMG is still higher than that for Mg-based BMG. The failure strain of BMGs is related to bond breaking and shear band formation, and in-turn related to the glass transition temperature, shear and bulk modulus, and Poisson ratio, etc. Here, we note that the correlation between the kinetic energy for one serration and failure strain exhibits a direct relationship with the compression ductility for the three BMGs: ductile phase-separated Zr-based BMG (4.1×10^{-4} J and >10% plastic strain) > Pd-based BMG (2.2×10^{-4} J and ~3-5% plastic strain) > brittle Mg-based BMG (8.1×10^{-6} J and ~0% plastic strain), as illustrated in Figure 5.11. The data on the Au- and Cu-based BMGs, obtained in our parallel study, are also included for comparison. In this study, the ductility of BMG appears to be

closely related to the dynamics during shear band propagation. The kinetic energy stored during each serration of shear band propagation appears to be a promising indicator for the ductility of BMGs, and is a useful parameter easy to be experimentally measured.

5.8 Flow serration in porous Mo particles reinforced Mg-based BMGC

To gain the maximum benefit from a composite, certain requirements must be satisfied. The strength of the reinforced phase must be comparable or stronger than the glassy matrix itself. Otherwise, when the strength of the reinforced phase is notably smaller than the glassy matrix itself, the plastic instability, thereby catastrophic failure, will be developed prior to or upon the yielding of the glassy phase. It can be expected that, when yield strengths of the reinforced and glasy phases are similar, a optimum result wil be achieved. This would reduce the strength mismatch at the matrix-reinforcement interface and, thus, decrease the tnedency for crack initiation. In this study, the yield strength of the current $Mg_{58}Cu_{28.5}Gd_{11}Ag_{2.5}$ BMG is about 900 MPa [36]. As reported by McNally et al. [227], if the grain size in the particle scales was about 4 μm, the yield strength of the particle would approach to about 0.9 GPa. For the current Mg-based BMGC reinforced with 25 vol% porous Mo particles, the single porous Mo particle has an average size of ~50 μm and the size of fine-scale compartment islands within one porous Mo particle is in the range of 1-5 μm (λ in Figure 5.13), which is similar to the results of McNally et al. [227]. Therefore, the yield strength of the porous Mo particle would be about 0.9 GPa. This explains why the onset of yielding in this Mg-based BMGC also occurs at about 1 GPa, as indicated in Figure 4.42.

Generally, the plastic deformation is accompanied by flow serrations for BMGs. However, the engineering stress-strain curve of the current Mg-based BMGCs exhibited the disappearance of flow serrations in the overall plastic strain. Only slight and few serrations

temporarily occur before failure, as demonstrated in the Figure 4.43, which is different from the results obtained from the phase-separated Zr-based BMGs and monolithic Pd-based BMGs. It is attributed to the fact that the deformation mode in the current Mg-based alloy is the mechanism of BMG composite, especially for the porous Mo particles reinforced BMGC.

The porous Mo particles reinforced Mg-based BMGC was designed with the concept in separating homogeneous amorphous matrix into numerous individual compartments with smooth and distinctive interfaces, as shown in Figures 4.4 and 4.5. It is reasonable to assume that the complicated interaction of propagating shear bands with these compartments and particle-matrix interfaces would be operated during the deformation process. Apparently, the particular type of morphology and spacial distribution of the porous Mo particles is effective to absorb strain energy by deforming the porous Mo particles themselves, suppressing the rapid occurance of extensive localized principal shear-band propagation.

As previously demonstrated in the phase-separated Zr-based BMG with numerous flow serrations in the plastic region of stress-strain curves, a propagating shear band in the relatively softer glassy phase would encounter the resistance or friction resulted from free volume consumption whenever encountering the relatively harder glassy phase. Shear-band propagation along the principal shear plane would be slowed down, resulting in that the local shear strain is a function of distance along the shear plane. For the current porous Mo particles reinforced Mg-based BMGC, which has numerous individual compartments within amorphous matrix, also play the similar role like the harder glassy phase in the phase-separated Zr-based BMG to retard the consecutive shear band propagation along the principal shear plane by absorbing the partial shear stress. The porous Mo particles with a higher melting point (2610 ^{o}C) and rigid solid (327 GPa for a solid form) would contribute more delay of shear band propagation, namely, the shear band is not able to consecutively

propagate. As demonstrated in section 5.7, the shear-band propagation process involves the acceleration, steady state, and deceleration stages. For the current Mg-based BMGC, many shear bands propagating inside the small compartments might be limited within the initial acceleration stage, thus the shear-band propagating speed becomes slower. When the shear-band propagating speed and the crosshead speed are close, the signals of displacement burst or serration would be overshadowed by the travel of applied crosshead. For the current Mg-based BMGC, it is thought that the shear-band propagating speed would be dramatically reduced due to the lack of long-range shear-band propagation. This in-turn leads to the suppression of displacement burst in the displacement-time profile or flow serration in the stress-strain curve.

Meanwhile, since there are 25 vol% small porous Mo particles within BMG, there will be numerous interfaces between the amorphous matrix and Mo particles. There is either stress concentration resulting from the large elastic modulus difference between Mo particles (327 GPa for a solid form) and amorphous matrix (50 GPa) or higher free volume in the particle-matrix interfaces and, therefore, these interfaces will serve as the sites of shear-band nucleation. As a result of the uncorrelated multiple shear-band emission and the deceleration of shear-band propagation by the porous Mo particles, the plastic deformation of the current BMGC can be accommodated until fracture in which one mature shear-band travels through the Mo particles or multiple correlated shear bands are formed along a shear plane.

An effective spacing distance accounting for the free spacing between two porous Mo particles and the size of single porous Mo particle is adopted for interpreting the shear-band propagation of the current Mg-based BMGC. Morphologically, two length scales in BMGC need to be considered: the inter-Mo spacing and intra-Mo spacing (i.e. the spacing between two fine-scale compartment islands within single porous Mo particle). Assuming that the Mo

particles in the current Mg-based BMGC form a regular cubic array as illustrated in Figure 5.13, the volume fraction of Mo particles, *f*, can be expressed by

$$\frac{\pi(d/2)^2}{S^2} = f\ , \tag{5-8}$$

where *d* is the diameter of Mo particle and *s* is the center-to-center distance between two Mo particles. Then, the above Equation 1 can be simplified as

$$s = 0.88df^{-1/2}\ . \tag{5-9}$$

This formula indicates that the center-to-center spacing, *s*, is inversely propotional to the 1/2 power with respect to the volume fraction of porous Mo particles. When f = 25%, the effective free spacing, s-d, can be expressed as

$$s - d \sim 0.76d\ . \tag{3}$$

Taking into account the average diameter of single porous Mo particle of ~50 μm, as shown in Figure 3(b), thus the effective free spacing, *s-d*, is ~38 μm. The theoratical estimated inter-Mo spacing (~38 μm) is similar to the value obtained from SEM image analysis (50-70 μm). This length scale might be unfavorable to develop the consecutive shear-band propagation along the major shear plane. As reported by Hofmann et al. [228], the 40-70 vol% dendrite phase reinforced Zr-based BMGCs, which have the center-to-center dendrite spacing of 80-140 μm, showed the high tensile ductility of 10-13% with necking phenomenon. The inter-Mo spacing for the current Mg-based BMGC is in the similar range of the results of Hofmann et al. [228]. Taking 10 vol% [36] and 25 vol% porous Mo particles with the same particle size for comparison, the inter-Mo spacings are estimated to be ~90 μm and ~38 μm based on the Equation 2, which in turn result in 1% and 7% plastic strain,

respectivley. this demonstrates that the smaller inter-Mo spacing will restrict shear-band extension and suppress catastrophic crack opening, resulting in the stability against brittle failure of Mg BMG matrix.

Futhermore, the size of fine-scale compartment islands within one single porous Mo particle is in the range of 2-5 μm (σ) in Figure 5.13. The intra-Mo spacing (δ-σ) in Figure 5.13 is essentially the inner vacant space now infiltrated with Mg-based amorphous phase. Considering the porosity of ~40% for single porous Mo particle (~60% vol% of fine-scale compartment island) and assuming ideal arrangement of fine-scale compartment island within single porous Mo particle, the effective free spacing can be rewritten as $\delta-\sigma = 0.14\sigma$, where δ is the center-to-center distance between two fine-scale compartment islands, as shown in Figure 5.13. Taking into account the average size of fine-scale compartment island of ~3.5 μm, the effective free spacing, $\delta-\sigma$, is roughly estimated to be ~0.5 μm. Again, the theoratical estimated intra-Mo spacing (~0.5 μm) is well close to the value taken from SEM image analysis (~1.2 μm). Table 5.2 summarizes all parameters related to the inter-Mo pacing and intra-Mo spacing within single porous Mo particle. It is worthy of noting that this length scale of the intra-Mo spacing is too small to trigger a major crack, especially when the strengths of porous Mo particles and Mg-based amorphous matrix are close to each other. Such a small length scale is more unfavorable to trigger the macro and major shear-band propagation even through the localized shear band forms. Therefore, the effective free spacing is likely the key parameter in controling the final failure of the Mg-based BMGC.

To further examine the inter-Mo and intra-Mo spacing argument, micro-hardness testing was conducted on the current Mg-based BMGC. Figure 4(a) shows that several travels of shear bands were observed on the left side of the micro-indentation mark far away the porous Mo particles. In contrast, the tip of the micro-indenter on the right side was indented toward

the porous Mo particles and the micro-indentation mark was exactly located between two porous Mo particles, as indicated Figure 4.45(a). It is evident that there is no shear-band travel observed between the micro-indentation mark and porous Mo particles. In addition, when the tip of the micro-indenter was indented right onto one single porous Mo particle, no shear band is triggered within the single porous Mo particle, as shown in Figure 4.45(b). In this case, the Mo particle becomes the main phase at the local area of porous Mo particle. Metallic-glass matrix has ~2% elastic limit, in comparison with ~0.2% yielding in the crystalline Mo phase. Thus, the absence of shear bands resulting from the plastic deformation might be accommodated mainly by the dislocations within one single porous Mo particle. The abundant Mo particles on the surface also prevent shear band from propagating to the free surface. The Mo particles of the current Mg-based BMGC (1) contribute to suppress long-distance shear-band propagation, (2) accommodate the plastic strain, and (3) deplete the kinetic energy of shear bands, all of which in turn improve the ductility of BMGC.

For the porous Mo particles reinforced Mg-based BMGC, the diappearance of serrration is associated with the lack of long-range shear band propagagtion. By the approach with the concept in separating the homogeneous amorphous matrix into many individual compartments, only short-range shear band propgagation is possible in the current Mg-based BMGC. From the viewpoint of the morphology of BMGC, an effective free spacing considering the spacing between two porous Mo particles and the size of one single porous Mo particle is likely to control the final failure of BMGC and appears to be a useful indicator for the design of highly ductile BMGC.

Chapter 6 Conclusions

According to the present study, some major points and important conclusions about the phase-separated $Zr_{63.8}Ni_{16.2}Cu_{15}Al_5$ BMG, monolithic $Pd_{40}Ni_{40}P_{20}$ BMG and porous Mo particles reinforced Mg-based BMGC are summarized below.

1. Based on the computational thermodynamic approach, a good GFA $Zr_{63.8}Ni_{16.2}Cu_{15}Al_5$ BMG with the microstructure of microscaled phase separation shows a remarkable compressive plasticity of ~15%.

2. The ductile phase-separated Zr-based BMG samples compressed to different strains at a low strain rate underwent the initial ~2% elastic strain, followed by ~1% apparent uniform plastic strain and, then, the development of the principal shear together with several secondary shear bands until ~15% plastic strain. At a large compressive strain, test samples experienced either fast load drop to complete failure or gradual load rise caused by the multiple contacts between compression platform and fragmented sample. In the later case, the converted stress-strain curve would appear to indicate a highly plastic material, which is, in fact, an artifact.

3. For the phase-separated Zr-based BMG deformed at low strain rates (~10^{-4} s^{-1}), the dominant plastic deformation mode is single shear along the principal shear plane. The principal shear contributed the majority of the measured plastic strain, more than 2/3 of the overall plastic strain until failure.

4. Based on the analysis of plastic strain of the phase-separated Zr-based BMG, local shear

strain along the principal shear band varied; the local strain decreased monotonically with distance from the location where the shear band was initiated.

5. For the phase-separated Zr-based BMG, numerous flow serrations were observed in the plastic region of load-displacement curve. The fracture surface showed the presence of regularly spaced striations perpendicular to the shear direction with a spacing of ~1.58 μm. This striation spacing matches well with the serration spacing recorded in the load-displacement curve (~1.63 μm).

6. Further investigations were conducted on the $Pd_{40}Ni_{40}P_{20}$ BMG using in-situ compression experiments, the observed images demonstrate that there was a one-to-one correspondence between the intermittent ample sliding and flow serration.

7. In the compression tests equipped with high-sensitivity strain gauges directly attached to test samples, a detailed analysis of the dynamic event during shear band propagation for the monolithic $Pd_{40}Ni_{40}P_{20}$ BMG was carried out.

8. Based on the displacement-time profile, a propagating shear band initially accelerates and, then, the propagating shear band reaches a steady sate. Finally, the propagating shear band decelerates and is arrested. The elapsed time during the steady-state propagation lasts only ~1-2 ms. The average steady-state speed of shear band propagation was estimated to be ~530 μm/s or 5.3×10^4 s^{-1} in shear strain rate.

9. Using the shear strain-rate data, the average viscosity within a propagating shear band during inhomogeneous deformation was estimated to be 4.2×10^4 Pa·s, which is in the similar range to the viscosity values reported in the supercooled liquid region during

homogeneous deformation.

10. The relatively low viscosity within the propagating shear band is consistent with our general sense that shear resistance within a propagating shear band would become low, namely, the softening of shear band.

11. A self-consistent VFT equation based on the free volume model was applied to interpret the low viscosity within a propagating shear band. The result demonstrates that the excess free volume generation is mainly responsible for the shear-band dynamics.

12. Strain rate effect on shear band propagation shows that the shear-band propagating speed is insensitive to the applied strain rates (or the applied crosshead speed) within the range of 2×10^{-4}-1×10^{-2} s^{-1}.

13. The disappearance of serration in compression at high strain rates is not caused by the absence of shear band formation or a change of shear band propagation speed. It is rather caused by the fact that the shear-band propagating speed and crosshead speed are so close that the signal of displacement burst is overshadowed by the travel of applied crosshead.

14. In comparison with the ductile Pd-based and brittle Mg-based BMGs, the shear-band propagating speed during early deformation (stage 1) for $Mg_{58}Cu_{31}Y_6Nd_5$ (~492 μm/s) is faster than that for $Pd_{40}Ni_{40}P_{20}$ (~424 μm/s). The more ductile in nature the metallic glass is, the slower the shear-band propagating speed would become.

15. In the present study, the correlation between the kinetic energy for one serration and failure strain exhibits a direct relationship with the compressive ductility: ductile

phase-separated Zr-based BMG (4.2 x 10^{-4} J and > 10% plastic strain) > Pd-based BMG (2.4 x 10^{-4} J and ~3-5% plastic strain) > Cu-based BMG (1.4 x 10^{-4} J and ~2-3% plastic strain) > Au-based BMG (4.2 x 10^{-5} J and ~1% plastic strain) > brittle Mg-based BMG (8.5 x 10^{-6} J and ~0% plastic strain). The kinetic energy stored during each serration of shear band propagation appears to be a promising indicator for the ductility of BMGs, and is a useful parameter easy to be experimentally measured.

16. For the porous Mo particles reinforced Mg-based BMGC, the diappearance of serrration is associated with the lack of long-range shear band propagagtion. By employing the concept designed with separating the homogeneous amorphous matrix into many individual compartments, only short-range shear band propgagation is possible in the current Mg-based BMGC.

17. An effective free spacing considering the spacing between two porous Mo particles and the size of porous Mo particle is likely to control the final failure of the current Mg-based BMGC, and appears to be a useful indicator for the design of BMGC with high ductility.

References

[1] C. A. Pampillo, Journal of Materials Science 10 (1975) 1194-1227.

[2] H. S. Chen, Reports on Progress in Physics 43 (1980) 353-432.

[3] A. L. Greer, Science 267 (1995) 1947-1953.

[4] W. L. Johnson, MRS Bulletin 24 (1999) 42-56.

[5] A. Inoue, Acta Materialia 48 (2000) 279-306.

[6] W. H. Wang, C. Dong and C. H. Shek, Materials Science & Engineering R-Reports 44 (2004) 45-89.

[7] M. W. Chen, Annual Review of Materials Research 38 (2008) 445-469.

[8] W. Klement, R. H. Willens and P. Duwez, Nature 187 (1960) 869-870.

[9] S. Kavesh, *Metallic Glasses*, ed. J. J. Gillman and H. L. Leamy. 1978, Mark Park, OH: ASM International. Chapter 2.

[10] H. S. Chen and D. Turnbull, Acta Metallurgica 17 (1969) 1021-1031.

[11] H. S. Chen, J. T. Krause and E. A. Sigety, Journal of Non-Crystalline Solids 13 (1974) 321-327.

[12] H. S. Chen, Acta Metallurgica 22 (1974) 1505-1511.

[13] A. J. Drehman, A. L. Greer and D. Turnbull, Applied Physics Letters 41 (1982) 716-717.

[14] H. W. Kui, A. L. Greer and D. Turnbull, Applied Physics Letters 45 (1984) 615-616.

[15] A. Inoue, T. Zhang and T. Masumoto, Materials Transactions, JIM 30 (1989) 965-972.

[16] A. Inoue, H. Yamaguchi, T. Zhang and T. Masumoto, Materials Transactions, JIM 31 (1990) 104-109.

[17] A. Inoue, K. Kita, T. Zhang and T. Masumoto, Materials Transactions, JIM 30 (1989)

722-725.

[18] A. Inoue, T. Zhang and T. Masumoto, Materials Transactions, JIM 31 (1990) 425-428.

[19] A. Inoue, A. Kato, T. Zhang, S. G. Kim and T. Masumoto, Materials Transactions, JIM 32 (1991) 609-616.

[20] T. Zhang, A. Inoue and T. Masumoto, Materials Transactions, JIM 32 (1991) 1005-1010.

[21] A. Inoue, N. Nishiyama and H. Kimura, Materials Transactions, JIM 38 (1997) 179-183.

[22] M. Telford, *The case for bulk metallic glass*. Materials Today. 2004. 36-43.

[23] A. Inoue, *Bulk Amorphous Alloys*. 1998-1999, Zurich: Trans. Tech.

[24] C. Fan, A. Takeuchi and A. Inoue, Materials Transactions, JIM 40 (1999) 42-51.

[25] C. Fan and A. Inoue, Applied Physics Letters 77 (2000) 46-48.

[26] C. T. Liu, L. Heatherly, D. S. Easton, C. A. Carmichael, J. H. Schneibel, C. H. Chen, J. L. Wright, M. H. Yoo, J. A. Horton and A. Inoue, Metallurgical and Materials Transactions A 29 (1998) 1811-1820.

[27] C. A. Schuh, T. C. Hufnagel and U. Ramamurty, Acta Materialia 55 (2007) 4067-4109.

[28] Z. F. Zhang, F. F. Wu, G. He and J. Eckert, Journal of Materials Science and Technology 23 (2007) 747-767.

[29] J. Schroers and W. L. Johnson, Physical Review Letters 93 (2004) 255506.

[30] Y. H. Liu, G. Wang, R. J. Wang, D. Q. Zhao, M. X. Pan and W. H. Wang, Science 315 (2007) 1385-1388.

[31] C. C. Hays, C. P. Kim and W. L. Johnson, Physical Review Letters 84 (2000) 2901-2904.

[32] L. Q. Xing, Y. Li, K. T. Ramesh, J. Li and T. C. Hufnagel, Physical Review B 64

(2001) 180201.

[33] J. Das, M. B. Tang, K. B. Kim, R. Theissmann, F. Baier, W. H. Wang and J. Eckert, Physical Review Letters 94 (2005) 205501.

[34] K. F. Yao, F. Ruan, Y. Q. Yang and N. Chen, Applied Physics Letters 88 (2006) 122106.

[35] X. H. Du, J. C. Huang, K. C. Hsieh, Y. H. Lai, H. M. Chen, J. S. C. Jang and P. K. Liaw, Applied Physics Letters 91 (2007) 131901.

[36] J. S. C. Jang, J. Y. Ciou, T. H. Hung, J. C. Huang and X. H. Du, Applied Physics Letters 92 (2008) 011930.

[37] Y. Zhang, W. H. Wang and A. L. Greer, Nature Materials 5 (2006) 857-860.

[38] P. Yu, H. Y. Bai, J. G. Zhao, C. Q. Jin and W. H. Wang, Applied Physics Letters 90 (2007) 051906.

[39] Z. F. Zhang, H. Zhang, X. F. Pan, J. Das and J. Eckert, Philosophical Magazine Letters 85 (2005) 513-521.

[40] F. X. Liu, P. K. Liaw, G. Y. Wang, C. L. Chiang, D. A. Smith, P. D. Rack, J. P. Chu and R. A. Buchanan, Intermetallics 14 (2006) 1014-1018.

[41] W. H. Jiang, G. J. Fan, H. Choo and P. K. Liaw, Materials Letters 60 (2006) 3537-3540.

[42] H. Bei, S. Xie and E. P. George, Physical Review Letters 96 (2006) 105503.

[43] H. M. Chen, Y. C. Chang, T. H. Hung, X. H. Du, J. C. Huang, J. S. C. Jang and P. K. Liaw, Materials Transactions, JIM 48 (2007) 1802-1805.

[44] Z. F. Zhang, J. Eckert and L. Schultz, Acta Materialia 51 (2003) 1167-1179.

[45] B. J. Park, H. J. Chang, D. H. Kim and W. T. Kim, Applied Physics Letters 85 (2004) 6353-6355.

[46] B. J. Park, H. J. Chang, D. H. Kim, W. T. Kim, K. Chattopadhyay, T. A. Abinandanan and S. Bhattacharyya, Physical Review Letters 96 (2006) 245503.

[47] A. Takeuchi and A. Inoue, Materials Transactions, JIM 41 (2000) 1372-1378.

[48] 吳學陞, 工業材料 149 (1999) 154-165.

[49] H. S. Chen and C. E. Miller, Review of Scientific Instruments 41 (1970) 1237-1238.

[50] H. H. Liebermann and C. D. Graham, Ieee Transactions on Magnetics 12 (1976) 921-923.

[51] A. Inoue, T. Nakamura, N. Nishiyama and T. Masumoto, Materials Transactions, JIM 33 (1992) 937-945.

[52] I. W. Donald and H. A. Davies, Journal of Non-Crystalline Solids 30 (1978) 77-85.

[53] A. Hruby, Czechoslovak Journal of Physics Section B 22 (1972) 1187-1193.

[54] K. Mondal and B. S. Murty, Journal of Non-Crystalline Solids 351 (2005) 1366-1371.

[55] Z. J. Yan, J. F. Li, S. R. He and Y. H. Zhou, Materials Research Bulletin 38 (2003) 681-689.

[56] X. S. Xiao, S. S. Fang, L. Xia, W. H. Li, Q. Hua and Y. D. Dong, Journal of Alloys and Compounds 351 (2003) 324-328.

[57] O. N. Senkov and D. B. Miracle, Materials Research Bulletin 36 (2001) 2183-2198.

[58] Z. P. Lu, C. T. Liu and Y. D. Dong, Journal of Non-Crystalline Solids 341 (2004) 93-100.

[59] T. H. Hung, J. C. Huang, J. S. C. Jang and S. C. Lu, Materials Transactions, JIM 48 (2007) 239-243.

[60] O. N. Senkov, D. B. Miracle and H. M. Mullens, Journal of Applied Physics 97 (2005) 103502.

[61] D. B. Miracle and O. N. Senkov, Journal of Non-Crystalline Solids 319 (2003) 174-191.

[62] T. H. Hung, Y. C. Chang, Y. N. Wang, C. W. Tang, J. N. Kuo, H. M. Chen, Y. L. Tsai, J. C. Huang, J. S. C. Jang and C. T. Liu, Materials Transactions, JIM 48 (2007) 1621-1625.

[63] T. Egami and Y. Waseda, Journal of Non-Crystalline Solids 64 (1984) 113-134.

[64] T. Egami, Materials Science and Engineering A 226 (1997) 261-267.

[65] T. Egami, Journal of Non-Crystalline Solids 207 (1996) 575-582.

[66] Y. M. Wang, W. P. Xu, J. B. Qiang, C. H. Wong, C. H. Shek and C. Dong, Materials Science and Engineering A (2004) 411-416.

[67] Y. M. Wang, C. H. Shek, J. B. Qian, C. H. Wong, W. R. Chen and C. Dong, Scripta Materialia 48 (2003) 1525-1529.

[68] Q. Wang, Y. M. Wang, J. B. Qiang, X. F. Zhang, C. H. Shek and C. Dong, Intermetallics 12 (2004) 1229-1232.

[69] C. H. Shek, Y. M. Wang and C. Dong, Materials Science and Engineering A 291 (2000) 78-85.

[70] M. Iqbal, W. S. Sun, H. F. Zhang, J. I. Akhter and Z. Q. Hu, Materials Science and Engineering A 447 (2007) 167-173.

[71] S. S. Fang, X. Xiao, X. Lei, W. H. Li and Y. D. Dong, Journal of Non-Crystalline Solids 321 (2003) 120-125.

[72] W. Chen, Y. Wang, J. Qiang and C. Dong, Acta Materialia 51 (2003) 1899-1907.

[73] S. Azad, A. Mandal and R. K. Mandal, Materials Science and Engineering A 458 (2007) 348-354.

[74] Z. P. Lu, Y. Li and S. C. Ng, Journal of Non-Crystalline Solids 270 (2000) 103-114.

[75] Z. P. Lu, H. Tan, Y. Li and S. C. Ng, Scripta Materialia 42 (2000) 667-673.

[76] Y. Li, S. C. Ng, C. K. Ong, H. H. Hng and T. T. Goh, Scripta Materialia 36 (1997) 783-787.

[77] T. A. Waniuk, J. Schroers and W. L. Johnson, Applied Physics Letters 78 (2001) 1213-1215.

[78] A. Inoue, W. Zhang, T. Zhang and K. Kurosaka, Acta Materialia 49 (2001) 2645-2652.

[79] A. Inoue, W. Zhang, T. Zhang and K. Kurosaka, Materials Transactions 42 (2001) 1149-1151.

[80] T. D. Shen, Y. He and R. B. Schwarz, Journal of Materials Research 14 (1999) 2107-2115.

[81] Z. P. Lu and C. T. Liu, Acta Materialia 50 (2002) 3501-3512.

[82] Z. P. Lu and C. T. Liu, Physical Review Letters 91 (2003) 115505.

[83] G. J. Fan, H. Choo and P. K. Liaw, Journal of Non-Crystalline Solids 353 (2007) 102-107.

[84] Q. J. Chen, J. Shen, D. L. Zhang, H. B. Fan, J. Sun and D. G. McCartney, Materials Science and Engineering A 433 (2006) 155-160.

[85] X. H. Du, J. C. Huang, C. T. Liu and Z. P. Lu, Journal of Applied Physics 101 (2007) 086108.

[86] X. K. Xi, D. Q. Zhao, M. X. Pan and W. H. Wang, Intermetallics 13 (2005) 638-641.

[87] D. Ma, H. Cao, L. Ding, Y. A. Chang, K. C. Hsieh and Y. Pan, Applied Physics Letters 87 (2005) 171914.

[88] Z. P. Lu and C. T. Liu, Journal of Materials Science 39 (2004) 3965-3974.

[89] E. S. Park, H. G. Kang, W. T. Kim and D. H. Kim, Journal of Non-Crystalline Solids 279 (2001) 154-160.

[90] K. Amiya and A. Inoue, Materials Transactions 42 (2001) 543-545.

[91] K. Amiya and A. Inoue, Materials Transactions, JIM 41 (2000) 1460-1462.

[92] H. Men, Z. Q. Hu and J. Xu, Scripta Materialia 46 (2002) 699-703.

[93] H. Ma, L. L. Shi, J. Xu, Y. Li and E. Ma, Applied Physics Letters 87 (2005) 181915.

[94] Y. T. Cheng, T. H. Hung, J. C. Huang, P. J. Hsieh and J. S. C. Jang, Materials Science and Engineering A 449 (2007) 501-505.

[95] Y. T. Cheng, T. H. Hung, J. C. Huang, J. S. C. Jang, C. Y. A. Tsao and F. Lee, Intermetallics 14 (2006) 866-870.

[96] T. Zhang and A. Inoue, Materials Transactions, JIM 39 (1998) 857-862.

[97] Y. Yokoyama, K. Yamano, K. Fukaura, H. Sunada and A. Inoue, Materials Transactions, JIM 40 (1999) 1015-1018.

[98] Y. Yokoyama, N. Nishiyama, K. Fukaura, H. Sunada and A. Inoue, Materials Transactions, JIM 40 (1999) 696-699.

[99] A. Inoue, A. Takeuchi and T. Zhang, Metallurgical and Materials Transactions A 29 (1998) 1779-1793.

[100] A. Inoue, Y. Shinohara and J. S. Gook, Materials Transactions, JIM 36 (1995) 1427-1433.

[101] A. Inoue, H. Koshiba, T. Zhang and A. Makino, Journal of Applied Physics 83 (1998) 1967-1974.

[102] A. Inoue and A. Katsuya, Materials Transactions, JIM 37 (1996) 1332-1336.

[103] A. Inoue, K. Fujita, T. Zhang and A. Makino, Materials Transactions, JIM 39 (1998) 327-333.

[104] A. Inoue, T. Zhang, W. Zhang and A. Takeuchi, Materials Transactions, JIM 37 (1996) 99-108.

[105] A. Inoue, T. Zhang, A. Takeuchi and W. Zhang, Materials Transactions, JIM 37 (1996) 636-640.

[106] Chaudhar.P, J. J. Cuomo and R. J. Gambino, Applied Physics Letters 22 (1973) 337-339.

[107] K. H. J. Buschow and A. M. Vanderkraan, Journal of Magnetism and Magnetic Materials 22 (1981) 220-226.

[108] C. L. Qin, W. Zhang, K. Asami, H. Kimura and A. Inoue, Journal of Materials Research 22 (2007) 1710-1717.

[109] C. L. Qin, K. Asami, T. Zhang, W. Zhang and A. Inoue, Materials Transactions 44 (2003) 1042-1045.

[110] S. J. Pang, T. Zhang, K. Asami and A. Inoue, Acta Materialia 50 (2002) 489-497.

[111] S. Pang, T. Zhang, K. Asami and A. Inoue, Materials Transactions 43 (2002) 2137-2142.

[112] K. Asami, C. L. Qin, T. Zhang and A. Inoue, Materials Science and Engineering A 375-377 (2004) 235-239.

[113] H. B. Yao, Y. Li and A. T. S. Wee, Electrochimica Acta 48 (2003) 2641-2650.

[114] Y. Li, H. Y. Bai, P. Wen, Z. X. Liu and Z. F. Zhao, Journal of Physics 15 (2003) 4809-4815.

[115] Y. Li and H. Y. Bai, Journal of Non-Crystalline Solids 351 (2005) 2378-2382.

[116] H. Tanaka, H. Senoh, N. Kuriyama, K. Aihara, N. Terashita and T. Nakahata, Materials Science and Engineering B 108 (2004) 81-90.

[117] T. Shoji and A. Inoue, Journal of Alloys and Compounds 292 (1999) 275-280.

[118] K. Isogai, T. Shoji, H. Kimura and A. Inoue, Materials Transactions, JIM 41 (2000) 1486-1489.

[119] Z. F. Zhang, G. He, J. Eckert and L. Schultz, Physical Review Letters 91 (2003) 045505.

[120] F. Spaepen, Scripta Materialia 54 (2006) 363-367.

[121] F. Spaepen, Acta Metallurgica 25 (1977) 407-415.

[122] J. Schroers, Q. Pham and A. Desai, Journal of Microelectromechanical Systems 16 (2007) 240-247.

[123] J. Schroers, T. Nguyen, S. O'Keeffe and A. Desai, Materials Science and Engineering A 449 (2007) 898-902.

[124] H. Q. Li, K. X. Tao, C. Fan, P. K. Liaw and H. Choo, Applied Physics Letters 89 (2006) 041921.

[125] H. Q. Li, C. Fan, H. Choo and P. K. Liaw, Materials Transactions, JIM 48 (2006) 1752-1754.

[126] C. Fan, P. K. Liaw, V. Haas, J. J. Wall, H. Choo, A. Inoue and C. T. Liu, Physical Review B 74 (2006) 014205.

[127] C. Fan, H. Q. Li, L. J. Kecskes, K. X. Tao, H. Choo, P. K. Liaw and C. T. Liu, Physical Review Letters 96 (2006) 145506

[128] C. Fan, Y. F. Gao, H. Q. Li, H. Choo, P. K. Liaw, A. Inoue and C. T. Liu, Journal of Materials Research 22 (2007) 445-452.

[129] F. H. Dalla Torre, A. Dubach, M. E. Siegrist and J. F. Loffler, Applied Physics Letters 89 (2006) 091918.

[130] J. Zhang, J. M. Park, D. H. Kim and H. S. Kim, Materials Science and Engineering A 449 (2007) 290-294.

[131] X. S. Xiao, S. S. Fang, L. Xia, W. H. Li, Q. Hua and Y. Dong, Journal of Non-Crystalline Solids 330 (2003) 242-247.

[132] W. H. Jiang, F. X. Liu, F. Jiang, K. Q. Qiu, H. Choo and P. K. Liaw, Journal of Materials Research 22 (2007) 2655-2658.

[133] T. Mukai, T. G. Nieh, Y. Kawamura, A. Inoue and K. Higashi, Intermetallics 10 (2002) 1071-1077.

[134] W. H. Jiang, G. J. Fan, F. Liu, G. Y. Wang, H. Choo and P. K. Liaw, International Journal of Plasticity 24 (2008) 1-16.

[135] Q. Zheng, S. Cheng, J. H. Strader, E. Ma and J. Xu, Scripta Materialia 56 (2007) 161-164.

[136] S. Xie and E. P. George, Intermetallics 16 (2008) 485-489.

[137] W. F. Wu, Z. Han and Y. Li, Applied Physics Letters 93 (2008) 061908.

[138] F. F. Wu, Z. F. Zhang, S. X. Mao and J. Eckert, Philosophical Magazine Letters 89 (2009) 178-184.

[139] C. A. Volkert, A. Donohue and F. Spaepen, Journal of Applied Physics 103 (2008) 083539.

[140] B. E. Schuster, Q. Wei, T. C. Hufnagel and K. T. Ramesh, Acta Materialia 56 (2008) 5091-5100.

[141] B. E. Schuster, Q. Wei, M. H. Ervin, S. O. Hruszkewycz, M. K. Miller, T. C. Hufnagel and K. T. Ramesh, Scripta Materialia 57 (2007) 517-520.

[142] C. J. Lee, J. C. Huang and T. G. Nieh, Applied Physics Letters 91 (2007) 161913.

[143] Y. H. Lai, C. J. Lee, Y. T. Cheng, H. S. Chou, H. M. Chen, X. H. Du, C. I. Chang, J. C. Huang, S. R. Jian, J. S. C. Jang and T. G. Nieh, Scripta Materialia 58 (2008) 890-893.

[144] Y. J. Huang, J. Shen and J. F. Sun, Applied Physics Letters 90 (2007) 081919.

[145] Y. Yang, J. C. Ye, J. Lu, F. X. Liu and P. K. Liaw, Acta Materialia 57 (2009) 1613-1623.

[146] W. F. Wu, C. Y. Zhang, Y. W. Zhang, K. Y. Zeng and Y. Li, Intermetallics 16 (2008) 1190-1198.

[147] W. F. Wu, Y. Li and C. A. Schuh, Philosophical Magazine 88 (2008) 71-89.

[148] G. Sunny, J. Lewandowski and V. Prakash, Journal of Materials Research 22 (2007) 389-401.

[149] K. Mondal and K. Hono, Materials Transactions 50 (2009) 152-157.

[150] W. H. Jiang, K. Q. Qiu, F. X. Liu, H. Choo and P. K. Liaw, Advanced Engineering Materials 9 (2007) 147-150.

[151] K. Wang, T. Fujita, Y. Q. Zeng, N. Nishiyama, A. Inoue and M. W. Chen, Acta Materialia 56 (2008) 2834-2842.

[152] C. Fan and A. Inoue, Materials Transactions, JIM 41 (2000) 1467-1470.

[153] C. Fan, R. T. Ott and T. C. Hufnagel, Applied Physics Letters 81 (2002) 1020-1022.

[154] C. Fan, D. C. Qiao, T. W. Wilson, H. Choo and P. K. Liaw, Materials Science and Engineering A 431 (2006) 158-165.

[155] T. Wada, A. Inoue and A. L. Greer, Applied Physics Letters 86 (2005) 251907.

[156] S. Pauly, J. Das, J. Bednarcik, N. Mattern, K. B. Kim, D. H. Kim and J. Eckert, Scripta Materialia 60 (2009) 431-434.

[157] S. Pauly, J. Das, N. Mattern, D. H. Kim and J. Eckert, Intermetallics 17 (2009) 453-462.

[158] D. G. Pan, H. F. Zhang, A. M. Wang and Z. Q. Hu, Applied Physics Letters 89 (2006) 261904.

[159] C. A. Pampillo and Reimschu.Ac, Journal of Materials Science 9 (1974) 718-724.

[160] M. H. Cohen and D. Turnbull, Journal of Chemical Physics 31 (1959) 1164-1169.

[161] D. E. Polk and D. Turnbull, Acta Metallurgica 20 (1972) 493-498.

[162] A. S. Argon, Acta Metallurgica 27 (1979) 47-58.

[163] D. Srolovitz, V. Vitek and T. Egami, Acta Metallurgica 31 (1983) 335-352.

[164] C. A. Schuh and A. C. Lund, Nature Materials 2 (2003) 449-452.

[165] M. L. Falk, Physical Review B 60 (1999) 7062-7070.

[166] A. S. Argon and H. Y. Kuo, Materials Science and Engineering 39 (1979) 101-109.

[167] D. Pan, A. Inoue, T. Sakurai and M. W. Chen, Proceedings of the National Academy of Sciences of the United States of America 105 (2008) 14769-14772.

[168] M. Zink, K. Samwer, W. L. Johnson and S. G. Mayr, Physical Review B 73 (2006) 172203.

[169] S. G. Mayr, Physical Review Letters 97 (2006) 195501.

[170] J. S. Langer, Physical Review E 77 (2008) 021502.

[171] B. Yang, C. T. Liu, T. G. Nieh, M. L. Morrison, P. K. Liaw and R. A. Buchanan, Journal of Materials Research 21 (2006) 915-922.

[172] B. Yang, C. T. Liu and T. G. Nieh, Applied Physics Letters 88 (2006) 221911.

[173] W. L. Johnson and K. Samwer, Physical Review Letters 95 (2005) 195501.

[174] P. E. Donovan, Acta Metallurgica 37 (1989) 445-456.

[175] Z. F. Zhang and J. Eckert, Physical Review Letters 94 (2005) 094301.

[176] T. Mukai, T. G. Nieh, Y. Kawamura, A. Inoue and K. Higashi, Scripta Materialia 46 (2002) 43-47.

[177] G. He, J. Lu, Z. Bian, D. J. Chen, G. L. Chen, G. C. Tu and G. J. Chen, Materials Transactions, JIM 42 (2001) 356-364.

[178] S. Takayama, Scripta Metallurgica 13 (1979) 463-467.

[179] N. I. Noskova, N. F. Vildanova, Y. I. Filippov and A. P. Potapov, Physica Status Solidi A 87 (1985) 549-557.

[180] J. Megusar, A. S. Argon and N. J. Grant, Materials Science and Engineering 38 (1979) 63-72.

[181] P. Lowhaphandu, S. L. Montgomery and J. J. Lewandowski, Scripta Materialia 41 (1999) 19-24.

[182] A. Inoue, H. M. Kimura and T. Zhang, Materials Science and Engineering A 294-296 (2000) 727-735.

[183] L. A. Davis and Y. T. Yeow, Journal of Materials Science 15 (1980) 230-236.

[184] V. Z. Bengus, P. Diko, K. Csach, J. Miskuf, V. Ocelik, E. B. Korolkova, E. D. Tabachnikova and P. Duhaj, Journal of Materials Science 25 (1990) 1598-1602.

[185] A. T. Alpas, L. Edwards and C. N. Reid, Materials Science and Engineering 98 (1988) 501-504.

[186] W. J. Wright, R. Saha and W. D. Nix, Materials Transactions 42 (2001) 642-649.

[187] H. B. Cao, Y. Pan, L. Ding, C. Zhang, J. Zhu, K. C. Hsieh and Y. A. Chang, Acta Materialia 56 (2008) 2032-2036.

[188] H. B. Cao, D. Ma, K. C. Hsieh, L. Ding, W. G. Stratton, P. M. Voyles, Y. Pan, M. D. Cai, J. T. Dickinson and Y. A. Chang, Acta Materialia 54 (2006) 2975-2982.

[189] X. Y. Yan, Y. A. Chang, Y. Yang, F. Y. Xie, S. L. Chen, F. Zhang, S. Daniel and M. H. He, Intermetallics 9 (2001) 535-538.

[190] X. H. Lin and W. L. Johnson, Journal of Applied Physics 78 (1995) 6514-6519.

[191] N. Sanders and A. P. Miodownik, *CALPHAD, Calculation of Phase Diagrams: A Comprehensive Guide*. 1998, Oxford, UK: Elsevier Science.

[192] L. Kaufman and H. Bernstein, *Computer Calculation of Phase Diagrams*. 1970, New York: Academic Press.

[193] Y. A. Chang, S. L. Chen, F. Zhang, X. Y. Yan, F. Y. Xie, R. Schmid-Fetzer and W. A. Oates, Progress in Materials Science 49 (2004) 313-345.

[194] S. L. Chen, F. Zhang, S. Daniel, F. Y. Xie, X. Y. Yan, Y. A. Chang, R. Schmid-Fetzer and W. A. Oates, JOM: Journal of the Minerals Metals & Materials Society 55 (2003) 48-51.

[195] S. L. Chen, S. Daniel, F. Zhang, Y. A. Chang, X. Y. Yan, F. Y. Xie, R. Schmid-Fetzer and W. A. Oates, Calphad: Computer Coupling of Phase Diagrams and Thermochemistry 26 (2002) 175-188.

[196] J. S. C. Jang, C. C. Tseng, L. J. Chang, C. F. Chang, W. J. Lee, J. C. Huang and C. T. Liu, Materials Transactions, JIM 48 (2007) 1684-1688.

[197] F. Spaepen, Acta Metallurgica 23 (1975) 615-620.

[198] R. D. Conner, Y. Li, W. D. Nix and W. L. Johnson, Acta Materialia 52 (2004) 2429-2434.

[199] P. J. Tao, Y. Z. Yang, X. J. Bai, Z. W. Xie, X. C. Chen, Z. J. Dong, J. G. Wen and H. J. Long, Journal of Non-Crystalline Solids 354 (2008) 3742-3746.

[200] Y. Zhang and A. L. Greer, Applied Physics Letters 89 (2006) 071907.

[201] M. Q. Jiang, W. H. Wang and L. H. Dai, Scripta Materialia 60 (2009) 1004-1007.

[202] J. S. C. Jang, C. T. Tseng, L. J. Chang, J. C. C. Huang, Y. C. Yeh and J. L. Jou, Advanced Engineering Materials 10 (2008) 1048-1052.

[203] J. Lu, G. Ravichandran and W. L. Johnson, Acta Materialia 51 (2003) 3429-3443.

[204] Y. Kawamura, T. Nakamura, H. Kato, H. Mano and A. Inoue, Materials Science and Engineering A 304-306 (2001) 674-678.

[205] Y. Kawamura, T. Nakamura and A. Inoue, Scripta Materialia 39 (1998) 301-306.

[206] Y. Kawamura and A. Inoue, Applied Physics Letters 77 (2000) 1114-1116.

[207] J. S. C. Jang, C. F. Chang, Y. C. Huang, J. C. Huang, W. J. Chiang and C. T. Liu, Intermetallics 17 (2009) 200-204.

[208] J. P. Chu, C. L. Chiang, T. G. Nieh and Y. Kawamura, Intermetallics 10 (2002) 1191-1195.

[209] Y. C. Chang, T. H. Hung, H. M. Chen, J. C. Huang, T. G. Nieh and C. J. Lee, Intermetallics 15 (2007) 1303-1308.

[210] Y. C. Chang, J. C. Huang, C. W. Tang, C. I. Chang and J. S. C. Jang, Materials Transactions, JIM 49 (2008) 2605-2610.

[211] Y. C. Chang, J. C. Huang, Y. T. Cheng, C. J. Lee, X. H. Du and T. G. Nieh, Journal of Applied Physics 103 (2008) 103521.

[212] S. X. Song, H. Bei, J. Wadsworth and T. G. Nieh, Intermetallics 16 (2008) 813-818.

[213] H. S. Chen, Scripta Metallurgica 7 (1973) 931-935.

[214] W. J. Wright, R. B. Schwarz and W. D. Nix, Materials Science and Engineering A 319 (2001) 229-232.

[215] F. H. Dalla Torre, A. Dubach, J. Schallibaum and J. F. Loffler, Acta Materialia 56 (2008) 4635-4646.

[216] J. J. Lewandowski and A. L. Greer, Nature Materials 5 (2006) 15-18.

[217] T. C. Hufnagel, T. Jiao, Y. Li, L. Q. Xing and K. T. Ramesh, Journal of Materials Research 17 (2002) 1441-1445.

[218] C. J. Gilbert, J. W. Ager, V. Schroeder, R. O. Ritchie, J. P. Lloyd and J. R. Graham, Applied Physics Letters 74 (1999) 3809-3811.

[219] K. Georgarakis, M. Aljerf, Y. Li, A. LeMoulec, F. Charlot, A. R. Yavari, K. Chornokhvostenko, E. Tabachnikova, G. A. Evangelakis, D. B. Miracle, A. L. Greer and T. Zhang, Applied Physics Letters 93 (2008) 031907.

[220] T. Masumoto and R. Maddin, Acta Metallurgica 19 (1971) 725.

[221] S. X. Song and T. G. Nieh, Intermetallics 17 (2009) 762-767.

[222] W. J. Wright, T. C. Hufnagel and W. D. Nix, Journal of Applied Physics 93 (2003) 1432-1437.

[223] W. L. Johnson, J. Lu and M. D. Demetriou, Intermetallics 10 (2002) 1039-1046.

[224] M. H. Cohen and G. S. Grest, Physical Review B 20 (1979) 1077-1098.

[225] G. S. Grest and M. H. Cohen, Advances in Chemical Physics 48 (1981) 455-525.

[226] H. Kimura and T. Masumoto, Acta Metallurgica 31 (1983) 231-240.

[227] C. M. McNally, W. H. Kao and T. G. Nieh, Scripta Metallurgica 22 (1988) 1847-1850.

[228] D. C. Hofmann, J. Y. Suh, A. Wiest, G. Duan, M. L. Lind, M. D. Demetriou and W. L. Johnson, Nature 451 (2008) 1085-U3.

[229] R. E. Reed-hill and R. Abbaschian, *Physical Metallurgy Principles*. 1994: I.T. Publishing, 3rd. 432.

[230] T. H. Hung, Ph.D. Thesis, *Study of Thermal and Mechanical Properties in Mg-Cu-Gd Amorphous Alloys*, National Sun Yat-Sen University, Kaohsiung, Taiwan, 2008.

Table 1.1 Fundamental properties and application fields of bulk amorphous and nanocrystalline alloys [5].

Fundamental characteristic	Application field
High strength	Machinery structural materials
High hardness	Optical precision materials
High fracture toughness	Die materials
High impact fracture energy	Tool materials
High fatigue strength	Cutting materials
High elastic energy	Electrode materials
High corrosion resistance	Corrosion resistant materials
High wear resistance	Hydrogen storage materials
High viscous flowability	Ornamental materials
High reflection ratio	Composite materials
Good soft magnetism	Writing appliance materials
High frequency permeability	Sporting goods materials
High magnetostriction	Bonding materials
Efficient electrode (Chlorine gas)	Soft magnetic materials
High hydrogen storage	High magnetostrictive materials

Table 1.2 Relationship of heats of mixing among the component elements in the Zr-Ni-Cu-Al alloy system (unit: kJ/mol) [47].

	Zr	**Cu**	**Ni**	**Al**
Zr		**-23**	**-49**	**-44**
Cu	**-23**		**+4**	**-1**
Ni	**-49**	**+4**		**-22**
Al	**-44**	**-1**	**-22**	

Table 2.1 The classification of amorphous alloy systems and calendar years when details about each alloy system were first published [5].

1. Nonferrous metal base	Years
Mg-Ln-M (Ln = Lanthanide metal, M = Ni, Cu or Zn)	1988
Ln-Al-TM; Ln-Ga-TM (TM = VI~ VIII group transition metal)	1989
Zr-Al-TM; Zr-Ti-AL-TM	1990
Ti-Zr-TM; Zr-Ti-TM-Be	1993
Zr-(Nb,Pd)-Al-TM	1995
Pd-Cu-Ni-P; Pd-Ni-Fe-P	1996
Pd-Cu-B-Si	1997
Ti-Ni-Cu-Sn	1998
2. Ferrous group metal base	
Fe-(AL,Ga)-(P,C,B,Si,Ge); Fe-(Nb,Mo)-(Al,Ga)-(P,B,Si)	1995
Co-(Al,Ga)-(P,B,Si); Fe-(Zr,Hf,Nb)-B; Co-Fe-(Zr,Hf,Nb)-B; Ni-(Zr,Hf,Nb)-(Cr,Mo)-B	1996
Fe-Co-Ln-B	1998
Fe-(Nb,Cr,Mo)-(P,C,B); Ni-(Nb,Cr,Mo)-(P,C)	1999

Table 2.2 The classification of amorphous alloy systems reported to date [5].

I	ETM(or Ln) + Al + LTM	Zr-Al-Ni, Zr-Al-Cu, Zr-Al-Ni-Cu, Zr-Ti-Al-Ni-Cu, Zr-Nb-Al-Ni-Ln, Zr-Ga-Ni.
		Ln-Al-Ni, Ln-Al-Cu, Ln-Al-Ni-Cu, Ln-Ga-Ni, Ln-Ga-Cu.
II	LTM + ETM + Metalloid	Fe-Zr-B, Fe-Hf-b, Fe-Zr-Hf-B, Fe-Co-Ln-B, Co-Zr-Nb-B.
III	LTM(Fe) + Al or Ga + Metalloid	Fe-(Al, Ga)-Metalloid.
IV	Mg + Ln +LTM	Mg-Ln-Ni, Mg-Ln-Cu.
	TM(Zr or Ti) + Be + LTM	Zr-Ti-Be-Ni-Cu.
V	LTM + Metalloid	Pd-Ni-P, Pd-Cu-Ni-P, Pt-Ni-p.

ETM = IVB~VIB Group Transition Metal.

LTM = VIIB~VIIIB Group Transition Metal.

Table 2.3 Summary of ΔT_x (= T_x - T_g), T_{rg} (= T_g/T_l), γ [= $T_x/(T_g+T_l)$], critical cooling rate R_c and critical section thickness Z_c for typical BMGs [81].

Alloy	**T_x-T_g**	**T_g/T_l**	**$T_x/(T_g+T_l)$**	**R_c(K/s)**	**Z_c(mm)**
$Mg_{80}Ni_{10}Nd_1$	16.3	0.517	0.353	1251.4	0.6
$Mg_{75}Ni_{15}Nd_{10}$	20.4	0.57	0.379	46.1	2.8
$Mg_{70}Ni_{15}Nd_{15}$	22.3	0.553	0.373	178.2	1.5
$Mg_{65}Ni_{20}Nd_{15}$	42.1	0.571	0.397	30	3.5
$Mg_{65}Ni_{25}Nd_{10}$	54.9	0.551	0.401	50	7
$Zr_{66}Al_8Ni_{26}$	35.6	0.537	0.368	66.6	
$Zr_{66}Al_8Cu_7Ni_{19}$	58.4	0.552	0.387	22.7	
$Zr_{66}Al_8Cu_{12}Ni_{14}$	77.4	0.559	0.401	9.8	
$Zr_{66}Al_9Cu_{16}Ni1_9$	79.5	0.561	0.403	4.1	
$Zr_{65}Al_{7.5}Cu_{17.5}Ni_{10}$	79.1	0.562	0.403	1.5	16
$Zr_{57}Ti_5Al_{10}Cu_{20}Ni_8$	43.3	0.591	0.395	10	10
$Zr_{38.5}Ti_{16.5}Ni_{9.75}Cu_{15.25}Be_{20}$	48	0.628	0.415	1.4	
$Zr_{39.88}Ti_{15.12}Ni_{9.98}Cu_{13.77}Be_{21.25}$	57	0.625	0.42	1.4	
$Zr_{41.2}Ti_{13.8}Cu_{12.5}Ni_{10}Be_{22.5}$	49	0.626	0.415	1.4	50
$Zr_{42.63}Ti_{12.37}Cu_{11.25}Ni_{10}Be_{23.75}$	89	0.589	0.424	5	
$Zr_{44}Ti_{11}Cu_{10}Ni_{10}Be_{25}$	114	0.518	0.404	12.5	
$Zr_{45.38}Ti_{9.62}Cu_{8.75}Ni_{10}Be_{26.25}$	117	0.503	0.397	17.5	
$Zr_{46.25}Ti_{8.25}Cu_{7.5}Ni_{10}Be_{27.5}$	105	0.525	0.402	28	
$La_{55}A_{l25}Ni_{20}$	64.3	0.521	0.388	67.5	3
$La_{55}Al_{25}Ni_{15}Cu_5$	67.6	0.526	0.394	34.5	
$La_{55}Al_{25}Ni_{10}Cu_{10}$	79.8	0.56	0.42	22.5	5
$La_{55}Al_{25}Ni_5Cu_{15}$	60.9	0.523	0.389	35.9	
$La_{55}Al_{25}Cu_{20}$	38.9	0.509	0.366	72.3	3
$La_{55}Al_{25}Ni_5Cu_{10}Co_5$	76.6	0.566	0.421	18.8	9
$La_{66}Al_{14}Cu_{20}$	54	0.54	0.399	37.5	2
$Pd_{40}Cu_{30}Ni_{10}P_{20}$	78.9	0.69	0.464	0.1	72
$Pd_{81.5}Cu_2Si_{16.5}$	37	0.577	0.387	2	
$Pd_{79.5}Cu_4Si_{16.5}$	40	0.585	0.392	500	0.75
$Pd_{77.5}Cu_6Si_{16.5}$	41	0.602	0.4	100	1.5
$Pd_{77}Cu_6Si_{17}$	44	0.569	0.388	125	2
$Pd_{73.5}Cu_{10}Si_{16.5}$	40	0.568	0.385	2	
$Pd_{40}Ni_{40}P_{20}$	63	0.585	0.409	0.167	25
$Nd_{60}Al_{15}Ni_{10}Cu_{10}Fe_5$	45	0.552	0.393	5	
$Nd_{61}Al_{11}Ni_8Co_5Cu_{15}$	24	0.598	0.394	6	
$Cu_{60}Zr_{30}Ti_{10}$	50	0.619	0.409	4	
$Cu_{54}Zr_{27}Ti_9Be_{10}$	42	0.637	0.412	5	
$Ti_{34}Zr_{11}Cu_{47}Ni_8$	28.8	0.597	0.389	100	4.5
$Ti_{50}Ni_{24}Cu_{20}B_1Si_2Sn_3$	74	0.554	0.393	1	

Table 2.4 Summary of the mechanical properties of the previously reported Mg-based BMGs under compression tests [135].

Alloy composition (at%)	Sample diameter (mm)	σ_f (MPa)	ε_p (%)
$Mg_{65}Cu_{20}Ag_{10}Y_2Gd_8$	1	956	0.3
$Mg_{65}Cu_{20}Ag_5Gd_{10}$	1	909	0.5
$Mg_{65}Cu_{15}Ag_{10}Gd_{10}$	1	935	0.2
$Mg_{65}Cu_{7.5}Ni_{7.5}Zn_5Ag_5Y_{10}$	1	832	0
$Mg_{65}Cu_{7.5}Ni_{7.5}Zn_5Ag_5Y_5Gd_5$	1	928	0.57
$Mg_{65}Cu_{15}Ag_5Pd_5Gd_{10}$	2	817	0.2
$Mg_{75}Cu_{15}Gd_{10}$	2	743	0
$Mg_{75}Cu_5Ni_{10}Gd_{10}$	2	874	0.2
$Mg_{65}Cu_{25}Gd_{10}$	2	834	0
$Mg_{65}Ni_5Cu_{20}Gd_{10}$	2	904	0.15
$Mg_{65}Cu_{7.5}Ni_{7.5}Zn_5Ag_5Y_{10}$	4	490-650	0
$Mg_{65}Cu_{15}Ag_5Pd_5Y_{10}$	5	770	0
$Mg_{61}Cu_{28}Gd_{11}$	4	461-732	0
$Mg_{61}Cu_{28}Gd_{11}$	1	1075 ± 35	0.4

Table 2.5 Tensile (θ_T) and compressive (θ_C) fracture angles for various BMG samples.

Investigators	**Compositions**	**θ_T**
Alpas et al. [185]	$Ni_{78}Si_{10}B_{12}$	55^o
Bengus et al. [184]	$Fe_{70}Ni_{10}B_{20}$	60^o
Davis & Yeow [183]	$Ni_{49}Fe_{29}P_{14}B_6Si_2$	53^o
He et al. [177]	$Zr_{52.5}Al_{10}Cu_{17.9}Ni_{14.6}Ti_5$	55^o-65^o
Inoue et al. [182]	$Zr_{65}Al_{7.5}Cu_{7.5}Ni_{10}Pd_{10}$	50^o
Inoue et al. [78]	$Cu_{60}Zr_{30}Ti_{10}$	54^o
Liu et al. [26]	$Zr_{52.5}Al_{10}Cu_{17.9}Ni_{14.6}Ti_5$	53^o-60^o
Lowhaphandu et al. [181]	$Zr_{62}Cu_{14.5}Ni_{10}Ti_{10}Be_{3.5}$	$53.3^o \pm 3.7^o$
Megusar et al. [180]	$Pd_{80}Si_{20}$	50^o
Mukai et al. [176]	$Pd_{40}Ni_{40}P_{20}$	56^o
Noskova et al. [179]	$Co_{70}Si_{15}B_{10}Fe_5$	60^o
Takayama [178]	$Pd_{77.5}Cu_6Si_{16.5}$	50^o-51^o
Zhang et al. [119]	$Zr_{59}Al_{10}Cu_{20}Ni_8Ti_3$	54^o
Zhang et al. [119]	$Zr_{52.5}Al_{10}Cu_{17.9}Ni_{14.6}Ti_5$	56^o
Investigators	**Compositions**	**θ_C**
He et al. [177]	$Zr_{52.5}Al_{10}Cu_{17.9}Ni_{14.6}Ti_5$	40^o-45^o
Lowhaphandu et al. [181]	$Zr_{62}Cu_{14.5}Ni_{10}Ti_{10}Be_{3.5}$	$41.6^o \pm 2.1^o$
Donovan [174]	$Pd_{40}Ni_{40}P_{20}$	$41.9^o \pm 1.2^o$
Wright et al. [186]	$Zr_{40}Cu_{12}Ni_{10}Ti_{14}Be_{24}$	42^o
Mukai et al. [133]	$Pd_{40}Ni_{40}P_{20}$	42^o
Zhang et al. [119]	$Zr_{59}Al_{10}Cu_{20}Ni_8Ti_3$	43^o
Zhang et al. [119]	$Zr_{55}Al_{10}Cu_{30}Ni_5$	40^o-43^o
Zhang et al. [119]	$Zr_{54.5}Al_{10}Cu_{20}Ni_8Ti_{7.5}$	42^o
Zhang et al. [119]	$Zr_{52.5}Al_{10}Cu_{17.9}Ni_{14.6}Ti_5$	42^o
Zhang et al. [119]	$Ti_{56}Cu_{16.8}Ni_{14.4}Sn_{4.8}Nb_8$	27^o

Table 3.1 Fundamental data related to the component elements in this study.

Symbol	Atomic weight	Structure	Electron-negativity	Atomic size (Å)	Melting point (^{o}C)	Density (g/cm^{3})	Poisson ratio
Zr	91.220	HCP	1.33	1.6025	1855.00	6.49	0.34
Cu	63.546	FCC	2.00	1.2780	1084.62	8.96	0.34
Ni	58.690	FCC	1.91	1.2459	1455.00	8.90	0.31
Al	26.982	FCC	1.61	1.4317	660.32	2.70	0.35
Pd	106.420	FCC	2.20	1.3754	1554.90	12.02	0.39
Mg	24.305	HCP	1.31	1.6013	650	1.74	0.29
Ag	107.860	FCC	1.93	1.4447	961.78	10.50	0.37
Gd	157.250	HCP	1.20	1.8013	1311.20	7.89	0.26
Y	88.906	HCP	1.22	1.8015	1526.00	4.47	0.24
Nd	144.240	HCP	1.14	1.6400	1024.00	7.00	0.28

Table 4.1 Summary of thermal properties for the $Zr_{63.8}Ni_{16.2}Cu_{15}Al_5$, $Pd_{40}Ni_{40}P_{20}$ and $Mg_{58}Cu_{31}Y_6Nd_5$ BMGs obtained from DSC.

BMGs	T_g (K)	T_x (K)	ΔT_x (K)	T_m (K)	T_l (K)	ΔT_l (K)	T_{rg}	γ	γ_m
$Zr_{63.8}Ni_{16.2}Cu_{15}Al_5$	647	745	98	1114	1178	64	0.549	0.408	0.716
$Pd_{40}Ni_{40}P_{20}$	584	675	91	937	991	54	0.589	0.429	0.772
$Mg_{58}Cu_{31}Y_6Nd_5$	430	503	73	715	783	68	0.549	0.415	0.736

$\Delta T_x = T_x - T_g$

$\Delta T_l = T_l - T_m$

$T_{rg} = T_g/T_l$

$\gamma = T_x/(T_g + T_l)$

$\gamma_m = (2T_x - T_g)/T_l$

Table 4.2 Summary of mechanical properties for the as-cast BMG sample deformed at a low strain rate (~1 x 10^{-4} s^{-1}) and room temperature based on the engineering stress-strain curve.

BMG type	E (GPa)	σ_y (GPa)	ε_e (%)	ε_p (%)	ε_{total} (%)	θ_c (^{o})
$Zr_{63.8}Ni_{16.2}Cu_{15}Al_5$	90	~1.7	2	~14	16	42
$Pd_{40}Ni_{40}P_{20}$	100	~1.8	2	~2	4	41
$Mg_{58}Cu_{28.5}Gd_{11}Ag_{2.5}$ BMGC	60	~1.0	2	~7	9	43

E: elastic modulus (GPa)

σ_y: yielding strength (MPa)

σ_{max}: maximum fracture strength (MPa)

ε_e: elastic strain (%)

ε_p: plastic strain (%)

ε_{total}: total compressive strain (%)

θ_c: compressive fracture angle with respect to the loading axis (^{o})

Table 4.3 Comparison of dimensional changes measured from SEM observations and the load-displacement curves. Subscripts LD and SEM denote measurements from the L-D curves and SEM observations. $\Delta d_{p,SEM}$ and $\Delta d_{v,SEM}$ are the offset displacement along the shear plane and the resolved vertical displacement, respectively.

Nominal strain	L-D curves		SEM observations		
	d_{LD} (mm)	$\varepsilon_{p,LD}$ (%)	$d_{p,SEM}$ (mm)	$d_{v,SEM}$ (mm)	$\varepsilon_{p,SEM}$ (%)
~3%	0.066	1.6	---	---	---
~7%	0.238	5.7	0.229	0.168	4.1
~10%	0.315	8.7	0.365	0.271	7.4

Table 4.4 Comparison of the displacement before and after an intermittent sliding of principal shear, obtained from four major serrations in Figure 4.31, and the displacement calculated from load drop in Figure 4.30.

n	$l_{i,n}$ (mm)	$l_{f,n}$ (mm)	Δl (mm)	Δl_v (mm)	Δl_{LD} (mm)	ΔP (N)
1	---	---	---	---	0.006	104.84
2	0.006	0.009	0.003	0.004	0.004	116.45
3	0.015	0.017	0.002	0.003	0.005	120.30
4	0.022	0.026	0.004	0.005	0.008	164.10

Note that Δl and Δl_v are the horizontal and vertical displacements during a single sliding event in Figure 4.31. $\Delta l_v = \Delta l/\tan\theta$ (where θ is the shear angle). Δl_{LD} is the displacement calculated from the load drop in Figure 4.30. ΔP is the amplitude of load drop in load-displacement curve.

Table 4.5 Comparison of first burst occurrence level, the average shear-band propagating speed, average steady-state strain rate and average viscosity within the propagating shear band obtained from the ductile Pd-based and brittle Mg-based BMGs compressed at a low strain rate of 2×10^{-4} s^{-1}. σ_{max} denotes the stress level at which the stress-strain curve reaches an apparent steady-state after yielding.

BMGs	First burst level	Propagating speed (μm/s)		Strain rate (s^{-1})	Viscosity (Pa·s)	Plastic strain (%)
		Stage 1	Stage 2			
$Pd_{40}Ni_{40}P_{20}$	$0.83\sigma_{max}$	424	532	4.7×10^{4}	4.2×10^{4}	~3
$Mg_{58}Cu_{31}Y_6Nd_5$	$0.81\sigma_{max}$	492	---	5.0×10^{4}	6.2×10^{3}	0

Table 5.1 Comparison of the hardness in nanoindentation for the as-cast phase-separated sample and the deformed sample with nominal compressive strain of 3%, 7% and 10%. The applied strain rate is at 5 x 10^{-2} s^{-1}.

BMG	Nominal strain	Nano-indentation in GPa
$Zr_{63.8}Ni_{16.2}Cu_{15}Al_5$	0%	6.17 ± 0.040
	~3%	6.12 ± 0.057
	~7%	5.82 ± 0.415
	~10%	5.57 ± 0.172

Table 5.2 Parameters related to the inter-Mo spacing and intra-Mo spacing within a single porous Mo particle in the current Mg-based BMG composite.

Items	**Symbol**	**Size**
Volume fraction of Mo particles	f	25%
Porosity of single Mo particle	---	~40%
Diameter of Mo particle	d	~50 μm
Inter-Mo spacing	s - d	~38 μm
Diameter of fine-scale compartment island	σ	2-5 μm
Intra-Mo spacing	$\delta - \sigma$	0.5 μm

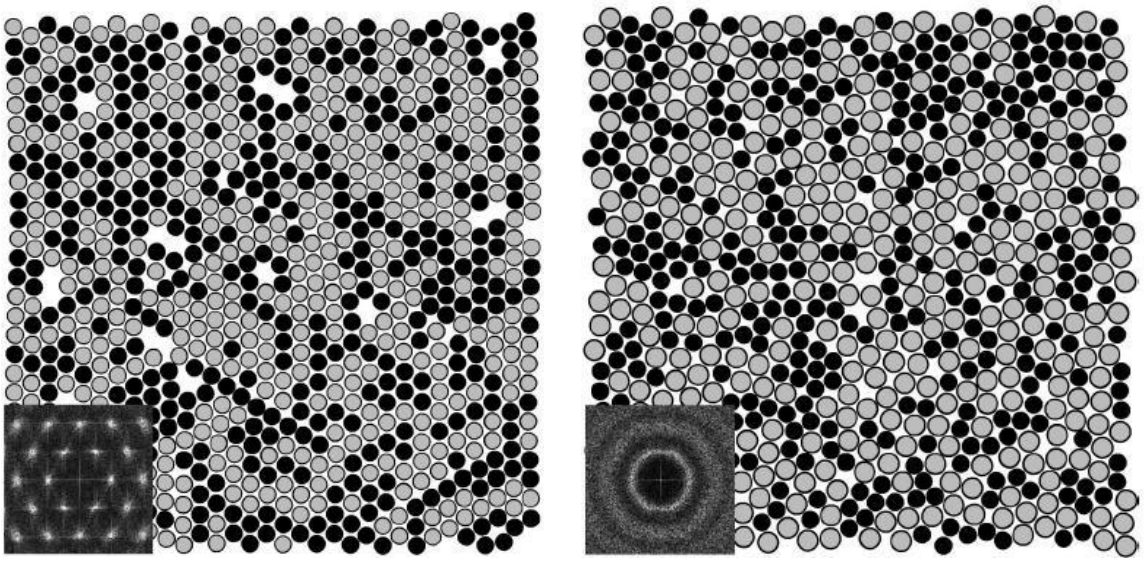

Crystal **Amorphous**

Figure 1.1 Configuration of atomic arrangements in crystal and amorphous alloy.

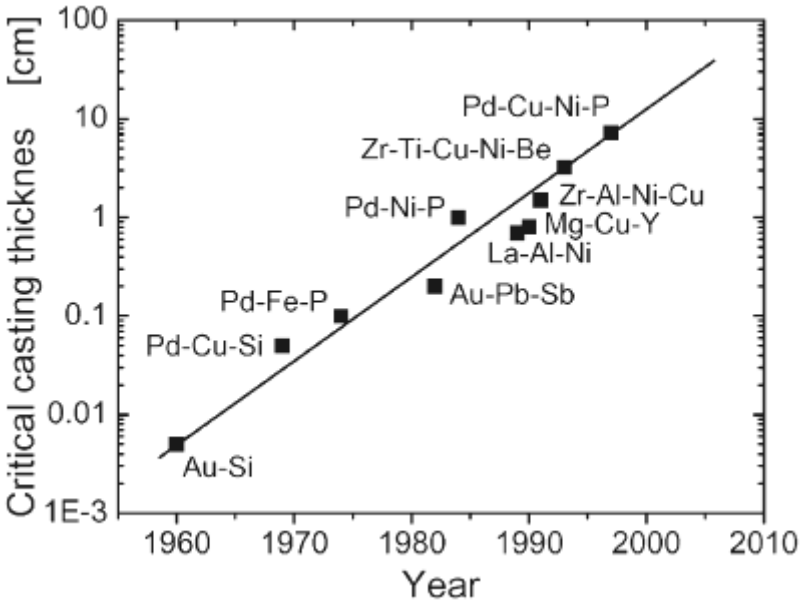

Figure 1.2 Critical casting thicknesses for glass formation as a function of the year and corresponding alloy [22].

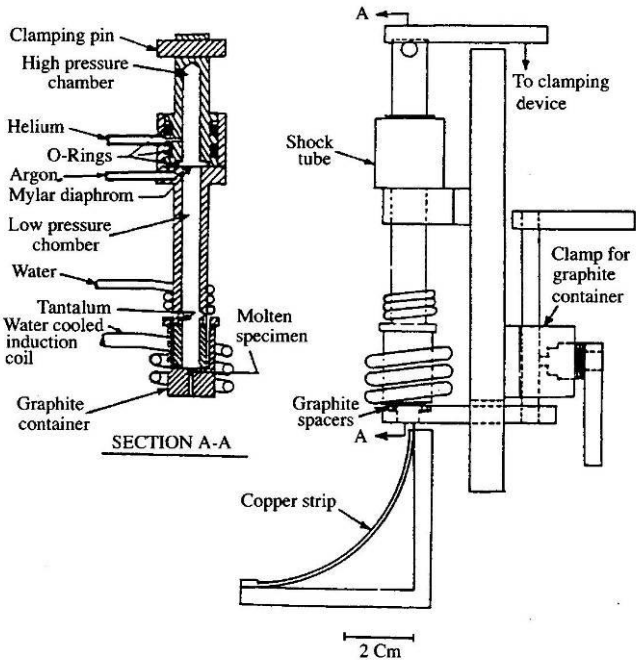

Figure 2.1 A schematic diagram of the splat quenching method [48].

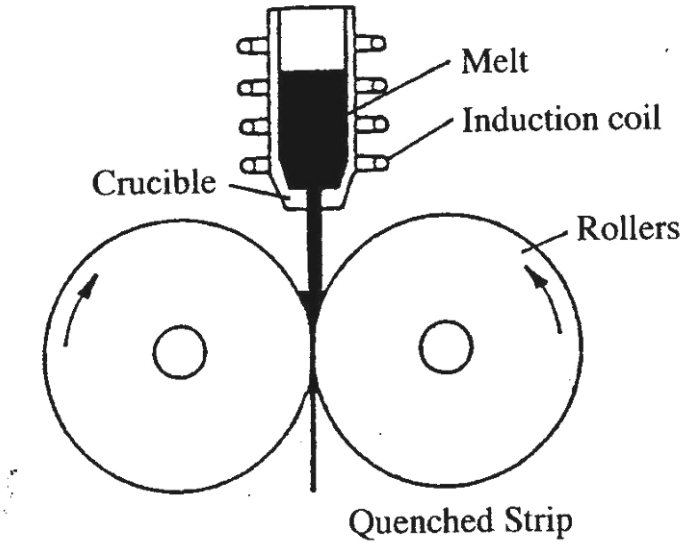

Figure 2.2 A schematic diagram of the two roller quenching method [48].

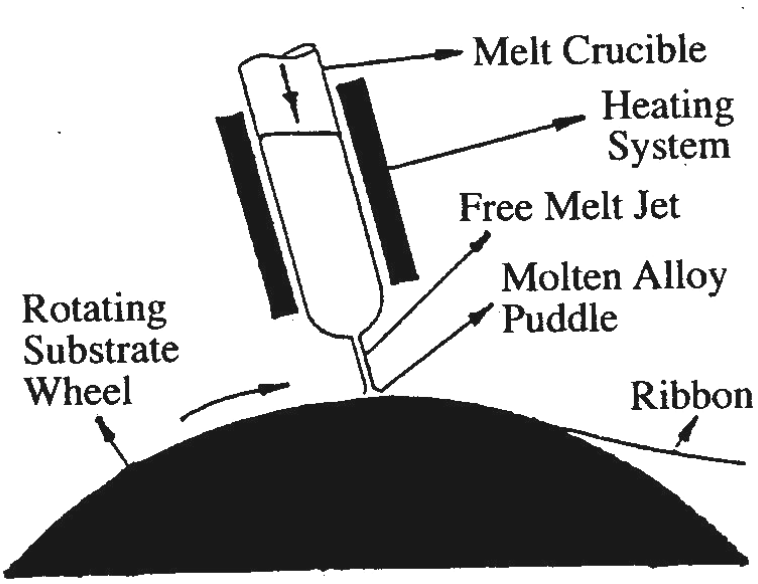

Figure 2.3 A schematic diagram of the chill block melt spinning [48].

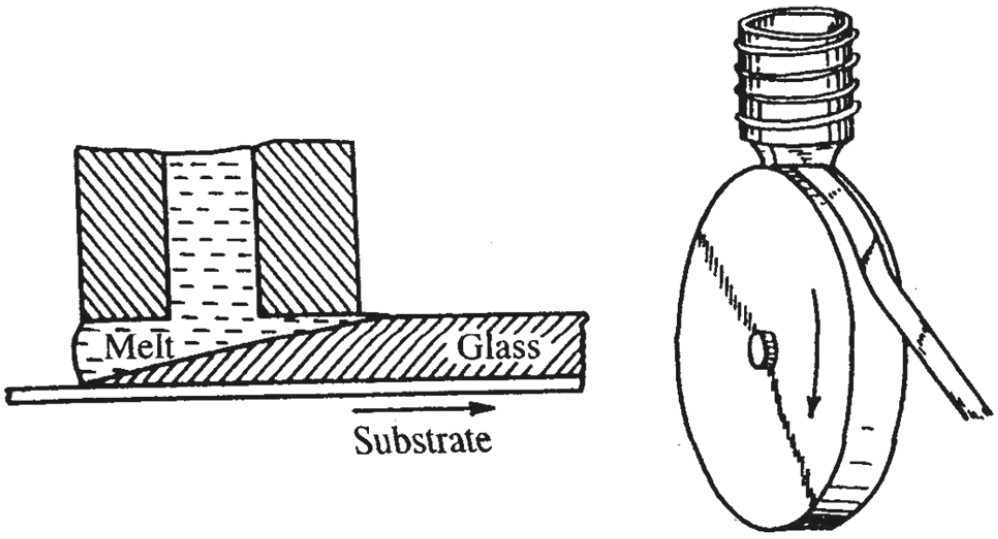

Figure 2.4 A schematic diagram of the planar flow casting process [48].

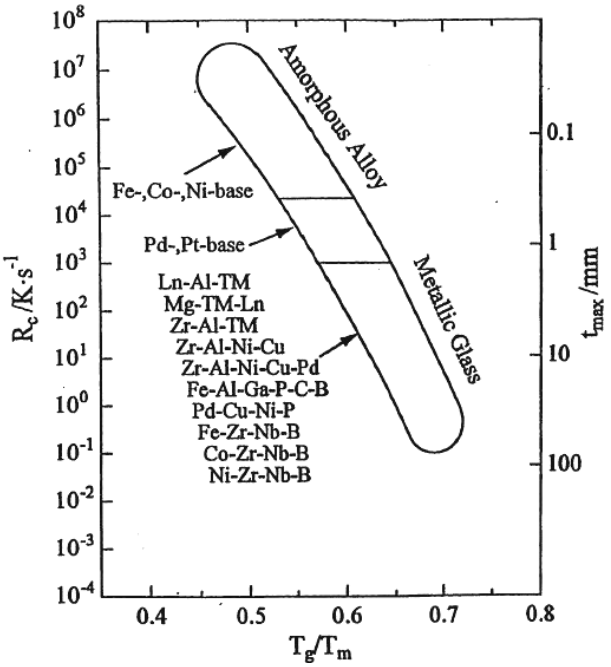

Figure 2.5 Relationship between the critical cooling rate (R_c), the maximum sample thickness (t_{max}) and reduced glass transition temperature (T_g/T_m) for BMG systems [5].

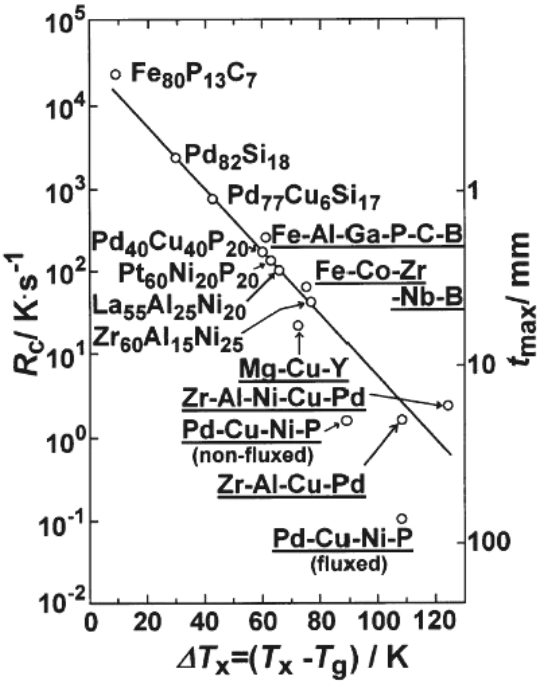

Figure 2.6 Relationship between the critical cooling rate (R_c), the maximum sample thickness (t_{max}) and supercooled liquid region (ΔT_x) for BMG systems [5].

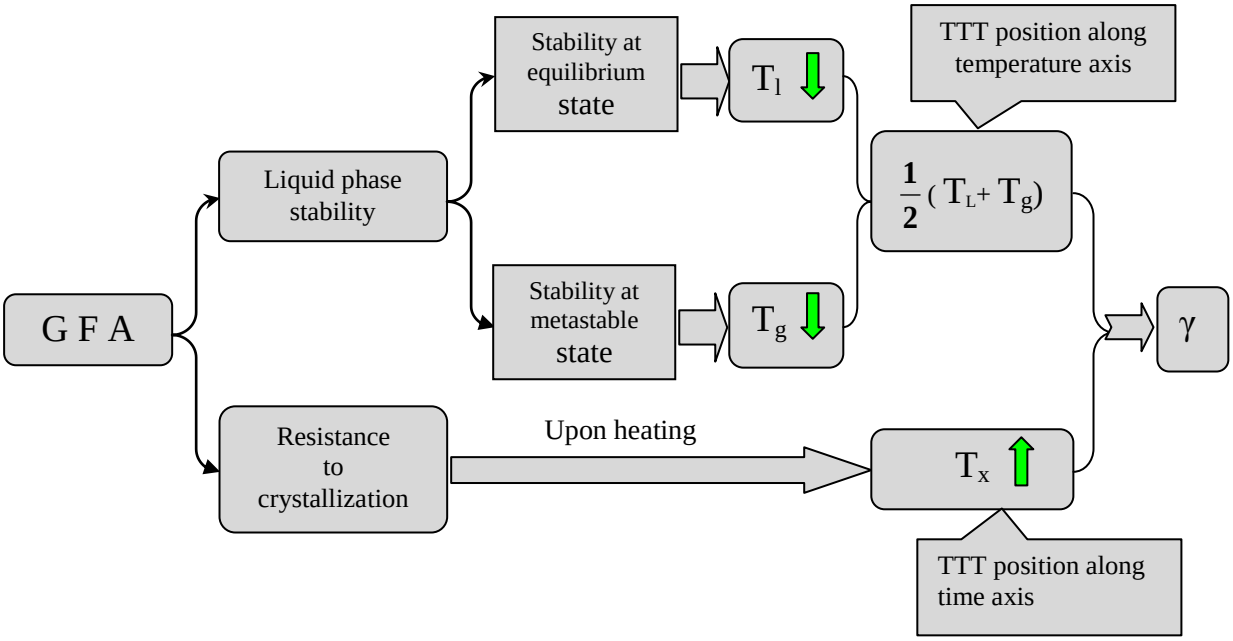

Figure 2.7 The γ parameter of GFA for metallic glasses [81].

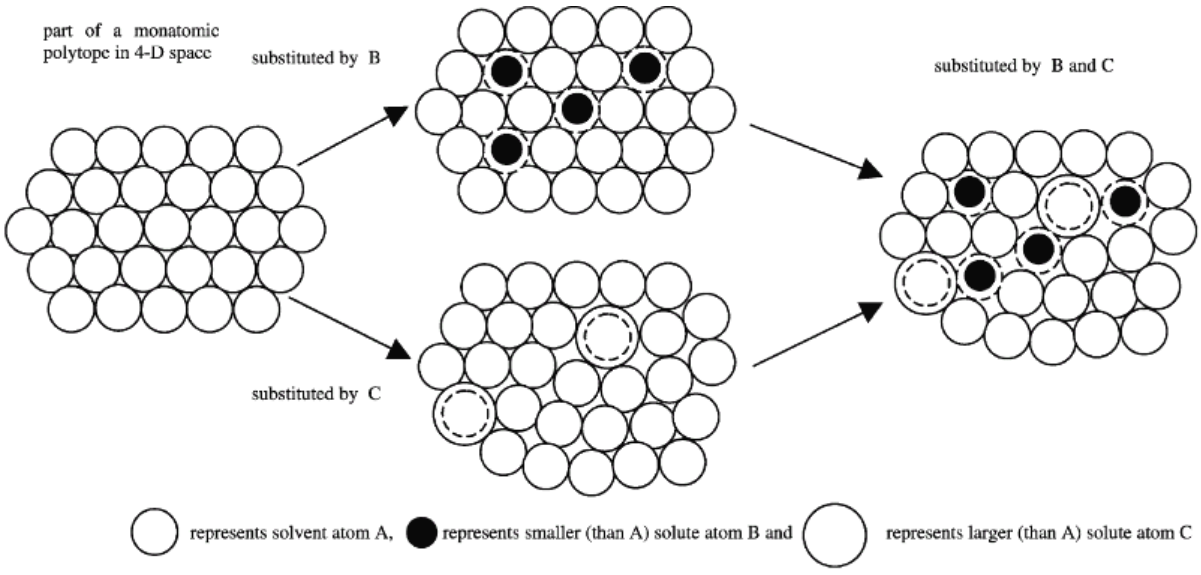

Figure 2.8 The atomic configuration of different atomic size system [5].

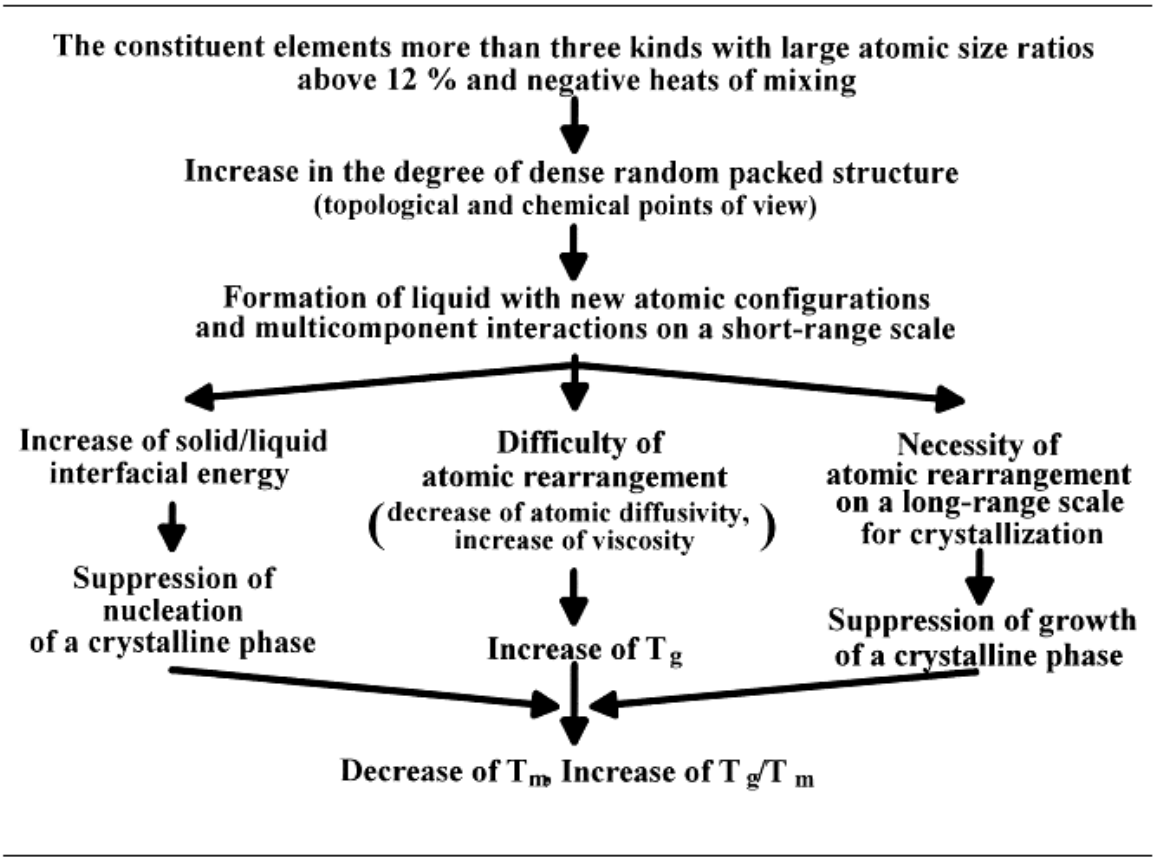

Figure 2.9 Mechanisms for the stabilization of supercooled liquid and high glass-forming ability for the multicomponent alloys which satisfy three empirical rules [5].

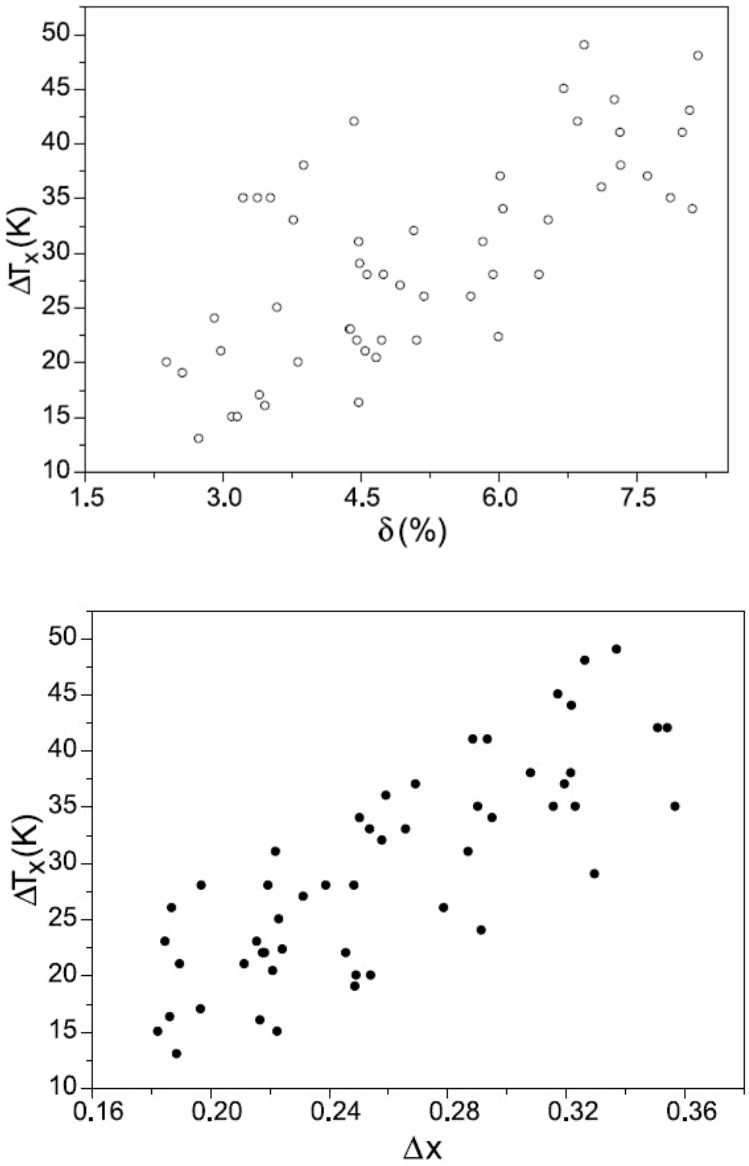

Figure 2.10 The relationship between the bond parameters, including electronegativity difference (Δx) and atomic size parameters (δ), and the temperature interval of supercooled liquid region (ΔT_x) in Mg-Based bulk metallic glasses [71].

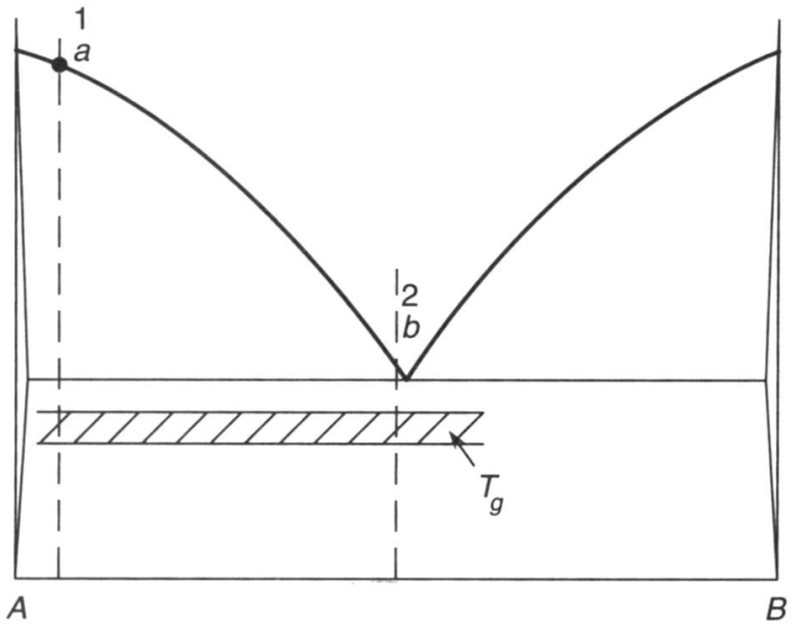

Figure 2.11 A illustration of binary alloy system in phase diagram with a single deep eutectic point [229].

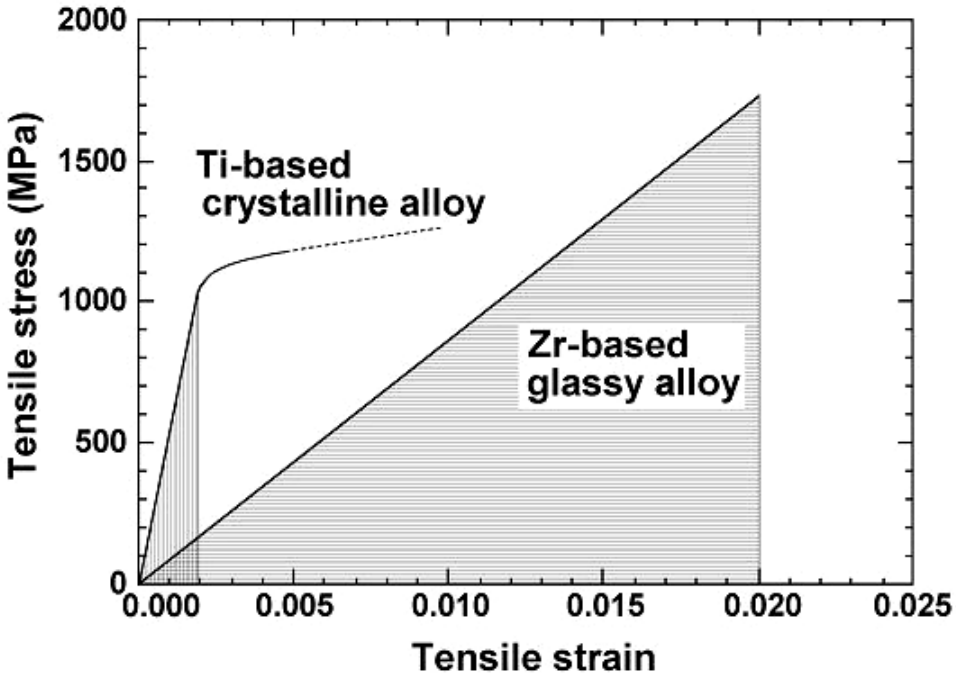

Figure 2.12 The stress-strain curves of a Zr-based bulk amorphous alloy and a Ti-based crystalline alloy [23].

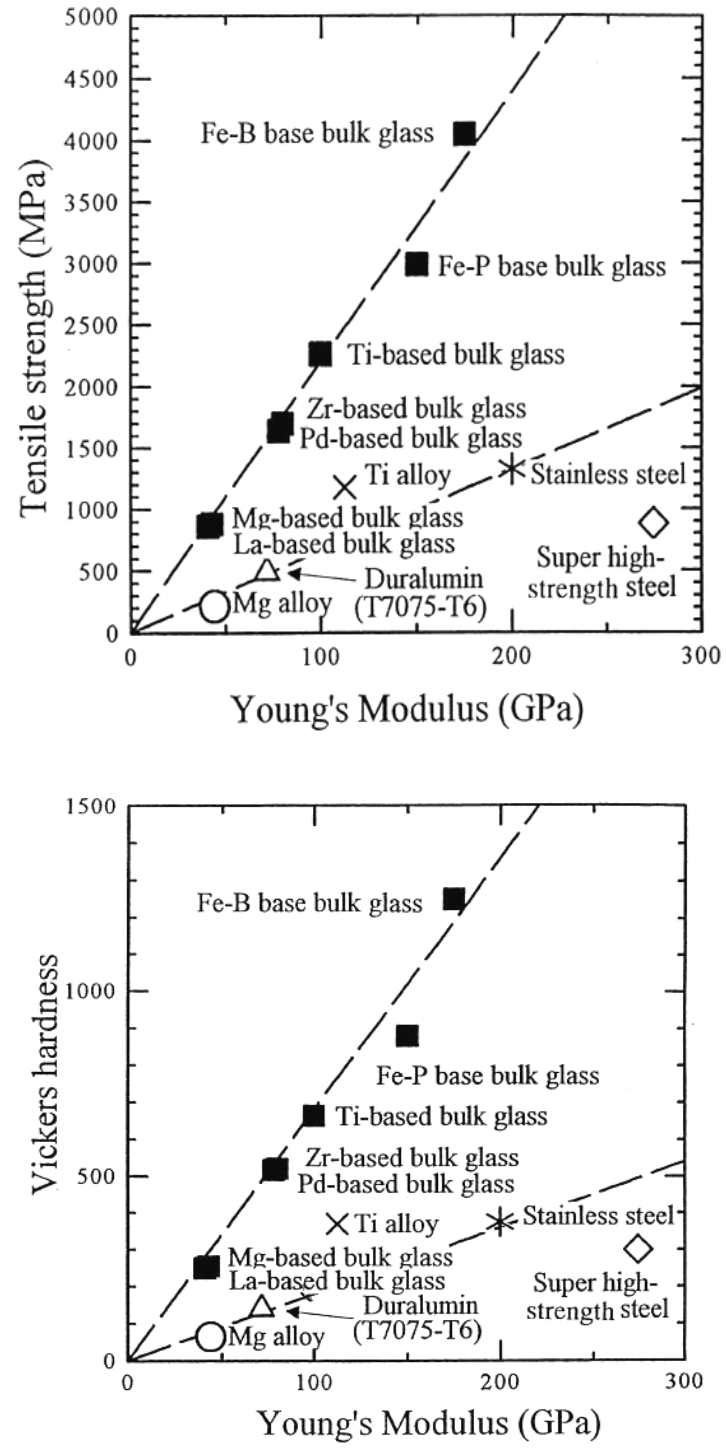

Figure 2.13 Relationship between tensile fracture strength, Vickers hardness and Young's modulus for bulk amorphous alloys and conventional crystalline alloys [5].

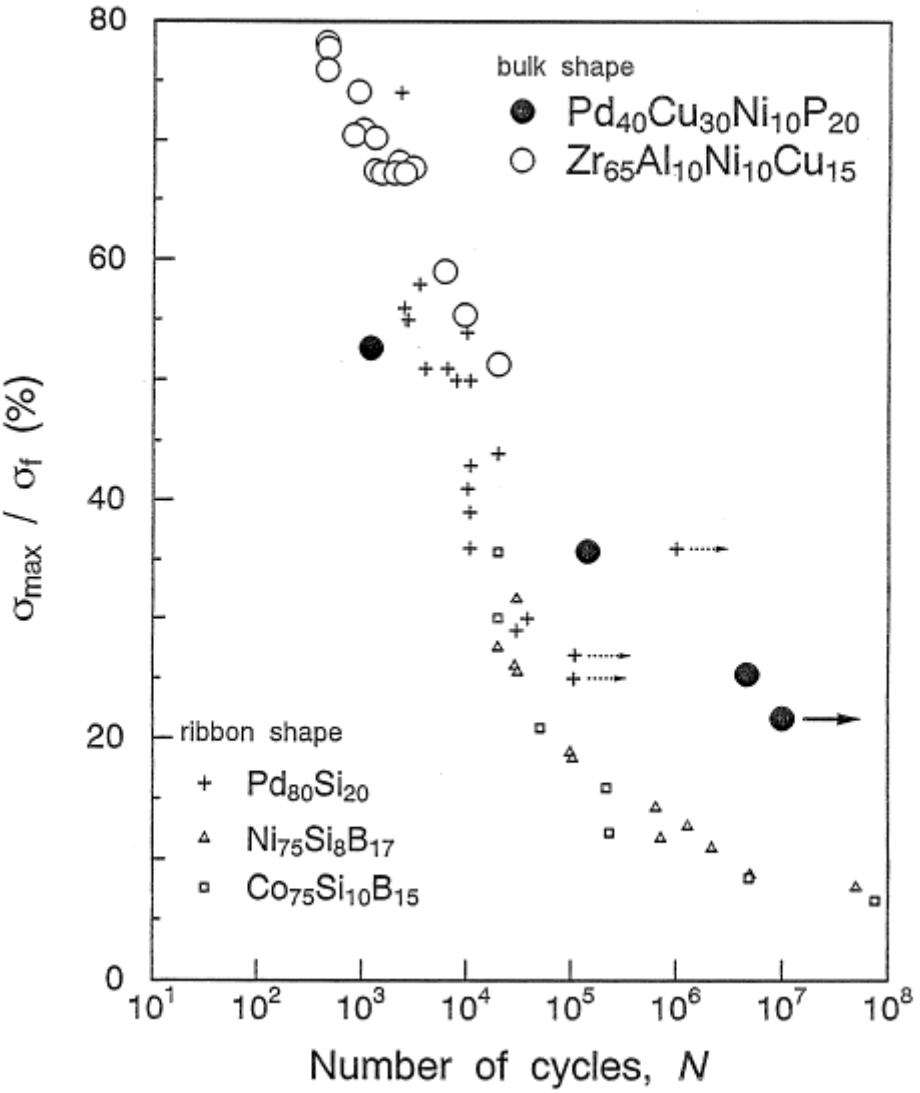

Figure 2.14 Maximum bending and rotating beam fatigue stress as a function of cyclic number up to failure for $Zr_{65}Al_{10}Ni_{10}Cu_{15}$ and $Pd_{40}Cu_{30}Ni_{10}P_{20}$ BMGs. The data for the melt-spun Pd-, Ni- and Co-based amorphous ribbons are also shown for comparison [5].

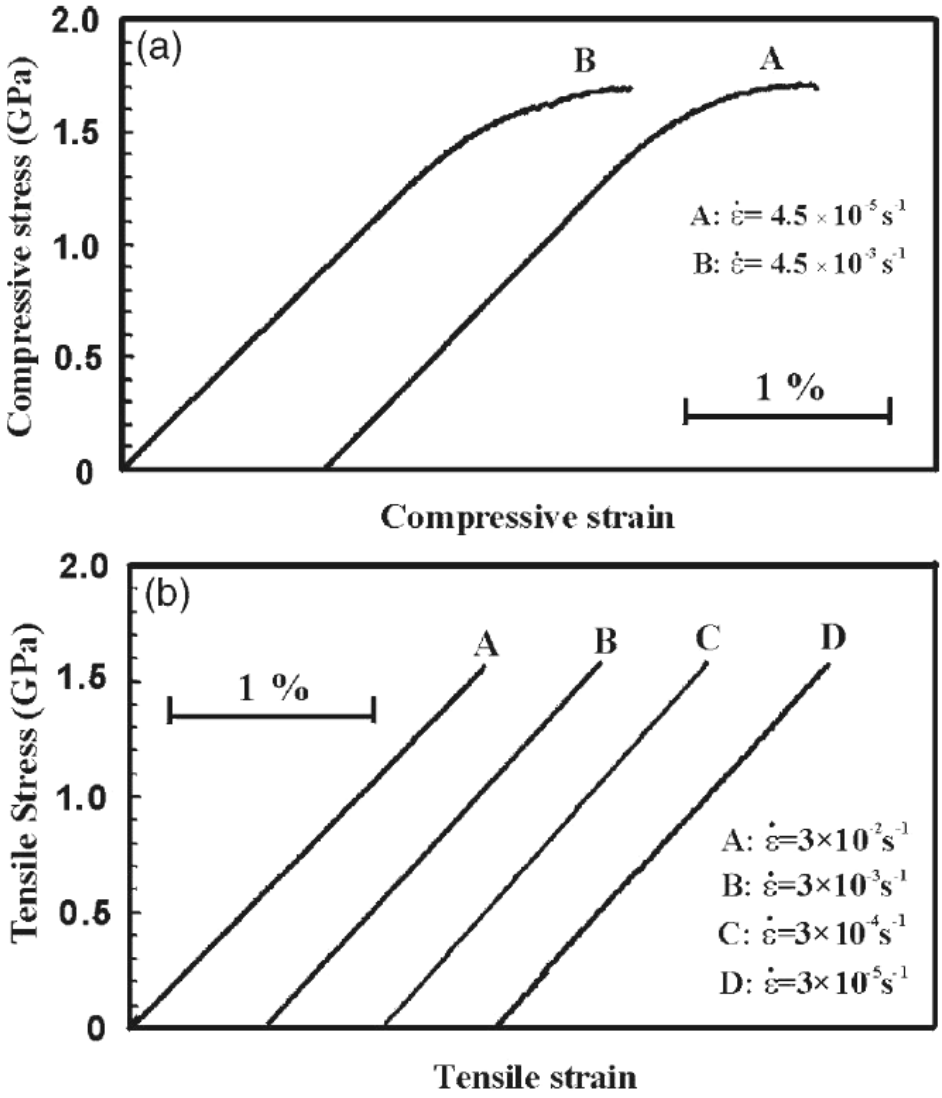

Figure 2.15 Typical (a) compressive and (b) tensile stress–strain curves of the $Zr_{59}Cu_{20}Al_{10}Ni_8Ti_3$ BMGs at different applied strain rates from 4.5 x 10^{-5} to 3 x 10^{-2} s^{-1} [44].

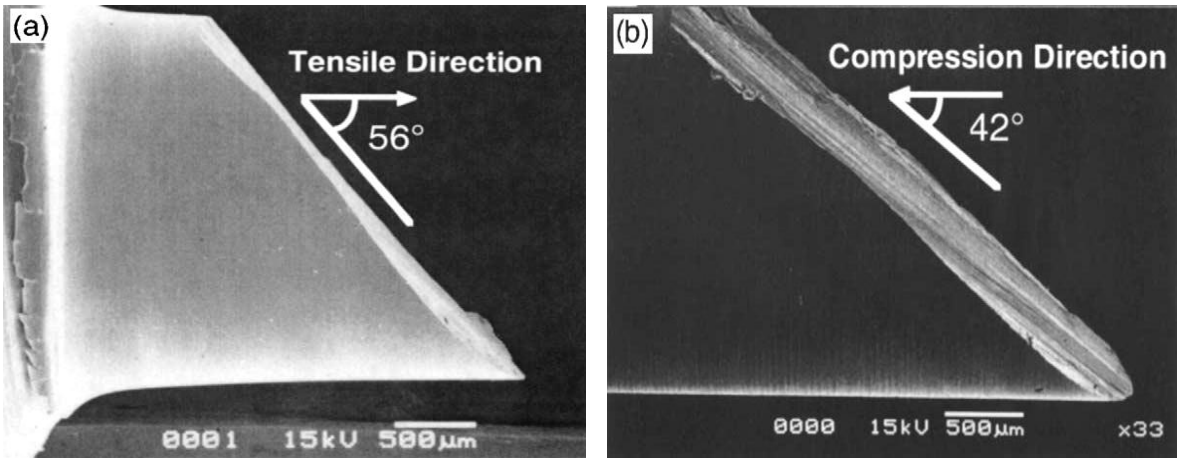

Figure 2.16 Typical side view of the $Pd_{40}Ni_{40}P_{20}$ BMGs with (a) tensile (θ_T) and (b) compressive (θ_c) fracture angle at a low strain rate [133].

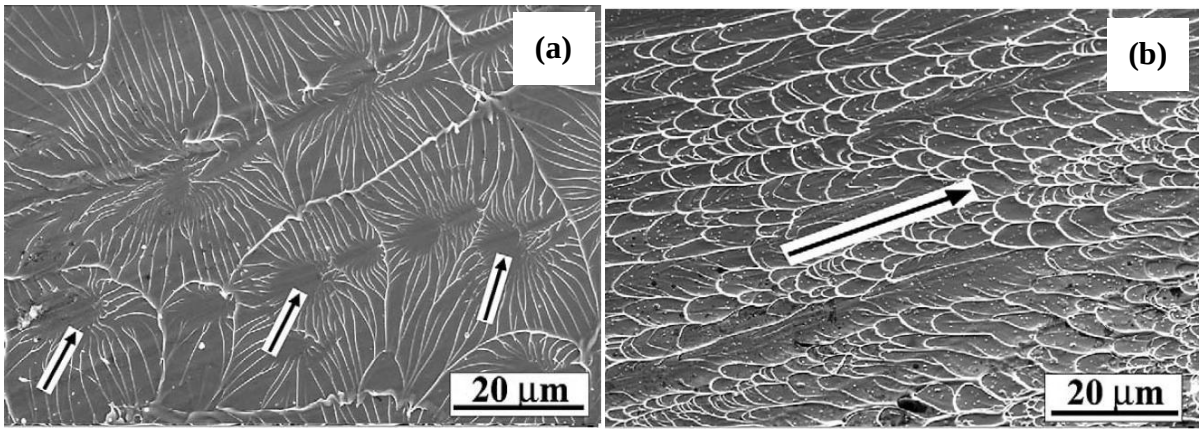

Figure 2.17 Typical fracture morphologies of the $Zr_{59}Cu_{20}Al_{10}Ni_8Ti_3$ BMGs with tensile and compressive fracture surfaces [44].

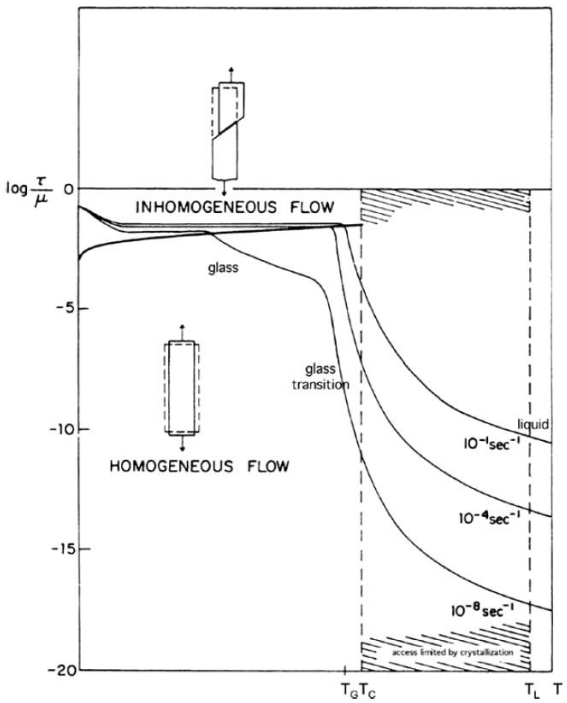

Figure 2.18 Schematic deformation mechanism map of a metallic glass [121].

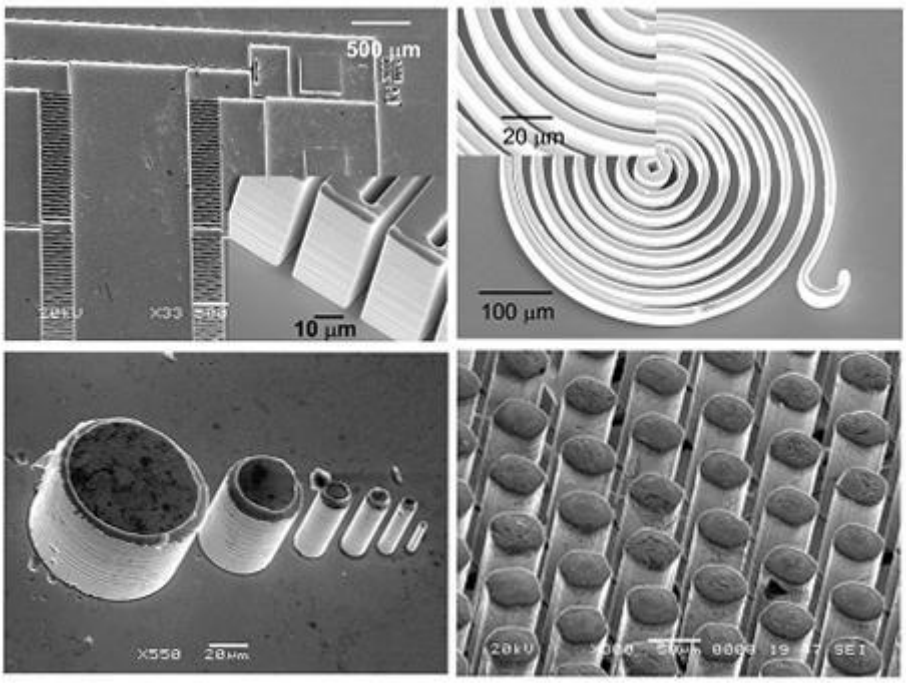

Figure 2.19 Device applied to the MEMS for BMGs [122].

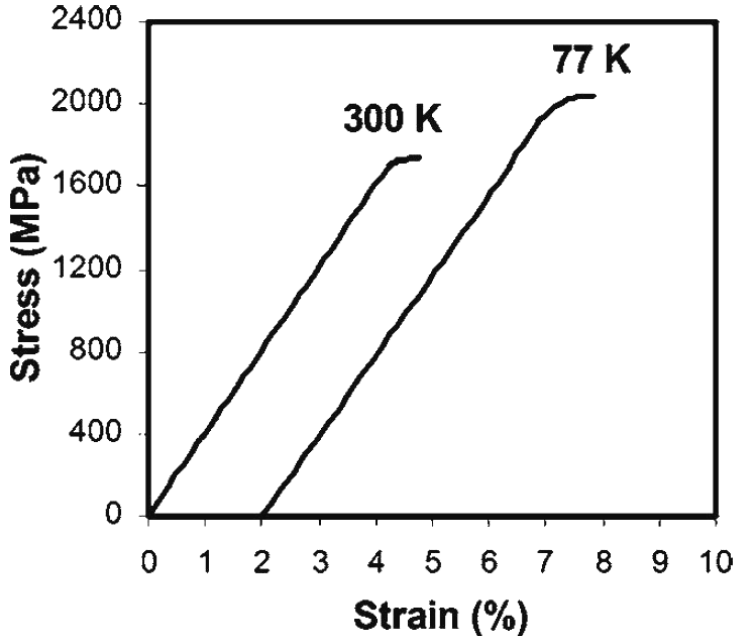

Figure 2.20 Compressive stress-strain curves of the Zr-based BMG at room temperature (300 K) and liquid nitrogen temperature (77 K) at a strain rate of $2x10^{-4}$ s^{-1} [124].

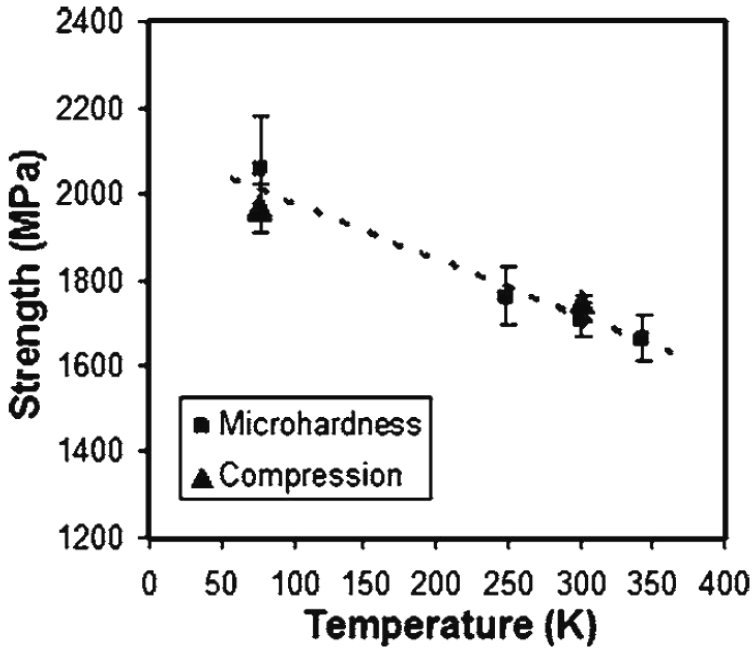

Figure 2.21 Dependence of strength variation as a function of testing temperatures in compression and microhardness [124].

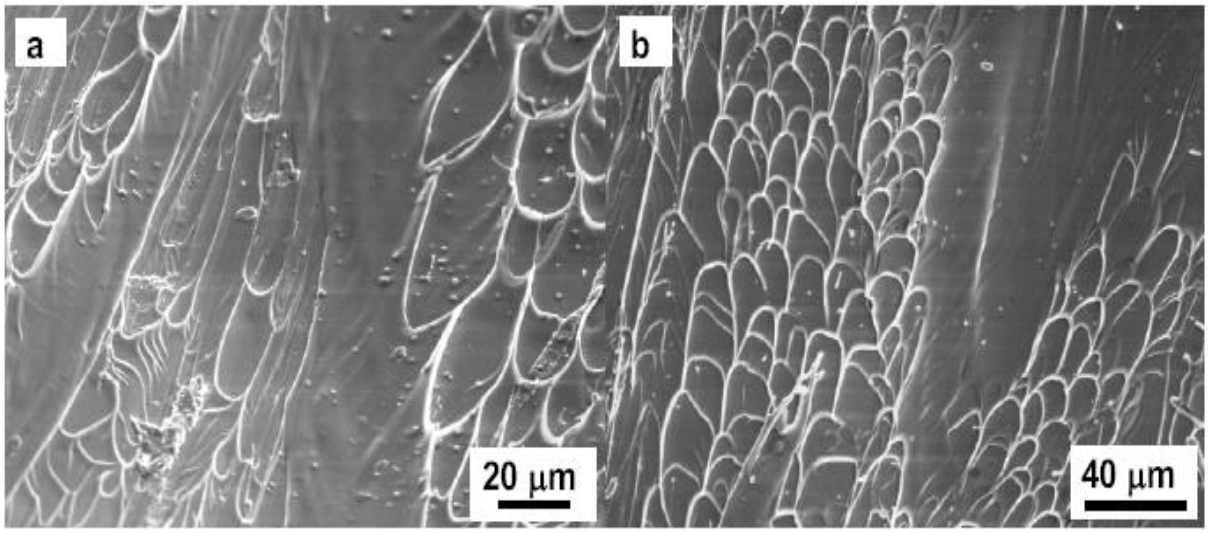

Figure 2.22 SEM micrographs of fracture surfaces of BMG samples tested at (a) 300 K and (b) 77 K under compression tests [125].

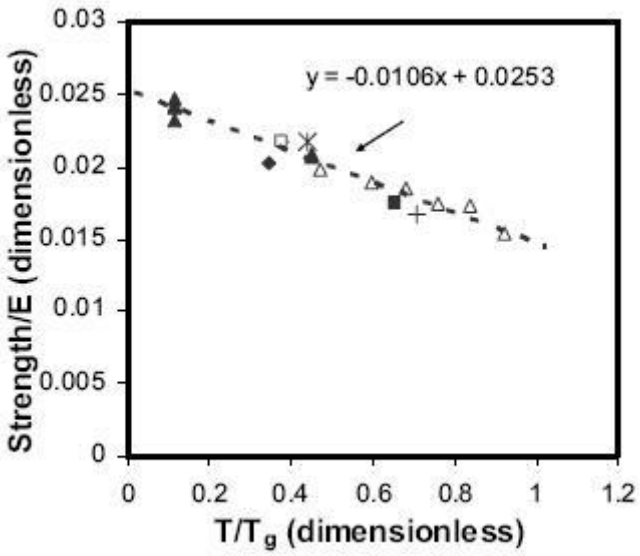

Figure 2.23 Dependence of the normalized strength as a function of the normalized temperature for the BMGs deformed under compression tests [125].

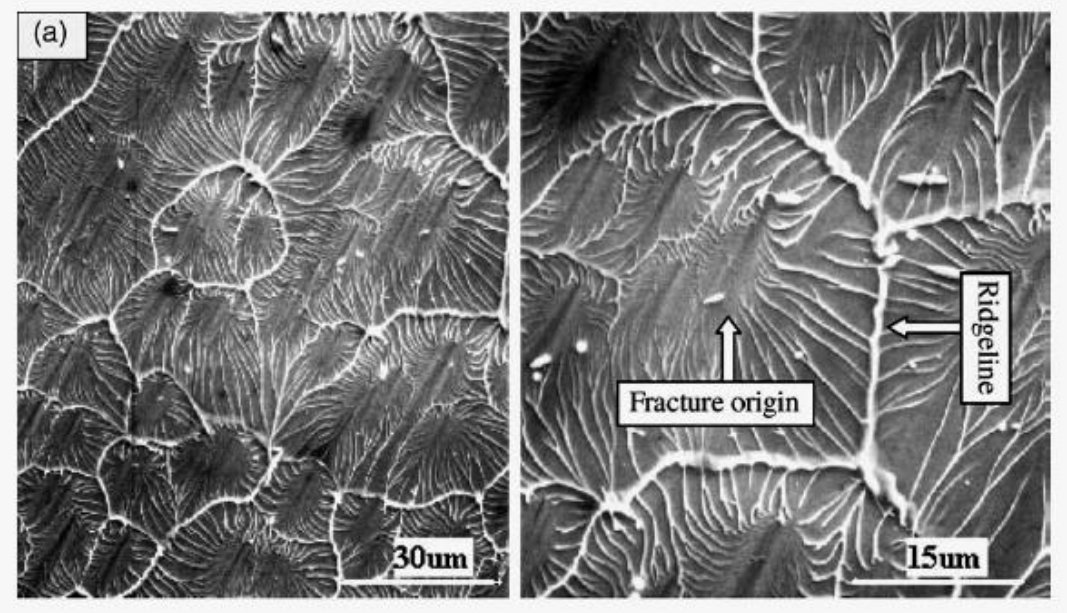

Figure 2.24 Fracture surface morphologies of the $Zr_{52.5}Al_{10}Ni10Cu_{15}Be_{12.5}$ BMG at low strain rates under the tensile deformation [131].

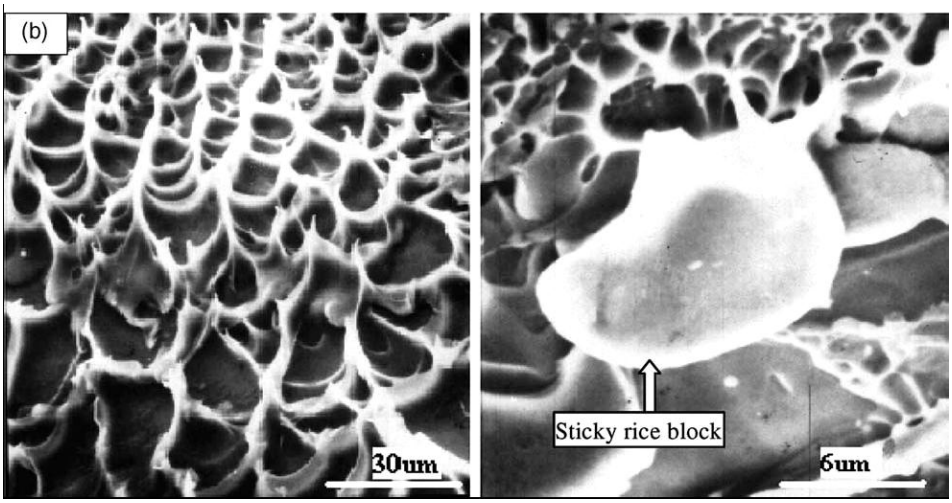

Figure 2.25 Fracture surface morphologies of the $Zr_{52.5}Al_{10}Ni10Cu_{15}Be_{12.5}$ BMG at high strain rates under the tensile deformation [131].

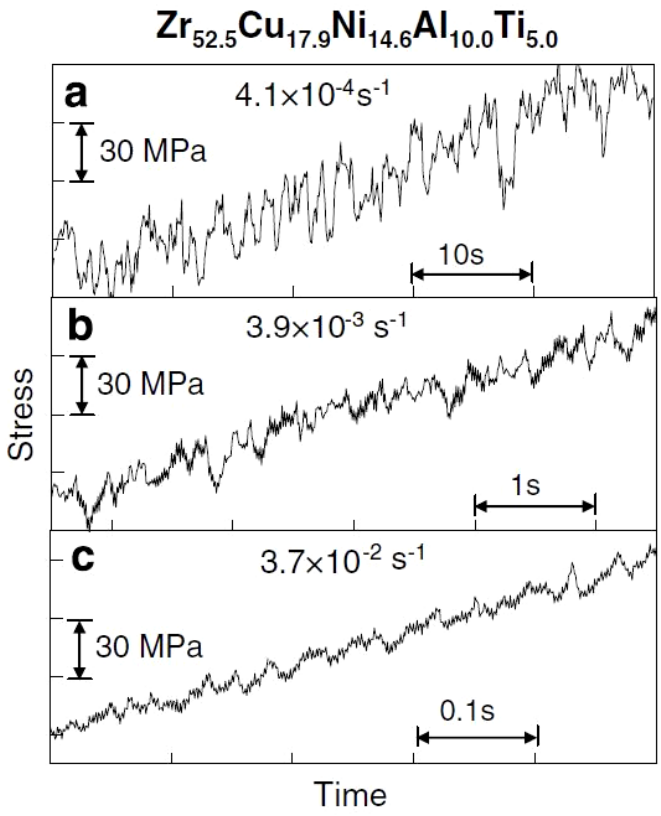

Figure 2.26 Stress as a function of time of of Zr-based BMGs at various applied strain rates of (a) 4.1 x 10^{-4} s^{-1}, (b) 3.9 x 10^{-3} s^{-1} and (c) 3.7 x 10^{-2} s^{-1} [134].

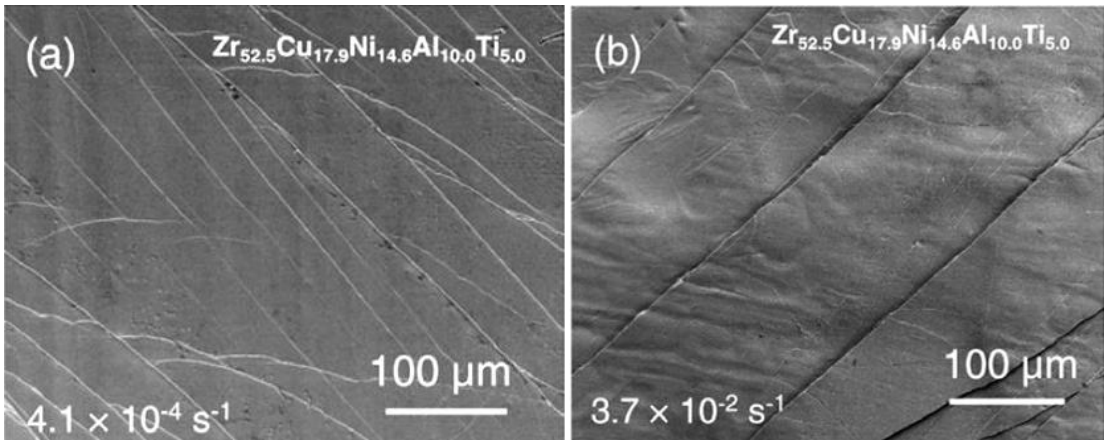

Figure 2.27 SEM micrographs of sample outer appearances of Zr-based BMG tested to a plastic strain of 26.4% at the strain rates of (a) 4.1 x 10^{-4} s^{-1} and 3.7 x 10^{-2} s^{-1} [134].

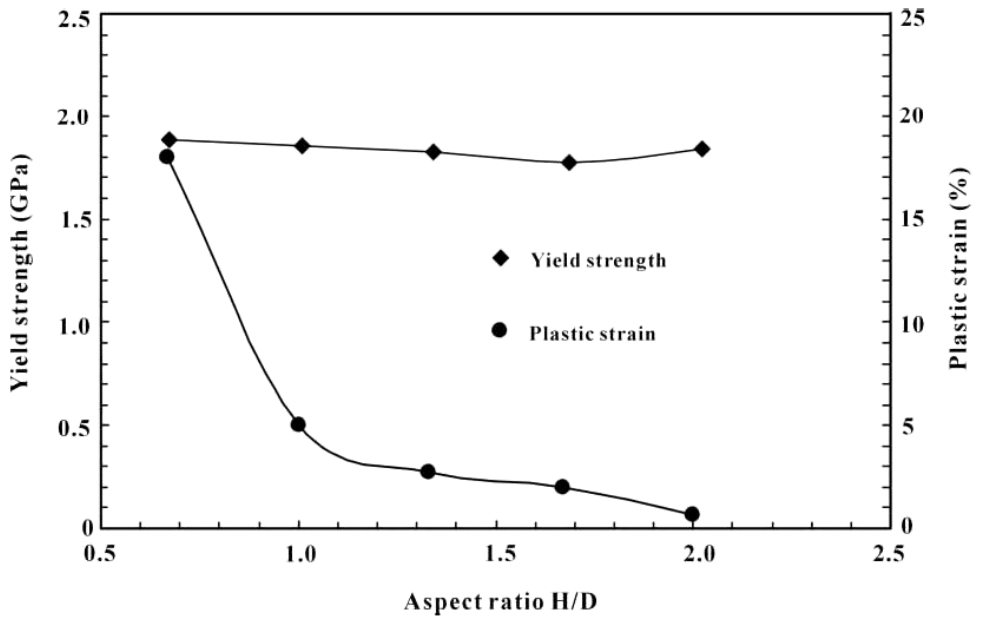

Figure 2.28 Dependence of yield strength and plastic strain on the aspect ratio of the $Zr_{59}Cu_{20}Al_{10}Ni_8Ti_3$ BMGs in compression [39].

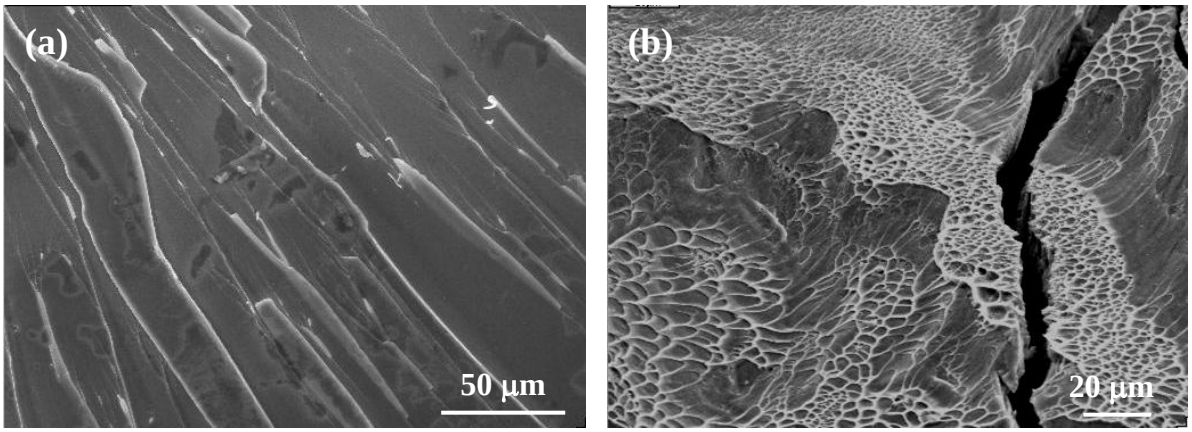

Figure 2.29 Fracture surfaces of the cylindrical $Mg_{65}Cu_{25}Gd_{10}$ samples with the aspect ratio of (a) 2 and (b) 0.25 in compression [43].

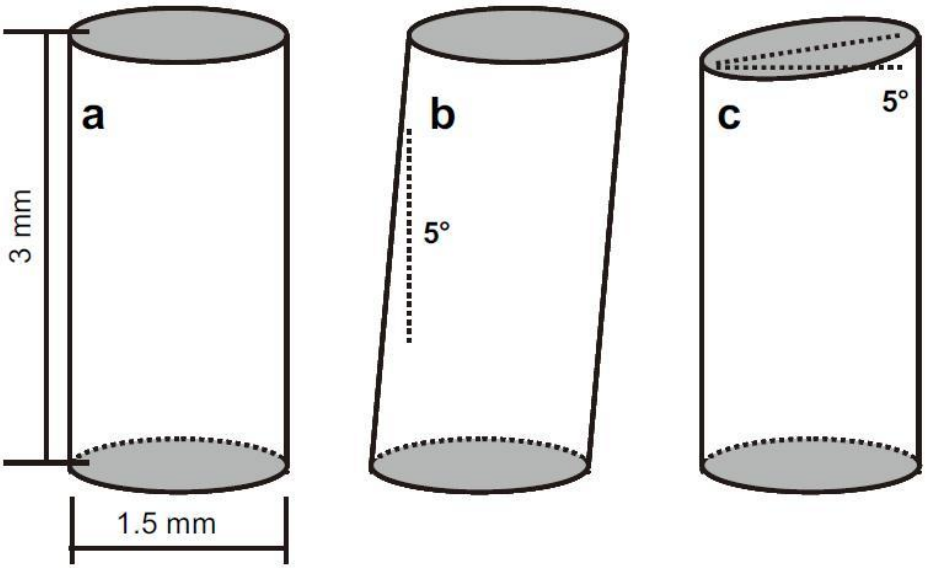

Figure 2.30 BMG samples with three various designed geometries (a) orthogonal, (b) monoclinic and (c) transitional [146].

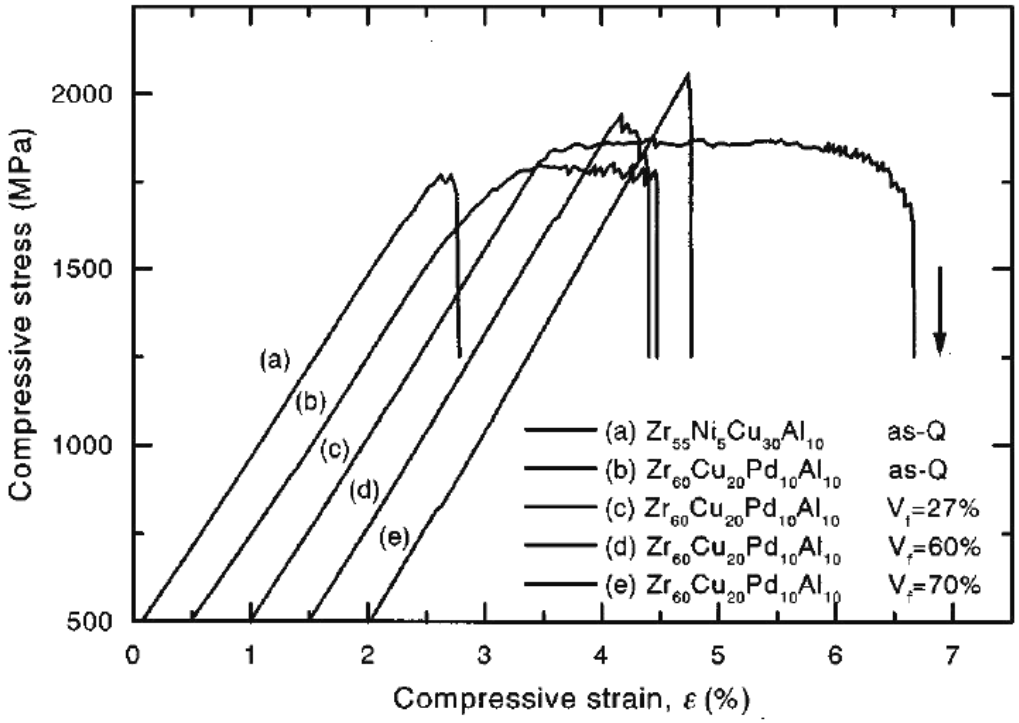

Figure 2.31 Compressive stress-strain curves of the $Zr_{60}Al_{10}Cu_{20}Pd_{10}$ BMG and BMGCs with various volume fraction of Zr_2(Cu, Pd) precipitated nanocrystals [25].

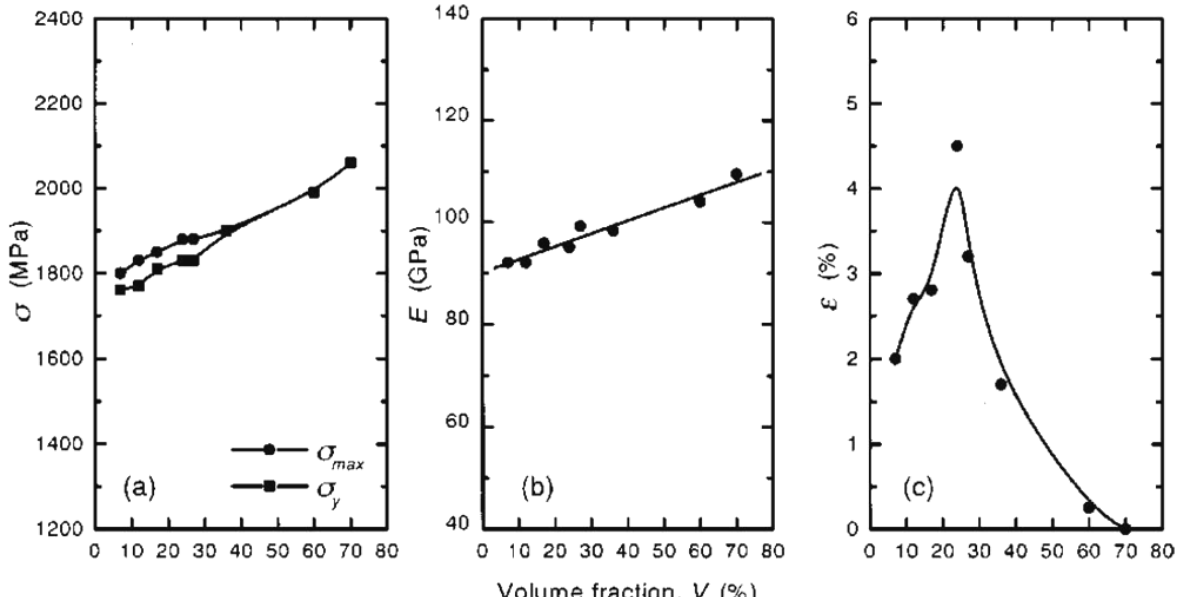

Figure 2.32 Mechanical properties of the $Zr_{60}Al_{10}Cu_{20}Pd_{10}$ BMG and BMGCs with various volume fraction of Zr_2(Cu, Pd) precipitated nanocrystals: (a) yield strength, σ_y, and the maximum fracture strength, σ_{max}; (b) Young's modulus, E and (c) plastic strain to failure after yielding, ε_p [25].

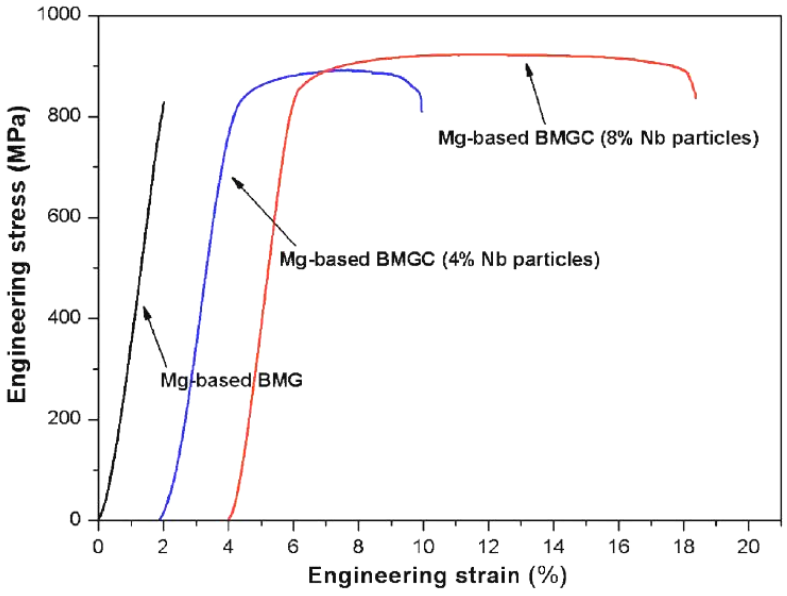

Figure 2.33 Compressive stress-strain curves for the monolithic Mg-based BMG and Nb-containing Mg-based BMGC with volume fraction of 4% and 8%, respectively [158].

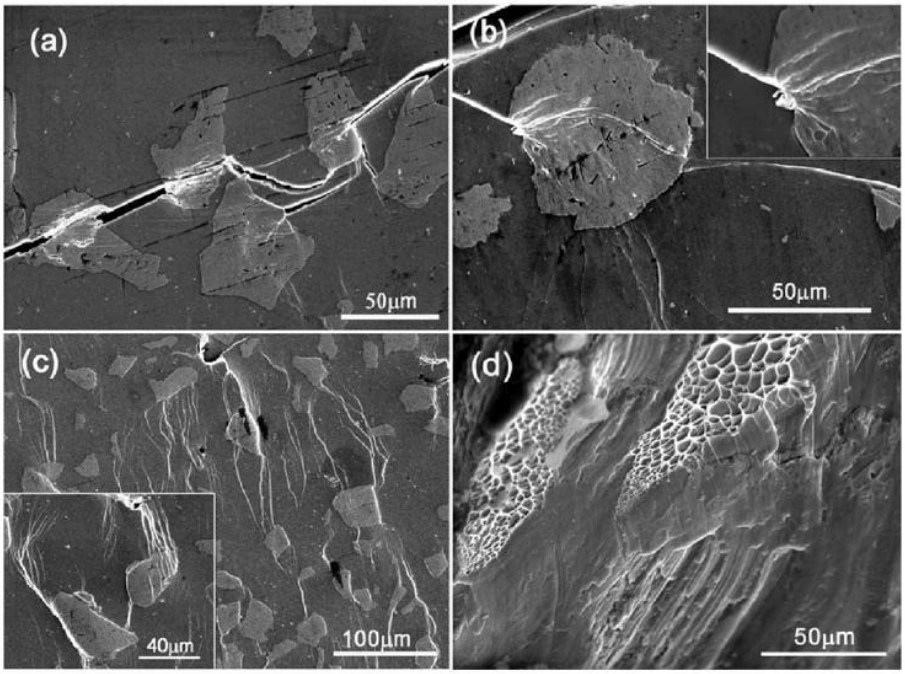

Figure 2.34 SEM micrographs of (a) outer surface and (d) fracture surface for the Mg-based BMGC. The inset in (b) shows the enlarged view of the interface where a shear band travels into a particle; the inset in (c) shows the shear bands propagation and branching from deformed Nb particles [158].

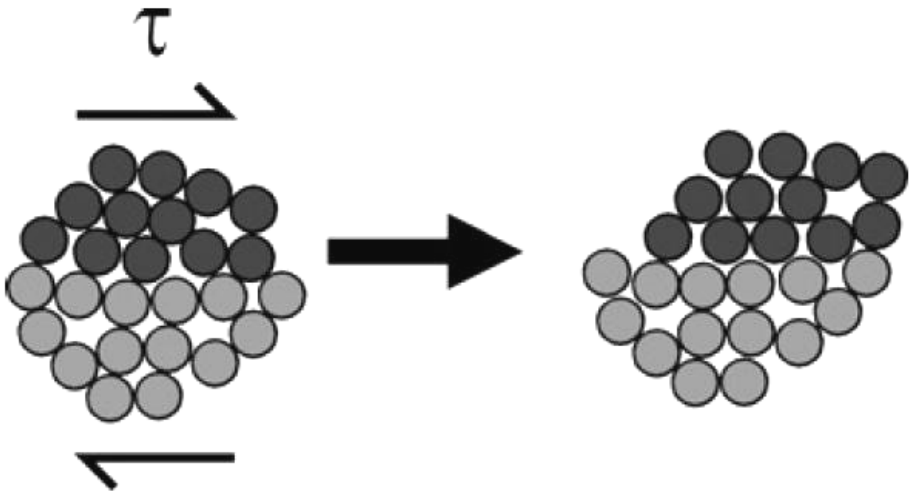

Figure 2.35 Two-dimensional schematic diagram of atomistic deformation mechanism for metallic glasses under applied loading [27].

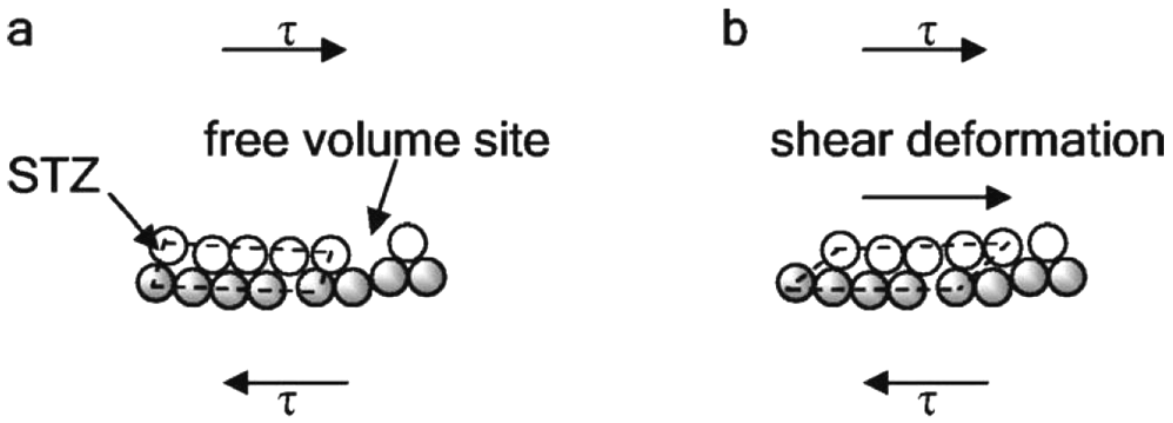

Figure 2.36 Simplified illustration of STZ deformation. (a) STZ before shear deformation and (b) STZ after shear deformation [172].

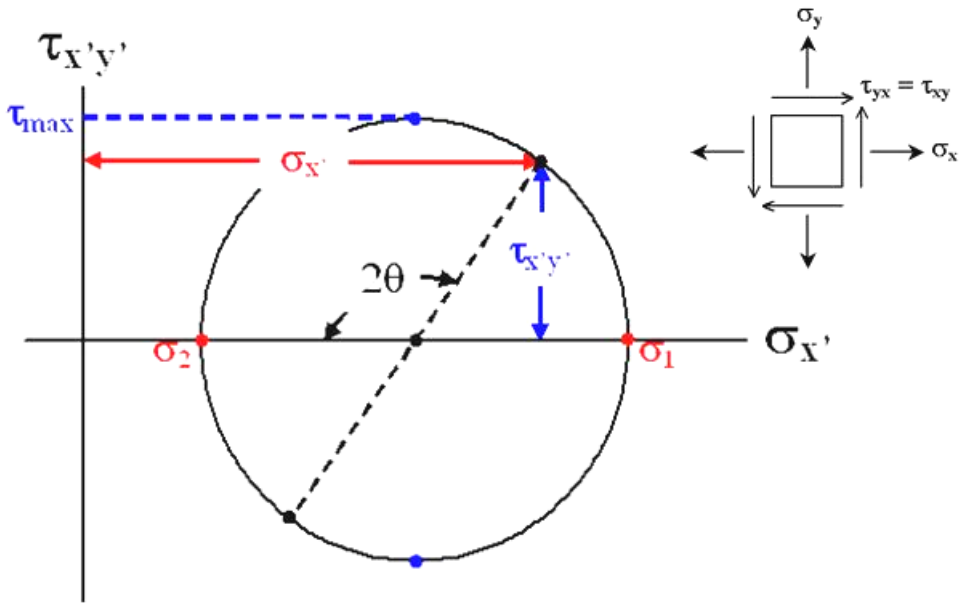

Figure 2.37 Schematic illustration of the Mohr circle for the 2-D stress state [230].

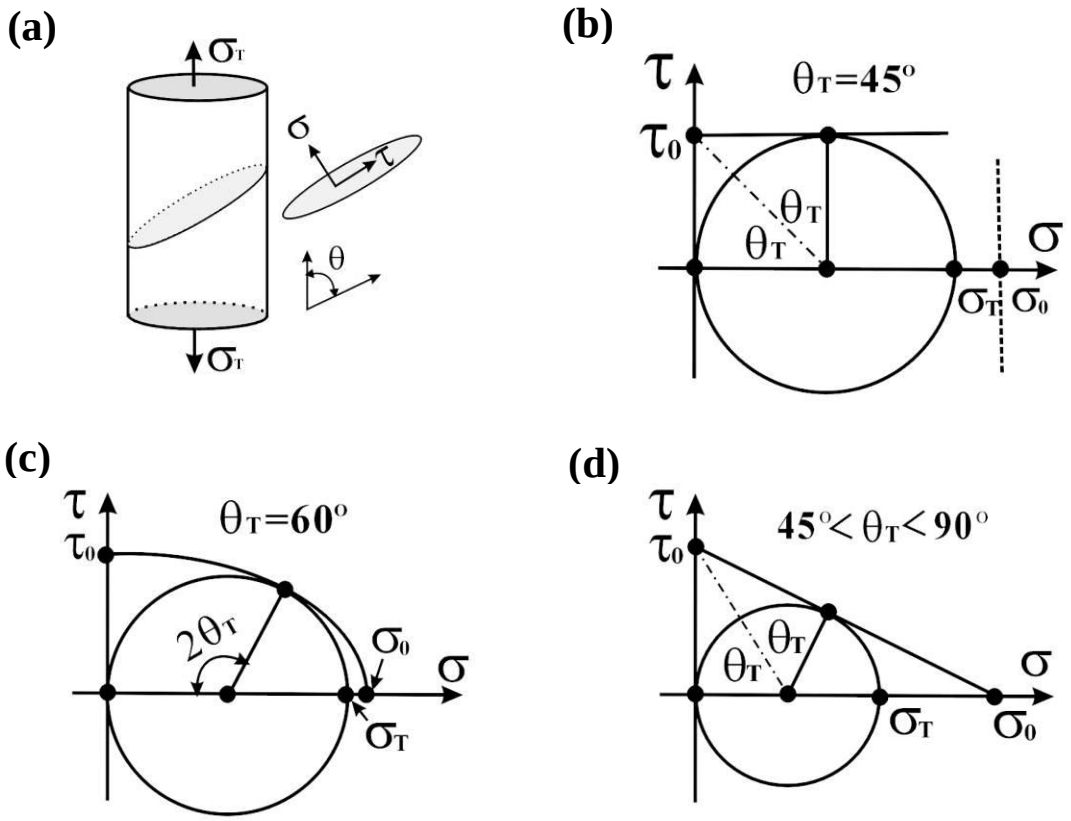

Figure 2.38 (a) Illustration of a sample under tensile test and shear plane. The tensile failure based on the (b) Tresca, (c) von Mises and (d) Mohr-Coulomb criterion [175].

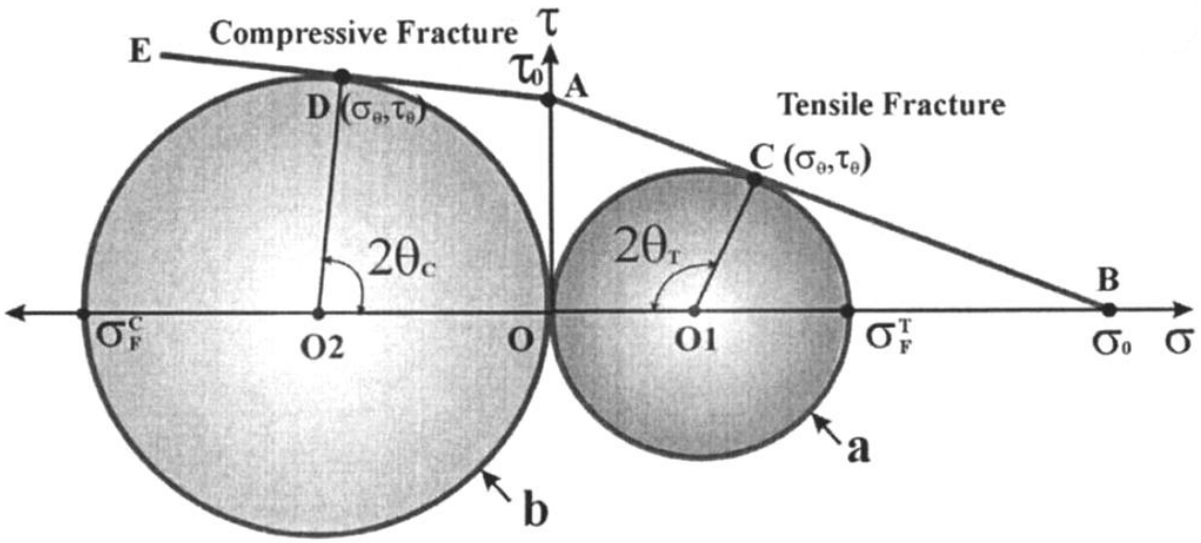

Figure 2.39 Illustration of critical fracture lines and stress distribution on the two Mohr circles in tension and compression based on the Mohr-Coulomb criterion [119].

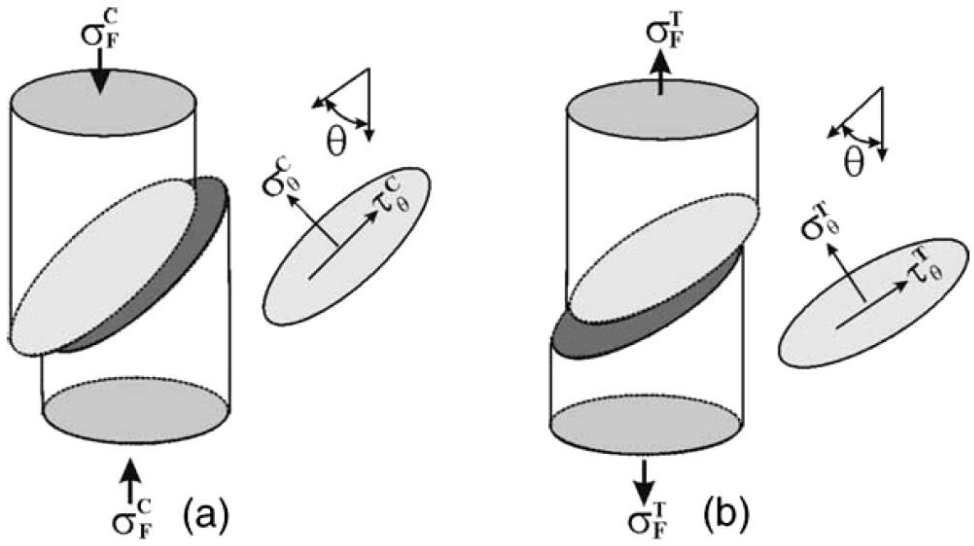

Figure 2.40 Schematic illustration of (a) compressive and (b) tensile fracture of the BMG samples [44].

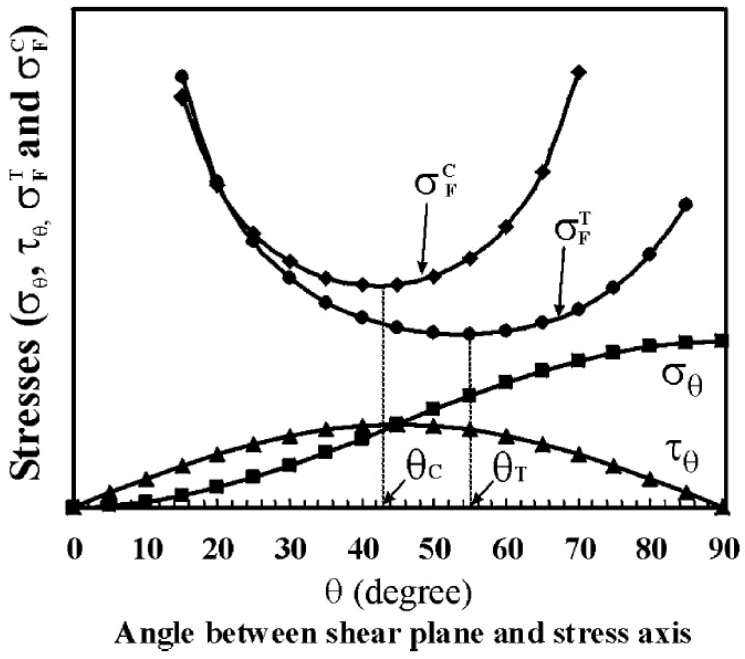

Figure 2.41 Dependence of the normal, shear and two fracture stresses on fracture plane as a function of fracture angle under tensile and compressive loading [44].

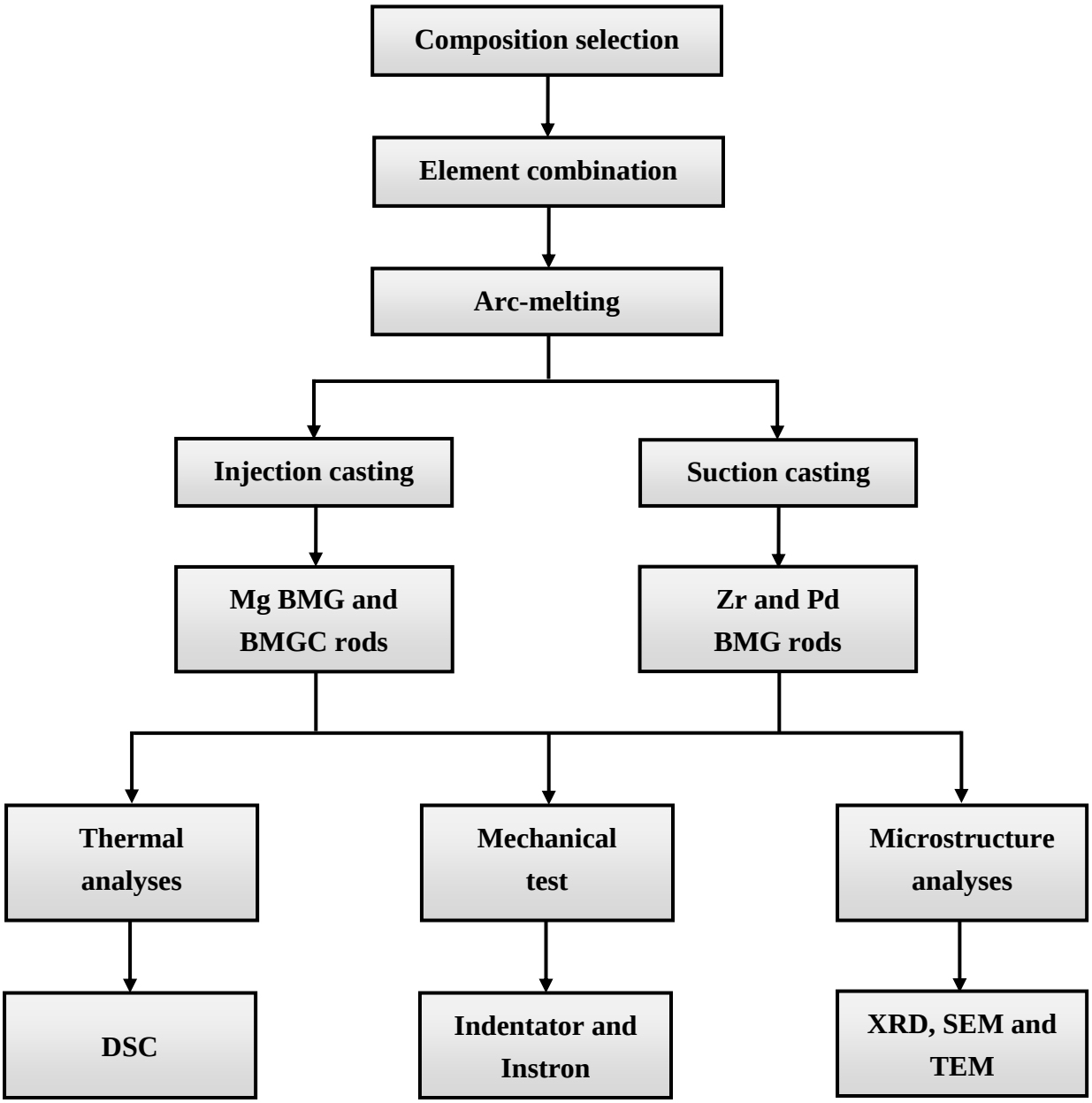

Figure 3.1 Flow chart of experimental procedures in this study.

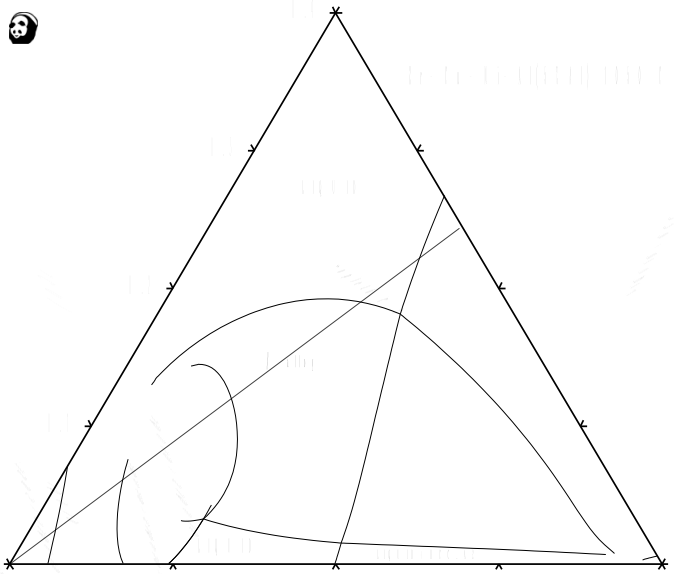

Figure 3.2 The simulated phase diagram for Zr-rich isothermal section calculated under constant 5 at% Al at 1050^{o}C, showing the selected *X* alloy within two liquid phase region and isopleth C-C marked by dotted line[35].

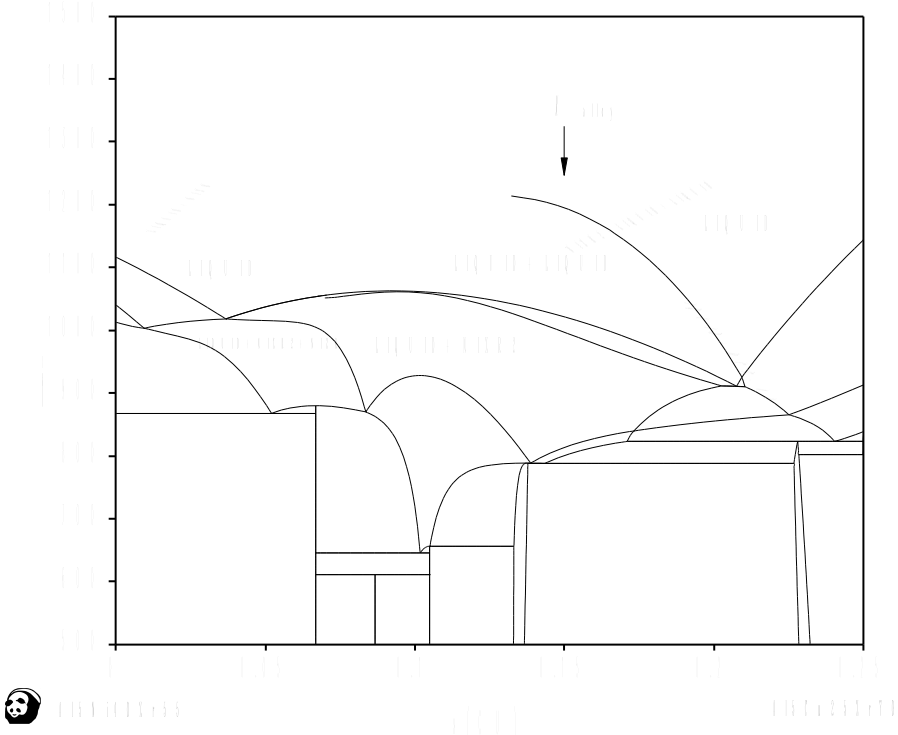

Figure 3.3 The simulated phase diagram for the temperature dependence as a function of composition between $Al_5Ni_{40}Zr_{55}$ and $Al_5Cu_{25}Zr_{70}$, obtained from the isopleth C-C [35].

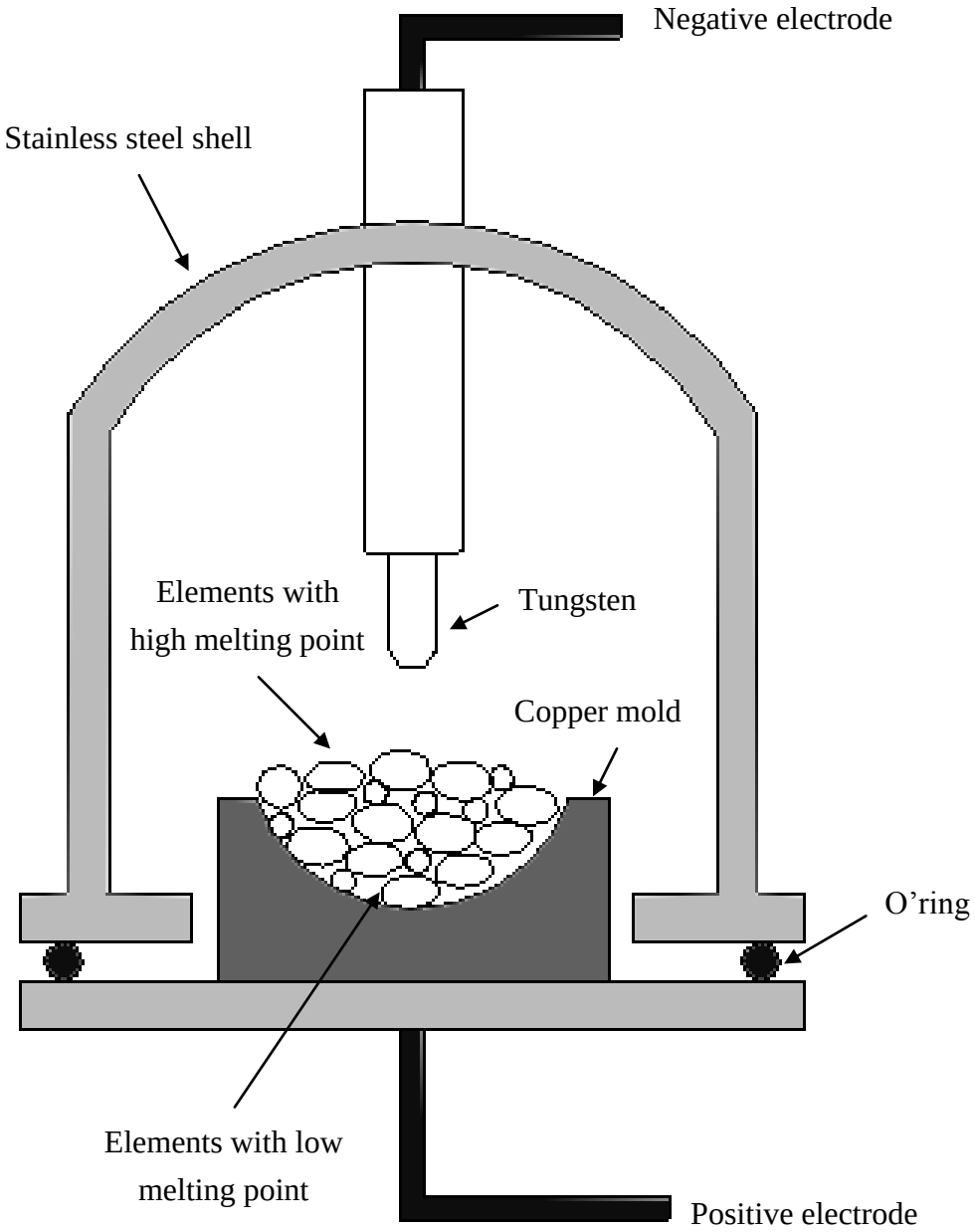

Figure 3.4 Illustration of an arc melting furnace.

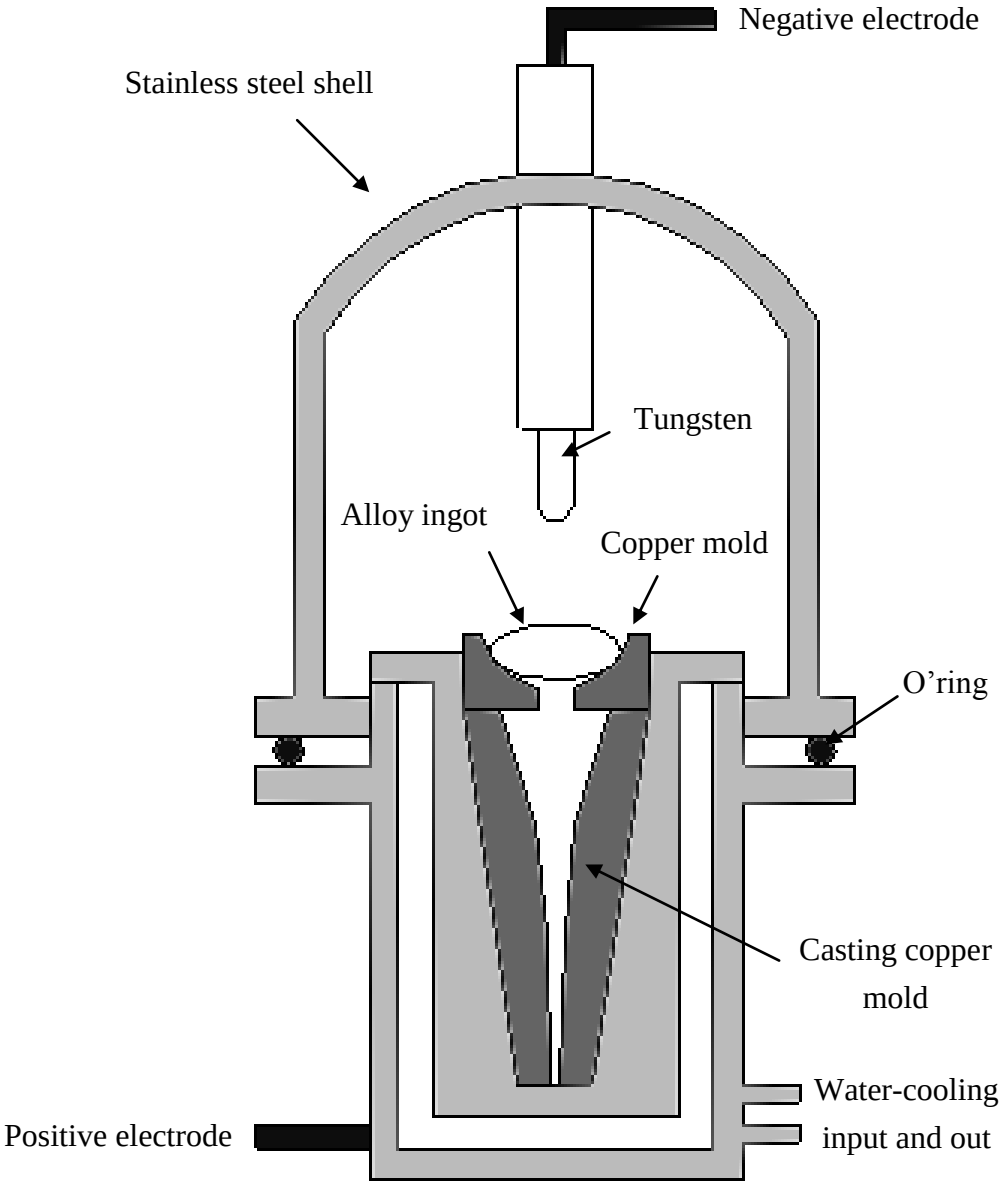

Figure 3.5 Illustration of a suction casting furnace.

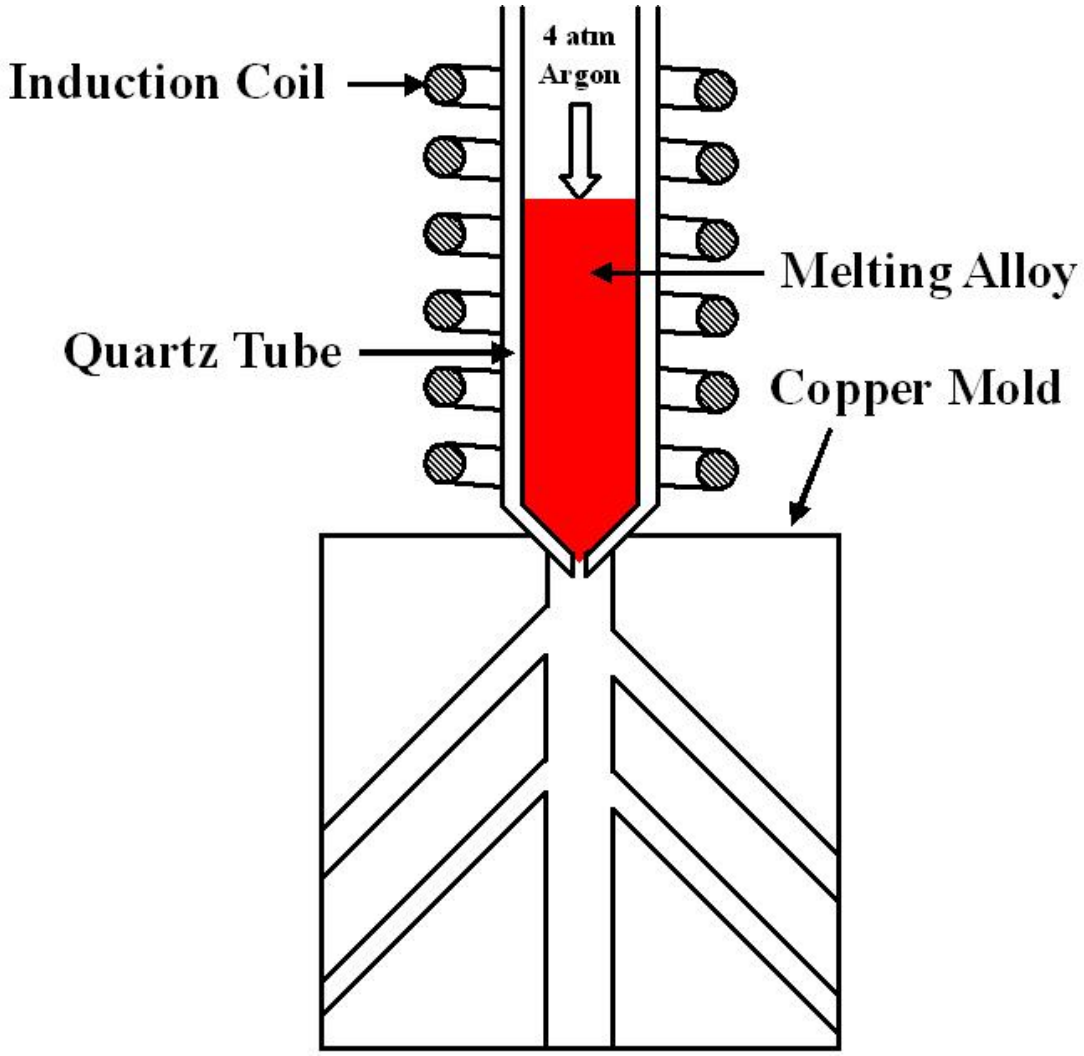

Figure 3.6 Illustration of an injection casting process [230].

Figure 3.7 Instron 5582 universal testing machine equipped with the Linear Variable Differential Transformer (LVDT) displacement transducer.

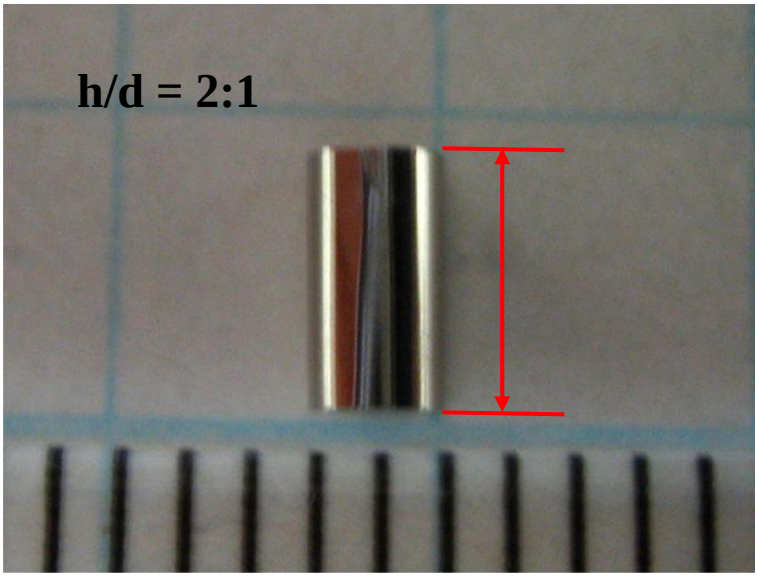

Figure 3.8 Ideal geometry of test sample for compression test in this study.

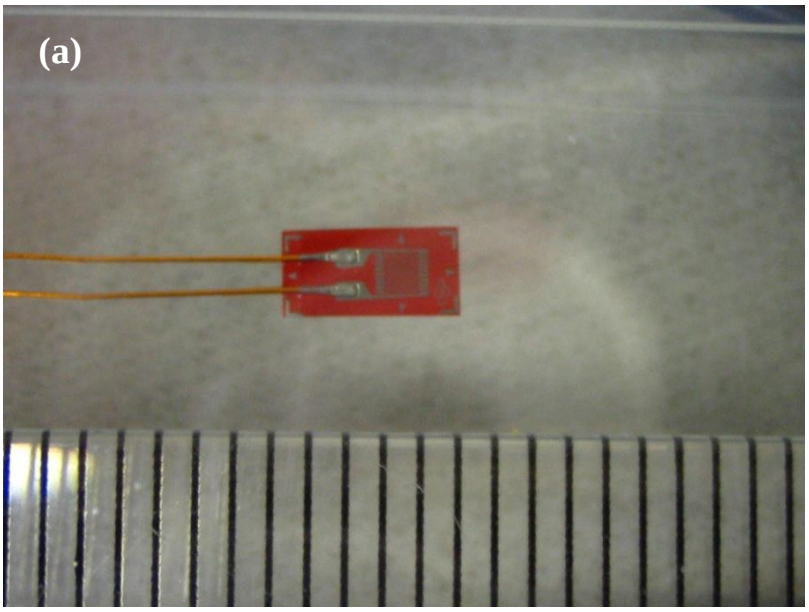

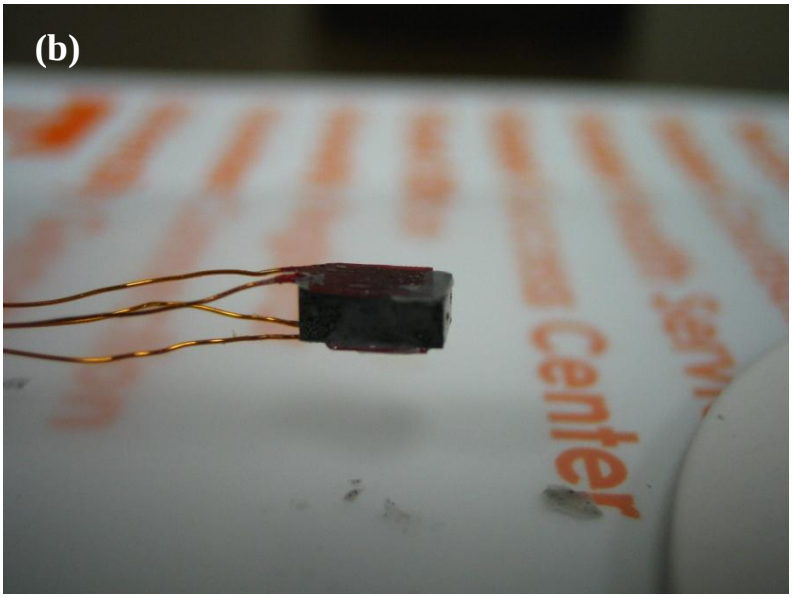

Figure 3.9 (a) Appearance of FLA strain gauge produced from Tokyo Sokki Kenkyujo Company and (b) illustration of two strain gauges directly attached to two opposite side of test sample using epoxy adhesive.

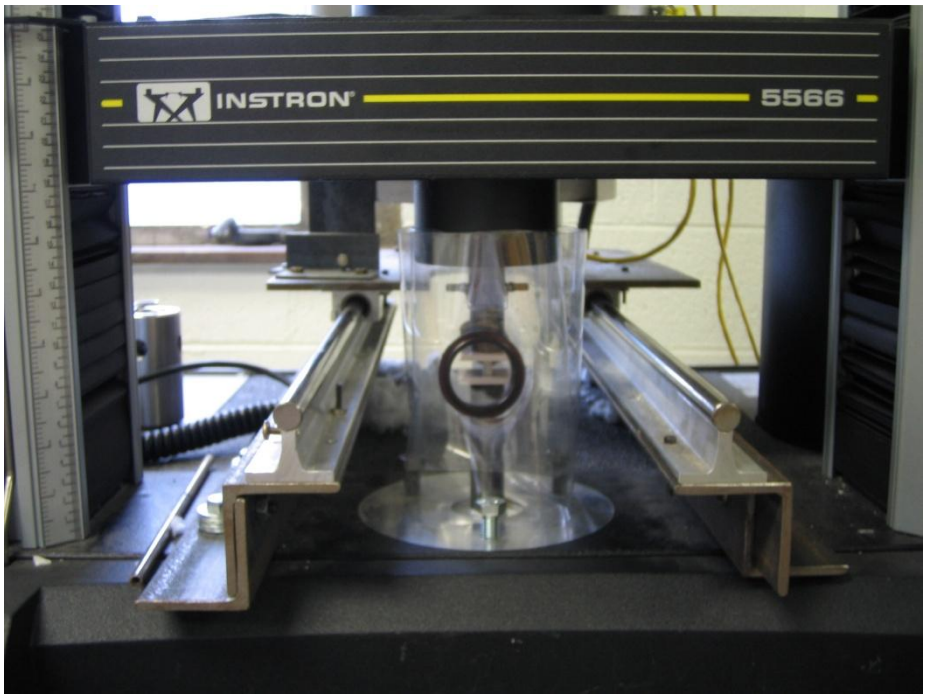

Figure 3.10 Instron 5566 universal testing machine in the University of Tennessee.

Figure 4.1 Surface appearance of the as-cast Mg-based alloy rods with various dimensions.

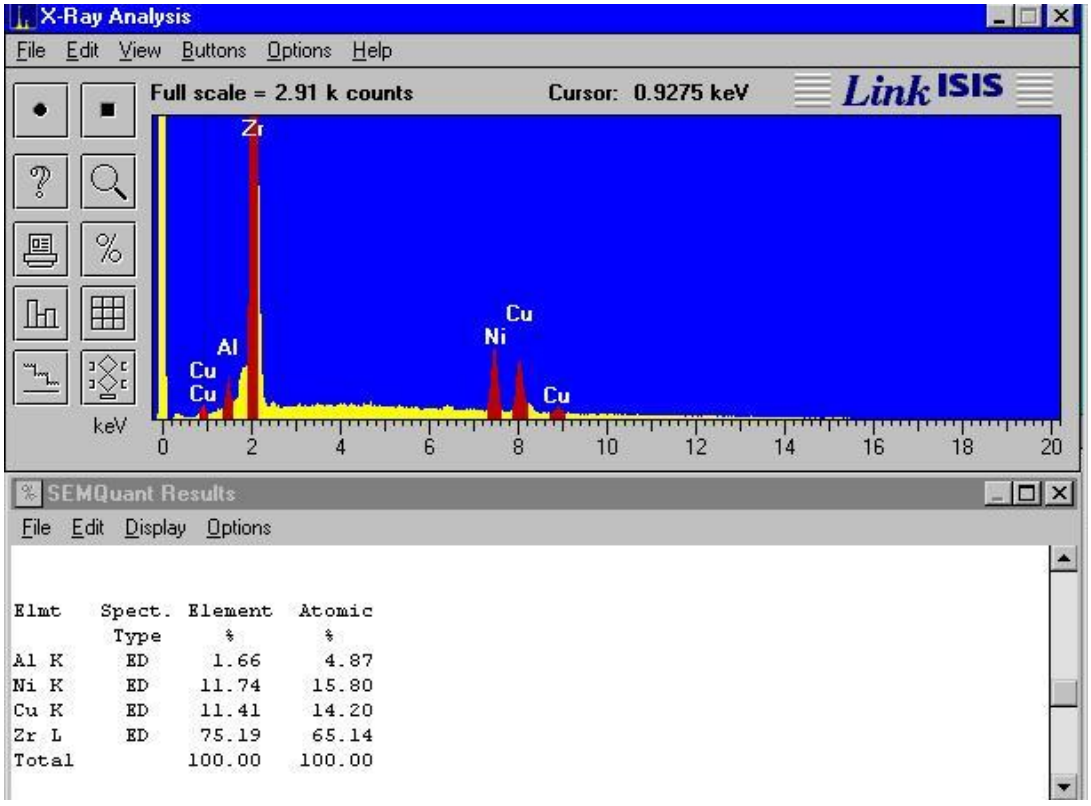

Figure 4.2 SEM/EDS result of the $Zr_{63.8}Ni_{16.2}Cu_{15}Al_5$ rod with the diameter of 2 mm.

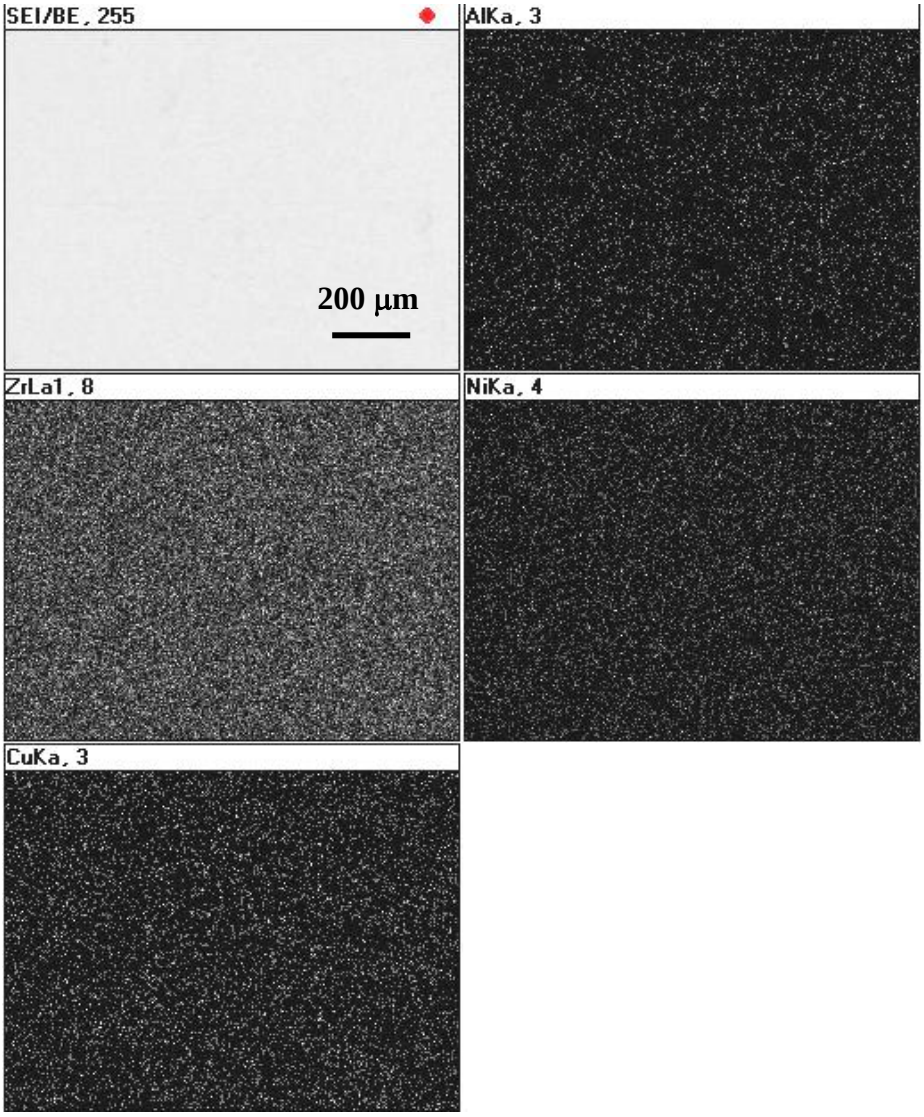

Figure 4.3 SEM morphology of the as-cast $Zr_{63.8}Ni_{16.2}Cu_{15}Al_5$ rod with the diameter of 2 mm: (a) BEI image (100X) and (b) Mapping image (100X) for Zr, Al, Cu and Ni.

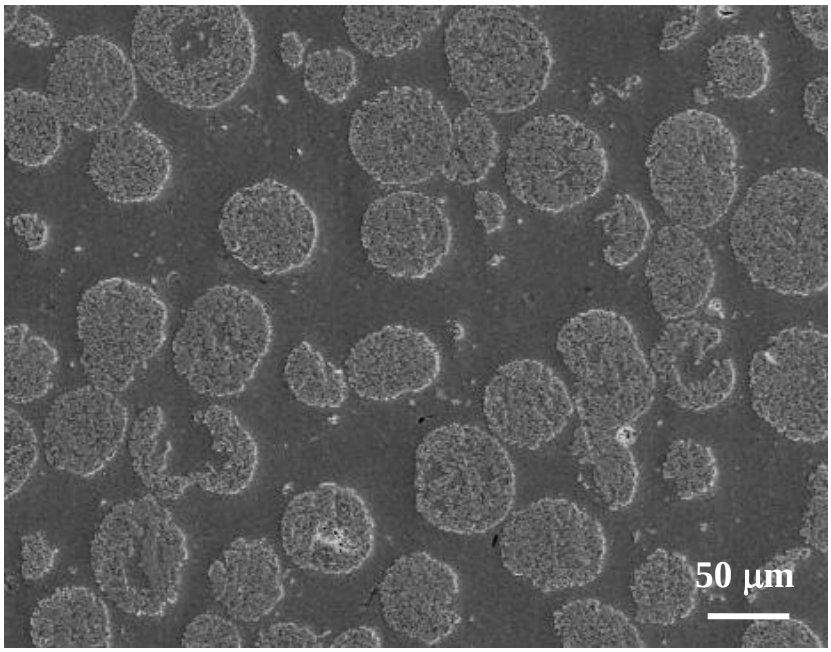

Figure 4.4 SEM observation of porous Mo particles homogeneously dispersed in the Mg-based BMG matrix.

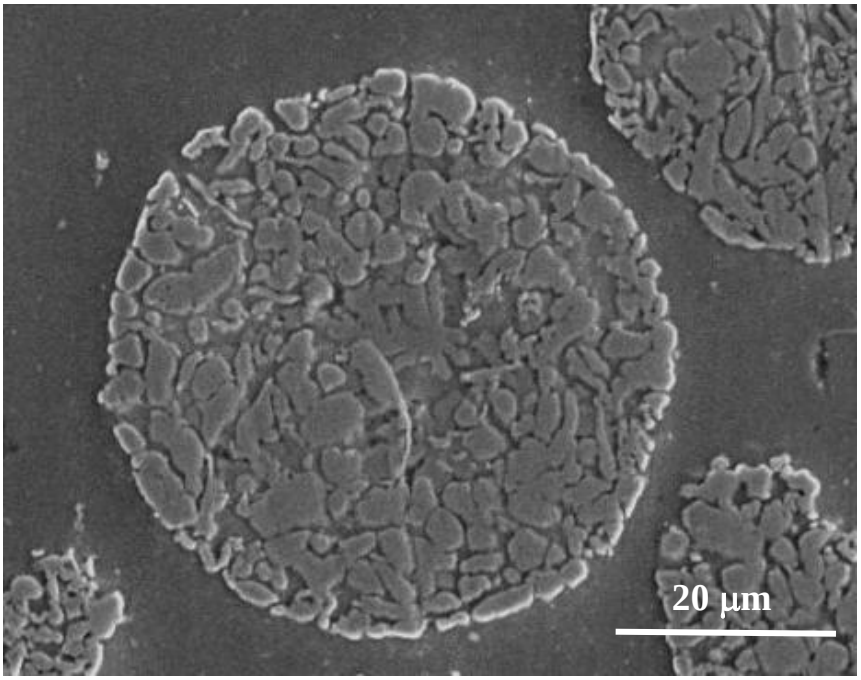

Figure 4.5 Enlarged view of single porous Mo particle with a average size of ~50 μm.

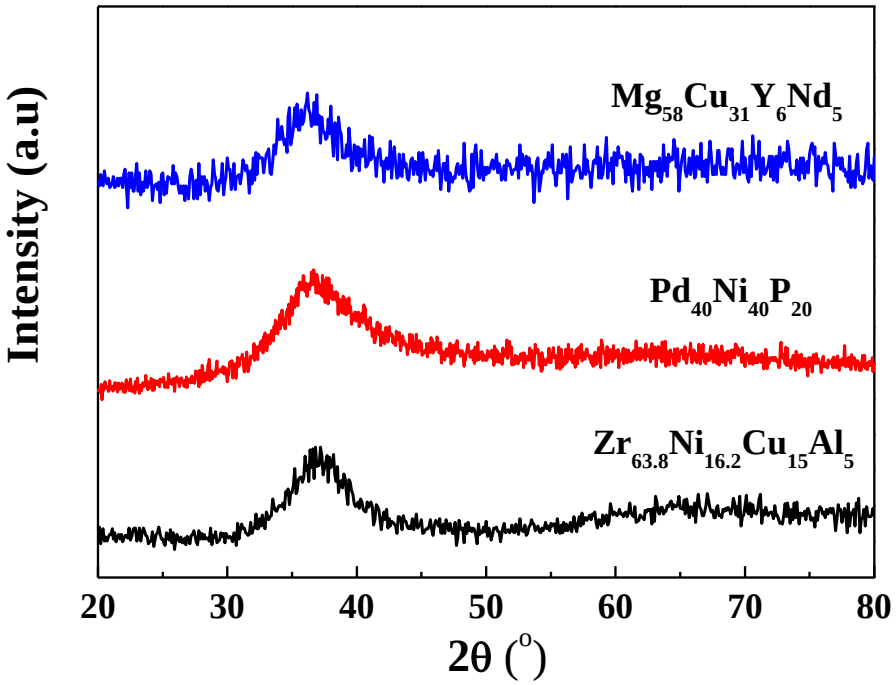

Figure 4.6 XRD pattern of the 2 mm as-cast $Zr_{63.8}Ni_{16.2}Cu_{15}Al_5$, $Pd_{40}Ni_{40}P_{20}$, and $Mg_{58}Cu_{31}Y_6Nd_5$ BMG rods.

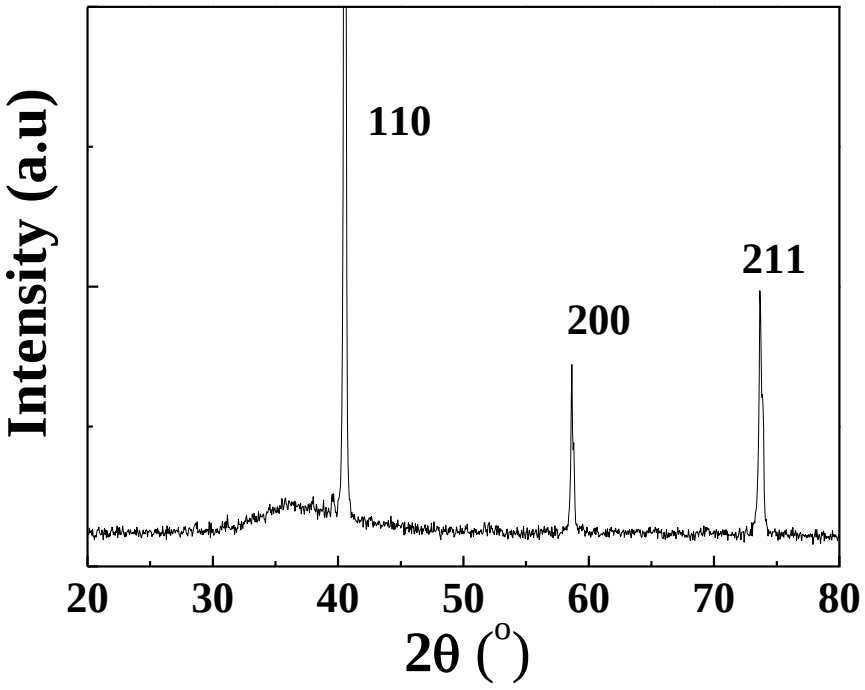

Figure 4.7 XRD pattern of the 2 mm er as-cast Mg-based BMGC rod.

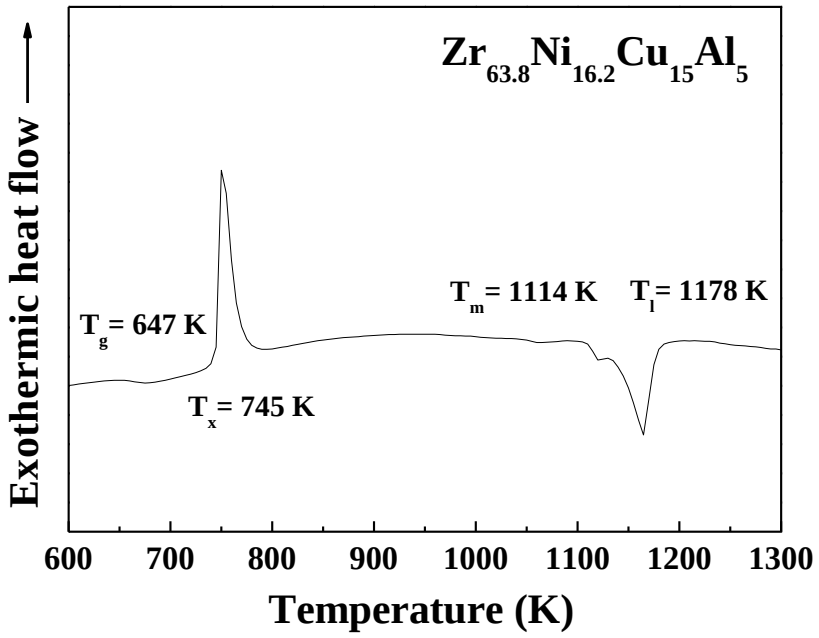

Figure 4.8 DSC thermogram obtained from the as-cast $Zr_{63.8}Ni_{16.2}Cu_{15}Al_5$ BMG with a constant heating rate of 0.33 K/s.

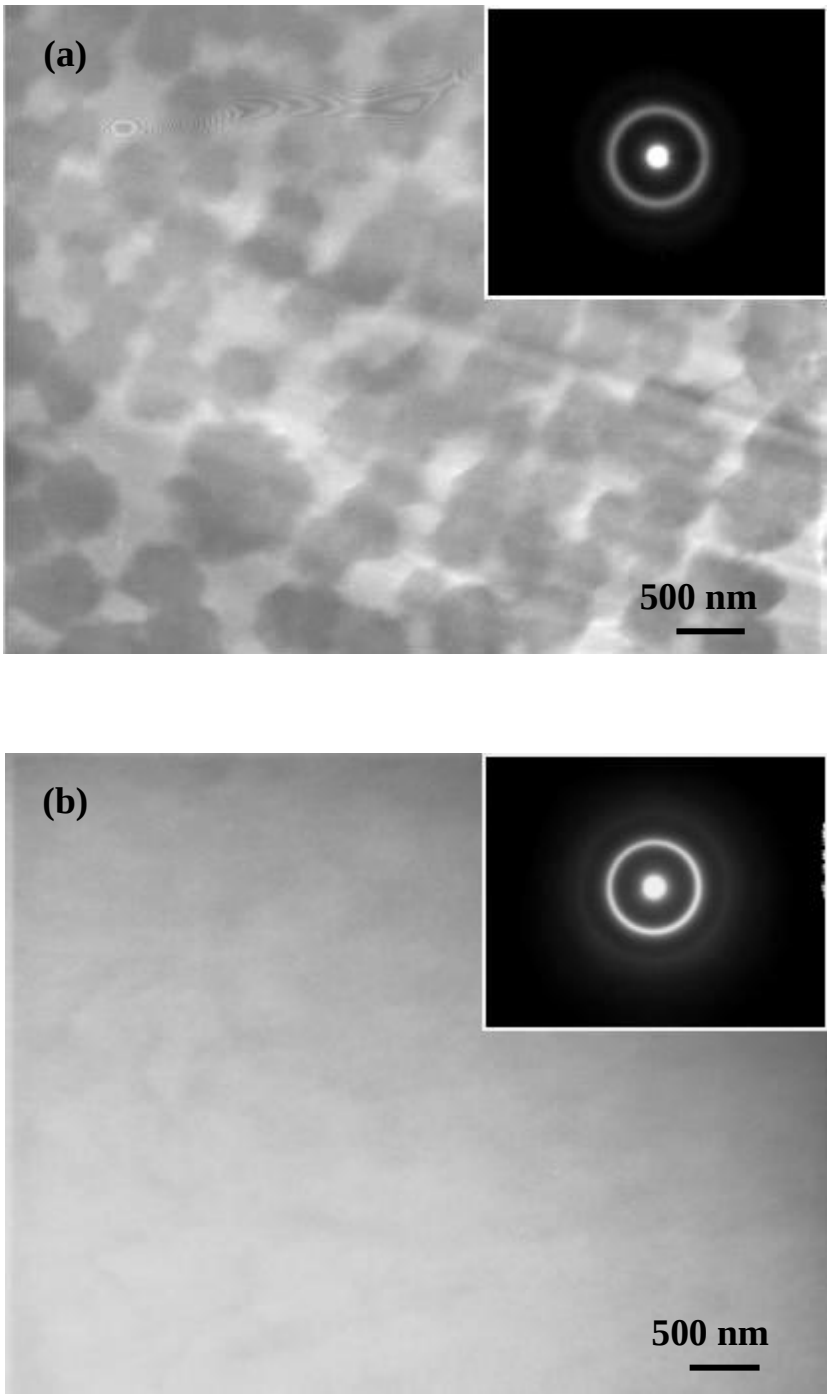

Figure 4.9 TEM bright-field image of the 2 mm as-cast $Zr_{63.8}Ni_{16.2}Cu_{15}Al_5$ BMG for different regions: (a) phase separation region and (b) glassy matrix region with no phase separation. The inserts show their corresponding selected area diffraction patterns.

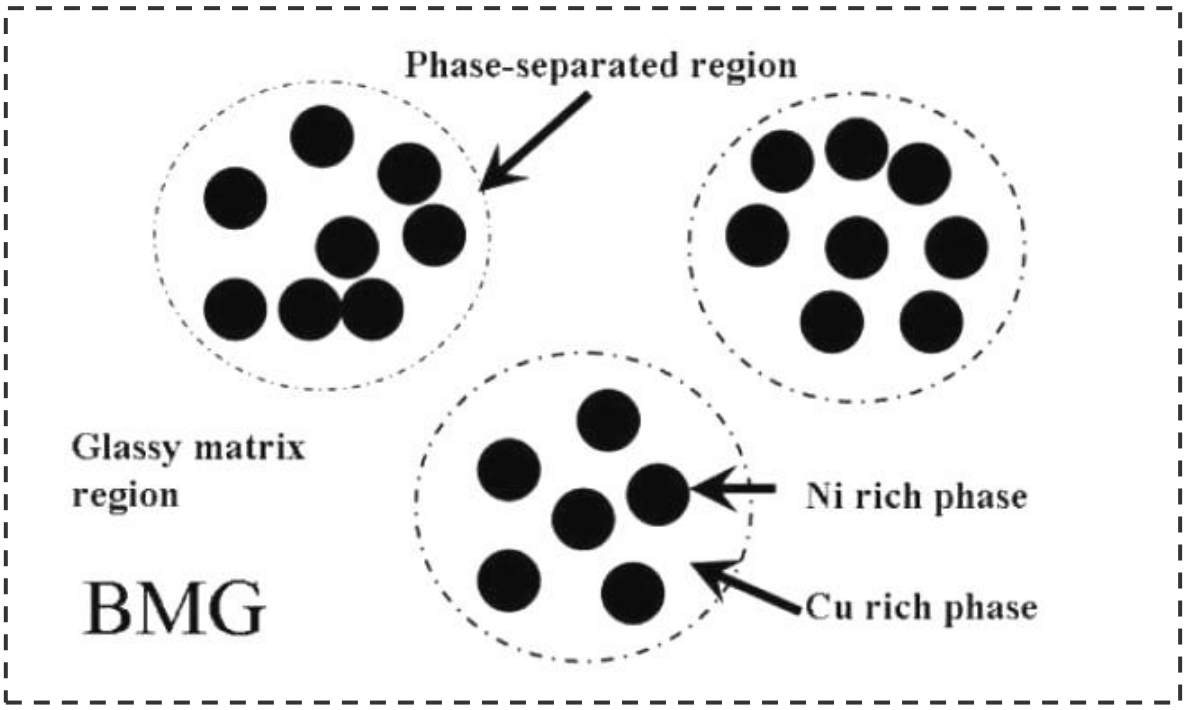

Figure 4.10 The overall microstructure of the current Zr-based BMG consisting of phase separation region (including Ni-rich and Cu-rich phases) and glassy matrix.

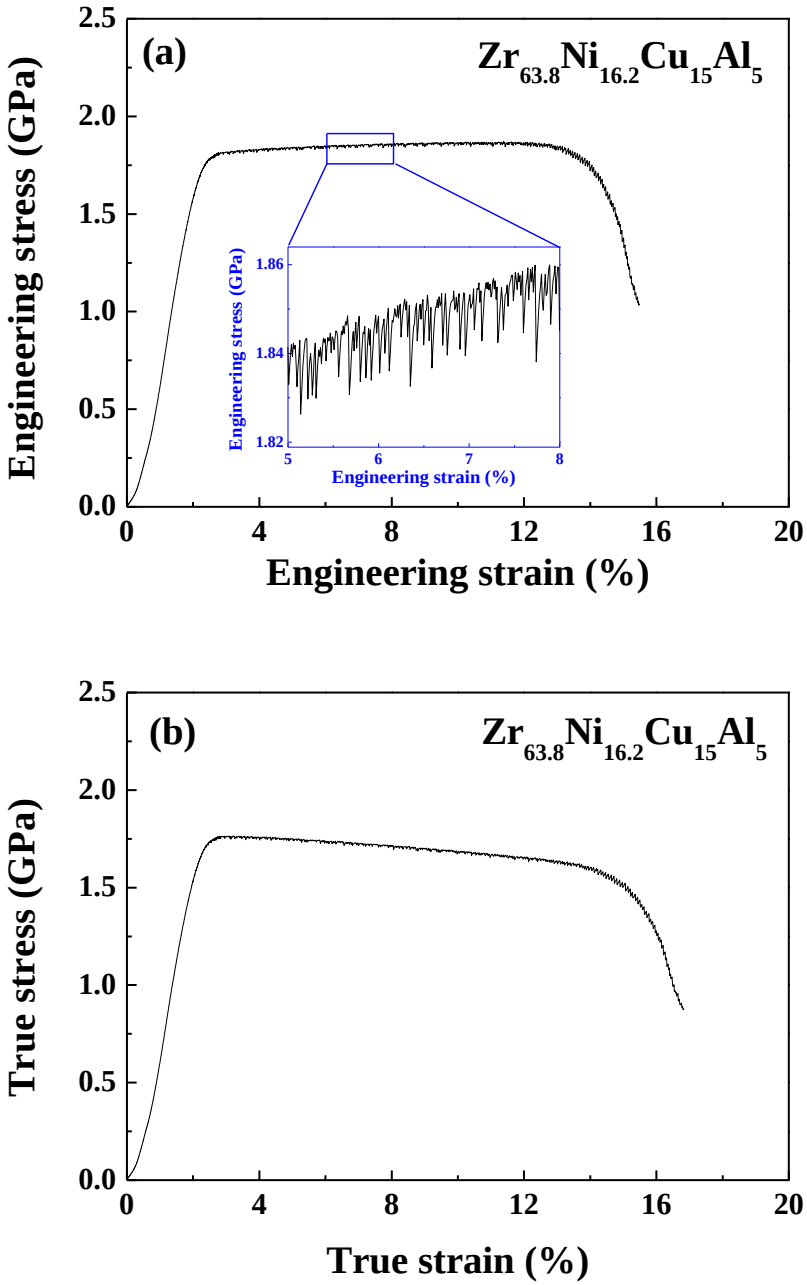

Figure 4.11 (a) Engineering and (b) true stress-strain curves obtained from the uniaxial compression test of the as-cast $Zr_{63.8}Ni_{16.2}Cu_{15}Al_5$ BMG with 2 mm in diameter at a strain rate of 1 x 10^{-4} s^{-1}. The insert shows the amplified curve at the serrated flow area of the $Zr_{63.8}Ni_{16.2}Cu_{15}Al_5$ BMG.

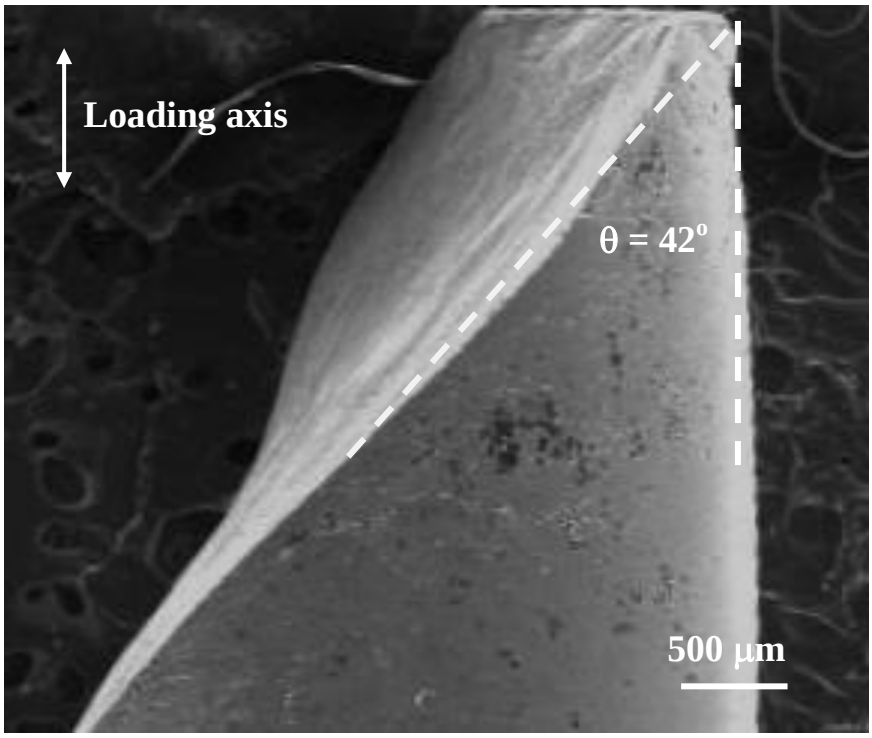

Figure 4.12 Outer appearance of the $Zr_{63.8}Ni_{16.2}Cu_{15}Al_5$ BMG with an aspect ratio of 2, showing the fracture plane and angle with respect to the loading axis.

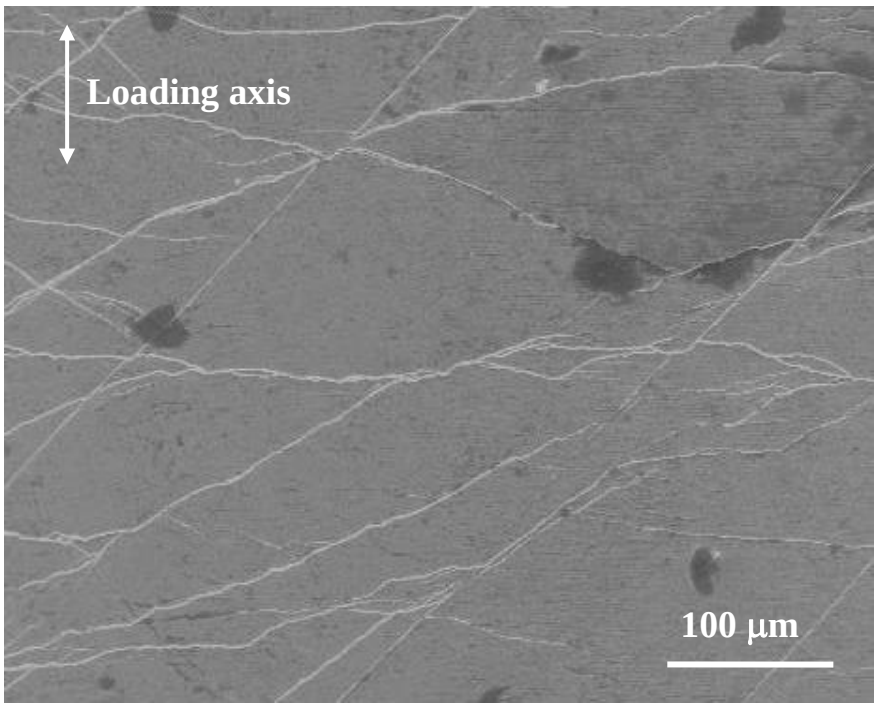

Figure 4.13 Sample surface of the $Zr_{63.8}Ni_{16.2}Cu_{15}Al_5$ BMG with an aspect ratio of 2, showing several variants of shear bands.

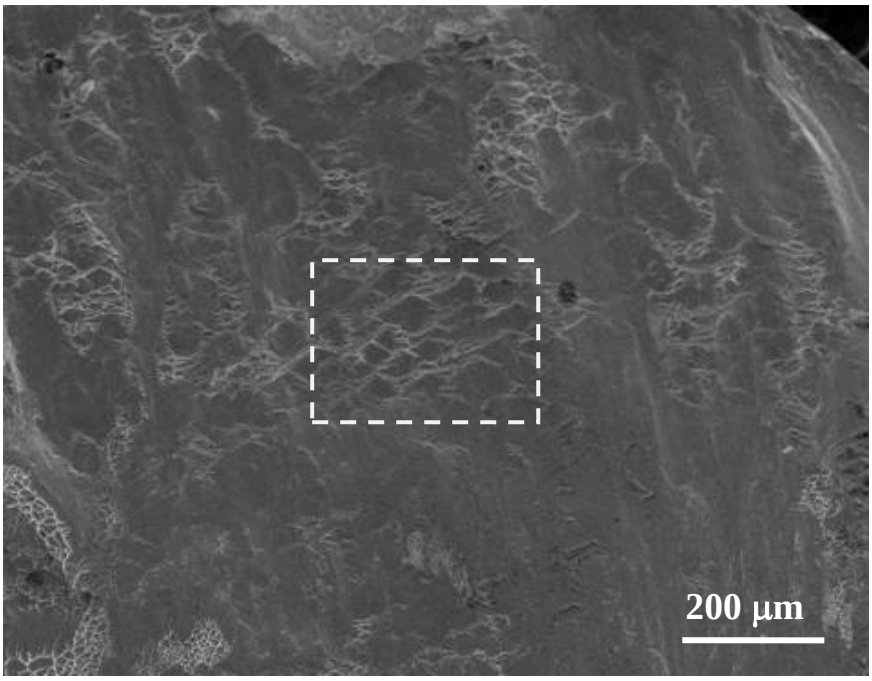

Figure 4.14 Overview on the fracture surface obtained from the $Zr_{63.8}Ni_{16.2}Cu_{15}Al_5$ BMG with an aspect ratio of 2.

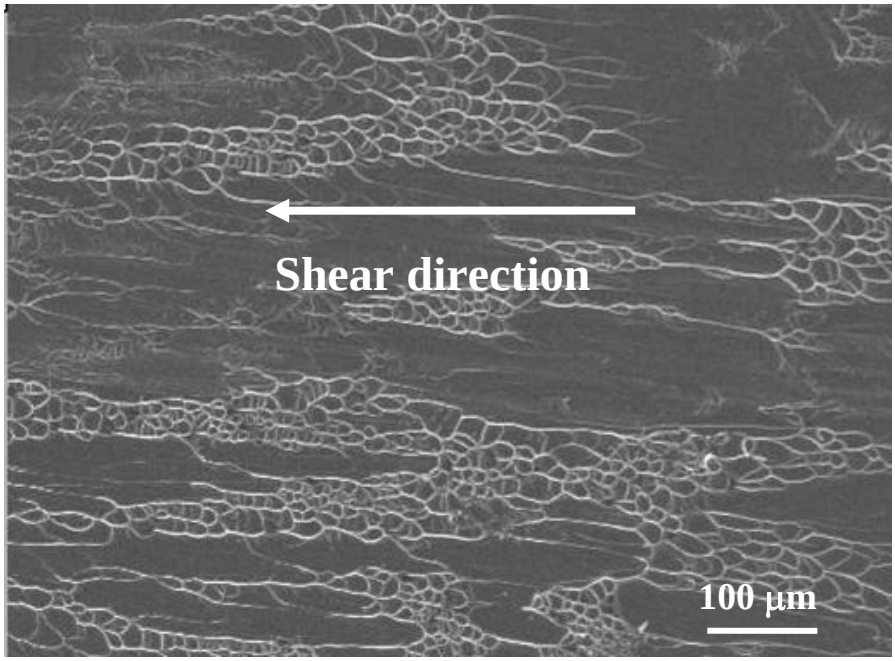

Figure 4.15 Fracture surface of the $Zr_{63.8}Ni_{16.2}Cu_{15}Al_5$ BMG with an aspect ratio of 2, showing the vein-like patterns and shear direction.

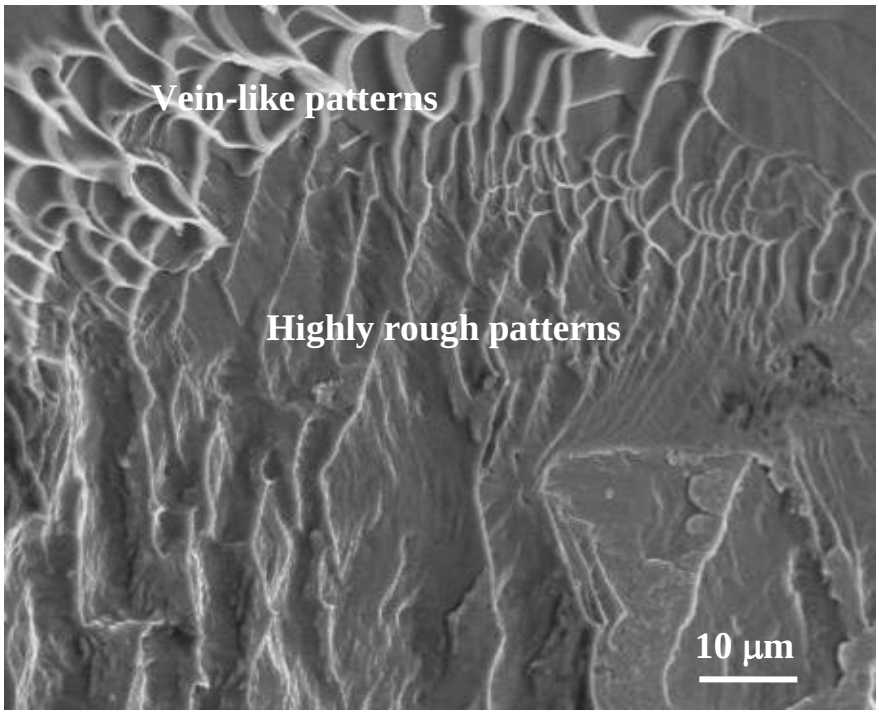

Figure 4.16 Fracture surface of the $Zr_{63.8}Ni_{16.2}Cu_{15}Al_5$ BMG with an aspect ratio of 2, showing the vein-like patterns on the top and rough patterns in the center.

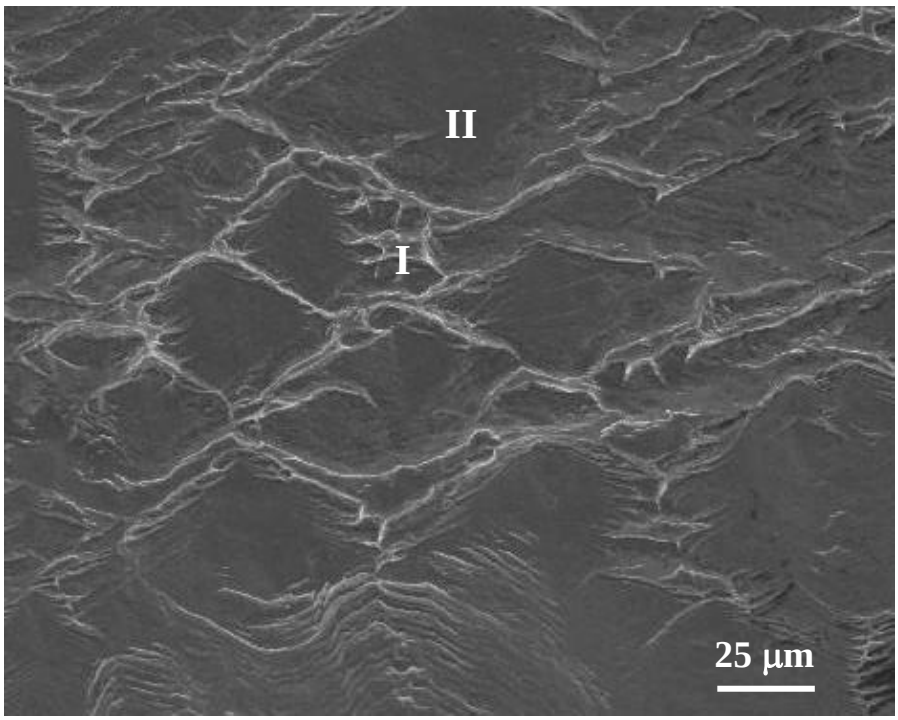

Figure 4.17 Fracture surface of the $Zr_{63.8}Ni_{16.2}Cu_{15}Al_5$ BMG with an aspect ratio of 2, showing the shear-banding patterns taken from the square marked in Figure 4.10.

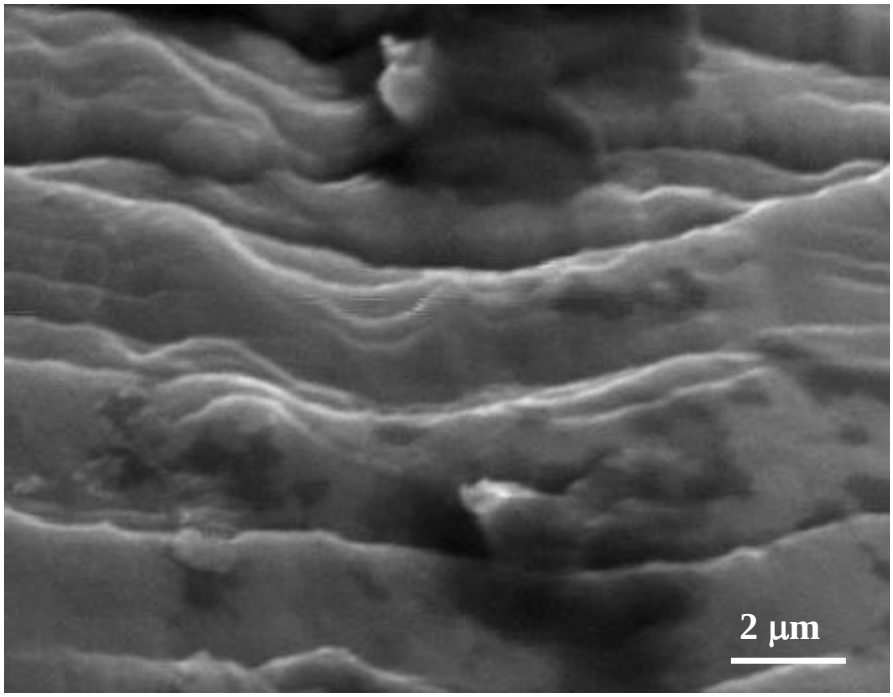

Figure 4.18 Fracture surface of the $Zr_{63.8}Ni_{16.2}Cu_{15}Al_5$ BMG with an aspect ratio of 2, showing the shear banding in region I of Figure 4.13.

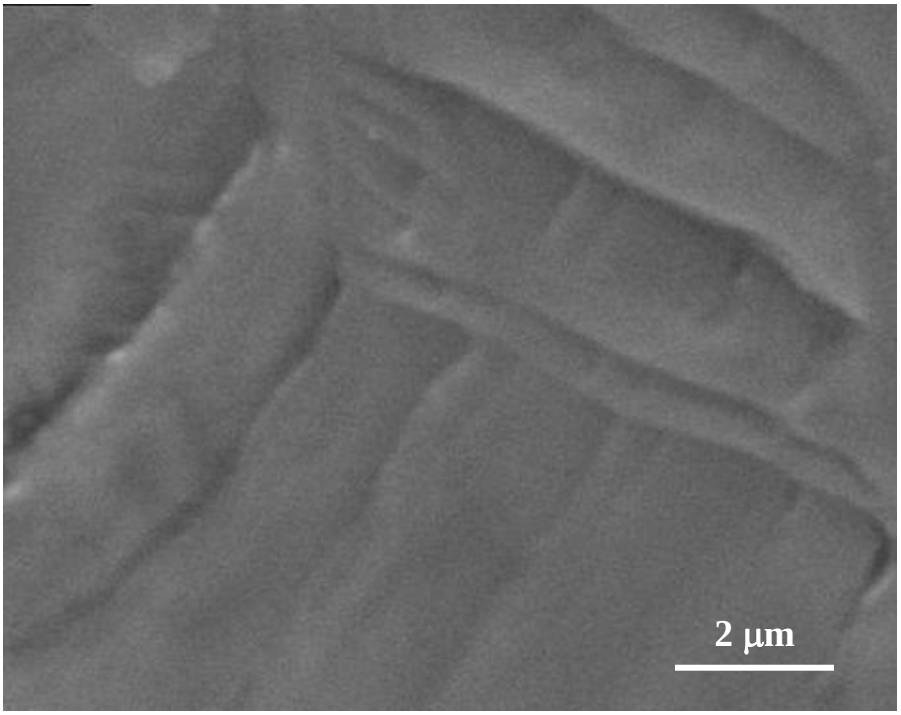

Figure 4.19 Fracture surface of the $Zr_{63.8}Ni_{16.2}Cu_{15}Al_5$ BMG with an aspect ratio of 2, showing the shear banding in region II of Figure 4.13.

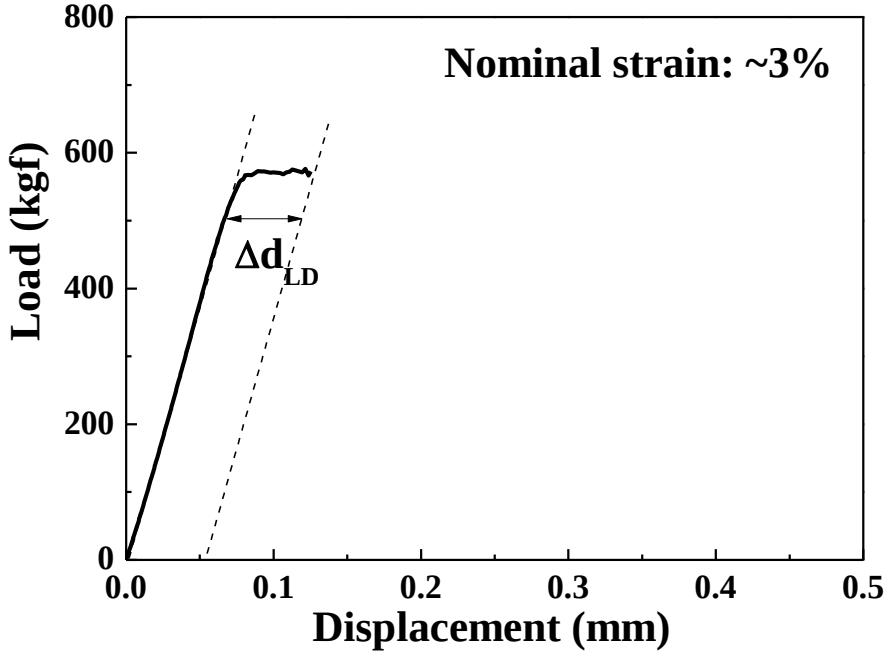

Figure 4.20 Representative load-displacement curve of the $Zr_{63.8}Ni_{16.2}Cu_{15}Al_5$ BMG Sample compressed to a nominal total strain of ~3%.

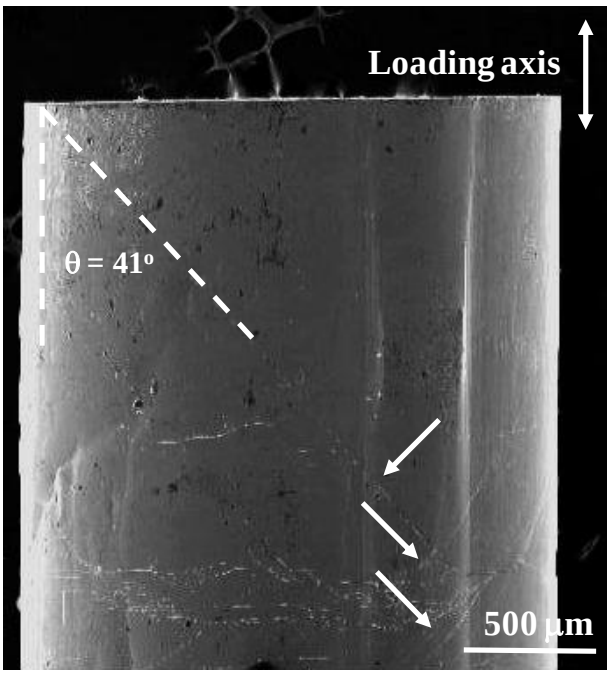

Figure 4.21 SEM observations for the deformed $Zr_{63.8}Ni_{16.2}Cu_{15}Al_5$ BMG with the nominal strain of ~3%, showing the intact appearance with the major shear-band direction and secondary directions.

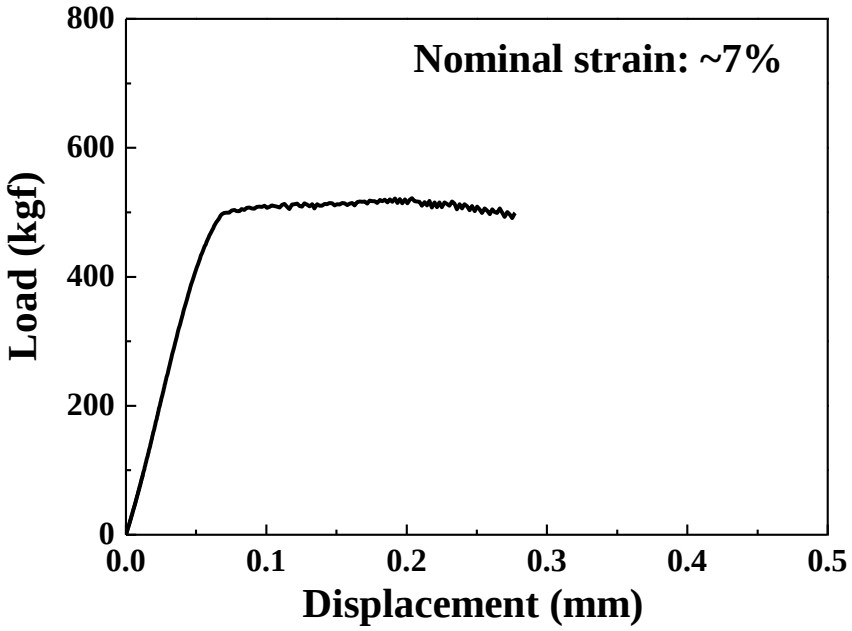

Figure 4.22 Representative load-displacement curve of the $Zr_{63.8}Ni_{16.2}Cu_{15}Al_5$ BMG Sample compressed to a nominal total strain of ~7%.

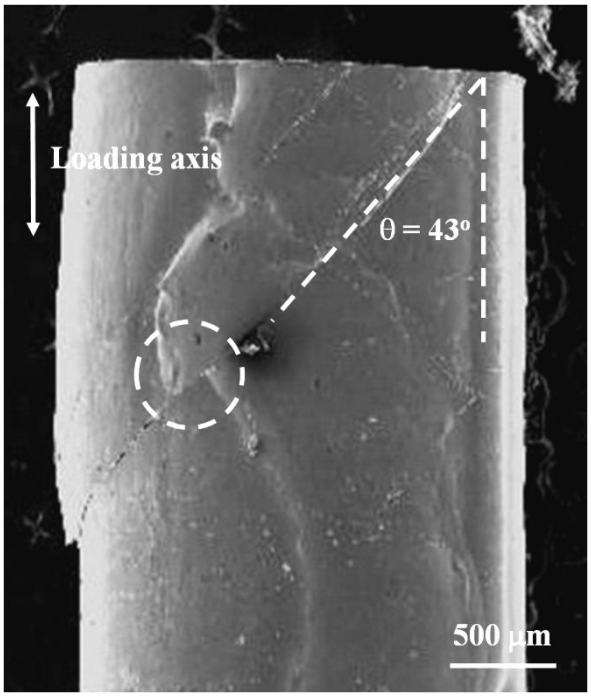

Figure 4.23 SEM observations for the deformed $Zr_{63.8}Ni_{16.2}Cu_{15}Al_5$ BMG with the nominal strain of ~7%, showing the principal shear along the shear plane and resultant offset displacement marked by circle.

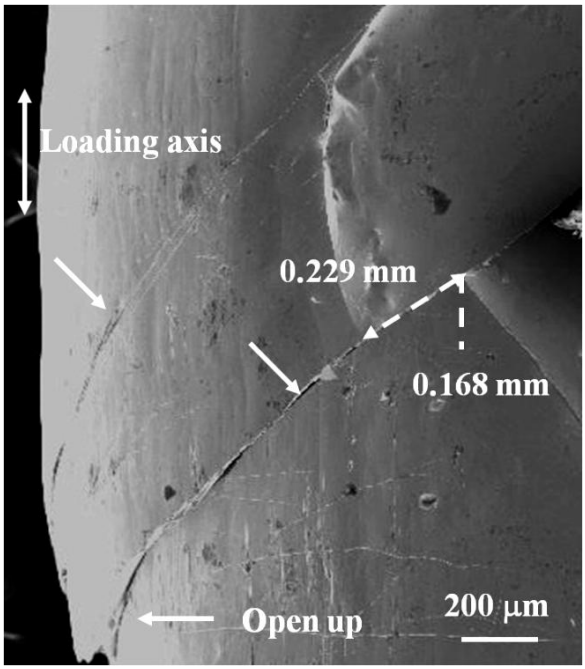

Figure 4.24 Enlarged SEM image of the deformed $Zr_{63.8}Ni_{16.2}Cu_{15}Al_5$ BMG with the nominal strain of ~7%, showing the offset displacement along the shear plane.

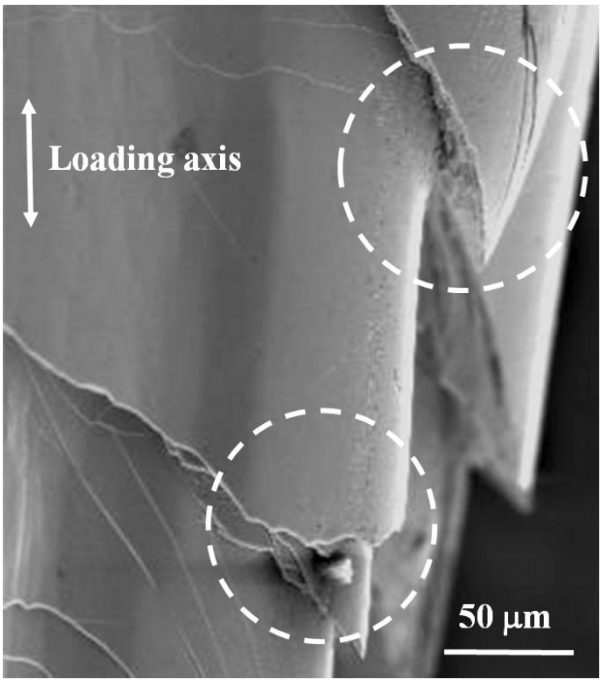

Figure 4.25 SEM image of the opposite side of Figure 4.20, showing multiple shear events as marked by circles.

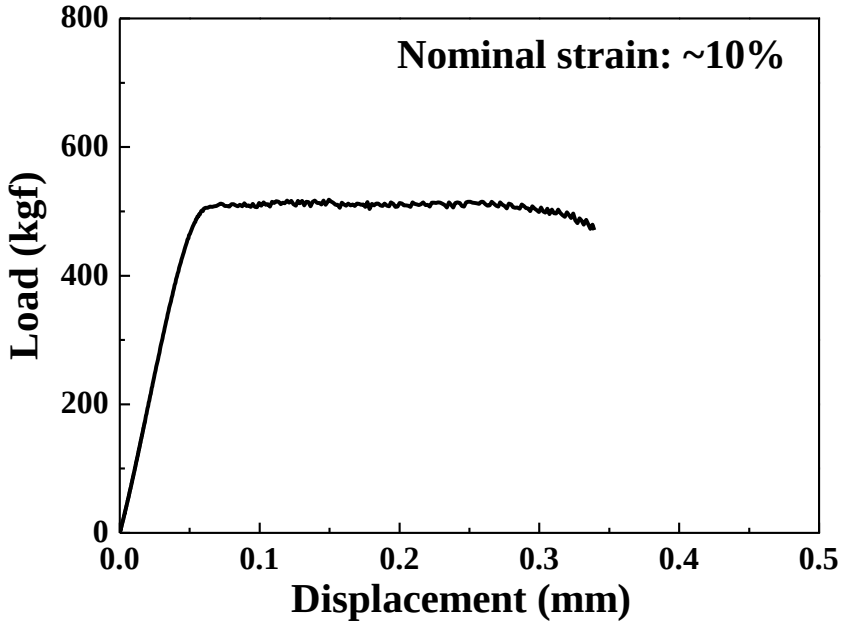

Figure 4.26 Representative load-displacement curve of the $Zr_{63.8}Ni_{16.2}Cu_{15}Al_5$ BMG Sample compressed to a nominal total strain of ~10%.

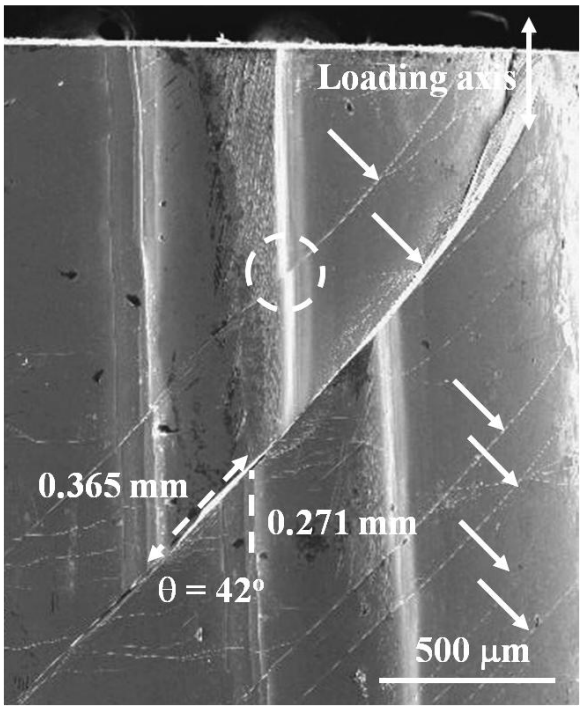

Figure 4.27 SEM observations for the deformed $Zr_{63.8}Ni_{16.2}Cu_{15}Al_5$ BMG with the nominal strain of ~10%, showing parallel multiple shear bands. The major and minor offset displacements are marked.

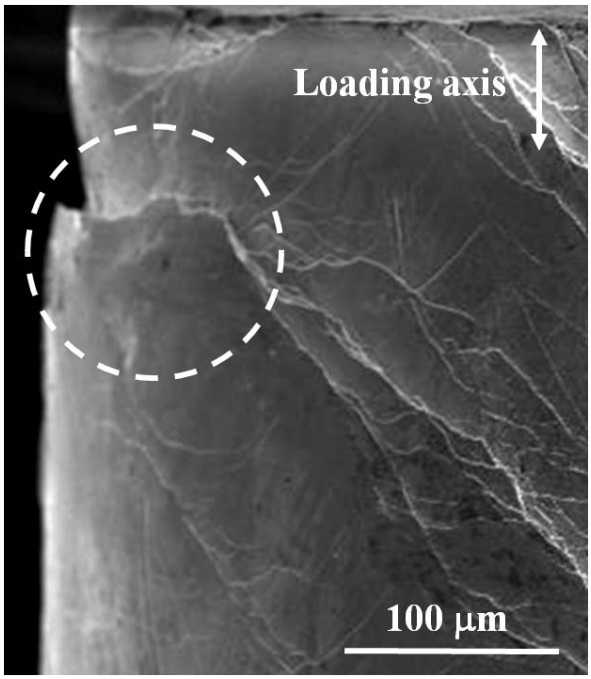

Figure 4.28 SEM image of the opposite side of Figure 4.24, showing significant offset displacement associated with the principal shear band.

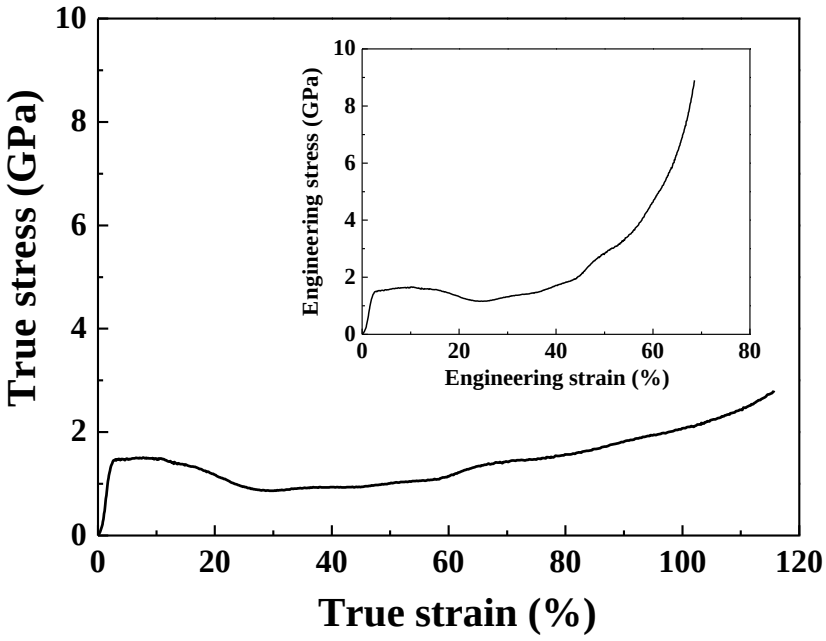

Figure 4.29 Room-temperature compressive stress-strain curves of the as-cast $Zr_{63.8}Ni_{16.2}Cu_{15}Al_5$ sample, showing the nominal "superplastic-like" behavior. Sample compressed to an "apparent" 70% engineering strain or ~120% true strain.

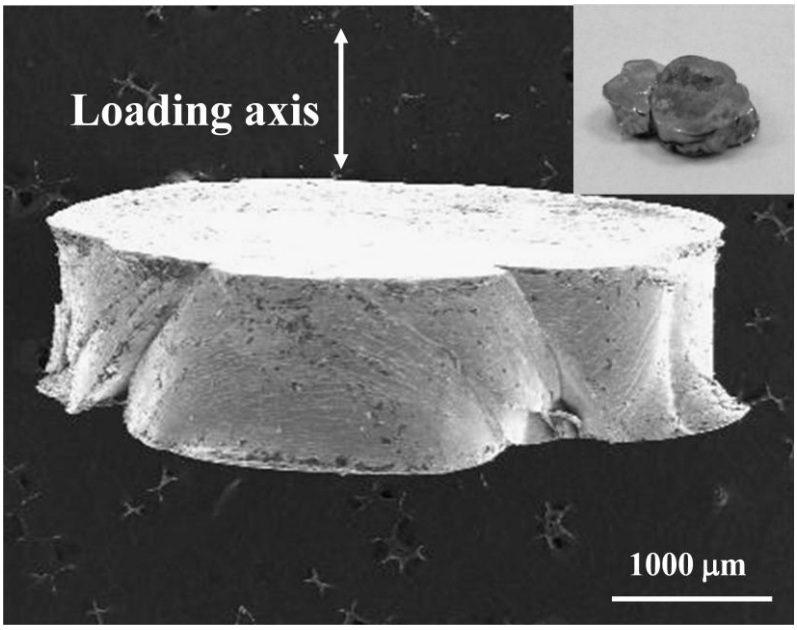

Figure 4.30 Top and side views of the deformed $Zr_{63.8}Ni_{16.2}Cu_{15}Al_5$ sample, showing the welding of the two halves of the sheared sample.

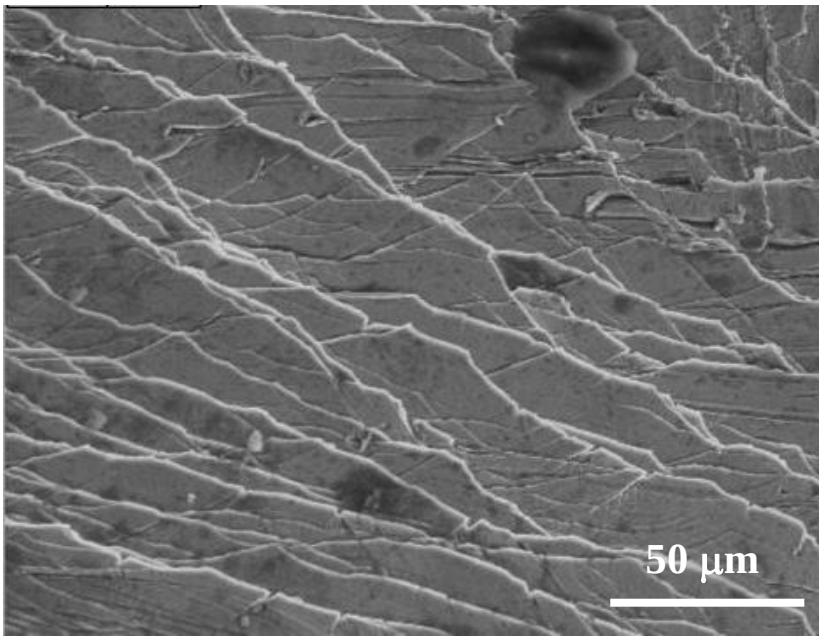

Figure 4.31 Enlarged SEM image of the sample surface of the deofrmed $Zr_{63.8}Ni_{16.2}Cu_{15}Al_5$ sample, showing the presence of intense and numerous shear bands.

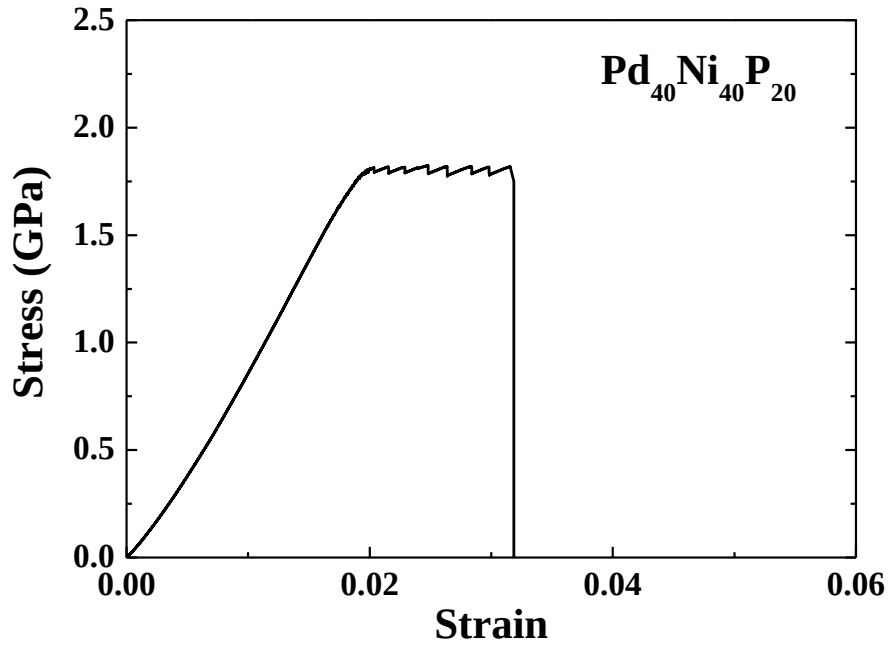

Figure 4.32 Engineering compressive stress-strain curve of the monolithic $Pd_{40}Ni_{40}P_{20}$ BMG at a nominal initial strain rate of 1 x 10^{-4} s^{-1}.

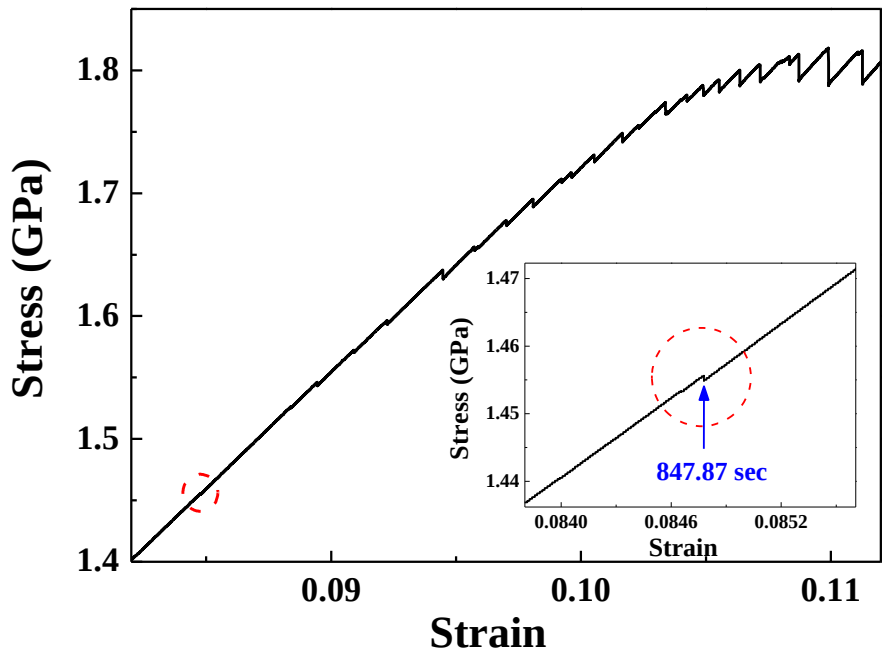

Figure 4.33 Serration region before yielding obtained from the $Pd_{40}Ni_{40}P_{20}$ BMG. The inset shows the enlarged view of first observation on load drop at 847.87 s.

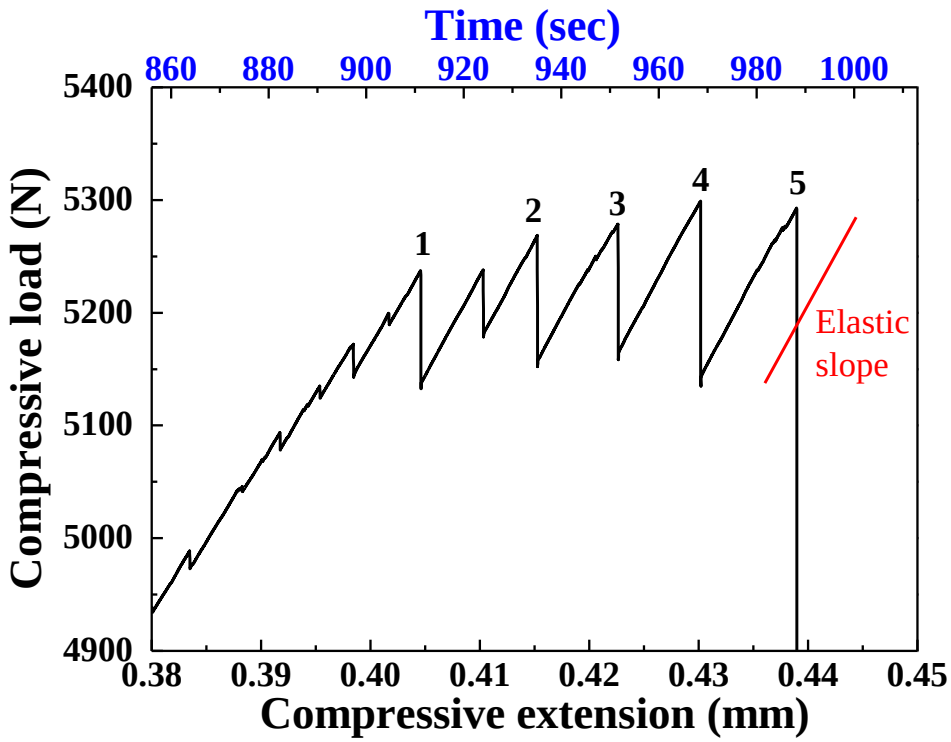

Figure 4.34 Dependence of the compressive load as a function of displacement and time for the Pd-based BMG sample, showing 5 notable serrations in the plastic region.

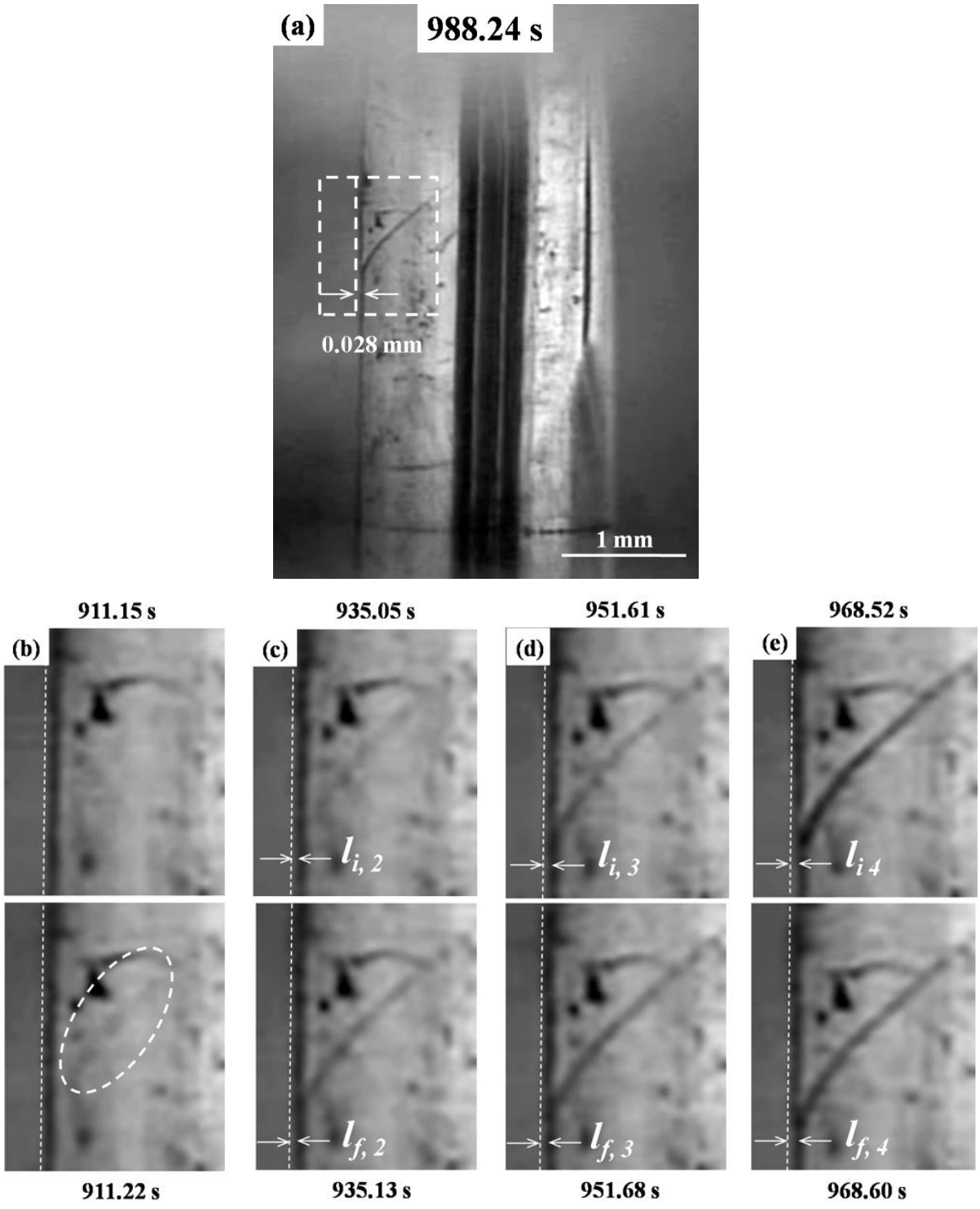

Figure 4.35 In-situ image of the Pd-based BMG sample at four shear events and their corresponding time at which serrations occur: (a) the final image at serration #5 (time = 988.24 s); (b), (c), (d) and (e) are the initial (upper) and final (lower) images at serration #1, 2, 3 and 4, respectively. In the legend, *l* represents the horizontal relative position of the upper part and lower part of the sample. The subscripts, *i* and *f*, mean the initial and final images at a principal shear event, namely, images before and after an intermittent sliding. The second subscript is the number of the captured serration.

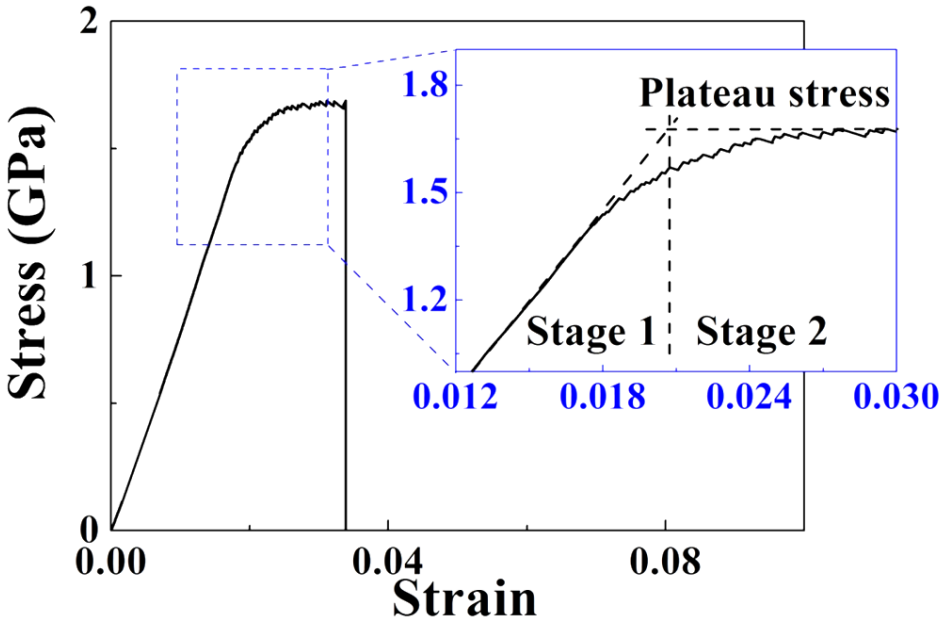

Figure 4.36 Typical engineering stress-strain curve of the $Pd_{40}Ni_{40}P_{20}$ BMG at a nominal strain rate of 2 x 10^{-4} s^{-1} in compression. The insert shows the separation of two stages.

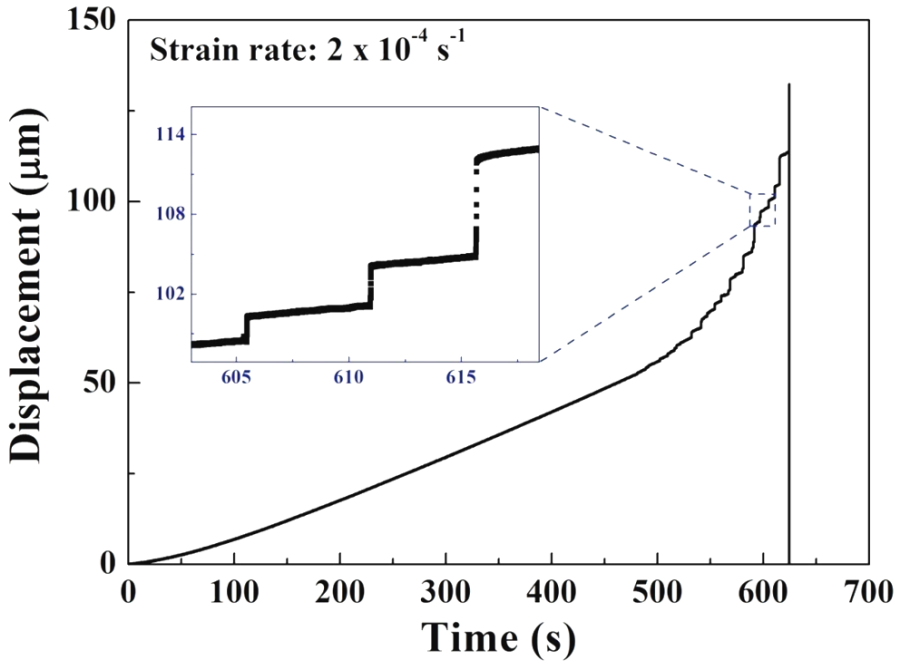

Figure 4.37 Dependence of displacement as a function of time taken from the record of strain gauges. The insert shows the enlarged view of the displacement burst.

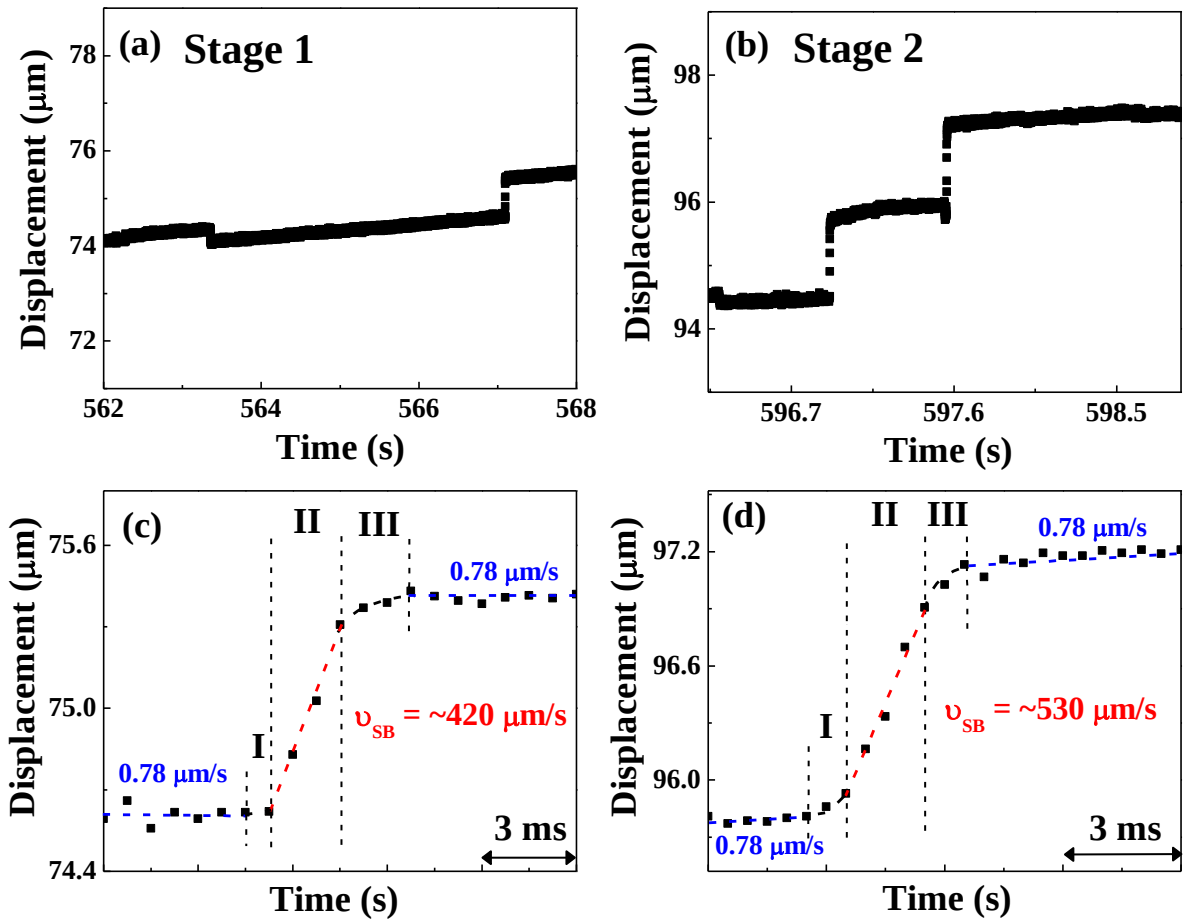

Figure 4.38 Displacement as a function of time in serrated region obtained from the $Pd_{40}Ni_{40}P_{20}$ BMG at a strain rate of 2 x 10^{-4} s^{-1}: (a) Stage 1; (b) Stage 2; (c) and (d) show typical serration profiles in (a) and (b). υ_{SB} denotes the steady-state speed of shear band propagation on the shear plane.

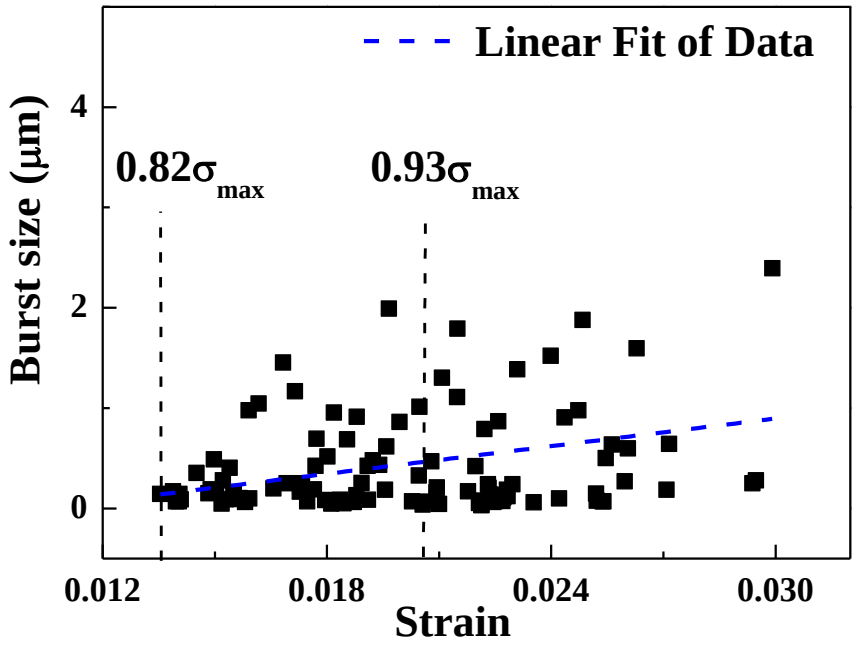

Figure 4.39 Dependence of displacement burst size as a function of compressive strain for $Pd_{40}Ni_{40}P_{20}$ deformed at a nominal strain rate of 2 x 10^{-4} s^{-1}.

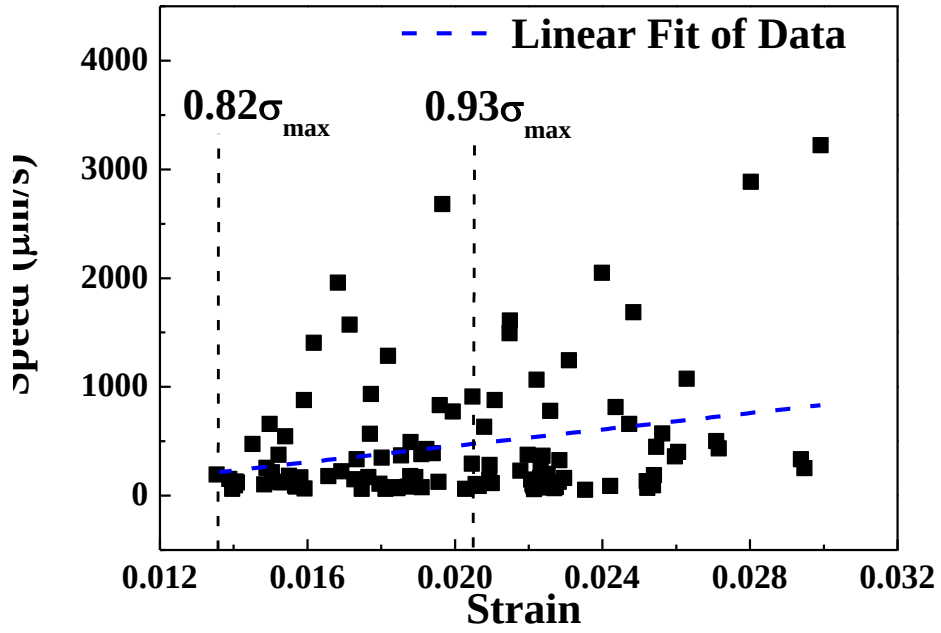

Figure 4.40 Dependence of shear-band propagating speed as a function of compressive strain for $Pd_{40}Ni_{40}P_{20}$ deformed at a nominal strain rate of 2 x 10^{-4} s^{-1}.

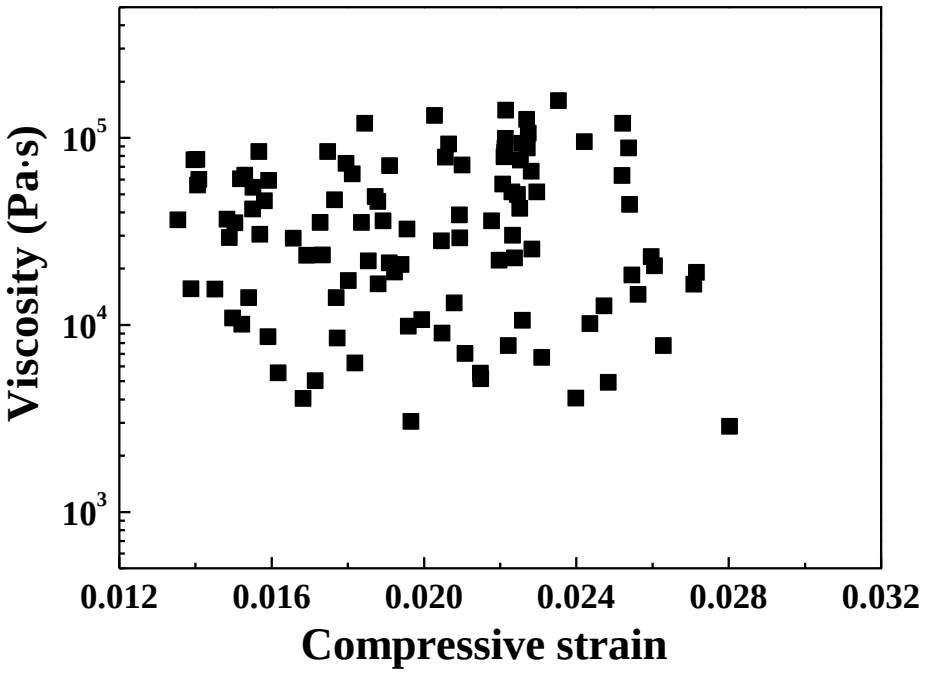

Figure 4.41 Dependence of viscosity within a propagating shear band as a function of compressive strain for the $Pd_{40}Ni_{40}P_{20}$ BMG at a nominal strain rate of 2×10^{-4} s^{-1}.

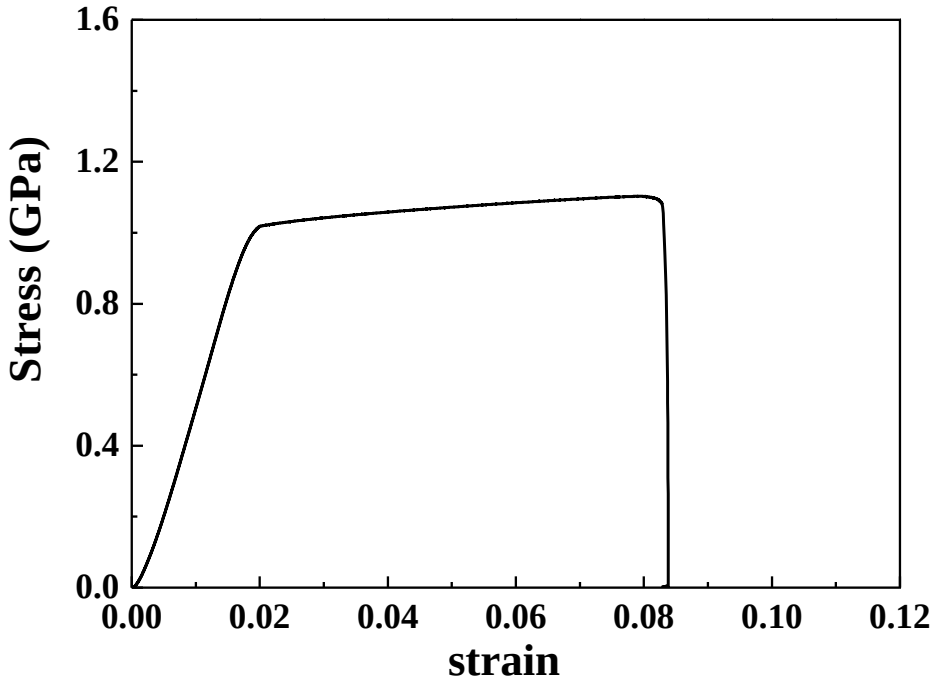

Figure 4.42 Typical engineering stress-strain curve of the Mg-based BMG with 25 vol % porous Mo particles at a nominal strain rate of 2 x 10^{-4} s^{-1} in compression.

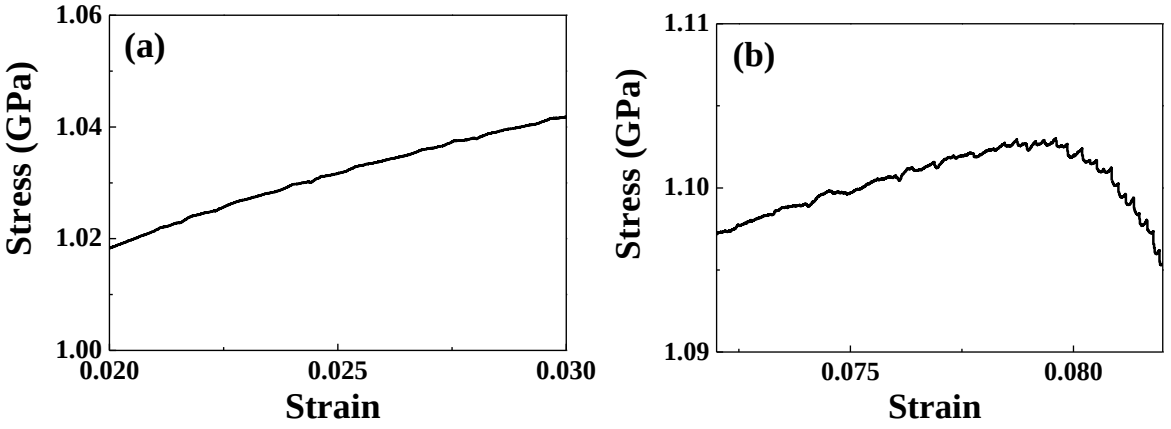

Figure 4.43 Enlarged view of (a) the plastic region right after yielding and (b) the plastic region before failure, showing no obvious flow serration.

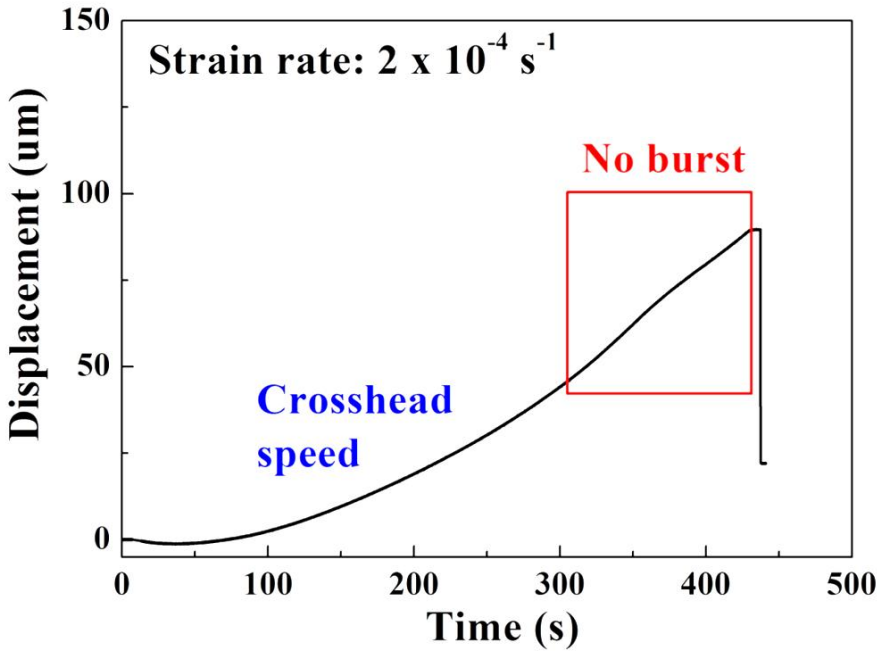

Figure 4.44 Displacement as a function of time of taken from the record of strain gauges for the Mg-based BMGC with porous Mo particles. The insert shows no distinct occurrence of displacement burst.

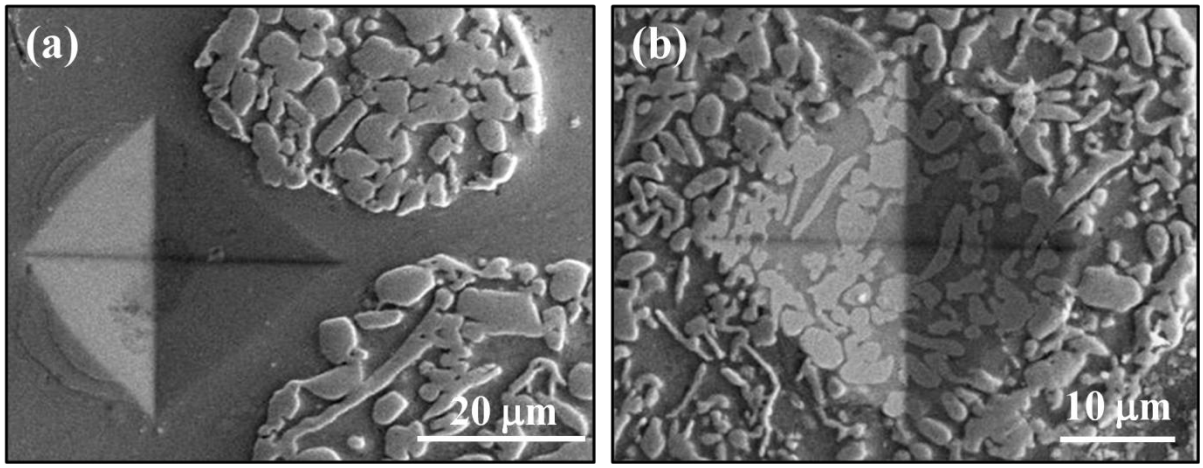

Figure 4.45 SEM observation of micro-indentation mark near the porous Mo particles within the Mg-based amorphous matrix.

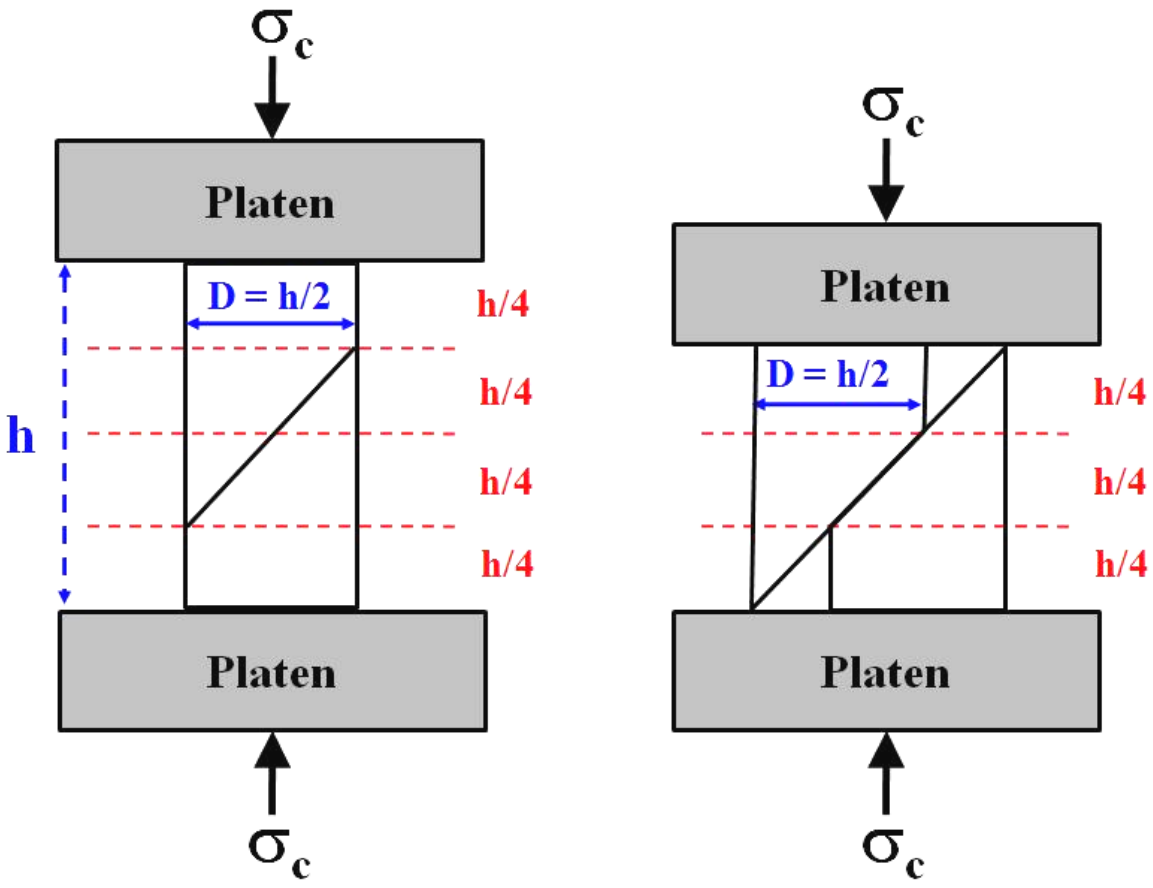

Figure 5.1 Left one shows the schematic illustration of a compression test on the sample with an aspect ratio of 2. Right one shows that, under the deformation mode of single shear along the principal plane, compressive data have no physical meaning once the strain is over 25%.

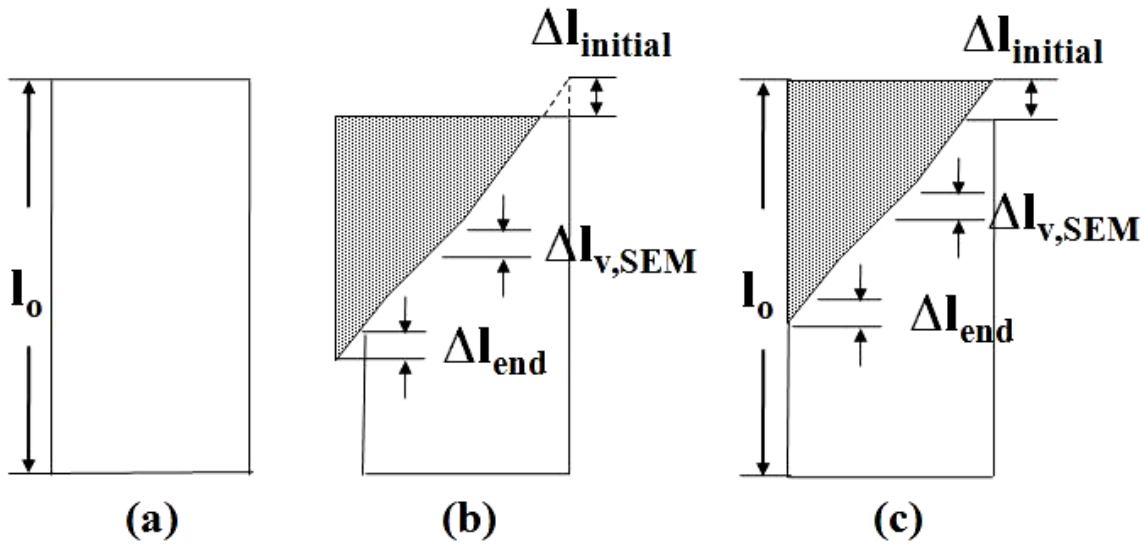

Figure 5.2 Schematic analysis of the sample compressed to a 7% strain: (a) the original sample, (b) after deformation, and (c) the restored sample.

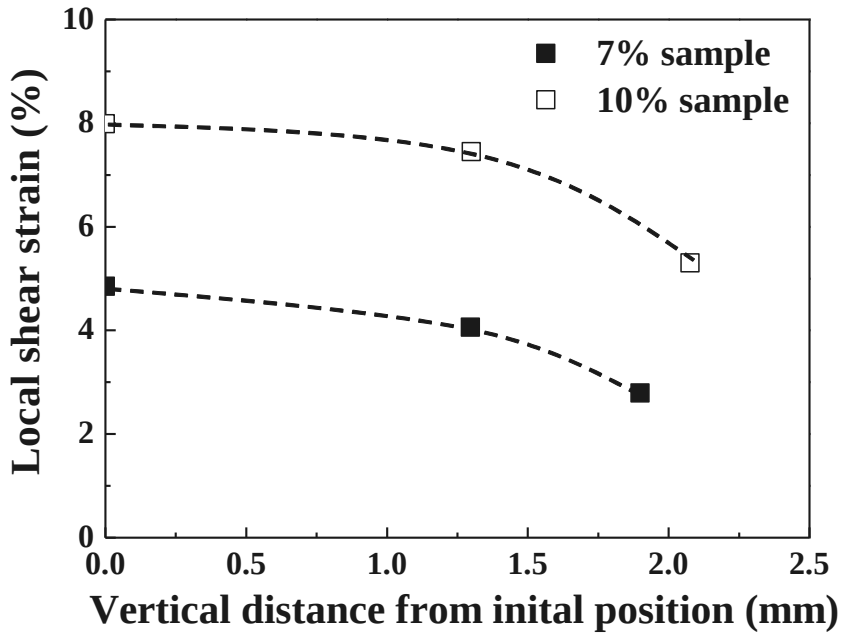

Figure 5.3 The local shear strain as a function of vertical distance from the shear band initiation site for the 7% and 10% samples.

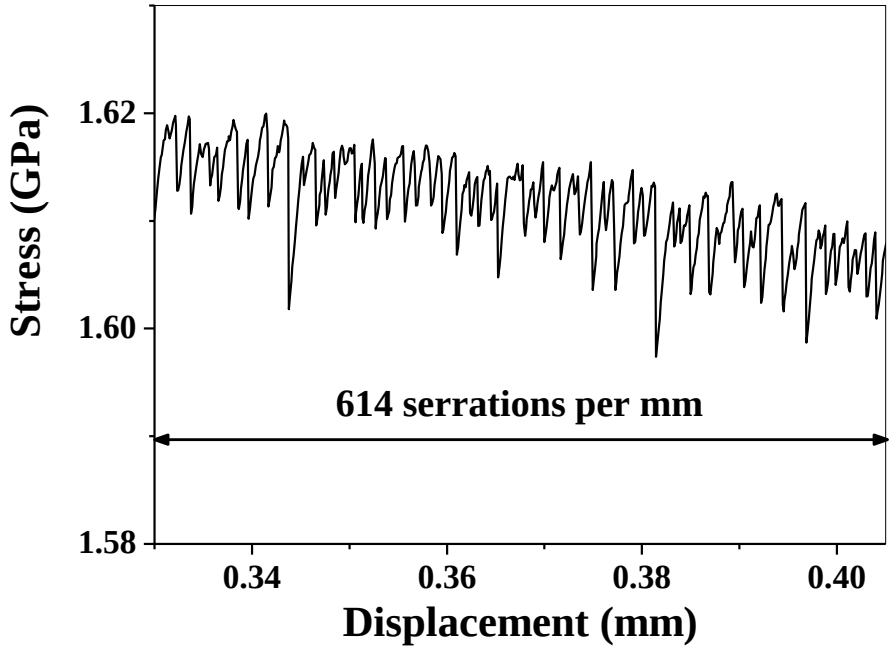

Figure 5.4 Enlarged view of the serrated region taken from the stress-displacement curve of the phase-separated Zr-based BMG at a nominal strain rate of 2×10^{-4} s^{-1}.

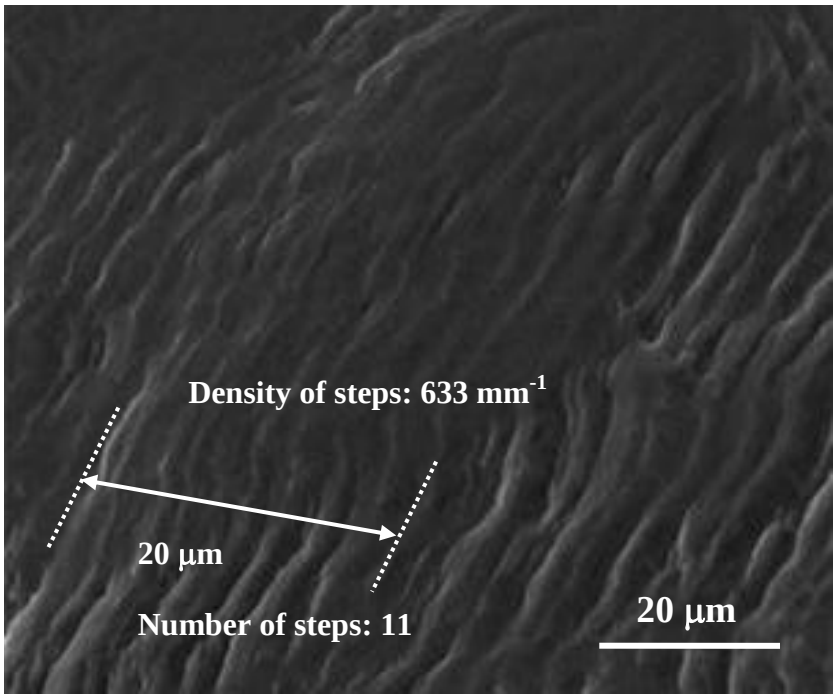

Figure 5.5 Enlarged SEM image of the sheared surface of the phase-separated Zr-based BMG.

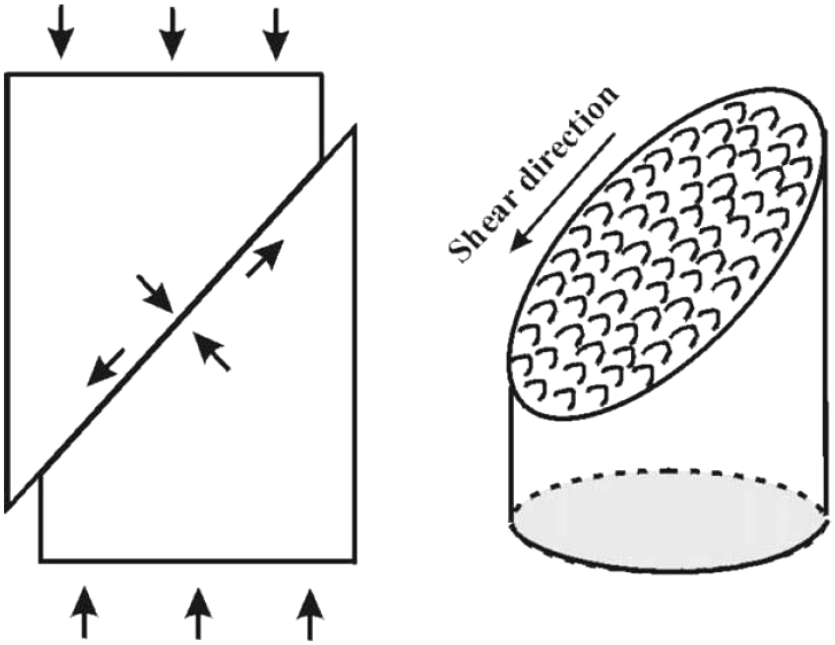

Figure 5.6 Schematic illustration of fracture process in metallic glasses under compressive loading, showing the vein-like patterns on the fracture surface [44].

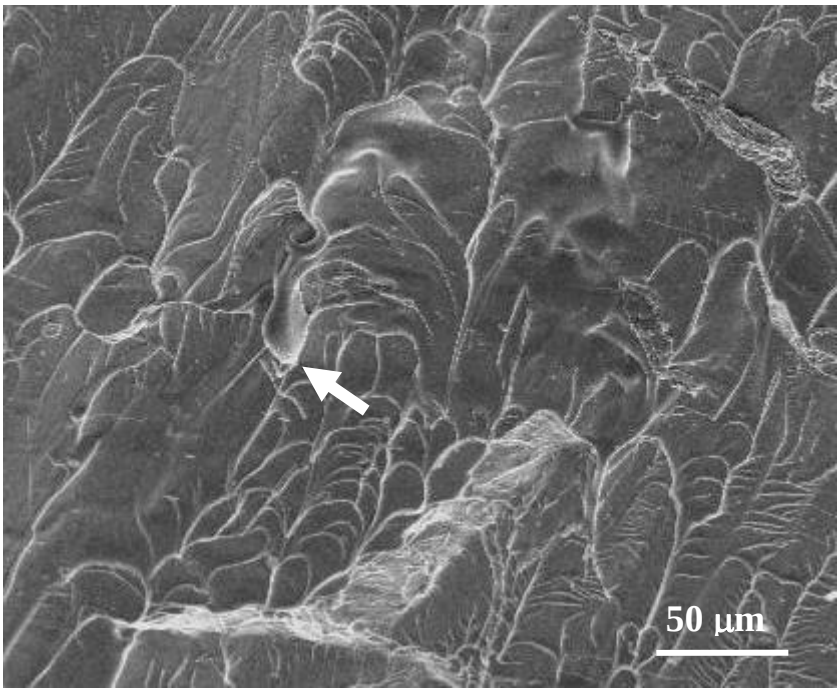

Figure 5.7 Re-solidified droplets on the fracture surface of the phase-separated Zr-based BMGs, as marked by an arrow.

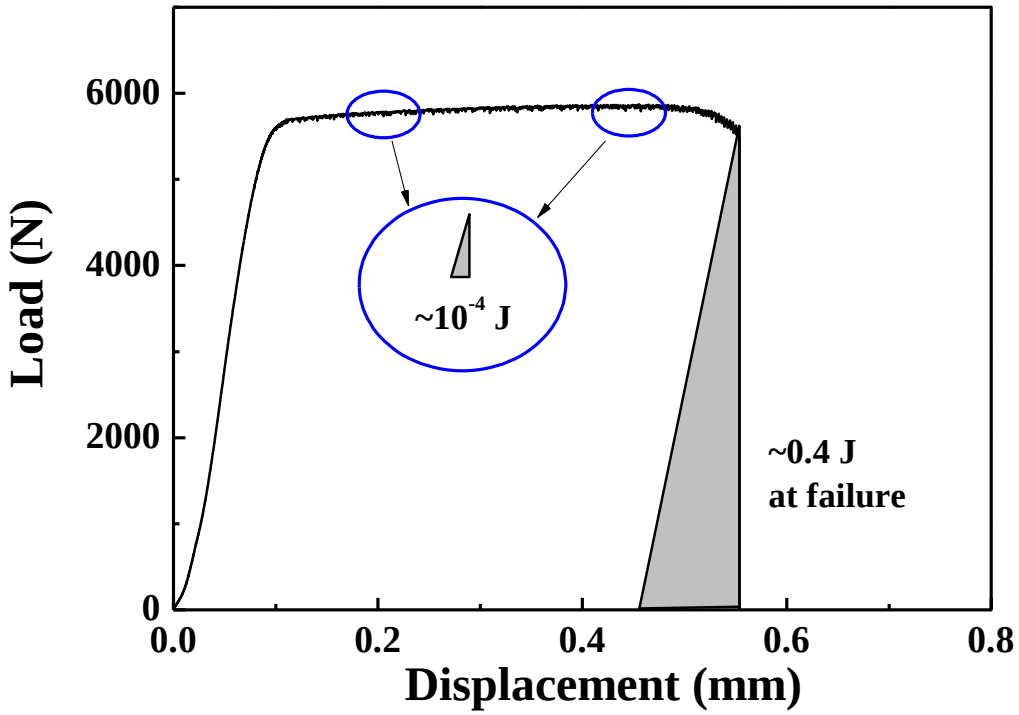

Figure 5.8 The compressive load-displacement curve of the phase-separated Zr-based BMG during inhomogeneous deformation. The triangles represent the work released during one serration and at fracture.

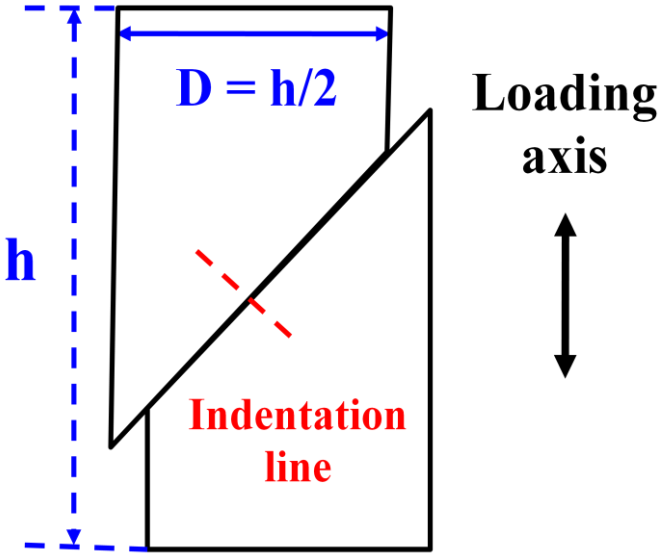

Figure 5.9 Schematic illustration of nanoindentation on the deformed sample.

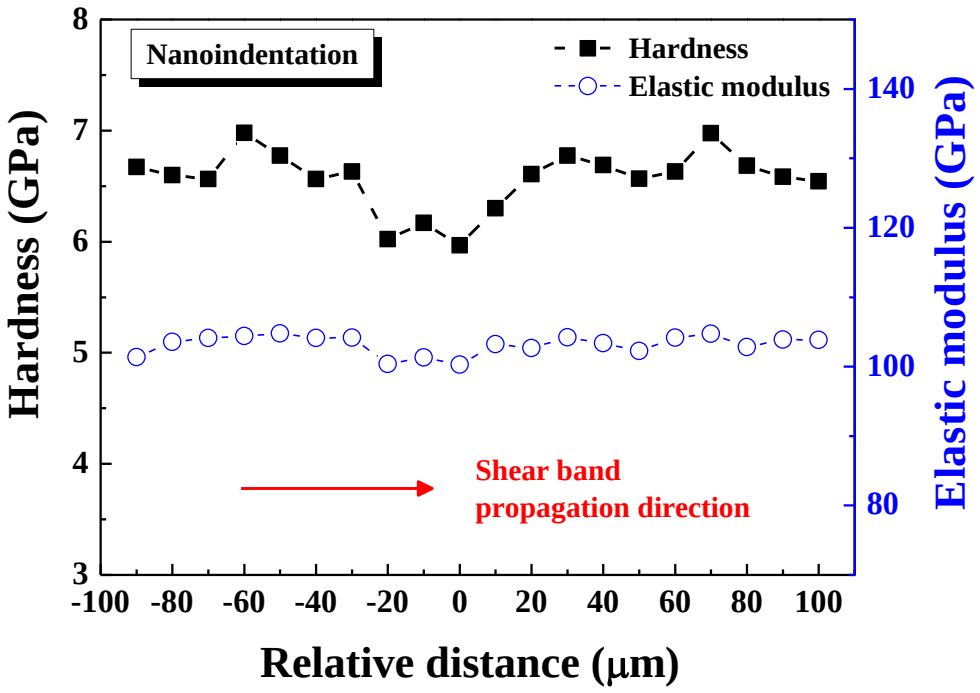

Figure 5.10 Hardness and elastic modulus in nanoindentation as a function of the relative distance from major shear band. The nanoindentation follows the direction perpendicular to the shear band, as illustrated in Figure 5.9. The interval of two indented points is 10 μm.

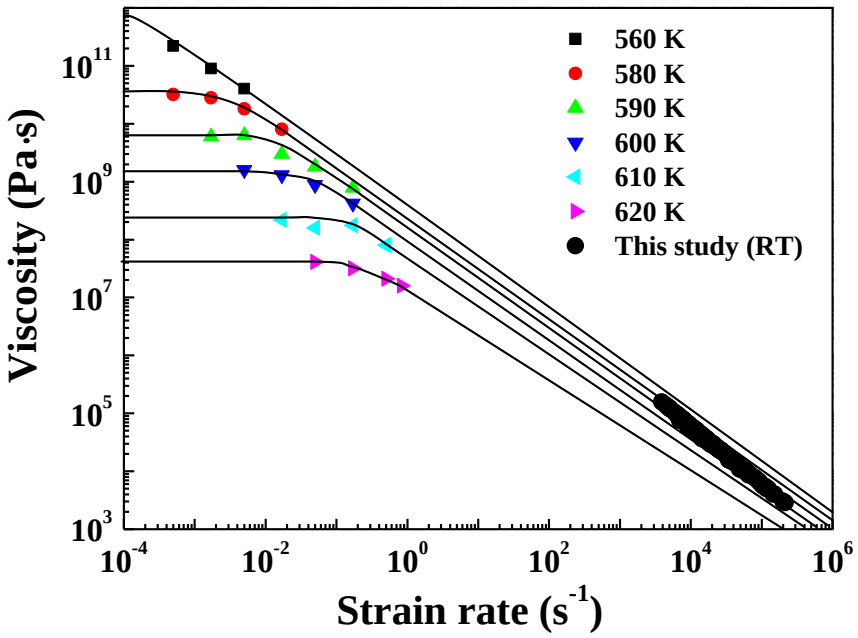

Figure 5.11 Viscosity as a function of strain rate for the Pd-based BMG at room temperature (RT) and data taken from a Pd-based BMG at various temperatures [205]. Solid lines represent the numerical solution to a self-consistent VFT equation.

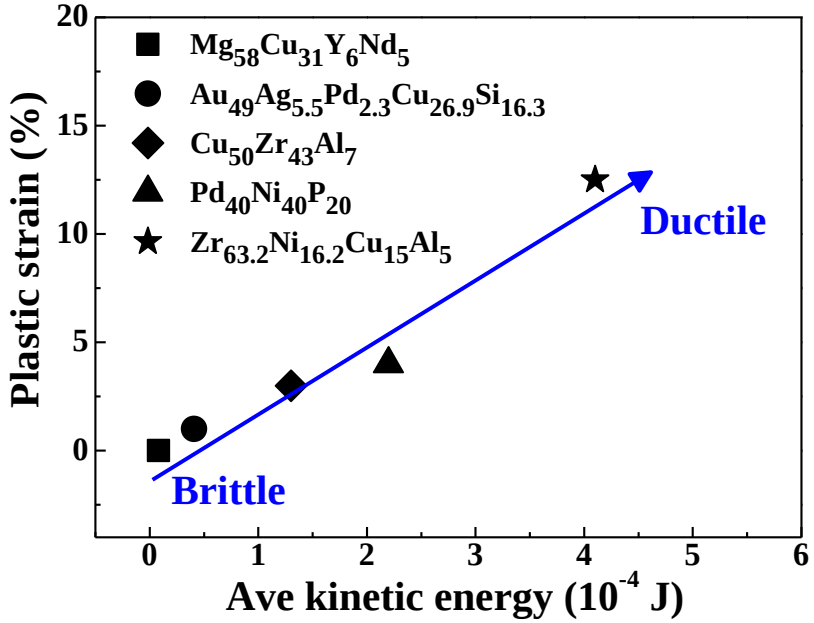

Figure 5.12 Relationship of compressive plastic stain and kinetic energy stored during each serration in different alloy systems (Zr-, Pd-, Cu-, Au- and Mg-based BMGs) at a low strain rate of 2 x 10^{-4} s^{-1}.

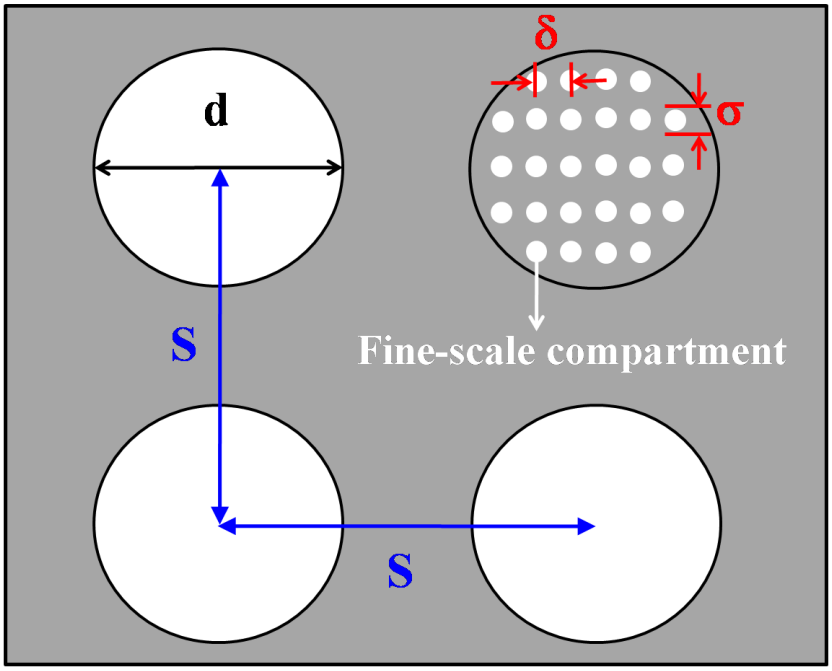

Figure 5.13 Schematic illustration of regular cubic array of the porous Mo particles reinforced Mg-based BMGC.